

THERMAL PHENOMENA IN
NANOSTRUCTURED MATERIALS & DEVICES

A DISSERTATION
SUBMITTED TO THE DEPARTMENT OF
MECHANICAL ENGINEERING
AND THE COMMITTEE ON GRADUATE STUDIES
OF STANFORD UNIVERSITY
IN PARTIAL FULFILLMENT OF THE REQUIREMENTS
FOR THE DEGREE OF
DOCTOR OF PHILOSOPHY

Amy Marie Marconnet

August 2012

© 2012 by Amy Marie Marconnet. All Rights Reserved.

Re-distributed by Stanford University under license with the author.



This work is licensed under a Creative Commons Attribution-Noncommercial 3.0 United States License.

<http://creativecommons.org/licenses/by-nc/3.0/us/>

This dissertation is online at: <http://purl.stanford.edu/hf944pf2976>

I certify that I have read this dissertation and that, in my opinion, it is fully adequate in scope and quality as a dissertation for the degree of Doctor of Philosophy.

Kenneth Goodson, Primary Adviser

I certify that I have read this dissertation and that, in my opinion, it is fully adequate in scope and quality as a dissertation for the degree of Doctor of Philosophy.

Jelena Vuckovic

I certify that I have read this dissertation and that, in my opinion, it is fully adequate in scope and quality as a dissertation for the degree of Doctor of Philosophy.

Xiaolin Zheng

Approved for the Stanford University Committee on Graduate Studies.

Patricia J. Gumpert, Vice Provost Graduate Education

This signature page was generated electronically upon submission of this dissertation in electronic format. An original signed hard copy of the signature page is on file in University Archives.

ABSTRACT

Nanostructuring leads to unique material properties and combinations of properties not naturally available in bulk materials. The study of these properties is critical to improving the device performance and reliability for a range of applications including electronics, thermoelectrics, and nanophotonics. This work focuses on efforts to push the thermal conductivity of nanostructured materials to the extremes: the thermal conductivity of carbon nanotubes (CNT) and nanotube-based materials can exceed that of metals, while the introduction of nanoscale boundaries (e.g. nanoscale pores in silicon nanowires) yields extremely low thermal conductivity materials. Furthermore, this nanostructuring also leads to unique combinations of properties. Porous silicon nanowires are a step towards the desired electron-crystal, phonon-glass combination ideal for thermoelectric applications, while thermally-conductive, mechanically-compliant carbon nanotube films for promising for electronics packaging.

This work first explores how the high axial thermal conductivity of carbon nanotubes can be leveraged effectively in thin film and composites through detailed understanding of the phonon transport. A detailed review of past research, both theoretical and experimental, combined with new experiments probing the impact of volume fraction and interface resistances in CNT arrays yields new insight into the mechanisms impacting phonon transport in both individual carbon nanotubes and films and composites formed from CNTs.

In contrast, nanostructuring silicon significantly reduces the thermal conductivity through enhanced boundary scattering and the possibility of phononic crystal effects. Measurements of individual, porous silicon nanowires show reduction in the thermal conductivity beyond that which is predicted by boundary scattering using a modified Callaway-Holland thermal conductivity model. A new method for calculating the increased scattering rate due to the pore boundaries is developed to account for these nanoporous geometries. Experimental data for aligned arrays of silicon nanowires with

varying diameter and degrees of porosity show that the combination of porosity and nanoscale dimensions effect severely reduces the thermal conductivity.

Finally, the composition and annealing conditions impact both thermal transport and photoluminescence in silicon-rich silicon nitride films. A significant correlation between the thermal conductivity and the PL lifetime suggests that the microstructure and bonding defects strongly influence both properties. Furthermore, erbium doping reduces the thermal conductivity due to enhanced phonon scattering. These data facilitate optimization of the microstructure through stoichiometry control and annealing temperature selection.

ACKNOWLEDGEMENTS

I would first like to thank my research advisor, Professor Kenneth E. Goodson. From my first discussions with Ken, I realized that not only would working in the Microscale Heat Transfer Lab lead to interesting research, but also Ken would provide a supportive, engaging, stimulating research environment. Since those initial meetings, I have greatly enjoyed the many discussions and appreciated the honest advice as I transitioned from a new graduate student through my defense and applying for faculty positions. The freedom to pursue a variety of research topics over the past five years has kept me engaged and excited about nanoscale thermal transport. I would also like to thank Professors Xiaolin Zheng and Jelena Vuckovic, who have provided guidance and advice over the past few years, first as collaborators and later as members of my reading committee. I would also like to thank Professor Prinz for serving on my defense committee. For serving as my defense committee chair (and on my quals committee), I would like to thank Professor David A.B. Miller. I would also like to thank my undergraduate research advisor, Professor John Booske, for continuing to provide invaluable advice and support throughout my graduate studies. I would also like to thank Professor Mehdi Asheghi for his advice which aided many of my research projects.

I am extremely grateful to a number of collaborators who have made my research possible – not only in providing samples, but also for the interesting discussions following the measurements. In particular, I would like to thank Dr. Namiko Yamamoto, Dr. Hai Duong, and Professor Brian Wardle (CNT films and composites); Dr. Selcuk Yerci and Professor Luca Dal Negro (silicon nitride films); Dr. Yiyang Gong, Professor Jelena Vuckovic, and the Nanoscale and Quantum Photonics Lab (nanophotonic crystal cavities); and Jeff Weisse, Professor Xiaolin Zheng, and the Zheng Research Group (silicon nanowire arrays); Dr. Ruxandra Vidu and her students (thermoelectric nanowires and films); and Dr. Munekazu Motoyama and Professor Prinz (Cu-on-CNT electrodeposition). I would also like to thank Chuan Hu of Intel and the Semiconductor Research Consortium for his continual interest in my work and the stimulating discussions.

I cannot thank my fellow group members enough for their support and encouragement over the past five years. In particular, I would like to thank Dr. Milnes David for his mentorship during my first year in the lab working on microfluidic heat exchangers and for the continued friendship. Dr. Matthew Panzer and Dr. Jeremy Rowlette were instrumental in my seamless transition from the “Bubbles” to the “Phonons” and provided countless hours of training on the laser-based measurement rigs and detailed physics discussions. Dr. Takashi Kodama has been instrumental in the development and fabrication of nanocharacterization platforms – I cannot thank Takashi enough for the countless hours spent in the fab. My mentees (Sri Lingamneni, Michael Barako, and Woosung Park) have been instrumental in my ability to simultaneously conduct multiple projects these last few years and I appreciate their support, intellectual curiosity, and dedication. My “contemporaries” in the lab and throughout MERL (including Yuan Gao, Shilpi Roy, Zijian Li, Jaeho Lee, Joe Miler, Anita Rogacs, and Jeff Weisse) have been a great support system. I truly appreciate their feedback, advice, and friendship over the years.

I am extremely grateful for the support of my family and friends. My parents, Donna and Greg, have always encouraged my interests and have provided endless love and support. My brothers, Alex and Andrew, and my sister-in-law, Kari, have just been awesomely supportive every step of this long journey. My whole extended family has always celebrated my successes, listened to my worries, provided distractions when needed, and helped me to succeed. Ray Sierra, Elia Junco, Matthew Suss, Gaurav Bahl, Milnes David, and all my friends at Stanford have made the last five years very enjoyable. I truly appreciate the continuing friendship and support of Michael and Kris Buehler, who helped me find a great work-life balance during our time at UW-Madison. It was a pleasure to get to know Dr. Sung Ki (Albert), Hailey, and Matthew Kim during their time at Stanford and I am grateful for our ongoing friendship.

Financial support for this research was provided by the National Science Foundation Graduate Research Fellowship Program and the Brit and Alex d'Arbeloff Stanford Graduate Fellowship, as well as grants from the Air Force Research Laboratory Small Business Technology Transfer, the ONR, the NSF-DOE thermoelectrics partnership, and MARCO Interconnect Focus Center.

TABLE OF CONTENTS

ABSTRACT	iv
ACKNOWLEDGEMENTS	vi
TABLE OF CONTENTS	viii
LIST OF TABLES	xi
LIST OF FIGURES	xii
CHAPTER 1: INTRODUCTION.....	1
1.1 Scope of Work.....	4
1.2 Organization	5
CHAPTER 2: Review of Thermal Conduction Phenomena in Carbon Nanotubes and Related Nanostructured Materials	7
2.1 Introduction	7
2.2 Thermal Conduction by Individual Nanotubes	9
2.2.1 Physical Mechanisms	9
2.2.2 Experimental Progress.....	12
2.2.3 Theoretical Progress	18
2.2.3.1 Landauer Approach	19
2.2.3.2 Phonon Transport Calculations.....	23
2.2.3.3 Molecular Dynamics Simulations.....	27
2.2.4 Summary of Key Findings.....	30
2.2.4.1 Geometrical Effect.....	30
2.2.4.1.1 Length	30
2.2.4.1.2 Chirality and Diameter	35
2.2.4.2 Temperature Dependence	38
2.2.4.3 Influence of Defects.....	41
2.3 Thermal Conduction in Carbon Nanotube Arrays and Mats.....	43

2.3.1	Thermal Conductivity	45
2.3.2	Boundary Resistance	52
2.3.3	Applications.....	57
2.4	Conclusions	58
CHAPTER 3: Thermal Conduction in Carbon Nanotubes Films and Composites.....		61
3.1	Introduction	61
3.2	Thermal Conduction in Mechanically-Densified, Aligned CNT Films	62
3.3	Thermal Conduction in Aligned Carbon Nanotube-Polymer Nanocomposites with High Packing Density	67
3.3.1	Overview	67
3.3.2	Methods	70
3.3.2.1	Fabrication	70
3.3.2.2	Comparative Infrared Thermal Microscopy	71
3.3.3	Results & Discussion.....	73
3.3.4	Summary.....	80
3.4	Nanoscale Conformable Coatings for Enhanced Thermal Conduction of Carbon Nanotube Films.....	82
3.4.1	Introduction	82
3.4.2	Fabrication.....	82
3.4.3	Thermal Characterization: Cross-Sectional Infrared Microscopy	86
3.4.4	Conclusions	89
CHAPTER 4: Thermal Conduction in Nanostructured Silicon		90
4.1	Introduction	90
4.2	Phonon Conduction in Periodically Porous Silicon Nanobridges	90
4.2.1	Introduction	90
4.2.2	Electrothermal Measurements	91

4.2.2.1	Details of the Numerical Electrothermal Model	97
4.2.3	Modeling the Thermal Conductivity of Silicon Nanoladders	100
4.2.3.1	Model for Bulk Silicon	100
4.2.3.2	Nanobeam Boundary Scattering	102
4.2.3.3	Pore Boundary Scattering	106
4.2.3.4	Details of the Random Path Tracing Phonon Scattering Model	108
4.2.3.5	Estimate of Impact of Modified Phonon Dispersion Relationships.....	109
4.2.4	Concluding Remarks	111
4.3	Effects of Porosity on the Thermal Conductivity of Silicon Nanowires in Aligned Silicon Nanowire–Parylene Composites	113
4.3.1	Fabrication.....	113
4.3.2	Nanosecond Transient Thermorefectance (TTR).....	115
4.3.3	Results & Discussion.....	116
4.3.4	Conclusion.....	120
CHAPTER 5:	Thermal Conduction in Silicon Nitride Films.....	121
5.1	Introduction	121
5.2	Methodology.....	122
5.3	Results & Discussion.....	123
5.4	Summary.....	128
CHAPTER 6:	Conclusion.....	129
6.1	Summary.....	129
6.2	Discussion and Suggestions for Future Work	131
6.2.1	Individual Nanowires: Impact of Nanostructured Pores	131
6.2.2	Nanowire Arrays	133
6.2.3	Embedded Nanoparticles: Thermal Conduction & Heat Generation ...	135
Bibliography	137

LIST OF TABLES

Table 2.1: Measured Room Temperature Thermal Conductivities of Individual Carbon Nanotubes. Data from all authors is standardized here using the enclosed cross-sectional area of the nanotube (i.e. using the outside diameter for MWCNTs). Additionally, for SWCNT samples, the thermal conductivity calculated with the circumference times the thickness of a nanotube shell is shown for comparison. Yu <i>et al.</i> [63] measured the thermal conductance and uncertainty in the diameter of the nanotube resulted in a wide range for the thermal conductivity. Pettes and Shi [60] report a lower bound in thermal conductivity for SWCNT and double-wall carbon nanotube (DWCNT), but extract an estimate of the intrinsic thermal conductivity for the MWCNTs. Choi et al. [57, 67] did not explicitly state which definition of area they used to calculate thermal conductivity, so the value in the table is as reported in the articles.	14
Table 2.2: Phonon Transport Model Summary	24
Table 2.3: Molecular Dynamics Simulations Summary. Room temperature thermal conductivity values for the maximum length simulated.....	29
Table 2.4: Temperature Dependence of the Thermal Conductivity of Carbon Nanotubes. Experimental results for MWCNTs appear to follow similar trends with temperature as SWCNTs.	39
Table 3.1: Electroplating Conditions & Film Thickness.....	83
Table 4.1: Summary of SiNW array diameter and porosity control.....	115

LIST OF FIGURES

Figure 1.1: *Thermal Conductivities of Bulk and Nanostructured Materials*. (a) At room temperature, the thermal conductivities of bulk materials span a large range: from gases and aerogels with thermal conductivities less than 0.1 W/m/K to highly-crystalline diamond with a thermal conductivity >1000 W/m/K. (b) The introduction of nanoscale feature generally leads to a significant reduction in thermal conductivity in crystalline materials. Crystalline, bulk silicon has a thermal conductivity of ~ 150 W/m/K and enhanced phonon-boundary scattering reduces the thermal conductivity of silicon thin films, nanowires, and porous materials to as low as ~ 20 W/m/K [24], ~ 1 W/m/K [27, 28], ~ 1 W/m/K [26], respectively, depending on geometrical parameters. (c) Graphite has a highly anisotropic crystal structure with sheets of carbon atoms stacked on top of each other (as shown the center of panel c). In along the c-axis (perpendicular to the stacked sheets of carbon atoms), the thermal conductivity is quite low (~ 1 to 10 W/m/K [29]). In the direction perpendicular to the c-axis (in the plane of the sheets of carbon atoms), the thermal conductivity is quite high (exceeding 1000 W/m/K [29]). Graphene (a single sheet of carbon atoms) can have an in-plane thermal conductivity exceeding 1000 W/m/K [29]. Carbon nanotubes (a sheet or sheets of carbon atoms rolled into a tube) can also have high thermal conductivities (>1000 W/m/K) along the direction of the CNT-axis [29, 30]. In contrast, if the crystalline structure of the carbon atoms is removed (*i.e.* amorphous carbon), the thermal conductivity is reduced to < 1 W/m/K [29]. References for figures: [28, 31-37]. 2

Figure 2.1: Two differing strategies for measuring thermal conductivity of individual carbon nanotubes. (a) Passive Technique. A temperature difference generated by a heater at one end of the nanotube is captured using sensors at both ends. (b) Self-Heating Technique. Heat is generated by applying a voltage across the nanotube, resulting in electrical heating of the nanotube, and the temperature

distribution is deduced from the resulting electrical resistance change and calibration data. 13

Figure 2.2: (a) Phonon dispersion relationship for (10,10) nanotube calculated by Yamamoto *et al.* [86]. The inset shows that the energy gap of the lowest optical mode ($\hbar\omega_{op}$) decreases with nanotube radius. With this model, all four acoustic modes exhibit a linear dispersion relationship because the impact of bond bending is neglected. (b) Phonon dispersion relationship for (10,10) armchair nanotube calculated by Mahan and Jeon [87]. Two transverse (“flexure”) modes exhibit a quadratic dispersion relationship, while the longitudinal and twist modes are linear..... 20

Figure 2.3: Room temperature thermal conductance of carbon nanotubes as a function of length. Filled-in symbols denote MWCNTs, while open symbols denote SWCNTs. The solid line indicates the $1/L$ trend expected for a fixed thermal conductivity, i.e. diffusive conduction in nanotubes. 32

Figure 2.4: Predictions and data for the thermal conductance of single-wall carbon nanotubes with comparable nanotube diameters. The models of Wang *et al.* [84], Wang *et al.* [56, 70], and Shang *et al.* [83] were computed with nanotubes with approximately 1.9 nm diameter and for Wang *et al.* [84] and Shang *et al.* [83] a mean free path of 180 nm was used in the calculations. For the empirical model of Pop *et al.* [68], a phonon mean free path of 500 nm was extracted from experiments. The ballistic conductance models can be extended to any chirality of nanotube and to multi-wall nanotubes, however, the model from Pop *et al.* [68] was developed in conjunction with experimental data for thermal conductivity versus temperature, so is strictly only valid for nanotubes of the same diameter and chirality. For the wave vector model of Wang *et al.* [56], the Grüneisen parameter and the specularly of boundary scattering were adjusted to match the data from their experiment. The molecular dynamics simulation of Che *et al.* [1] was computed only up to lengths of 50 nm, but above ~10 nm a

uniform value of the thermal conductivity was achieved and that is what is plotted. All measurements and predictions are at room temperature. 33

Figure 2.5: Thermal conductivity data as a function of nanotube diameter. Open and filled data points are for single-wall and multi-wall nanotubes, respectively. A decrease in thermal conductivity with increasing diameter is observed. The range of values shown for Yu *et al.* [63] is due to the uncertainty in the measurement of the nanotube diameter. The SWCNT data for Pettes and Shi [60] is a lower bound on the thermal conductivity, while the effect of contact resistance at the ends of the nanotubes is accounted for in the MWCNTs. Thermal conductivity values are standardized using the enclosed area of the nanotube, $A = \pi d^2 / 4$ 35

Figure 2.6: (a) Low temperature thermal conductance of nanotubes with varying chirality as calculated by Yamamoto *et al.* [86]. (b) When the temperature is scaled by the energy gap of the lowest optical mode, the thermal conductance for each of the different chiralities collapses to a single curve [86]. 38

Figure 2.7: (a) Diameter-adjusted CNT thermal conductivity as a function temperature. Pop *et al.* [68] used this data to calculate the empirical model of thermal conductivity with temperature shown in the right panel of the figure. (b) Thermal conductivity as a function of temperature using an empirical model based on experimental data in the left panel. Figures from Pop *et al.* [68]. 41

Figure 2.8: Effect of Defects on Thermal Conductivity. Effect of (a) vacancy and (b) (5,7,7,5) defect concentration from Che *et al.* [1] using MD simulations. The solid lines are the best fit to the molecular dynamics simulations. (c) Effect of ^{14}C isotope impurity as computed by Zhang and Li [11] using non-equilibrium molecular dynamics simulations. 42

Figure 2.9: Schematic showing the sources of thermal resistance in an aligned CNT array including thermal boundary resistance between the growth substrate and the CNT film, the volumetric thermal resistance of the CNT film, and the

thermal boundary resistance between the free surface of the CNT and the metals or other material deposited or placed on top of the CNT layer. The volumetric thermal resistance of the CNT has contributions due to defects, inter-tube contacts, and the intrinsic thermal resistance of the individual CNTs. The color gradients in the schematic show that for a top-heated CNT array, only nanotubes in contact with the top heat source and the bottom substrate transfer heat efficiently to the substrate. 44

Figure 2.10: Intrinsic thermal conductivity as a function of volume fraction for aligned CNT films. These data are for the intrinsic thermal conductivity of the arrays, which have been determined separately from the interface resistances. The solid line shows the predicted film thermal conductivity for an ideal array of nanotubes each with an individual thermal conductivity of $3000 \text{ W m}^{-1} \text{ K}^{-1}$, while the dashed line shows the predicted film thermal conductivity with an individual CNT conductivity of $30 \text{ W m}^{-1} \text{ K}^{-1}$. Individual nanotubes thermal conductivities are provided on the left axis with volume fraction = 1. The volume fractions of aligned arrays range up to about 0.2, though unaligned densified arrays can achieve higher volume fractions. The densified arrays of Zhang *et al.* [118, 119] report volume fractions of ~0.8-0.9 through spark plasma sintering of unaligned CNT mats. All of the nanotube arrays perform lower than predicted by the high thermal conductivity of individual nanotubes, however, recent data is approaching that limit as nanotube array fabrication improves and the resistances at the interfaces are addressed. 46

Figure 2.11: Individual nanotube thermal conductances plotted as a function of nanotube length, as extracted from reported measurements for arrays of MWCNTs and from measurements of MWCNTs. Dashed line shows L^{-1} trend of the thermal conductance which is expected if the thermal conductivity of a nanotube saturates at lengths longer than the mean free path. Error bars due to uncertainty or variation in nanotube diameters in the arrays. 48

- Figure 2.12: Individual CNT thermal conductivities as a function of length extracted from reported data of the thermal conductivity or thermal conductance of CNT arrays. 50
- Figure 2.13: (a) Schematic and resistance models illustrating the conduction by two nanotubes in contact. In this example, one nanotube makes contact with both a heater and a heat sink. A second nanotube crosses the first but makes contact only with the heat sink. (b) Resistor network describing nanotubes in contact. While the second nanotube provides a second pathway for heat to transfer to the heat sink, the contact also provides a scattering site for the energy carriers. If the contact resistance is large, instead of aiding in the thermal conduction, the major effect of the second nanotube is to add a defect resistance to the conducting nanotube as modeled approximately by the extra resistor in the network in (c).52
- Figure 2.14: Representative TEM of Single-Wall CNT Array coated with thin film of aluminum from Panzer *et al.* [140] showing voids within the SWCNT array and, qualitatively, the regions of incomplete contact between the nanotubes with the aluminum layer. 54
- Figure 2.15: Total thermal resistance of CNT arrays plotted according to length. The total thermal resistance includes the thermal boundary resistance between growth substrate and CNT film, the intrinsic thermal resistance of the CNT film, and the thermal boundary resistance between the free surface of the CNT and the metals or other material deposited or placed on top of the CNT layer. The solid line shows the lower limit for the thermal resistance of a CNT array at a packing density of 3 percent if each individual CNT has a thermal conductivity of $3000 \text{ W m}^{-1} \text{ K}^{-1}$ and the thermal boundary resistance is negligible. The dot-dashed line shows an approximate lower bound on thermal resistance of commercial thermal greases used for thermal interface materials. Thermal greases and phase change materials have low thermal conductivities (on the order of $0.1\text{-}10 \text{ W m}^{-1} \text{ K}^{-1}$). The dashed line shows the approximate thermal resistance of commercial alloy solders. Metallic solders have higher thermal

conductivities (on the order of $40\text{-}90\text{ W m}^{-1}\text{ K}^{-1}$). Some of the best data for CNT arrays as thermal interface materials have achieved total thermal resistances less than commercially available greases, gels, and phase change materials and approaching that of metallic solders..... 58

Figure 3.1: *Sample geometries for thermal characterization of CNT films.* (a) *Original sample geometry with no reference layer.* The heat flux across the sample film is calculated from the current and voltage applied to the aluminum-coated silicon heater and the cross-sectional area of the CNT film. The infrared microscope is used to generate a two-dimensional temperature map across the length of the CNT film and surrounding materials. The two-dimensional temperature map is reduced to a one-dimension temperature profile (as sketched next to the sample geometry) by averaging in the direction perpendicular to the heat flux. From the heat flux and temperature gradient in the CNT film, the thermal conductivity of the CNT film is calculated with Fourier's law. (b) *Modified sample geometry with a quartz reference layer.* The infrared microscope is used to generate a two-dimensional temperature map across the length of the CNT film, quartz reference layer, and surrounding materials. With this geometry, the heat flux is calculated from the known thermal conductivity of quartz and the measured temperature gradient in the quartz. With the heat flux calculated from the quartz region and the temperature gradient in the CNT film, the thermal conductivity of the CNT film is calculated using Fourier's law. The modified geometry improves the estimate of the heat flux through the sample as in the original geometry, some of the power dissipated in the heater is lost through convection on the epoxy-coated side of the heater. 62

Figure 3.2: Temperature profile across the CNT film and quartz reference layer. Inset shows the two-dimensional temperature map spanning the (a) quartz reference layer, (b) CNT sample film, and (c) aluminum-coated silicon heater. The two-dimensional temperature map is averaged in the direction perpendicular to the heat flux to generate the 1-d temperature profile. The slopes in the linear portions of the curve are used for calculating the thermal conductivity, while the

jump in temperature between region (a), (b), and (c) are indicative of thermal interface resistances..... 63

Figure 3.3: Effect of length on the (a) thermal conductivity and (b) thermal resistance of 1 *vol.%* dense, vertically-aligned MWCNT films. No length dependence of the thermal conductivity is observed. The total thermal resistance (circles) consists of the thermal resistance between the CNTs and the heater (triangles), the intrinsic resistance through the thickness of the CNT film, and the resistance between the CNT-film and the growth substrate. For the thinnest sample, the resistance between the CNT film and the heater was smaller than resolvable with this technique. Note that no reference layer is used in these measurements..... 64

Figure 3.4: Thermal conductivity of mechanically-densified MWCNT films as a function of volume fraction. Note that a single quartz reference layer is used in these measurements to determine the heat flux through the sample film..... 66

Figure 3.5: Previous data for the thermal conductivity enhancement as a function of volume fraction for randomly dispersed CNT composites. This chart represents a subset of the available data where the matrix material has a thermal conductivity of 0.18 to 0.26 W m⁻¹ K⁻¹. 69

Figure 3.6: Schematic and SEMs of nanocomposite fabrication [147, 148]. (a) As grown CNT films with 1 *vol.%* CNTs. (b) Biaxial mechanical compression of CNTs up to 20 *vol.%* CNTs. (c) A-CNT-PNC fracture surface after capillary-driven epoxy infiltration of the CNT arrays. 71

Figure 3.7: IR Microscopy technique for thermal conductivity measurements. (a) Schematic of the testing configuration with an example temperature map. The sample sandwiched between two reference layers. A metallized piece of silicon is used as a heater and the structure is affixed to a silicon substrate with silver paste. The silicon substrate is affixed to the temperature controlled copper baseplate using thermal grease. (b): Temperature distribution across sample

including best fit slopes for both reference regions and the sample (temperatures averaged across the width of sample, i.e. each column in image (a)). 72

Figure 3.8: The axial (\square) and transverse (\circ) thermal conductivity of CNT nanocomposites and unfilled CNT forests (filled diamonds) as a function of volume fraction. The schematic below the legend shows the axial and transverse measurement directions for the aligned CNT composites. Best fits from the effective medium approach (solid lines) and with a power law (dashed line) are shown for the composite data. For the effective medium approach, the axial and transverse thermal conductivities are fit simultaneously with a non-linear least squares algorithm, assuming an alignment factor of 0.77 from the SEM analysis, with two free parameters: the individual CNT thermal conductivity ($22.1 \text{ W m}^{-1} \text{ K}^{-1}$) and the CNT-polymer boundary resistance ($<1 \times 10^{-9} \text{ m}^2 \text{ K W}^{-1}$). For the power law relationship $(k_e - k_m) = A \cdot f^B$, the prefactor, A , and the exponent, B , are fit with a non-linear least squares algorithm, while the measured matrix thermal conductivity, $k_m = 0.26 \text{ W m}^{-1} \text{ K}^{-1}$, is held constant. The fitted values are $A = 72.9 \text{ W m}^{-1} \text{ K}^{-1}$ and $B = 1.72$ for the axial thermal conductivity and $A = 11.3 \text{ W m}^{-1} \text{ K}^{-1}$ and $B = 1.37$ for the transverse thermal conductivity. The dashed green line indicates the thermal conductivity of the epoxy. 74

Figure 3.9: Cartoon illustrating of key mechanisms impacting thermal conduction in CNT composites including variations in the intrinsic CNT thermal conductance, interface resistances, variations in CNT lengths, spatially-varying CNT alignment and CNT-CNT contacts, as well as defects within CNTs and voids in the polymer matrix. 78

Figure 3.10: SEM images of CNT film highlighting the non-uniformity in the surface of the CNT film. SEM images courtesy of Xidex Corporation. 82

Figure 3.11: Close-up SEM images of copper films on CNT arrays. Panels (A) through (E) correspond to samples A through E. Note that the image in panel E is from a region of the sample without the CNT film. (F) Zoomed-out SEM image of

electroplated copper film on the CNT array (sample B) showing uniform coverage of the CNT film with copper..... 84

Figure 3.12: SEM images of surface of copper film (sample B) near the (a) center and (b) edge of the sample. Uniform surface roughness and grain size is observed across the top surface of the sample. In panel (b), a layer of small grains is evident below the large grains at the surface..... 85

Figure 3.13: Infrared Microscopy Measurement Strategy. (a) Schematic showing metalized CNT film on the silicon growth substrate attached to a secondary silicon handle wafer mounted to a temperature controlled copper baseplate. Current passed through the metal film generates a heat flux through the CNT film. (b) Two-dimensional temperature map of the CNT film during test. The temperatures are averaged for each row of pixels in the image to yield the one-dimensional temperature profile shown in panel (c). The temperature gradient in the CNT film is calculated from a least-squares linear fit (red line) to the region of the temperature profile containing the CNT film..... 87

Figure 3.14: Thermal conductivity as a function of volume fraction for CNT films from this work (red circles) compared to values reported for measurements for vertically-aligned CNT arrays and individual nanotubes (volume fraction = 1). For individual nanotubes, the hollow and filled symbols indicate measurements of SWCNTs and MWCNTs, respectively. The solid line shows the ideal CNT film thermal conductivity estimated for a given volume fraction using an individual nanotube conductivity of 3,000 W/m/K, while the dashed line is the estimate using an individual nanotube conductivity of 30 W/m/K. References: [56, 57, 62-64, 67-70, 108-116, 118-120, 124, 125, 178, 179]. 88

Figure 4.1: (a) SEM of a nanoladder measurement device. The nanoladder is connected to 4 electrical probe pads (two for applying current (marked I) and two for measuring voltage (marked V)). The dashed rectangle approximately marks the extent of the suspended region. (b) Cross-section of a nanoladder measurement device. The nanoladder is fabricated using electron beam lithography from a

silicon-on-insulator wafer with 200 nm device layer and a 1 micron thick oxide layer. Forty nanometers of palladium is deposited on the devices and serves as both a heater and a thermometer in the system. (c) Calculated temperature profile along the nanobeam and corresponding electrical conductivity for the beam without holes at 300 mA applied current. For each current level, a numerical electrothermal model is used to calculate the temperature profile along the nanoladder and extract the increase in electrical resistance. (d) Comparison of measured and predicted increase in electrical resistance as a function of the square of the applied current for a silicon nanobeam without holes. The measured increase in resistance depends strongly on the thermal conductivity of the silicon layer as indicated by the best fit line with $k_S = 112 \text{ W m}^{-1} \text{ K}^{-1}$ (solid black line) compared to $k_S = 100 \text{ W m}^{-1} \text{ K}^{-1}$ (dashed blue line) and $k_S = 125 \text{ W m}^{-1} \text{ K}^{-1}$ (dashed red line)..... 92

Figure 4.2: Silicon Nanoladder Thermal Conductivity. For the 200 nm thick nanoladders, the pores are spaced by 385. For the nanoladders with 110 nm diameter pores, the uncertainty in the thermal conductivity of the non-porous regions of the beam dominates the uncertainty in thermal conductivity of the porous region. For the larger diameter pore cases, the uncertainty is largely due to uncertainty in the measured value of pore diameter. For comparison, the thermal conductivity data for two-dimensional phononic crystals with pore spacings ranging from 500 nm to 800 nm fabricated from 500 nm thick Si films from Kim *et al.* [196] (diamonds, in-plane conductivity) and Hopkins *et al.* [183] (circles, out-of-plane conductivity)..... 95

Figure 4.3: Schematic showing the geometry and key parameters for the numerical model of the temperature distribution in the nanobeams and nanoladders. (a) In the top view of the porous nanobeam, three regions of the beam are indicated including two non-porous regions at the end of the beam of length L_e where $k_s(x)=k_e$ and the porous region in the center of the beam with $k_s(x)=k_p$. Four example discretized elements are shown with dashed boxes and correspond to the discretized elements shown in panel (b). The leftmost two boxes correspond

to case 1 (no hole) with the discretized element spanning the full width of the nanobeam. The rightmost two elements each contain a portion of a pore, corresponding to case 2, and consist of two sub-elements with widths less than the full beam width. 98

Figure 4.4: Calculated silicon thermal conductivity. (a) Comparison of bulk (blue line) and nanobeam (red lines) thermal conductivity. The estimated thermal conductivity for a rectangular nanobeam with a 550 nm x 200 nm cross-section calculated using the Sondheimer-Chambers [206, 207] approach is shown with the dashed red line and from the random phonon path calculation with the solid red line. (b) Comparison of bulk (blue line) and nanoladder (cyan lines) thermal conductivity. For 550 nm x 200 nm nanoladders with 200 nm pores spaced by 400 nm, the dashed cyan line shows the estimation from $\tau_{pores} = P/v_j(q)$, while the solid cyan line shows the estimation from the random phonon path calculation. In both cases, the reduction due to the outer nanobeam boundaries is calculated with the random phonon path calculation method. 101

Figure 4.5: Conductivity Reduction Function. (a) Thermal conductivity reduction function for a rectangular nanobeams with $AR = W/H$ of 2.75 (no holes) following the technique of Sondheimer and Chambers [206, 207] using numerical integration (dashed lines) compared with that using the random phonon path calculation (solid line). For the Sondheimer-Chambers approach, three specularities are considered $p=0$ (fully diffuse), $p=0.3$, and $p=0.9$ (mostly specular). (b) Thermal conductivity reduction for nanoladders (blue dashed line) with $AR = 2.75$, $W/D = 2.75$, and $S/D = 2$ using the random phonon path calculation compared to that of a nanobeam without holes ($AR = 2.75$) (solid red line). 104

Figure 4.6: (a) Fraction of phonons scattered by boundaries (green) compared to intrinsic scattering mechanisms (red) for a nanobeam with $AR = 2.75$. (b) Fraction of phonons scattered by pores (blue) and external nanobeam boundaries

(green) compared to intrinsic scattering mechanisms (red) for a nanoladder with $AR = 2.75$, $W/D = 2.75$, and $S/D = 2$ 105

Figure 4.7: Impact of hole (a) diameter and (b) spacing on the thermal conductivity of 550 nm x 200 nm silicon nanoladders. In panel (a) the pore spacing is fixed at 400 nm and the experimental results from this work are shown with black squares. In panel (b) the pore diameter is fixed at 200 nm. Calculations using the random pore scattering model are shown in blue, while those using the model $\tau_{pores} = P/v_j(q)$ are shown in red. 107

Figure 4.8: Ratio of the nanoladder [(a) 550 nm x 200 nm, $D = 200$ nm, $S = 400$ nm; (b) 55 nm x 20 nm, $D = 20$ nm, $S = 40$ nm] thermal conductivity considering coherent phonon effects to that neglecting coherent phonon effects. Calculations using the random pore scattering model are shown with solid lines, while those using the model $\tau_{pores} = P/v_j(q)$ are shown with dashed lines. 111

Figure 4.9: Fabrication of the vertical SiNW arrays for the nanosecond thermoreflectance measurements. (a,e) SiNW arrays are formed using the top-down etching; (b,f) Parylene is conformally deposited in between NWs and acts as a mechanical scaffold for the top metal transducer layer; (c,g) the SiNW tips are exposed by chemical mechanical polishing to ensure good thermal contact between the SiNWs and the metal film; and (d,h) a metal film is deposited over the SiNW array. The scale bars on the SEM images are 5 μm 114

Figure 4.10: Thermal conductivity of (~ 350 nm) large diameter SiNWs (10^{14} cm^{-3} p-type doping) with three levels of porosity, corresponding to different etching conditions. The thermal conductivity decreases significantly with increasing porosity. The inset images show the top view of the SiNWs and the scale bars are 200 nm. 117

Figure 4.11: (a) Thermal conductivity of nonporous and porous SiNW arrays of large diameter as a function of doping concentrations. TEM images show the relative porosity for Ag-MACE SiNW arrays fabricated with doping concentrations of

(b) 10^{14} , (c) 10^{16} , and (d) 10^{18} cm^{-3} . The scale bars on the TEM and inset TEM images are 5 nm and 200 nm, respectively..... 118

Figure 4.12: Thermal conductivity of SiNWs (10^{14} cm^{-3}) with small diameter ($d_{avg} \sim 130 \text{ nm}$) as a function of porosity. For comparison, the thermal conductivity of the large diameter SiNW etched at the same condition is shown as the red circle. Increasing nanowire porosity is realized by increasing the H_2O_2 concentration during MACE, as evidenced by the inset TEM images. The scale bars on all the TEM images are 100 nm. 119

Figure 5.1: Impact of annealing temperature and silicon concentration on (a) thermal conductivity, k , and (b) effective PL lifetime, τ_{PL} . (c) Correlation of the trend of increasing thermal conductivity and PL lifetime with anneal temperature for samples with a relative Si concentration of 45.5%. (d) Correlation of the trend of decreasing thermal conductivity and PL lifetime with increasing excess silicon concentration for samples annealed at 1000°C 124

Figure 5.2: (a) Impact of silicon concentration on Young's modulus and hardness of amorphous SiN_x films. The straight line is a best fit to the data and serves mainly as a guide for the reader. (b) SiN_x thermal conductivity as a function of silicon concentration for samples annealed at 1000°C . The solid line shows the predicted trend in thermal conductivity using the measured elastic modulus (best-fit line from (a)) in the calculation of acoustic velocity and a constant phonon lifetime estimated from a best fit to the data with relative Si concentration $< 55\%$ 126

Figure 5.3: Impact of Erbium concentration on the thermal conductivity of an Er-doped silicon-rich nitride film with a relative Si concentration of 50%. 127

Figure 6.1: Several example geometries for electron beam lithography fabricated porous nanowire structures..... 131

Figure 6.2: (a) Conventional nanowire measurement structure. The nanowire is suspended between two resistive heating elements. Heat generated in the left element conducts through the nanowire, but some fraction conducts through the support legs. Estimates of the conductive heat loss allow calculation of the nanowire thermal conductivity. (b) Modified nanowire measurement structure. Heat is generated in the leftmost resistive element and either conducts through the support legs or through the reference and test nanowires. The heat flux through the test nanowire is calculated from the temperature drop across the reference nanobeams (which also serve as mechanical supports)..... 132

Figure 6.3: Schematic of integrated Z-meter and 3- ω characterization structure. The top patterned heater for 3- ω measurements is electrically isolated from the metal contact layer for the ZT measurement. Micromanipulator probes provide electrical connection to metalized top and bottom electrodes..... 133

Figure 6.4: (a) Sample configuration for thermoreflectance. (b) Example probe data signal for Time Domain Thermoreflectance. The sample is heated by a pump laser pulse and the change in the reflected intensity of the probe laser corresponds to the temperature at the metal surface. The thermal properties of the sample layer govern the shape of thermal decay curve. (c) Frequency Domain Thermoreflectance. The sample is heated by a sine-wave modulated pump laser causing a periodic heat flux. The temperature rise at the metal surface lags behind the heating signal. The dependence of the amplitude and phase of the temperature signal on the frequency is governed by the thermal properties of the sample..... 134

CHAPTER 1: INTRODUCTION

A wide range of application from thermal interface materials (TIMs) [21] to energy storage applications [22] to photonic devices [23] could benefit from the continued development of novel nanostructured materials and the investigation of their thermal properties. Bulk materials span a range of thermal conductivities from gases and aerogels with low thermal conductivity (<0.1 W/m/K) to diamond with extremely high thermal conductivity (>1000 W/m/K) (as illustrated in Figure 1.1(a)). However, some combinations of material properties are impossible or prohibitively expensive to find in bulk materials. For instance, typical bulk materials with high thermal conductivity (metals, diamond) tend also to be mechanically stiff. In contrast, the properties (thermal, mechanical, electrical, etc.) of nanostructured materials can be tailored, sometimes independently, to a desired application due to the precise control over fabrication procedures, geometry, and chemical composition of the nanostructures. For example, vertically-aligned carbon nanotube (CNT) films can provide high thermal conductivity along the nanotube axis combined with mechanical compliance, due to the high aspect ratio of the individual CNTs and low density of the films.

Nanostructuring of crystalline materials often reduces the thermal conductivity through enhanced scattering of the energy carriers at the boundaries of the nanoscale features. For example, bulk silicon at room temperature has a thermal conductivity ~ 150 W/m/K and Figure 1.1(b) illustrates the impact of adding nanoscale boundaries on the thermal conductivity. Enhanced phonon-boundary scattering reduces the thermal conductivity of silicon thin films to as low as 22 W/m/K for 20 nm thick film [24]. Nanowires, which confine the geometry in two-dimensions increasing phonon scattering, are reported to have thermal conductivities as low as ~ 1 W/m/K at diameters <100 nm [25]. Introducing porosity into nanowires and films reduces the thermal conductivity from the solid nanowire or film [26]. “Electron crystal, phonon glasses” are one possible application of nanostructured materials with low thermal conductivity and are considered particularly useful for thermoelectric devices. In these materials, the geometry is chosen such that the nanoscale features impede phonon transport, while minimally impacting electron transport. Silicon-based nanostructures are particularly

INTRODUCTION

interesting for this application because the electron mean free path (~ 10 's of nanometers) is much smaller than the phonon mean free path (~ 100 's of nanometers) at room temperature. Thus, nanoscale features with dimensions larger than the electron mean free path but smaller than the phonon mean free path impede phonon transport without significantly impacting electron transport.

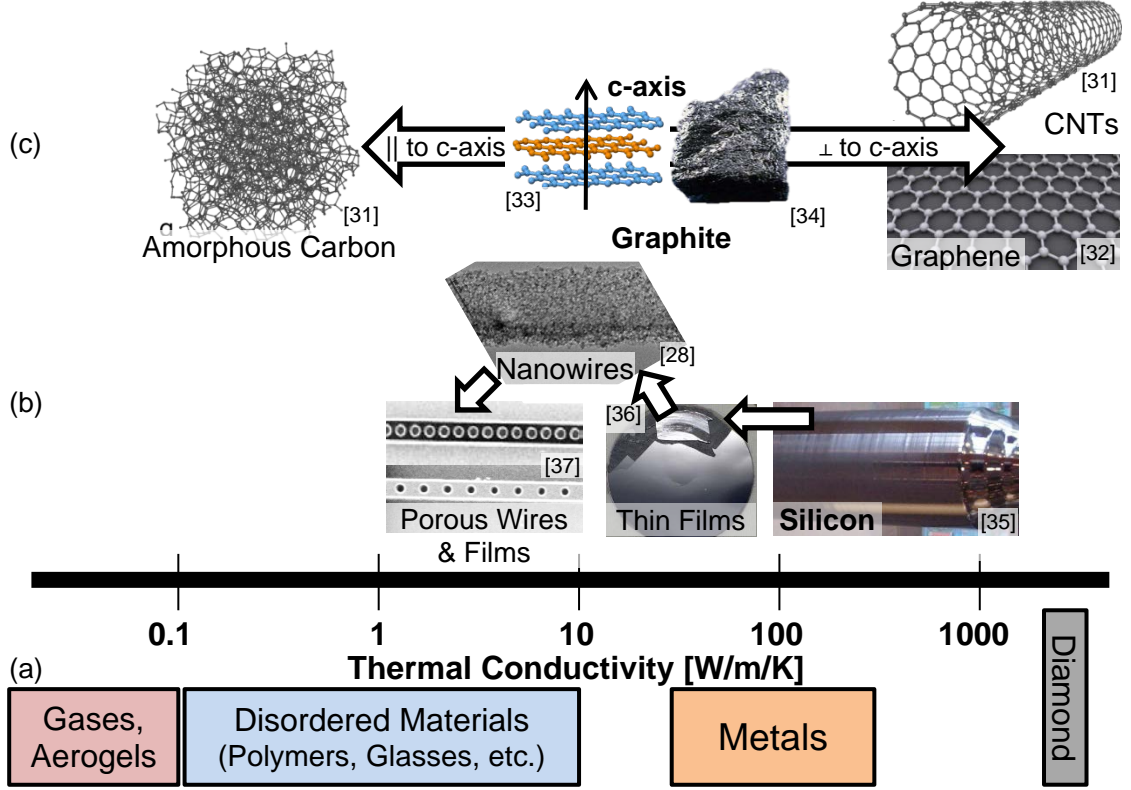


Figure 1.1: *Thermal Conductivities of Bulk and Nanostructured Materials.* (a) At room temperature, the thermal conductivities of bulk materials span a large range: from gases and aerogels with thermal conductivities less than 0.1 W/m/K to highly-crystalline diamond with a thermal conductivity >1000 W/m/K. (b) The introduction of nanoscale feature generally leads to a significant reduction in thermal conductivity in crystalline materials. Crystalline, bulk silicon has a thermal conductivity of ~ 150 W/m/K and enhanced phonon-boundary scattering reduces the thermal conductivity of silicon thin films, nanowires, and porous materials to as low as ~ 20 W/m/K [24], ~ 1 W/m/K [27, 28], ~ 1 W/m/K [26], respectively, depending on geometrical parameters. (c) Graphite has a highly anisotropic crystal structure with sheets of carbon atoms stacked on top of each other (as shown the center of panel c). In along the c-axis (perpendicular to the stacked sheets of carbon atoms), the thermal conductivity is quite low (~ 1 to 10 W/m/K [29]). In the direction perpendicular to the c-axis (in the plane of the sheets of carbon atoms), the thermal conductivity is quite high (exceeding 1000 W/m/K [29]). Graphene (a single sheet of carbon atoms) can have an in-plane thermal conductivity exceeding 1000 W/m/K [29]. Carbon nanotubes (a sheet or sheets of carbon atoms rolled into a tube) can also have high thermal conductivities (>1000 W/m/K) along the direction of the CNT-axis [29, 30]. In contrast, if the crystalline structure of the carbon atoms is removed (*i.e.* amorphous carbon), the thermal conductivity is reduced to < 1 W/m/K [29]. References for figures: [28, 31-37].

However, reduced thermal conductivity due to size effects can significantly impact performance and reliability in nanoscale device. For instance, nanophotonic crystal cavities have been investigated for achieving CMOS compatible, low-threshold lasers, and other active nanophotonic devices. Often these devices consist of suspended thin films or nanowires with patterned air holes. However, the suspended, porous design of these cavities lends itself to low thermal conductivity (due to the high density of boundaries leading to increased phonon scattering) and large temperature rises in the device. Previous work has shown a strong correlation between cavity temperature and device performance and more work is needed to understand thermal conduction within the cavities. The nanoscale geometry impacts phonon transport through boundary scattering, pore scattering, and the possibility of phonon bandgap effects. In addition to geometric effects, novel, nanostructured material systems are being developed and utilized for nanophotonic devices. For example, silicon-rich silicon nitride is a promising candidate for silicon-compatible active and passive photonic devices due to its light emitting properties and relatively high refractive index. In combination with understanding the impact of nanoscale geometry on thermal conduction in these materials, the underlying thermal transport phenomena in these new material systems must also be investigated.

Recent advances in fabrication of carbon-based nanostructured materials have shown that nanostructuring can also yield materials with extremely high thermal conductivity. In bulk crystal form, graphite has a highly anisotropic thermal conductivity due to its crystal structure. In the in-plane direction along the sheets of carbon atoms (perpendicular to the c-axis, see center image in Figure 1.1(c)), the thermal conductivity can exceed 1000 W/m/K and rival that of diamond [29]. In the direction parallel to the c-axis, the thermal conductivity is considerably lower (<10 W/m/K [29]). Amorphous carbon consists of carbon atoms without a crystal structure and has an even lower thermal conductivity. In contrast to the typical size effect observed with nanostructuring, if one single plane of carbon atoms is extracted from the graphite maintaining the hexagonal crystal structure (*e.g.* graphene), the material can have a thermal conductivity greater than 1000 W/m/K [29]. Similarly, carbon nanotubes, which consist of a sheet or sheets of graphene rolled into a tube, can have

INTRODUCTION

thermal conductivities >1000 W/m/K along the axis of the tube [29, 30]. Both graphene and CNTs maintain the high thermal conductivity of the in-plane direction of graphite despite the reduced dimensions of the system due to the unique crystal structure of the nanostructure.

Thermal interface materials (TIMs) for thermal management for computer chips and other high powered electronic devices require a material with high thermal conductivity and low elastic modulus. The high thermal conductivity reduces the thermal resistance of the interface, while the low elastic modulus can compensate for differences in the thermal expansion between the heat source and the heat sink. As previously discussed, this combination of properties is not readily available in bulk materials, however, carbon nanotube based materials, such as aligned CNT arrays and composites, provide high thermal conductivity along the direction of the CNT with the mechanical compliancy desired in a TIM. Additionally, recent progress on CNT-polymer composites, in particular those featuring aligned nanotubes, promises unique combinations of thermal and mechanical properties.

1.1 Scope of Work

First, this dissertation reports new data on the thermal properties of several, novel, nanostructured materials (including carbon nanotubes and CNT-based materials, silicon-based nanostructures, and silicon-rich silicon nitride films). Several techniques (cross-sectional infrared microscopy, nanosecond transient thermoreflectance, picosecond time-domain thermoreflectance, and electrothermal measurement techniques) are used to characterize the thermal conductivity and interface resistances within these materials system.

Second, the measurements reported in this dissertation have led to improvements in these metrology techniques. In particular, the cross-sectional infrared thermometry technique is improved through the introduction of reference layers into the testing geometry to improve the accuracy of the measurement. Additionally, a steady-state joule heating technique is developed, in conjunction with a numerical model, to measure the thermal properties of porous, non-electrically-conductive nanowires.

Third, this data provides key insight into the physics of phonon transport in nanostructured material and devices. Combined with a detailed review of past measurements of the thermal conductivity in carbon nanotubes and CNT-based materials, a detailed understanding of thermal transport in individual CNTs, CNT films, and CNT-based composites is developed considering the impact of nanotube geometry, film morphology, defects, and interfaces. A model for the thermal conductivity of porous silicon nanostructures is developed to investigate the relative impact of boundary scattering, pore scattering, and the possibility of phonon bandgap effects.

Finally, the data and models developed in this work provide key information for the critical to the use of these nanoscale materials in applications such as nanophotonic crystal cavities, thermal interface materials, and thermoelectrics.

1.2 Organization

This dissertation is organized into the following chapters:

Chapter 1 provides introductory and motivational material for this dissertation.

Chapter 2 provides a review of thermal conduction phenomena in carbon nanotubes and nanotube-based materials. This chapter includes separate sections on individual nanotubes and films, each of which includes sections addressing theory and experimental methods. Section 2.2 focuses on individual nanotubes including theoretical modeling and measurements. Section 2.2.1 summarizes the physical mechanisms which impact thermal transport in CNTs. Section 2.3 extends the discussion to nanotube films, focusing mainly on aligned arrays of nanotubes and their use in practical applications.

Chapter 3 discusses experimental investigations of thermal conduction in carbon nanotubes arrays and composites using cross-sectional infrared microscopy. Two methods for improving thermal performance are discussed. First, mechanical densification of vertically-aligned CNT (VACNT) films (Section 3.2) and composites (Section 3.3) is investigated as a method to increase the number of thermal pathways and improve the film thermal conductivity. Second, a novel method for improving the thermal conductance at CNT-copper interfaces and the effective VACNT thermal conductivity through the electrodeposition of copper films directly on to the VACNT

INTRODUCTION

film is discussed (Section 3.4). Specifically, electrodeposition of thin films of copper directly onto the CNT films improves the engagement of the individual carbon nanotubes within VACNT films compared to standard bonding techniques.

Chapter 4 investigates thermal conduction in silicon-based nanostructures. Section 4.2 attempts to clarify the impact of phonon-boundary scattering in periodically-porous silicon nanowires at room temperature using electrothermal measurements and modeling. The thermal conductivity along the length of the silicon nanobeams is measured using a steady-state Joule heating technique (Section 4.2.2). A Callaway-Holland model for the thermal conductivity is adapted to investigate the relative impact of boundary scattering, pore scattering, and phonon bandgap effects (Section 4.2.3). Section 4.3 measures the thermal conductivity along the axial direction of SiNW arrays with varying nanowire diameters, doping concentrations, surface roughness and internal porosities using nanosecond transient thermoreflectance. The relative importance of phonons scattering on external nanowire boundaries and pore boundaries is investigated through measurements across a range of diameters and porosities.

Chapter 5 investigates the thermal conductivity and photoluminescence of light emitting samples fabricated with a range of excess silicon concentrations and annealing temperatures using time-domain picosecond thermoreflectance and time-resolved photoluminescence. This work explores the role of annealing and stoichiometry control in the optimization of light emitting microstructures suitable for the demonstration of efficient Si-compatible light sources based on the silicon nitride platform.

Chapter 6 summarizes the major contributions of this dissertation and offers suggestions for future research directions.

CHAPTER 2: REVIEW OF THERMAL CONDUCTION PHENOMENA IN CARBON NANOTUBES AND RELATED NANOSTRUCTURED MATERIALS *

2.1 Introduction

Carbon nanotubes (CNTs) are very promising for applications leveraging their unique electrical, thermal, and mechanical properties. Early predictions and measurements [38, 39] suggested extremely high mechanical strength and strength-to-weight ratio. Nanotubes can be metallic or semiconducting based on their chirality and diameter leading to a wealth of research on CNT-based nanoelectronic devices [40]. High expectations for the thermal conductivity of CNTs were originally based on the high in-plane thermal conductivity of graphite and the high thermal conductivity of bulk and thin film diamond [41]. Molecular dynamics simulations [18] predicted thermal conductivities as high as $6600 \text{ W m}^{-1} \text{ K}^{-1}$ at room temperature. These findings motivated exploratory research for a wide variety of applications including reinforced composites [42], field emission devices [43], sensors and probes [43], and thermal interface materials [44].

This chapter provides a comprehensive overview of thermal conduction research on carbon nanotubes and nanostructured films consisting of arrays of nanotubes or disordered nanotube mats, with a focus on understanding the trends with geometrical parameters and the differences between predictions and data. For individual nanotubes, the problem of comparing data from differing groups is addressed by calculating thermal conductivities using a consistent definition of cross sectional area. For films containing aligned carbon nanotubes, the relatively low conductivities reported experimentally compared to the original prediction from individual nanotube data are discussed considering individual nanotube data and issues associated with CNT film fabrication and mechanical attachment. The highly productive period of research

* This section reproduced with permission from A.M. Marconnet, *et al.* "Thermal Conduction Phenomena in Carbon Nanotubes and Related Nanostructured Materials," *Reviews of Modern Physics* (in press). Copyright 2012 American Physical Society.

*REVIEW OF THERMAL CONDUCTION PHENOMENA IN CARBON NANOTUBES
AND RELATED NANOSTRUCTURED MATERIALS*

covered by this review has enriched the discipline of heat conduction with a variety of novel MEMS-based experimental methods and opportunities for calibration and validation of molecular dynamics simulations. In addition to covering the properties of nanotubes and related nanostructured materials, this review discusses these new experimental methodologies and their implications for future research.

This review fills an important gap in the literature already available on carbon nanotubes, which at present lacks a comprehensive, comparative review of the extensive and sometimes revolutionary experimental and theoretical research addressing this material system. Several articles [e.g., 40] and at least one book [e.g., 45] detailed the structure and synthesis of carbon nanotubes. Early reviews of CNT properties detailed the structure and synthesis of carbon nanotubes. Early reviews of CNT properties [46-50] discussed thermal transport but did not attempt a comprehensive comparison of data and predictions. Hone [51, 52] provided insightful summaries of the theoretical and experimental progress on CNT thermal transport, just a few years after the first experimental data were available. In the years since those reviews, rather substantial progress has been made in both theory and experiments, including approximately 75 additional articles cited in the current review. Lee *et al.* [53] reviewed molecular dynamics simulations of thermal conduction along single-wall carbon nanotubes (SWCNTs) and examined variations with nanotube length, chirality, and temperature. Balandin [29] reviewed thermal transport in many forms of nanoscale carbon materials from amorphous carbon to CNTs, with an emphasis on graphene and the unique characteristics of two-dimensional crystals. There remains a need for a more complete comparison of predictions and experimental data for individual nanotubes, with a focus on identifying both the resolved issues and the open questions. Furthermore, the maturing body of literature on nanotube-based films, when considered together with extrapolations of the data reviewed here for individual nanotubes, provides a compelling chance to examine the physical mechanisms that may be limiting the thermal conductance of nanotube ensembles. In addition to discussing and interpreting the research results, this review also highlights the rich variety of innovative methods, both for experiments and simulations, that have been developed for CNT thermal transport studies.

This review includes separate sections on individual nanotubes and films, each of which includes sections addressing theory and experimental methods. Section 2.2 focuses on individual nanotubes including theoretical modeling and measurements. Section 2.3 extends the discussion to nanotube films, focusing mainly on aligned arrays of nanotubes and their use in practical applications.

2.2 Thermal Conduction by Individual Nanotubes

2.2.1 Physical Mechanisms

The unusual properties of carbon nanotubes are governed by their unusual and simple atomic structure, which has been examined in a variety of chiralities and diameters. Comparison of the theoretical results and experimental data in the literature is complicated by the variety of nanotubes produced by different techniques.

A single-wall carbon nanotube consists of an atomic layer of carbon atoms (*i.e.* a sheet of graphene) rolled into the form of a tube. The axis of the nanotube can form along many different directions (*i.e.* chiral vectors (n,m)) in the carbon layer, yielding CNTs with different chiralities and diameters. Armchair (n,n) nanotubes are always metallic, while zigzag $(n,0)$ and other (n,m) chiralities are semiconducting [47]. Multi-wall carbon nanotubes (MWCNTs) include several concentric tubes that can have varying chiralities, and understanding the interactions between shells is critical for accurate modeling of thermal transport.

Heat conduction by carbon nanotubes is dominated by the coupled vibrations of carbon atoms and therefore can be analyzed as phonon transport. Phonon transport dominates over heat conduction by electrons even in those nanotube chiralities that exhibit metallic properties [29, 52]. The phonon dispersion relationship (see Figure 2.2(b)) consists of four acoustic modes (one longitudinal mode, two transverse modes, and one torsional or “twist” mode) and many optical modes. The “twist” acoustic mode arises from torsion of the tube about its axis, which can be described as a twisting motion [54]. The phonon conductivity can be computed from the phonon dispersion relationship, the heat capacity of each phonon mode, and their scattering rates or mean free paths.

*REVIEW OF THERMAL CONDUCTION PHENOMENA IN CARBON NANOTUBES
AND RELATED NANOSTRUCTURED MATERIALS*

Carbon nanotubes, and other low-dimensional carbon-based nanomaterials including graphene can have very high thermal conductivities, despite very small cross-sectional dimensions. This is in contrast to many crystalline nanowires with small cross-sectional dimensions, in which the thermal conductivity is strongly reduced by the increased rate of phonon-boundary scattering. The long range crystallinity, long phonon mean free path, and large speed of sound of the CNTs lead to the large thermal conductivity [47]. For an ideal perfect three-dimensional crystals, lattice anharmonicity limits thermal conduction. However, for low-dimensional structures, the intrinsic thermal conductivity of ideal one-dimensional (1D) and two-dimensional (2D) systems diverges with the number of atoms leading to infinite intrinsic thermal conductivity despite anharmonicity [29]. Practically, the thermal conductivity of 1D and 2D systems are limited by many factors including higher-order phonon scattering processes [55, 56], sample quality (*i.e.*, defects and impurities, see Section 2.2.4.3), and boundary scattering.

The phonon mean free path in carbon nanotubes depends on phonon-phonon, phonon-boundary, and phonon-defect scattering processes. Estimates of the phonon mean free path at room temperature range from about 50 nm [57] to 1.5 μm [58, 59], although MWCNTs with many defects may have phonon mean free paths as small as 4 nm [60]. The dominant phonon wavelength, λ_d , for heat transport can be estimated from $\hbar v / \lambda_d \approx k_B T$, where $\hbar = h / 2\pi$, h is Planck's constant, v is the phonon velocity, k_B is the Boltzmann constant, and T is the temperature [61]. For SWCNTs, the large phonon velocity predicts a large dominant phonon wavelength even at moderately high temperatures [61].

A challenge with interpreting the existing theory and data is the transition from the ballistic to the diffusive conduction regimes. In the ballistic regime, phonons scatter rarely along the length of the nanotube, and thus the thermal conductance is independent of nanotube length. Thus, carbon nanotubes are ballistic conductors when the mean free path is longer than the nanotube length and the dominant phonon wavelength is smaller than the nanotube diameter. At very low temperatures (a few Kelvin), only the four acoustic modes contribute to heat transfer and as the temperature

increases the optical modes begin to contribute. In the diffusive regime, phonons scatter many times within the length of the nanotube leading. Diffusive heat transport dominates when the CNT is much longer than both the phonon mean free path and the dominant phonon wavelength. Thermal conduction within carbon nanotubes transitions from the ballistic to diffusive regime with increasing temperature (see Section 2.2.4.2) or increasing length (see Section 2.2.4.1).

Another challenge faced by this review is the distinction between the thermal conductance, G , and the thermal conductivity, k . The thermal conductance simply quantifies the rate of heat transferred, q , for a given temperature rise ΔT , by means of $G=q/\Delta T$. The thermal conductivity is defined from Fourier's Law for diffusive thermal transport, by means of $q = -kA \frac{dT}{dx}$, where q is the heat flux, A is the cross-sectional area, and $\frac{dT}{dx}$ is the temperature gradient along the length of the nanotube. The thermal conductivity and thermal conductance are related through geometrical parameters by $G=kA/L$, where L is the length of the nanotube. The thermal resistance, R , at an interface is defined as the temperature rise across the interface due to a heat flux, $R=\Delta T/q$.

While the conductance is well defined for a given CNT sample, the precise meaning of the thermal conductivity relies on the definition of the cross-sectional area. Several definitions and considerable ambiguity have resulted from the annular geometry of the tube, some ambiguity in of the cross-sectional area of an individual atomic layer, especially in a SWCNT, and the challenges in measuring the inner diameter of MWCNTs. Typical definitions are (1) the whole area enclosed by the outermost tube of carbon atoms [e.g., 62] or (2) the approximate area of the carbon atoms in CNT [e.g., 63]. For SWCNTs, this second method is often approximated as the circumference of the CNT multiplied by the thickness of the carbon shell, which is typically chosen to be between the sp^2 bond length ($\delta=0.142 \text{ nm}$) and the interlayer spacing in graphite ($\delta=0.34 \text{ nm}$) [16]. For a single value of the nanotube thermal conductance, two different values of thermal conductivity can be extracted. Note that for (10,10) SWCNTs (1.35 nm diameter), both definitions of area are consistent to within 1% when assuming a carbon thickness of $\delta=0.34 \text{ nm}$. This paper standardizes the thermal conductivities

*REVIEW OF THERMAL CONDUCTION PHENOMENA IN CARBON NANOTUBES
AND RELATED NANOSTRUCTURED MATERIALS*

reported by different authors using the first definition of cross-sectional area (1), which is the entire enclosed area, which is necessitated by the fact that few experimental papers reported inner MWCNT diameters.

2.2.2 Experimental Progress

Measurements of thermal properties of individual CNTs usually require microfabricated devices and can be separated into two groups: (1) Experiments using an external heat source to establish a temperature gradient across the nanotubes and (2) Experiments using self-heating of the nanotube to extract the thermal properties (see Figure 2.1). Table 2.1 summarizes the available experimental data for the thermal conductivity of individual nanotubes. Using the external heating method, both Kim *et al.* [64] and Yu *et al.* [63] measured the thermal conductivity of a 2.5 μm long, 14 nm diameter MWCNT and a 2.76 μm long, 1-3 nm diameter SWCNT, respectively, by suspending the nanotubes between two resistive elements. Heat generated at one resistor flowed in part through the nanotube and was detected through a temperature rise at the second. Both resistors served as temperature sensors and the nanotube conductance was calculated considering losses through the support legs. As will be discussed later in more depth, a challenge with this method is isolating the conductance internal to the nanotube from the thermal resistances at the interfaces with the heating and sensing elements. For bundles of nanotubes similarly suspended between two resistive elements, the sensitivity to thermal conductivity was improved when using sinusoidal heating and lock-in detection of the voltage signals [65]. Using this method, Pettes and Shi [60] measured the thermal conductivity of several SWCNT and MWCNT. A similar external heating method was used by Fujii *et al.* [62] with a T-type nano-sensor [66] to measure the thermal conductivity of three MWCNTs ranging from 9.8 to 28.2 nm in diameter and 1.89 to 3.7 μm in length. Each CNT was connected from the center of a hot bridge to a heat sink. A lower bound for the thermal conductivity of the nanotube was extracted from the measured temperatures and heat generation rates neglecting contact resistance of the nanotube and the hot wire and heat sink.

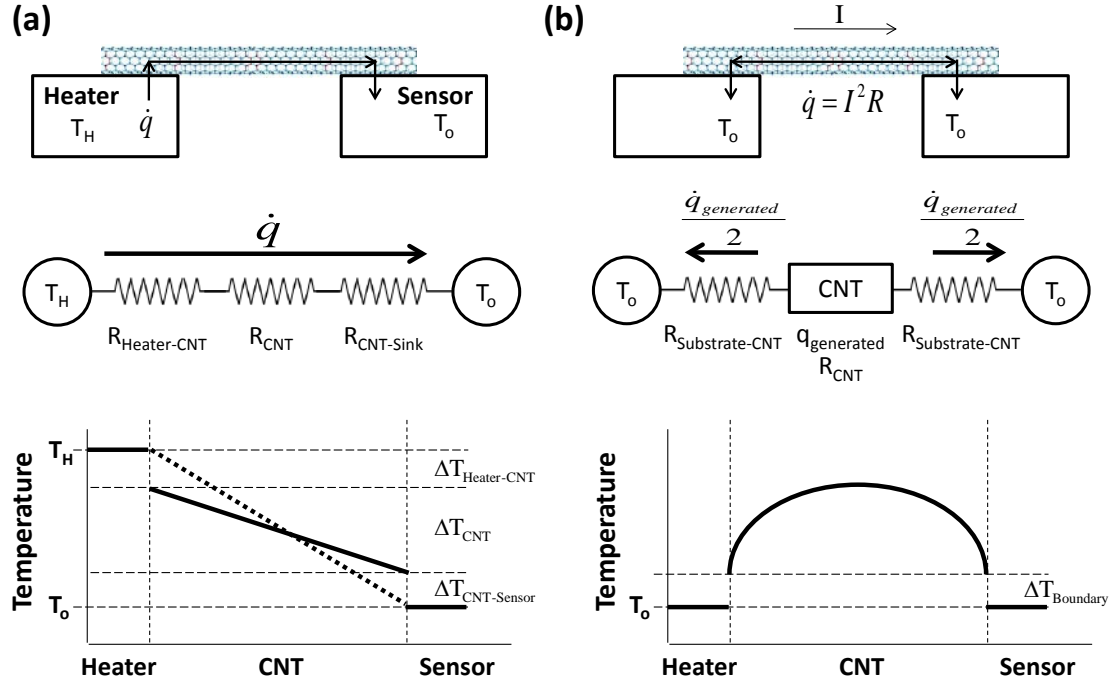


Figure 2.1: Two differing strategies for measuring thermal conductivity of individual carbon nanotubes. (a) Passive Technique. A temperature difference generated by a heater at one end of the nanotube is captured using sensors at both ends. (b) Self-Heating Technique. Heat is generated by applying a voltage across the nanotube, resulting in electrical heating of the nanotube, and the temperature distribution is deduced from the resulting electrical resistance change and calibration data.

*REVIEW OF THERMAL CONDUCTION PHENOMENA IN CARBON NANOTUBES
AND RELATED NANOSTRUCTURED MATERIALS*

Table 2.1: Measured Room Temperature Thermal Conductivities of Individual Carbon Nanotubes. Data from all authors is standardized here using the enclosed cross-sectional area of the nanotube (i.e. using the outside diameter for MWCNTs). Additionally, for SWCNT samples, the thermal conductivity calculated with the circumference times the thickness of a nanotube shell is shown for comparison. Yu *et al.* [63] measured the thermal conductance and uncertainty in the diameter of the nanotube resulted in a wide range for the thermal conductivity. Pettes and Shi [60] report a lower bound in thermal conductivity for SWCNT and double-wall carbon nanotube (DWCNT), but extract an estimate of the intrinsic thermal conductivity for the MWCNTs. Choi *et al.* [57, 67] did not explicitly state which definition of area they used to calculate thermal conductivity, so the value in the table is as reported in the articles.

Article	Measurement Technique	SWCNT/ MWCNT	Length [μm]	Diameter [nm]	k [W m ⁻¹ K ⁻¹]	k' [W m ⁻¹ K ⁻¹]	Boundary Resistance
Yu <i>et al.</i> [63]	Heater-Sensor	SWCNT	2.76	1 to 3	1480 to 13350	3270 to 9800	Neglected
Pop <i>et al.</i> [68]	Self-Heating	SWCNT	2.6	1.7	2749	3436	Estimated (6x10 ⁶ K W ⁻¹)
Li <i>et al.</i> [69]	Raman shift	SWCNT	41	1.8	1810	2400	Measurement independent of boundary resistance
		MWCNT	32	8.2	1400	-	
Pettes and Shi [60]	Heater-Sensor	SWCNT	4.31	2.34	>300	>600	Neglected for SWCNTs & DWCNT. Estimated for MWCNTs
		SWCNT	2.03	1.5	>580	>600	
		DWCNT	4.02	2.7	>540	-	
		MWCNT	1.97	11.4	160	-	
		MWCNT	3.31	14.0	34	-	
Fujii <i>et al.</i> [62]	T-Type Sensor	MWCNT	3.7	9.8	2950	-	Neglected
			1.89	16.1	1650	-	
			3.6	28.2	500	-	
Kim <i>et al.</i> [64]	Heater-Sensor	MWCNT	2.5	14	3000	-	Neglected
Wang <i>et al.</i> [56, 70]	4-Pad 3ω	SWCNT	0.509	1.9	2630	3680	Measurement independent of boundary resistance
			4.919	1.9	3160	4680	
			6.941	1.9	3210	4740	
Choi <i>et al.</i> [67]	2-Pad 3ω	MWCNT	1.0	46	650	Neglected Contact Resistance	
			1.1	42	830		
Choi <i>et al.</i> [57]	4-Pad 3ω	MWCNT	1.4	20	300		Measurements independent of boundary resistance

^a k values using $A = \pi d^2/4$. ^b k' values for SWCNTs using $A = \pi d\delta$, where $\delta=0.34$ nm.

Methods for extracting thermal information using self-heating of the nanotube include calibrating the thermal coefficient of resistance [68], the 3ω technique [56, 57, 67, 70], and Raman observation of the temperature profile [69]. Pop *et al.* [68] measured the I-V characteristics of a self-heated CNT suspended across a trench to extract the thermal conductivity as a function of temperature. Wang *et al.* [56, 70] and Choi *et al.* [57, 67] used the 3ω technique [71] to determine the thermal conductivity of nanotubes from 0.509 to 6.941 μm long. A novel technique by Li *et al.* [69] combined electrical self-heating of a nanotube with temperature measurements using the Raman shift method. Previously, Hsu *et al.* [72] used laser heating of the nanotube and the Raman shift method for measuring the temperature profile along the nanotube to extract information about the relative contribution of the intrinsic thermal resistance of the nanotube and the boundary resistance between the nanotube and the substrate. Since the exact magnitude of optical power absorbed by the nanotube was unknown, the thermal conductivity of the sample could not be determined. To address this challenge, Li *et al.* [69] combined electrical self-heating of the nanotube with temperature measurements via the Raman shift method. The shape of the temperature profile along the nanotube axis depends only on the intrinsic thermal conductivity allowing determination of the thermal conductivity independent of boundary resistance. A large portion of the CNT was in contact with the substrate and the thermal contact resistance at the ends of the nanowire was small compared to the intrinsic resistance of the nanotube.

During electrical self-heating, particularly at high bias, Joule heating generates nonequilibrium in the phonon population [73-78]. For suspended nanotubes, Joule heating increases the population of optical phonon modes significantly above that of acoustic phonon modes, an effect which has been modeled using distinct temperatures for the two branches [73-78]. In contrast to the data for suspended nanotubes, the on-substrate nanotube data of Pop *et al.* [75] could be explained without considering nonequilibrium effects, likely because of shorter optical phonon lifetimes for on-substrate nanotubes. Lazzeri *et al.* [73] showed that the small electron transport scattering length could be explained by hot optical phonons. Nonequilibrium phonon populations in electrically heated SWCNTs have been detected directly through Raman scattering experiments [76-78].

*REVIEW OF THERMAL CONDUCTION PHENOMENA IN CARBON NANOTUBES
AND RELATED NANOSTRUCTURED MATERIALS*

For on-substrate measurements, the thermal contact resistance between the nanotube and the substrate impacts the temperature profile in the nanotube and is critical to determining the intrinsic thermal conductivity. For their measurements using the 3 ω method, Wang *et al.* [56, 70] estimated 30-40% of the total heat power generated in their nanotubes conducted to the substrate. Interaction between the nanotube and the substrate may also directly impact the nanotube thermal conductivity. Measurements of supported graphene [79, 80] show reduced thermal conductivity compared to suspended sheets, suggesting a suppression of some phonon modes. Thermal conduction measurements of carbon nanotube composites [81] have suggested that a phonon modes and boundary scattering within a nanotube may also be impacted by contacting materials.

Measurement techniques which can extract the intrinsic thermal conductivity separately from the boundary resistance with a substrate require the nanotube to be suspended. While suspended devices for these experiments require more challenging fabrication, confidence in the thermal conductivity measurement is increased and the measured values from different experiments can be directly compared without considering substrate effect. However, even in suspended structures, contact resistances at the ends of the nanotube still need to be considered. In the diffusive regime, it is commonplace to convert the thermal conductance to thermal conductivity by means of $k=G/(LA)$, which requires important assumptions about the relative importance of contact resistances, as well as the cross-sectional area (as discussed in Section 2.2.1). Specifically, when a CNT is suspended between a heater and heat sink, the temperature rise measured between the heater and heat sink is composed of three parts, (1) the temperature rise due to the contact resistance between the heater and the CNT, (2) the temperature rise due to heat conduction within the CNT, and (3) the temperature rise due to the contact resistance between the CNT and the heat sink. The CNT thermal conductivity can be calculated from the measured temperature drop considering the boundary resistance using:

$$k = \frac{L}{A \left[\frac{\Delta T_{CNT}}{\dot{q}} \right]} = \frac{L}{A \left[\frac{\Delta T_{total} - \Delta T_{Heater-CNT} - \Delta T_{CNT-Sink}}{\dot{q}} \right]} = \frac{L}{A \left[\frac{\Delta T_{total}}{\dot{q}} - R_{Heater-CNT} - R_{CNT-Sink} \right]}, \quad (2.1)$$

The use of Eq. (2.1) yields a higher thermal conductivity than when the thermal boundary resistance is neglected, $k = L/A \left[\frac{\Delta T_{total}}{\dot{q}} \right]$. Decreasing the thermal contact resistance, such as by increasing the area of contact or reducing the intrinsic interface resistance, reduces the portion of the total thermal resistance due to contacts and provides a more accurate thermal conductivity value. For ballistic transport along a nanotube, the thermal conductance depends on the transmissivity of the contacts and is independent of the nanotube length. When extracting thermal conductivity from ballistic conductance data, the result incorporates contact effects. More details on ballistic and diffusive transport are presented in Sections 2.2.4.1 and 2.2.4.2.

Many authors working with suspended devices have attempted to account for or estimate the impact of the contact resistance at the ends of the nanotubes in measurements of the thermal conductance. Kim *et al.* [64] estimated a thermal contact conductance of $\sim 5 \times 10^{-7} \text{ W K}^{-1}$ for a 14 nm diameter MWCNT suspended over a trench with $\sim 1 \text{ }\mu\text{m}$ of the overlap between the CNT and the resistive elements as shown in the left panel of Figure 2.1. When compared to the total nanotube conductance of $1.6 \times 10^{-7} \text{ W K}^{-1}$, about 68% of the total resistance of the nanotube is due to the intrinsic thermal resistance of the nanotube compared to the contact resistance. This suggests the true thermal conductivity is about 1.5 times the reported value. Pettes and Shi [60] found that depositing Pt-C at the MWCNT-membrane contacts significantly reduced the total thermal resistance along the nanotube including both volume and contact components compared to the as-grown case. For the three MWCNT samples measured, the contact resistance after Pt-C deposition was estimated to be 12-54% of the total resistance allowing the intrinsic thermal conductivity to be estimated. To account for the contact resistance between the nanotube and substrate in the self-heating measurement of suspended SWCNTs, Pop *et al.* [68] used the fact that typical interfaces between dense materials have thermal interface resistance in the range of $1\text{-}3 \times 10^{-8} \text{ m}^2 \text{ K W}^{-1}$ [82]. The contact area was approximated as the product of the nanotube diameter and the length of overlap between the substrate and the nanotube, using $A_c = d L_c$ where $L_c \sim 2 \text{ }\mu\text{m}$ and $d \sim 1.7 \text{ nm}$. This resulted in a total thermal contact resistance between 3×10^6 and $9 \times 10^6 \text{ K W}^{-1}$ and yielded about 10% uncertainty in the extracted thermal conductivity. In an

*REVIEW OF THERMAL CONDUCTION PHENOMENA IN CARBON NANOTUBES
AND RELATED NANOSTRUCTURED MATERIALS*

early paper by Choi *et al.* [67], using a 2-point 3ω technique, the contact resistance was deemed negligible when the measurements of total thermal resistance of several MWCNTs of different lengths and diameters followed the expected relationship for the intrinsic resistance. Raman spectroscopy can be used to measure the temperature profile along the axis of the CNT based on the shift in the G band Raman frequency [72]. The relative magnitude thermal boundary resistance and intrinsic thermal resistance of a nanotube can be compared by combining (laser or electrical) heating of suspended nanotubes with Raman thermometry. Hsu *et al.* [72] found that the boundary resistance ranged from 0.02 to 17 times the intrinsic thermal resistance of the CNT depending on the quality of the nanotube and the contact.

2.2.3 Theoretical Progress

There are detailed theoretical studies of carbon nanotube thermal transport that complement the experimental data in the previous section. Transport of thermal energy in carbon nanotubes is primarily through atomic vibrations. Carbon nanotubes have a high aspect ratio with diameters on the order of nanometers and lengths as long as millimeters and can span the range from ballistic conductors to diffusive conductors. As mentioned in Section 2.2.1, carbon nanotubes are ballistic conductors when the mean free path is longer than the nanotube length and the dominant phonon wavelength is smaller than the nanotube diameter. Diffusive heat transport dominates when the CNT is much longer than both the phonon mean free path and the dominant phonon wavelength and the energy carriers scatter many times within the nanotube.

Ballistic transport can be modeled with a Landauer approach (see Section 2.2.3.1) and modifications to the ballistic transport models have been proposed to extend the estimation of the thermal properties into the diffusive regime [83, 84]. Strong mesoscopic effects modify the heat transfer characteristics in an intermediate regime, where the nanotube is much longer than the phonon mean free path and the dominant phonon wavelength is larger than the diameter of nanotube, but shorter than the nanotube length [61]. In the same nanotube, ballistic or mesoscopic conduction is often observed at low temperatures, while diffusive conduction exists at higher temperatures.

CHAPTER 2

Phonon transport models (Section 2.2.3.2) and molecular dynamics simulations (Section 2.2.3.3) have also been used to investigate heat transport in carbon nanotubes. Phonon transport theory calculates the evolution of phonon populations in carbon nanotubes using, for example, the Boltzmann transport equation. Key parameters for these models include the phonon dispersion relationships and the scattering or relaxation times for different phonon interactions, which must be determined from experiments or treated as inputs from more fundamental models. Molecular dynamics simulations allow for calculation of thermal properties based on the dynamics of the atoms interacting through inter-atomic potentials. Several different proposed forms for the interaction potential between the atoms have been investigated.

2.2.3.1 Landauer Approach

The long mean free paths of phonons in carbon nanotubes compared to those in other materials cause the nanotube to exhibit strong ballistic behavior over submicron length scales. Ballistic quantized thermal conductance in quantum wires has been investigated by Rego and Kirczenow [85]. Ballistic thermal conductance for one dimensional conductors results in the quantum of thermal conductance, which can be derived using Landauer theory. For a one-dimensional system between a hot and cold heat bath, assuming perfect transmission at the interfaces, adiabatic system-heat bath contacts, and a linear temperature response regime [58, 86], the phonon thermal conductance in the limit where $\Delta T \ll T$ is

$$G_{phonon} = \frac{\dot{q}_{phonon}}{\Delta T} = \frac{k_B^2 T}{2\pi\hbar} \sum_m \int_{x_m^{\min}}^{x_m^{\max}} \frac{x^2 e^x}{(e^x - 1)^2} dx, \quad (2.2)$$

where $x = \frac{\hbar\omega}{k_B T}$, $T = \frac{T_{hot} + T_{cold}}{2}$, and m denotes the phonon branches. Each gapless acoustic phonon mode, independent of the exact dispersion relation, contributes a quantum of thermal conductance

$$G_{th} = \frac{\pi^2 k_B^2}{3h} T. \quad (2.3)$$

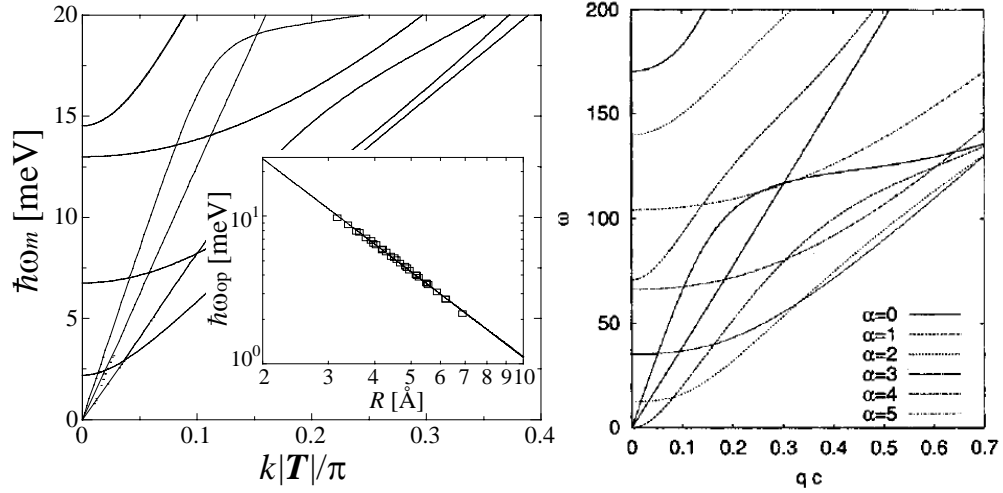


Figure 2.2: (a) Phonon dispersion relationship for (10,10) nanotube calculated by Yamamoto *et al.* [86]. The inset shows that the energy gap of the lowest optical mode ($\hbar\omega_{op}$) decreases with nanotube radius. With this model, all four acoustic modes exhibit a linear dispersion relationship because the impact of bond bending is neglected. (b) Phonon dispersion relationship for (10,10) armchair nanotube calculated by Mahan and Jeon [87]. Two transverse (“flexure”) modes exhibit a quadratic dispersion relationship, while the longitudinal and twist modes are linear.

For temperatures below the optical subband excitation temperature, the four modes contribute to the heat transport in quantum wires [85] and single wall nanotubes [58, 86]. Calculations of the dispersion relationship for various chiralities of single-wall carbon nanotubes have shown four phonon modes at low temperature [58, 86-88], which yields $G = 4G_{th}(T)$ in the low temperature limit. Figure 2.2 shows two examples of the calculated dispersion relationship for a (10,10) single-wall carbon nanotube. In early work, using zone-folding models [58, 86, 89-91], all four of the four acoustic modes had linear dispersion relationships (*e.g.*, [86], as shown in Figure 2.2(a)). Mahan and Jeon [87] showed that for CNTs, as the bonds are bent relative to the straight bonds in graphite or a graphene sheet, both the magnitude and symmetry rules used in the force-constant models must be modified. These authors [87] showed that the previously derived [58, 86, 89-91] linear dispersion relationship of the transverse modes should in fact be a quadratic relationship as shown in of Figure 2.2(b). Quadratic dispersion relations for the transverse mode have obtained by using several molecular dynamics models [87, 92-94], as well as *ab initio* calculations [95], and it is now widely accepted that the doubly-degenerate transverse modes should have a quadratic dependence. The

CHAPTER 2

energy gap of the lowest optical mode ($\hbar\omega_{op}$) depends on the radius of (n,n) single-wall carbon nanotubes as $\hbar\omega_{op} \sim R^{-2}$ (see the inset to Figure 2.2(a)).

Optical phonon modes begin to contribute to heat transfer as temperature increases above a few degrees Kelvin depending on the energy of the lowest optical phonon mode, which depends on the diameter of the nanotube [58]. Extending the estimate of the thermal conductance of SWCNTs in the low temperature limit ($G=4G_{th}$) to higher temperatures is possible by considering the chirality of the nanotube in determining the number of phonon modes for thermal conductance [83, 89, 96]. The number of phonon modes for a single-wall carbon nanotube (or in a single shell of a multi-wall carbon nanotube) in the ballistic regime is determined by the chirality [83, 89, 96]:

$$N_{ph} = \frac{12(n^2 + mn + m^2)}{d_R} = \frac{12\pi^2 d_j^2}{a_o^2 d_R} \quad (2.4)$$

where (n,m) is the chiral vector, d_R is the greatest common divisor of $(2n+m)$ and $(2m+n)$, d_j is the diameter of the nanotube, and $a_o = \sqrt{3}b_o$ is the length of the unit chiral vector, where $b_o=0.142$ nm is the equilibrium interatomic distance. The nanotube diameter can also be calculated from the chiral vector:

$$d_j = \frac{a_o}{\pi} \sqrt{n^2 + mn + m^2} . \quad (2.5)$$

Each phonon mode can transport a quantum of thermal conductance in the ballistic regime. Thus the total ballistic thermal conductance of a single-wall carbon nanotube or one shell in a multi-wall carbon nanotube is $G_j = N_{ph} G_{th}$. For a multi-wall carbon nanotube, the total ballistic thermal conductance is the sum of the conductance of each shell [83], $G = \sum_{N_{shells}} G_j$. This treatment neglects coupling between shells. Brown *et al.*

[96] measured the thermal conductance of MWCNTs to be consistent with this method within the range of expected number of phonon channels (100's to 1000). The conductance calculation can be extended to a bundle of nanotubes of mixed diameters by summation of the conductance of the individual nanotubes [83].

To extend the ballistic model of thermal conductance into the diffusive regime, Shang *et al.* [83] extended previous modeling work [1, 55, 97] showing that thermal

*REVIEW OF THERMAL CONDUCTION PHENOMENA IN CARBON NANOTUBES
AND RELATED NANOSTRUCTURED MATERIALS*

conductivity of carbon nanotubes stops increasing at lengths longer than the mean free path of the phonons, indicative of diffusive conduction. This suggests that for nanotube lengths greater than the phonon mean free path, l , the thermal conductance should vary according to

$$G_{j,diffuse} = G_{j,ballistic} \frac{l}{L}. \quad (2.6)$$

In other words, the total thermal conductance for nanotubes of any length can be expressed as

$$G_j = \begin{cases} N_{ph} G_{th} & \text{for } L < l \\ N_{ph} G_{th} \frac{l}{L} & \text{for } L > l \end{cases}. \quad (2.7)$$

In the derivation of the ballistic quantum conductance, perfect transmission was assumed at both heat baths. Wang and Wang [84] modified the energy transmission, ζ , for the ballistic to diffusive transition regime, where the mean free path is on the order of the CNT length, using $\zeta = \frac{l}{l+L}$, and in the diffusive regime ($L > l$), using $\zeta = \frac{l}{L}$. This provides a smooth cross-over between the ballistic and the diffusive regimes. Similarly, Yamamoto *et al.* [98] derived an expression for the thermal conductance valid from the ballistic to the diffusive regime given by

$$G = \sum_m \int_{\omega_m^{\min}}^{\omega_m^{\max}} \frac{d\omega}{2\pi} \hbar \omega \left[\frac{df(\omega, T)}{dT} \right] \frac{l_m(\omega)}{L + l_m(\omega)}, \quad (2.8)$$

where T is an average temperature, $\hbar \omega_m$ is the phonon energy, $f(\omega, T)$ is the distribution of phonons, and $l_m(\omega)$ is the mean free path of phonons in the m^{th} phonon mode. Equation (2.8) reduces to the ballistic thermal conductance for CNTs with lengths much shorter than the mean free path and to the Peierls-Boltzmann equation for CNTs of much longer lengths [98]. Estimating the mean free path using an expression for three-phonon Umklapp processes where $\hbar \omega / k_B T \gg 1$ yields

$$l_m(\omega) = \frac{c_m A}{\omega^2 T}, \quad (2.9)$$

where A is the coupling constant (using the value for graphene, $A = 3.35 \times 10^{23} \text{ m K s}^{-2}$) and c_m is a parameter used to represent the curvature of the CNT, allows the thermal conductance to be calculated from

$$G = \frac{k_B}{2\pi} \sum_m \Omega_m \left[\arctan\left(\frac{\omega_m^{\max}}{\Omega_m}\right) - \arctan\left(\frac{\omega_m^{\min}}{\Omega_m}\right) \right], \quad (2.10)$$

where $\Omega_m = \sqrt{\frac{c_m A}{TL}}$, which can be considered a length-dependent characteristic frequency. The thermal boundary resistance can be included by adding the inverses of the conductances: $G_{\text{total}}^{-1} = G^{-1} + G_{\text{int}}^{-1}$. Using a curvature parameter value of $c_m=0.65$ and a thermal boundary resistance of $G_{\text{int}}^{-1} = 0.09 \text{ K nW}^{-1}$, the analytical model matches well with molecular dynamic simulations of a (3,3) nanotube [98].

2.2.3.2 Phonon Transport Calculations

Predictions of nanotube thermal conductivity stem from descriptions of the wave vector models describing the transport of phonons within a CNT. Wave vector models begin from kinetic theory and require knowledge of the specific heat, the phonon group velocity, the mean free path or relaxation time. Solutions to the Peierls-Boltzmann equation, which describes the transport of phonons within a material, allow calculation of the thermal conductivity without making the relaxation time approximation.

Chantrenne and Barrat [97] developed an analytical model of thermal conductivity by analysis of the phonon spectrum with properties dependent on the wave vector. The thermal conductivity in the x -direction, k_x , becomes

$$k_x = \sum_q \sum_m C_m(q) v_m^2(q) \tau_m(q) \cos^2(\theta_m(q)), \quad (2.11)$$

where $C_m(q)$ and $v_m(q)$ are the specific heat and group velocity of the phonon with wave vector, q , and polarization (branch index), m , $\tau_m(q)$ is the phonon relaxation time due to scattering for the mode, and $\theta_m(q)$ is the angle between the wave vector q and the direction x . Yan *et al.* [99], Cao *et al.* [100], and Wang *et al.* [56] formulate comparable models, but neglect the cosine term. Through the dispersion curve, the dependence on the wave vector, q , can be transformed into the angular frequency, ω .

*REVIEW OF THERMAL CONDUCTION PHENOMENA IN CARBON NANOTUBES
AND RELATED NANOSTRUCTURED MATERIALS*

The scattering mechanisms include three-phonon (Umklapp) processes, boundary scattering, and defect scattering and the total relaxation time can be computed through

$$\tau^{-1}(\omega) = \tau_U^{-1}(\omega) + \tau_{BC}^{-1}(\omega) + \sum_{i=1}^{N_d} \tau_{D,i}^{-1}(\omega), \quad (2.12)$$

where τ_U is the relaxation time due to Umklapp processes, τ_{BC} is the relaxation time due to boundary scattering, $\tau_{D,i}$ is the relaxation time due to the i^{th} defect, and N_d is the total number of defects (including impurities, isotopes, vacancies, etc.). To validate their wave vector model, Chantrenne and Barrat [97] calculated the thermal conductivity of a cube of argon and compared the predictions with results from non-equilibrium molecular dynamics (NEMD) simulations of the same system. Upon finding good agreement between the models, the wave vector model was extended to sheets of graphene and carbon nanotubes.

Table 2.2: Phonon Transport Model Summary

Article	Chiralities	Umklapp Scattering	Boundary Scattering	Comments
Chantrenne and Barrat [97]	(9,0) (18,0) (36,0)	$\tau_U^{-1}(\omega) = A_1(T)\omega^2$	$\tau_{BC}^{-1}(q) = v(q, m) \frac{1-s}{L(q)}$	System size varied
Wang <i>et al.</i> [56]		$\tau_{1,U}^{-1}(\omega) = A\omega^2 \frac{T}{T_0}$ $\tau_{2,U}^{-1}(\omega) = \frac{32}{27} \gamma^4 \left(\frac{T}{T_0} \right)^2 \omega_b$	$\tau_{BC}^{-1}(q) = v(q, m) \frac{1-s}{L(q)}$	N-Phonon processes included. Length and temperature varied.
Yan <i>et al.</i> [99]	(5,5) to (20,20) (5,0) to (20,0)	$\tau_U^{-1}(q) = \frac{4\gamma^2 h}{3} \sum_{q'} \frac{F(\omega, v, N_0)}{\rho}$	$\tau_{BC} = 50 ps$	Length and Temperature varied. MWCNT. Weak and strong coupling
Cao <i>et al.</i> [100]	(6,0) to (14,0)	$\tau_U^{-1}(q) = \frac{4\gamma^2 h}{3} \sum_{q'} \frac{F(\omega, v, N_0)}{\rho}$	$\tau_{BC} = 50 ps$	Temperature varied.

Approximations for the relaxation times must be used to estimate thermal conductivity and several forms are plausible for the relaxation time due to Umklapp

processes. Chantrenne and Barrat [97] expressed the temperature and frequency dependence of the Umklapp relaxation time as

$$\tau_U^{-1}(\omega) = A\omega^2 T^\xi \exp\left(\frac{-B}{T}\right), \quad (2.13)$$

where A , B , and ξ are fitted to the temperature variations of the bulk thermal conductivity, though in their calculations, they used a simplified expression $\tau_U^{-1}(\omega) = A_I(T)\omega^2$ where A_I is determined by fitting the calculated thermal conductivity to the measured bulk thermal conductivity of the material. Since the bulk thermal conductivity of the carbon nanotubes is unknown, an arbitrary value of A_I was chosen and the variations in thermal conductivity were calculated rather than the absolute magnitude. Both Yan *et al.* [99] and Cao *et al.* [100] define the first-order relaxation time for Umklapp scattering as:

$$\tau_U^{-1}(q) = \frac{4\gamma^2 h}{3} \sum_{q'} \frac{F(\omega, \nu, N_0)}{\rho}, \quad (2.14)$$

where

$$F(\omega, \nu, N_o) = \left[\frac{\omega\omega'\omega''(N'_0 - N''_0)}{v_g^2} \right] \delta(\omega + \omega' - \omega''), \quad (2.15)$$

ρ is the mass density, and N'_0 and N''_0 are the equilibrium occupancies of q' and q'' phonons. Wang *et al.* [56] considered the first-order 3-phonon Umklapp process with a relaxation time of

$$\tau_{1,U}^{-1}(\omega) = A\omega^2 \frac{T}{T_0}, \quad (2.16)$$

but also included the Umklapp scattering to second-order:

$$\tau_{2,U}^{-1}(\omega) = \frac{32}{27} \gamma^4 \left(\frac{T}{T_0} \right)^2 \omega_b, \quad (2.17)$$

where $A = 4\pi\alpha\gamma^2/\nu$, T_0 is the characteristic temperature of the material, $T_0 = Mv^2/k_B$, α^3 is the atom volume, M is the atom mass, γ is the Grüneisen parameter, and ω_b is the phonon branch frequency at the zone boundary. Additionally, Wang *et al.* [56] considered N-phonon processes in the calculation of the total relaxation time, τ .

*REVIEW OF THERMAL CONDUCTION PHENOMENA IN CARBON NANOTUBES
AND RELATED NANOSTRUCTURED MATERIALS*

Boundary scattering should also be included in a comprehensive thermal conductivity model. The relaxation time due to the boundary scattering can be approximated as

$$\tau_{BC}^{-1}(q) = v(q, m) \frac{1-s}{L(q)}, \quad (2.18)$$

where s is the fraction of all phonons which scatter specularly from the boundaries ($s \in [0-1]$) and $L(q)$ is the distance a phonon with wavevector q and polarization m can travel between boundary surfaces [56, 97]. In contrast, some authors set the relaxation time for the boundary scattering to be 50 ps [59, 99, 100], independent of temperature and phonon energy, an approach that is supported by experimental and theoretical work [59, 64, 85, 101, 102]. Experimental measurements [59] of the thermal conductivity of a nanotube rope at low temperatures (<30 K) suggest an energy-independent mean free path consistent with boundary scattering. Similarly Kim *et al.* [64] observed a temperature-independent component of the mean free path on the order of the length of the nanotube. Yan *et al.* [99] and Cao *et al.* [100] investigate the effect of different chiralities in SWCNTs using wave vector models. Yan *et al.* [99] extends the model to multi-wall nanotubes and investigates the differences between strong and weak coupling between walls in multi-wall nanotubes. Table 2.2 summarizes different phonon transport models highlighting the different models for Umklapp and boundary scattering relaxation times.

The transport of phonons in a solid can be calculated using the Peierls-Boltzmann phonon transport equation [55]:

$$-v_p \frac{dn_p}{dx} = \left(\frac{\partial n_p}{\partial t} \right)_c, \quad (2.19)$$

where $p = \{q, m\}$ is the phonon wave vector, q , and the branch index, m , n_p is the distribution function, v_p is the phonon group velocity, and $\left(\frac{\partial n_p}{\partial t} \right)_c$ is from the collision of phonons. Mingo and Broido [55] iteratively solve the Peierls-Boltzmann phonon transport equation for single-wall carbon nanotubes with a linearized form of the

collision term $\left(\frac{\partial n_p}{\partial t}\right)_c$ and scattering due 3-phonon processes (up to second-order).

When only first-order 3-phonon processes are included, the thermal conductivity diverges with the nanotube length. Second-order processes must also be included for the thermal conductivity to saturate with length. From the solution to the Peierls-Boltzmann equation, the thermal conductivity can be computed without making the relaxation time approximation. At 316 K, for a (10,0) nanotube, the thermal conductivity saturates to $\sim 4000 \text{ W m}^{-1} \text{ K}^{-1}$, but this only an estimate due to the approximation used for the second-order 3-phonon process.

2.2.3.3 Molecular Dynamics Simulations

Molecular dynamics (MD) simulations compute thermal transport based on the interaction potentials between the carbon atoms. Several different empirical forms of the atomic interaction potential have been proposed [2, 4, 7, 9, 12, 15, 19]. Lepri *et al.* [103] described in detail molecular dynamics simulations in low dimensional lattices. Simulations based on equilibrium molecular dynamics (EMD), non-equilibrium molecular dynamics (NEMD) [8, 10, 11, 13, 14, 104], and homogeneous nonequilibrium molecular dynamics (HNEMD) [18, 20] were fruitful even before experiments on individual nanotubes were developed. EMD simulations use the Green-Kubo formula derived from linear response theory [17, 105]:

$$k_{\alpha\beta} = \frac{1}{Vk_B T^2} \int_0^\infty \langle J_\alpha(t) \cdot J_\beta(t) \rangle dt, \quad (2.20)$$

where $k_{\alpha\beta}$ is the (α, β) component of the thermal conductivity tensor, V is the volume, J_α and J_β are the components of the heat current in the α and β direction respectively. NEMD simulations use the Fourier conduction law to determine the thermal conductivity by applying either a fixed temperature gradient or heat flux to the system. The thermal conductivity is related to the thermal gradient by [105]

$$J_\alpha = - \sum_\beta k_{\alpha\beta} \frac{\partial T}{\partial x_\beta}, \quad (2.21)$$

*REVIEW OF THERMAL CONDUCTION PHENOMENA IN CARBON NANOTUBES
AND RELATED NANOSTRUCTURED MATERIALS*

where $\frac{\partial T}{\partial x_\beta}$ is the thermal gradient along the β -direction. HNEMD simulations apply an external field to mimic the heat flow without actually applying a heat flux or temperature gradient [105].

Table 2.3 summarizes the results of many of the different molecular dynamics simulations reported in literature. As with the experimental results, the MD calculations require definitions of the cross-sectional area for heat transport. For single-wall nanotube simulations, most authors select the area $A = \pi d \delta$ with δ ranging from 0.1 nm to 0.34 nm. For comparison, the results of all experimental and modeling reviewed in this paper are standardized using $A = \pi d_o^2/4$, although also shown in

Table 2.3 are values for k' , the thermal conductivity calculated with $A = \pi d \delta$, where $\delta = 0.34$ nm.

Many reports have simulated thermal conduction of CNTs with a chiral vector of (10,10) yielding values from $80 \text{ W m}^{-1} \text{ K}^{-1}$ [105] to $6600 \text{ W m}^{-1} \text{ K}^{-1}$ [18] at 300 K, with one extreme outlier at $10^{23} \text{ W m}^{-1} \text{ K}^{-1}$ [16]. Variations in the nanotube length, boundary conditions, molecular dynamics methods (EMD, NEMD, and HNEMD), and interatomic potentials contribute to the range of simulated values. The effect of nanotube length is discussed later in this review in combination with experimental data. Some of the MD work discussed here did not consider the effect of length in the simulations. Thus, it is unclear whether those MD results can be compared to the experiments with the long CNTs.

Table 2.3: Molecular Dynamics Simulations Summary. Room temperature thermal conductivity values for the maximum length simulated.

Article	Chirality	L [nm]	D [nm]	^a k [W m ⁻¹ K ⁻¹]	^b k' [W m ⁻¹ K ⁻¹]	Sim. Type	Potential	Converged with length?
Che <i>et al.</i> [1]	(10,10)	<40	1.36	880	880	EMD	Brenner [2]	Yes (>10 nm)
Padgett and Brenner [3]	(10,10)	<1500	1.351	355	350	NEMD	2 nd Generation REBO [4]	Yes (>150nm)
Grujicic <i>et al.</i> [5, 6]	(10,10)	2.477 to 39.632	1.351	895	890			
	(18,0)	2.145 to 34.320	1.404	790	815	EMD	AIREBO [7]	Yes (>~10 nm)
	(14,6)	3.813 to 30.504	1.387	765	780			
Osman and Srivastava [8]	(5,5)	Aspect ratio of 10 to 20 (~ 22 nm)	0.68	4500	2250			
	(10,10)		1.36	1700	1700	NEMD	Tersoff-Brenner [2, 9]	Not investigated. Assumed to be long enough because of the results of Che <i>et al.</i> [1].
	(15,5)		1.41	1640	1700			
	(10,0)		0.78	3900	2250			
Zhang <i>et al.</i> [10]	(5,5)		0.68	410	205			
	(6,6)		0.81	435	260	NEMD	COMPASS	Variation between 12.2 nm and 24.4 nm results
	(8,8)	12.2 and 24.4	1.08	365	290			
	(10,10)		1.35	300	300			
Zhang and Li [11]	(9,0)		0.714	710	370	NEMD	Tersoff [12]	No
	(10,0)	0.1 to 100	0.794	560	330			
	(5,5)		0.686	810	410			
Maruyama [13]	(5,5)	6 to 404	0.68	1000	500	NEMD	Tersoff-Brenner [2]	No
	(10,10)		1.36	400	400			
Maruyama [14]	(5,5)	12 to 404	0.68	1350	675	NEMD	Simplified Brenner [2, 15]	No
	(8,8)		1.09	560	450			
	(10,10)		1.36	400	400			
Yao <i>et al.</i> [16]	(5,5)	6 to 100	0.68	~10 ²⁴	~10 ²³	EMD	Tersoff [12]	No
	(10,10)		1.36	~10 ²³	~10 ²³			
	(15,15)		2.03	~10 ²²	~10 ²²			
Lukes and Zhong [17]	(10,10)	5 to 40	1.36	~120 to 150	~120 to 150	EMD	2 nd Generation REBO [4]	No (Free and periodic BC tested)
		5 to 10	1.36	~240 to 375	~240 to 375	HNEMD	and Lennard-Jones	No
Berber <i>et al.</i> [18]	(10,10)	2.47	1.36	6600	66000	HNEMD	Tersoff [19]	Not investigated (Periodic Boundary Conditions)
W. Zhang <i>et al.</i> [20]	(10,10)	--	1.36	2200	2200			
	(11,11)	30	1.49	3190	3500	HNEMD	Brenner [2]	Not investigated (Periodic Boundary Conditions)
	(10,13)	29	1.56	870	1000			
	(20,0)	26	1.57	6730	7750			

^ak values using ^bk' values using , where $\delta=0.34$ nm. ^cVariations due to fitting method.

2.2.4 Summary of Key Findings

2.2.4.1 Geometrical Effect

2.2.4.1.1 Length

Thermal conduction transitions from the ballistic to the diffusive conduction regime as the nanotube length increases. The phonon mean free path depends on temperature such that for the same nanotube ballistic conduction can be observed at low temperature, while diffusive conduction prevails at room temperature. In the ballistic conduction regime, the thermal conductance, $G_{ballistic}$, is fixed and the thermal conductivity apparently increases with nanotube length as $k = G_{ballistic}L/A$. The thermal conductivity reaches a constant value at lengths much longer than the mean free path, where the conduction is diffusive. Figure 2.3 shows experimental data for the thermal conductance of single-wall [56, 60, 63, 68-70] and multi-wall [57, 60, 62, 64, 67, 69] nanotubes at room temperature. The majority of the available experimental data is for nanotubes longer than 0.5 μm . Since the conductance data of the nanotubes follows approximate inverse proportionality with length, it appears that these nanotubes behave diffusively and have lengths much longer than the mean free path. Despite the varying diameters, and perhaps also varying chiralities, of the nanotubes characterized by the various authors, the $1/L$ trend remains present. Figure 2.4 compares experimentally measured thermal conductances [56, 63, 68-70] with the predictions of several modelling efforts [56, 68, 83, 84] for SWCNTs of approximately the same diameters (1.4 to 1.9 nm). The ballistic conductance model [83], with the extension to the diffusive regime as discussed in Section 2.2.3.1, was plotted for two chiralities of nanotubes with diameters of approximately 1.9 nm: a (24,0) zigzag nanotube with a 1.88 nm diameter and a (14,14) armchair nanotube with a 1.89 nm diameter. Though not included in the figure, the predictions of the model of Yamamoto *et al.* [98] (Eq. (2.8)) yield a smooth transition from the ballistic to the diffusive regime by considering the length-dependence of the Umklapp scattering processes (Eq. (2.9)) and compare well with molecular dynamics simulations of the (3,3) and (5,5) SWCNTs. An empirical model [68], developed from an analytical fit to the temperature dependency of

the measured thermal conductivity for a 1.7 nm SWCNT in conjunction with additional data from Yu *et al.* [63], predicts a thermal conductivity given by:

$$k' = \left[3.7 \times 10^{-7} T + 9.7 \times 10^{-10} T^2 + 9.3 \left(1 + \frac{0.5}{L} \right) T^{-2} \right]^{-1}, \quad (2.22)$$

where the temperature T is in units of Kelvin and nanotube length L is in units of microns. The length dependence is based on Matthiessen's rule assuming an intrinsic mean free path of 500 nm. The thermal conductivity (k') is defined with a cross-sectional area of $A = \pi d \delta$ and the thermal conductance as plotted in the figure is calculated from this model as $G = k' \pi d \delta / L$. The majority of the molecular dynamics simulations are for nanotubes of slightly smaller diameter, $d \sim 1.4$ nm, than those of the measured CNTs, $d \sim 1.8$ nm. However, the results the model of Che *et al.* [1] for (10,10) SWCNTs ($d=1.36$ nm) are included in Figure 2.4. Above lengths of ~ 10 nm, the MD simulation reached a constant thermal conductivity and the conductance plotted in Figure 2.4 is predicted from this value. The trend of the thermal conductance with length appears to agree well with several of the models, and this is perhaps surprising owing to the difference in CNT diameters. No experimental results are available for nanotubes shorter than approximately $0.5 \mu\text{m}$ and the fully ballistic conduction regime is predicted at room temperature only for these short lengths.

In MD simulations, variations in the size of the simulation domain, *i.e.* the nanotube length, and in the boundary conditions at the ends of the simulation domain, can lead to differences in the predicted thermal conductivity. Periodic boundary conditions along the axis of the nanotube are used to approximate nanotubes of infinite length [18, 20]. However, periodic boundary conditions do not accurately simulate long nanotubes. Lukes [17] and Zhong [105] reported that even with periodic boundary conditions, increasing the simulated length of the nanotube increased the predicted thermal conductivity. Lukes and Zhong [17] suggested that this arises from the fact that longer nanotubes have more vibrational modes with smaller wavevectors and longer wavelengths, which provide new pathways for heat transfer not captured by simulations with shorter period. The “new” low wavevector modes can be particularly effective contributors to the thermal conductivity since they are less likely to scatter due to

*REVIEW OF THERMAL CONDUCTION PHENOMENA IN CARBON NANOTUBES
AND RELATED NANOSTRUCTURED MATERIALS*

Umklapp processes. Finite lengths of the simulated nanotubes allow investigation the size effect [1, 3, 5, 6, 8, 10, 13, 14, 44]. Some simulations achieved convergence with length in as little as 10 nm [1, 5, 6] to ~150 nm [3]. In other MD simulations, no convergence is found within the range of lengths simulated (0.1 to 100 nm [11]; 6 to 400 nm [13, 14]) and a power law ($k \sim L^\alpha$) can be fit to these simulated results. The exponent, α , ranged from 0.1 to 0.4 depending on the chirality and temperature of the simulated nanotube [11, 13, 14]. However, in these simulations, the simulated CNT length is shorter than the expected mean free path and the conduction is not diffusive. The thermal conductivity may yet saturate if the simulation was carried out to longer lengths.

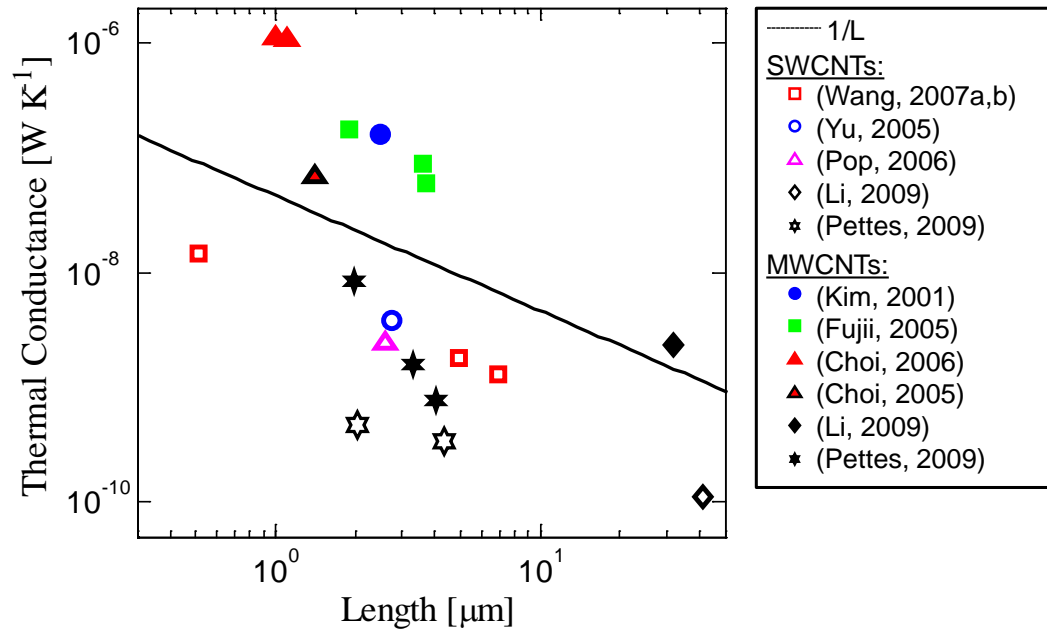
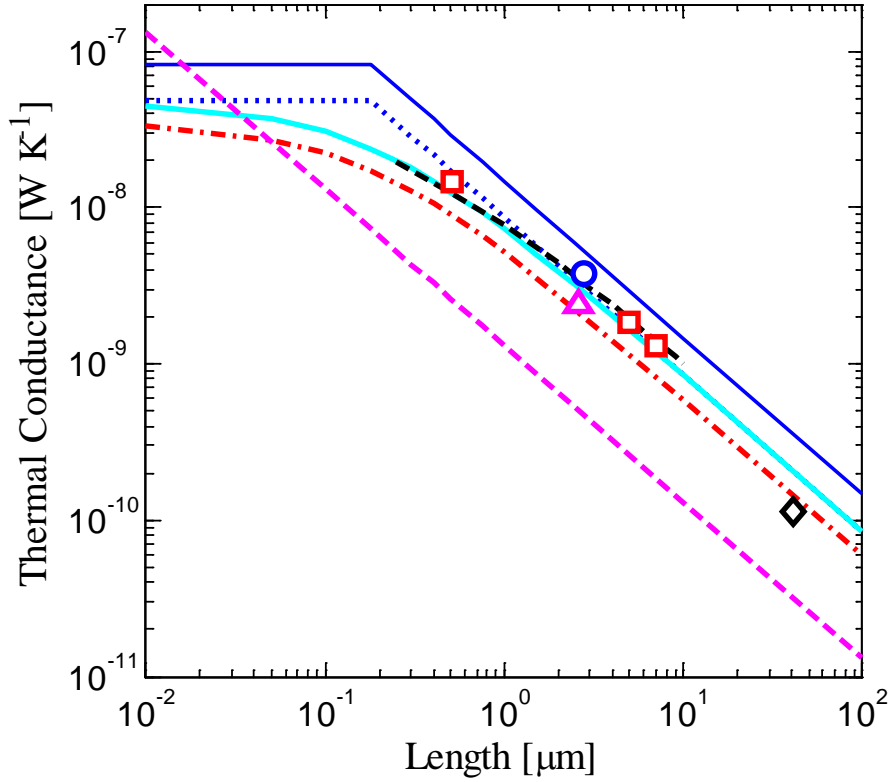


Figure 2.3: Room temperature thermal conductance of carbon nanotubes as a function of length. Filled-in symbols denote MWCNTs, while open symbols denote SWCNTs. The solid line indicates the 1/L trend expected for a fixed thermal conductivity, i.e. diffusive conduction in nanotubes.



Article	Chirality	Diameter (nm)	Model or Experiment
— Shang <i>et al.</i> [83]	(24,0)	1.88	Ballistic Conductance Model
..... Shang <i>et al.</i> [83]	(14,14)	1.89	Ballistic Conductance Model
— Wang <i>et al.</i> [84]	(14,14)	1.89	Ballistic-to-Diffusive Crossover
--- Wang <i>et al.</i> [56]	-	1.9	Wave Vector Model
--- Che <i>et al.</i> [1]	(10,10)	1.4	Molecular Dynamics
..... Pop <i>et al.</i> [68]	-	1.7	Empirical Model
□ Wang <i>et al.</i> [56, 70]	-	1.9	Experiment
○ Yu <i>et al.</i> [63]	-	1 to 3	Experiment
△ Pop <i>et al.</i> [68]	-	1.7	Experiment
◇ Li <i>et al.</i> [69]	-	1.8	Experiment

Figure 2.4: Predictions and data for the thermal conductance of single-wall carbon nanotubes with comparable nanotube diameters. The models of Wang *et al.* [84], Wang *et al.* [56, 70], and Shang *et al.* [83] were computed with nanotubes with approximately 1.9 nm diameter and for Wang *et al.* [84] and Shang *et al.* [83] a mean free path of 180 nm was used in the calculations. For the empirical model of Pop *et al.* [68], a phonon mean free path of 500 nm was extracted from experiments. The ballistic conductance models can be extended to any chirality of nanotube and to multi-wall nanotubes, however, the model from Pop *et al.* [68] was developed in conjunction with experimental data for thermal conductivity versus temperature, so is strictly only valid for nanotubes of the same diameter and chirality. For the wave vector model of Wang *et al.* [56], the Grüneisen parameter and the specularity of boundary scattering were adjusted to match the data from their experiment. The molecular dynamics simulation of Che *et al.* [1] was computed only up to lengths of 50 nm, but above ~ 10 nm a uniform value of the thermal conductivity was achieved and that is what is plotted. All measurements and predictions are at room temperature.

*REVIEW OF THERMAL CONDUCTION PHENOMENA IN CARBON NANOTUBES
AND RELATED NANOSTRUCTURED MATERIALS*

Divergence of the thermal conductivity with length has also been predicted for low-dimensional lattices [29, 103], and observed in models for CNTs when only first-order Umklapp scattering is considered. Wang and Wang [84] found that the thermal conductivity followed two separate power laws for the ballistic regime and the diffusive regimes, with the $\alpha_{ballistic} > \alpha_{diffusive}$. At low temperatures and short lengths (ballistic conductance), the relationship trended towards the ballistic limit $k \sim L$. However, for longer nanotubes or at higher temperatures the tubes demonstrated more diffusive behavior, $k \sim L^\alpha$ with $\alpha < 1$. Solutions to the Peierls-Boltzmann equation [55] and wavevector models [56] have both shown that considering only first-order 3-phonon processes leads to thermal conductivity diverging with length, but when 3-phonon processes are included to second order, the thermal conductivity saturates with length agreeing better with experimental results. Yamamoto *et al.* [98] discussed that when considering only first-order Umklapp processes, the thermal conductivity diverges with length as $k \sim L^{1/2}$ due to model for the acoustic phonon branches, but this can be corrected by considering higher-order scattering processes. However, these authors [98] obtained good agreement between MD simulations and their model including only first-order Umklapp processes indicating that for the lengths considered, higher-order effects may be negligible.

In general, in the ballistic conduction regime, the thermal conductance is constant (i.e. the thermal conductivity increases with length), while in the diffusive conduction regime, the thermal conductivity saturates to a constant value. In the intermediate regime, a smooth transition results from quasi-ballistic or mesoscopic effects. Models which neglect higher-order three-phonon processes result in predicted thermal conductivities which diverge with increasing length for all lengths, which is not physically observed. Additionally, MD models in which the domain is smaller than the mean free path exhibit increasing thermal conductivity. To accurately predict the thermal conductivity of long CNTs the models must be extended to longer lengths.

2.2.4.1.2 Chirality and Diameter

While the dependence of the electrical properties on the chirality is well documented, the impact of chirality on the thermal properties has received less attention. Experimentally it is difficult to measure or control the chirality of nanotube, although the outer diameter is typically measureable. In simulations, effects of both the diameter and the chirality can be explored, but many discrepancies exist between the results of different calculations.

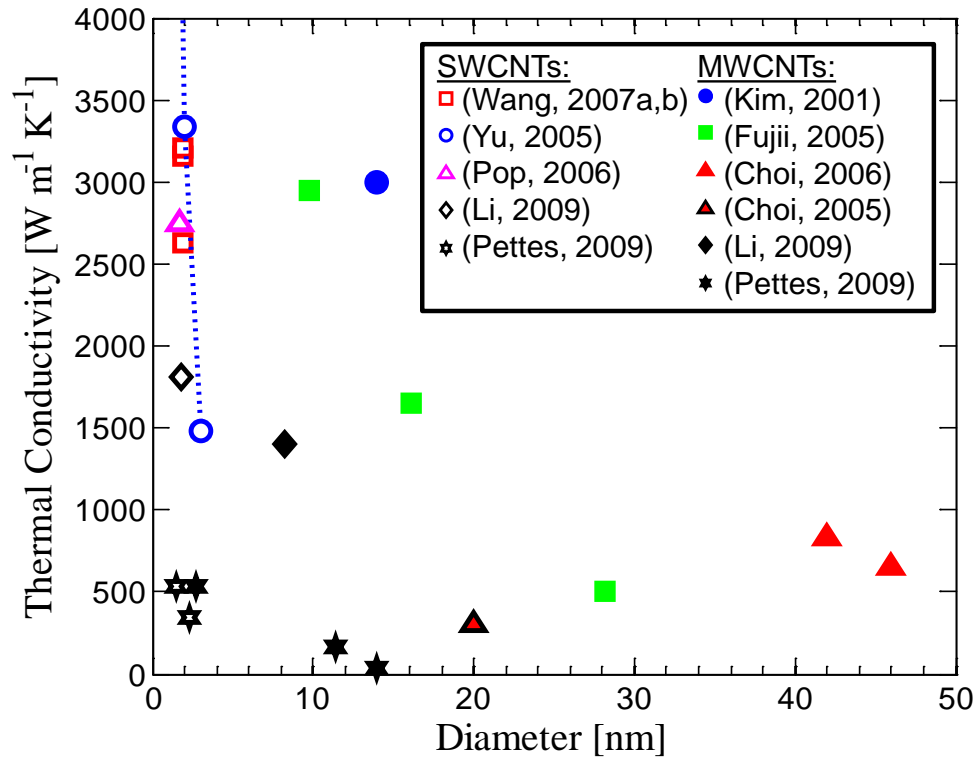


Figure 2.5: Thermal conductivity data as a function of nanotube diameter. Open and filled data points are for single-wall and multi-wall nanotubes, respectively. A decrease in thermal conductivity with increasing diameter is observed. The range of values shown for Yu *et al.* [63] is due to the uncertainty in the measurement of the nanotube diameter. The SWCNT data for Pettes and Shi [60] is a lower bound on the thermal conductivity, while the effect of contact resistance at the ends of the nanotubes is accounted for in the MWCNTs. Thermal conductivity values are standardized using the enclosed area of the nanotube, $A = \pi d^2 / 4$.

Figure 2.5 shows experimental results of the diameter dependence of the room temperature thermal conductivity for both single-wall and multi-wall nanotubes. For

*REVIEW OF THERMAL CONDUCTION PHENOMENA IN CARBON NANOTUBES
AND RELATED NANOSTRUCTURED MATERIALS*

SWCNTs, the diameter dependence of the thermal conductivity is difficult to observe because most data are for tubes with similar diameters (1.7 nm to 1.9 nm). Yu *et al.* [63] measured a nanotube which had a diameter in the range of 1 nm to 3 nm, but not exactly known due to the limits of the measurement technique, leading to the large range of thermal conductivities shown on the graph. Combining the SWCNT and the MWCNT data in the figure shows a general decrease in thermal conductivity with increasing diameter. Pettes and Shi [60] found that the thermal conductivity of MWCNTs decreased with the number of walls, but this apparently correlated with an increased concentration of defects in nanotubes with more walls.

Many authors have shown through simulations of tubes with the same chirality that the thermal conductivity decreases with increasing diameter [11, 84, 97, 99, 100]. The exact dependence of thermal conductivity on CNT diameter is due to a combination of the diameter dependence of scattering rates and change in number of conduction channels with tube diameter. For both armchair (n,n) and zigzag (n,0) nanotubes, Yan *et al.* [99] calculated that $k \sim n^{-2}$ with the explanation that the increased phonon energy gap in smaller diameter nanotubes relaxes requirements for conservation both of energy and momentum, suppressing Umklapp processes in small diameter nanotubes. The room temperature thermal conductivity of chiral nanotubes depends on the number of atoms in the unit cell, N , which depends on the diameter, and the density of the nanotube, ρ , [99]:

$$\frac{k|_{T=300K}}{\rho} \propto N^{-1.3}. \quad (2.23)$$

When comparing armchair nanotubes, Osman and Srivastava [8] found that the smaller diameter nanotubes had the highest thermal conductivity compared to the larger nanotubes at room temperature. Wang and Wang [84] found that the room temperature thermal conductance should follow the relationship $G \sim d$ for single-wall nanotubes. Since the diameter of a nanotube is given by (Eq. (2.5)), for both armchair (n,n) and zigzag (n,0) nanotubes, the diameter of the nanotube goes as n , the thermal conductivity from Wang and Wang [84] goes as n^{-1} , a slightly different dependence than from Yan *et al.* [99] but agreeing with the general trend of the thermal conductivity decreasing

with increasing diameter. In contrast, Zhang *et al.* [10] found that the thermal conductivity of armchair nanotubes at 300K increased with increasing diameter.

Several simulations show the peak in thermal conductivity with temperature shifts depending on nanotube diameter, although the direction of the shift is not consistent. Yan *et al.* [99] and Cao *et al.* [100] found that the temperature at which the thermal conductivity reaches its maximum value shifts to lower temperatures for larger diameter nanotubes. Cao *et al.* [100] note that this is because at all temperatures, the probability of Umklapp processes increases for larger diameter nanotubes. The geometry of one dimensional systems reduces the number of states into which phonons can scatter and therefore in larger diameter tubes, there are more lower energy phonon states [100]. This is contrary to the argument of Osman and Srivastava [8] that at all temperatures Umklapp processes are more likely in smaller diameter nanotubes with minimum wavevectors closer to the reciprocal lattice vector. Osman and Srivastava [8] predict that the peak in thermal conductivity with temperature occurs at a lower temperature in smaller diameter nanotubes. Measurements of several different SWCNTs [63, 68] and MWCNTs [62, 64] all show peaks in the thermal conductivity around 300 K regardless of diameter, suggesting that any shift in the peak with diameter is slight. Defects present in these measured nanotubes may be more important than the diameter and chirality determining the scattering rate and peak thermal conductivity [55].

Several authors have modeled the effect of nanotube chirality on the thermal conductivity. Many found no major effect of the chirality on the thermal conductivity [8, 11, 58, 84, 86, 88]. The phonon density of states is not significantly altered for different chirality of nanotubes suggesting that the thermal conductivity should not be significantly affected by chirality [11, 106]. Yamamoto *et al.* [58, 86] found that energy of the lowest optical phonon mode depended only on the nanotube radius, not the chirality.

Other modeling efforts reported thermal conductivity variations with chirality [8, 20, 83, 104], possibly due to the structural differences between the bonds in nanotubes of different chiralities. In armchair and chiral nanotubes, the sigma bonds form along the nanotube circumference, while in zigzag nanotubes, these bonds are along the nanotube axis. The stretching of the sigma bonds cause excess strain along the nanotube

*REVIEW OF THERMAL CONDUCTION PHENOMENA IN CARBON NANOTUBES
AND RELATED NANOSTRUCTURED MATERIALS*

circumference, which shortens the mean free path of armchair and chiral nanotubes and lowers the thermal conductivity [8, 20]. In a MD simulation of the propagation of a heat pulse in a SWCNT, Osman and Srivastava [104] found the amount energy carried by the longitudinal acoustic and twist phonon modes is larger for zigzag than for armchair nanotubes. This finding agrees with models which show that the zigzag nanotubes have higher thermal conductivity than other chiralities. Zhang *et al.* [20] found that below 400K the thermal conductivity of the (20,0) zigzag nanotube is higher than the (11,11) armchair nanotube of nearly identical diameter, but both peak at the same temperature and approximately the same maximum thermal conductivity. At all temperatures, a (10,13) chiral nanotube had lower thermal conductivity than zigzag and armchair nanotubes with the same diameter. The fact that zigzag nanotubes may have more phonon channels than armchair tubes for the same diameter compared to armchair nanotube is a possible explanation for the higher ballistic conductivity of zigzag tubes [83]. In contrast, Yan *et al.* [99] found that armchair nanotubes had a larger room temperature thermal conductivity than zigzag nanotubes at the same diameters. There is not a clear consensus on the effect of chirality and diameter on CNT thermal conductivity.

2.2.4.2 Temperature Dependence

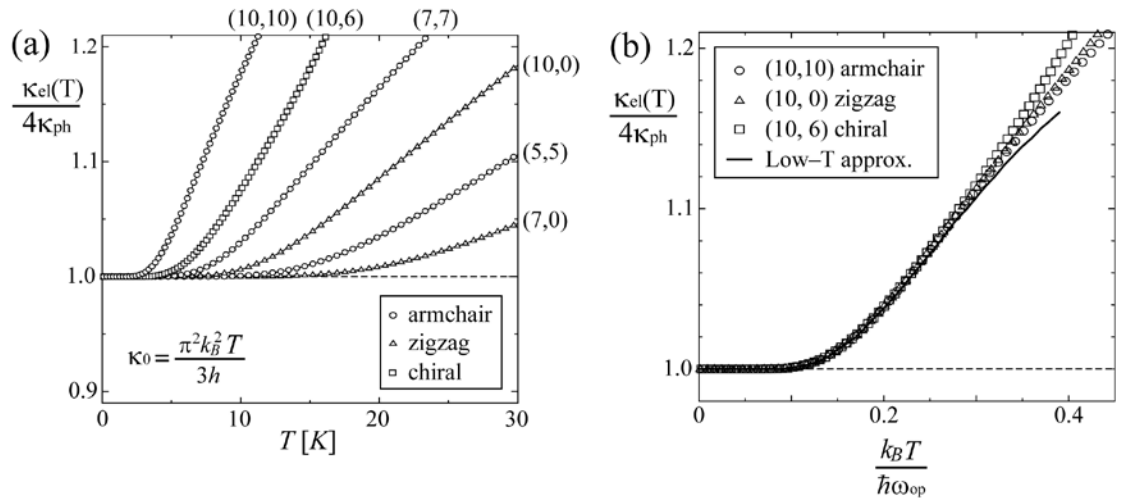


Figure 2.6: (a) Low temperature thermal conductance of nanotubes with varying chirality as calculated by Yamamoto *et al.* [86]. (b) When the temperature is scaled by the energy gap of the lowest optical mode, the thermal conductance for each of the different chiralities collapses to a single curve [86].

Several competing processes contribute to the temperature dependence of thermal conductivity of carbon nanotubes. At low temperatures, heat transport is ballistic and the thermal conductance and the thermal conductivity increase linearly with temperature, a trend that is present also in the quantum of thermal conductance in equation (2.3) [55, 58, 84, 86, 88]. The ballistic regime is predicted up to 100K for (10,10) nanotubes of moderate length ($\sim 1 \mu\text{m}$) [55]. As the temperature increases and additional phonon modes contribute, the total thermal conductivity increases along with the increase in specific heat [58, 86]. A peak in thermal conductivity with temperature is expected near room temperature [8, 10, 11, 18, 20, 100] due to competition between the excitation of more high-frequency phonons and the increased scattering rate [11]. At higher temperatures, the thermal conductivity begins to decrease with temperature as scattering processes dominate. The measurements and predictions in the literature follow the basic temperature dependence in Table 2.4.

Table 2.4: Temperature Dependence of the Thermal Conductivity of Carbon Nanotubes. Experimental results for MWCNTs appear to follow similar trends with temperature as SWCNTs.

Regime	Conductivity Dependence
Ballistic Regime (very low temperature)	$k \sim T$. Ballistic conductance.
Intermediate	$k \sim$ specific heat. More phonon branches excited increasing the specific heat.
Peak	Balance between increasing specific heat and increased scattering
Diffusive Regime (High temperature)	$k \sim T^{-1}$ Scattering processes dominate Second-order three-phonon scattering processes contribute as $k \sim T^{-2}$

Below a few Kelvin, only the four acoustic modes described in Section 2.2.3 contribute to the thermal conductance. As shown in Figure 2.6(a), the temperature at which the optical modes begin to contribute to the thermal conductance depends on the energy gap of the lowest-lying optical mode ($\hbar\omega_{op}$), which in turn depends on the chirality and nanotube diameter (see Figure 2.2). As shown in Figure 2.6 (b), when the temperature is normalized by the energy gap of the lowest lying optical mode (defining $\tau_{op} = k_B T / (\hbar\omega_{op})$), the predicted thermal conductance for all modelled CNTs collapses to a single curve, which at low temperature can be approximated as [86]

*REVIEW OF THERMAL CONDUCTION PHENOMENA IN CARBON NANOTUBES
AND RELATED NANOSTRUCTURED MATERIALS*

$$\frac{G}{4G_{th}} \approx 1 + \frac{3}{\pi^2} e^{-\frac{1}{\tau_{op}}} \left(1 + \frac{1}{\tau_{op}} + \frac{1}{2\tau_{op}^2} \right). \quad (2.24)$$

As the temperature increases from a few degrees Kelvin towards room temperature, phonon-phonon scattering remains negligible and boundary scattering governs the phonon mean free path. Using the approximation $k = \sum C v^2 \tau$, it is evident that thermal conductivity increases with temperature as the specific heat and number of phonon modes increases [52] and the scattering rate due to boundary scattering remains constant [88, 99]. Models by Yan *et al.* [99] and Kahaly and Waghmare [107] found that below about 200K, the thermal conductivity increased following the dependence of the specific heat. Specifically, Kahaly and Waghmare [107] predicted that the thermal conductivity will follow the $T^{1.5}$ trend in heat capacity in this temperature range.

The thermal conductivity reaches a maximum when the increasing phonon population is balanced by reductions in the phonon mean free paths due to scattering. Several molecular dynamics [8, 11, 20] and lattice dynamic models [100] found that the temperature at which the thermal conductivity achieves its maximum value depended on the nanotube chirality, with the peak conductivity in temperature in the range of 200K to 400K. Zhang and Li [11] found that the presence of isotope impurities modifies the temperature dependence of the carbon nanotube. Specifically, for a pure SWCNT, a peak in thermal conductivity was observed at 250 K, while when 40% ^{14}C impurity was introduced to the SWCNT model, the thermal conductivity decreased with increasing temperature from 100 K to 400 K [11].

At higher temperatures, the thermal conductivity decreases in thermal conductivity with temperature as Umklapp scattering processes dominate. First-order Umklapp scattering processes lead to a $k \sim T^{-1}$ dependence at high temperature [8, 14], but there is also a $\sim T^2$ contribution due to second-order three-phonon effects [68]. Figure 2.7 shows both the combined experimental data set used for extracting the coefficients in the temperature-dependent thermal conductivity model (Eq. (2.22)) of Pop *et al.* [68] and the resulting prediction of thermal conductivity at various lengths and temperatures.

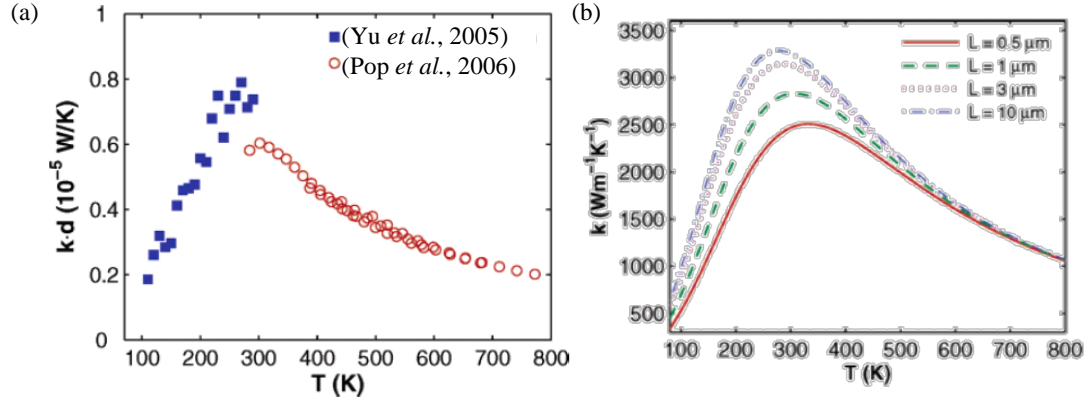


Figure 2.7: (a) Diameter-adjusted CNT thermal conductivity as a function temperature. Pop *et al.* [68] used this data to calculate the empirical model of thermal conductivity with temperature shown in the right panel of the figure. (b) Thermal conductivity as a function of temperature using an empirical model based on experimental data in the left panel. Figures from Pop *et al.* [68].

Experimental results for MWCNTs appear to follow similar trends with temperature as those reported for SWCNTs. Kim *et al.* [64] measured thermal conductivity of an individual multi-wall carbon nanotube with temperature up to ~ 350 K. At low temperatures, from 8 to 50 K, the thermal conductivity increased with temperature as $k \sim T^{2.5}$. From 50 to 150 K, the thermal conductivity increased quadratically with temperature as $k \sim T^2$ agreeing with the predictions for two-dimensional conductors. The measured thermal conductivity peaked at $\sim 3000 \text{ W m}^{-1} \text{K}^{-1}$ at ~ 320 K and then decreased with temperature. Fujii *et al.* [62] measured the thermal conductivity of three different diameter multi-wall carbon nanotubes. For a multi-wall carbon nanotube with a 16.1 nm outer diameter and a 4.9 nm inner diameter, the thermal conductivity increased from 100 to 320 K reaching a plateau or possible peak at 320K.

2.2.4.3 Influence of Defects

Molecular dynamics simulations enable systematic investigation of imperfect carbon nanotubes. Defects can arise from localized flaws in the atomic arrangement and from impurities. Figure 2.8 shows the predictions of Che *et al.* [1] for the impact of common CNT defects in CNT including vacancies and the (5,7,7,5) defect, which changes the bond structure from four hexagons into two hexagons and two pentagons.

*REVIEW OF THERMAL CONDUCTION PHENOMENA IN CARBON NANOTUBES
AND RELATED NANOSTRUCTURED MATERIALS*

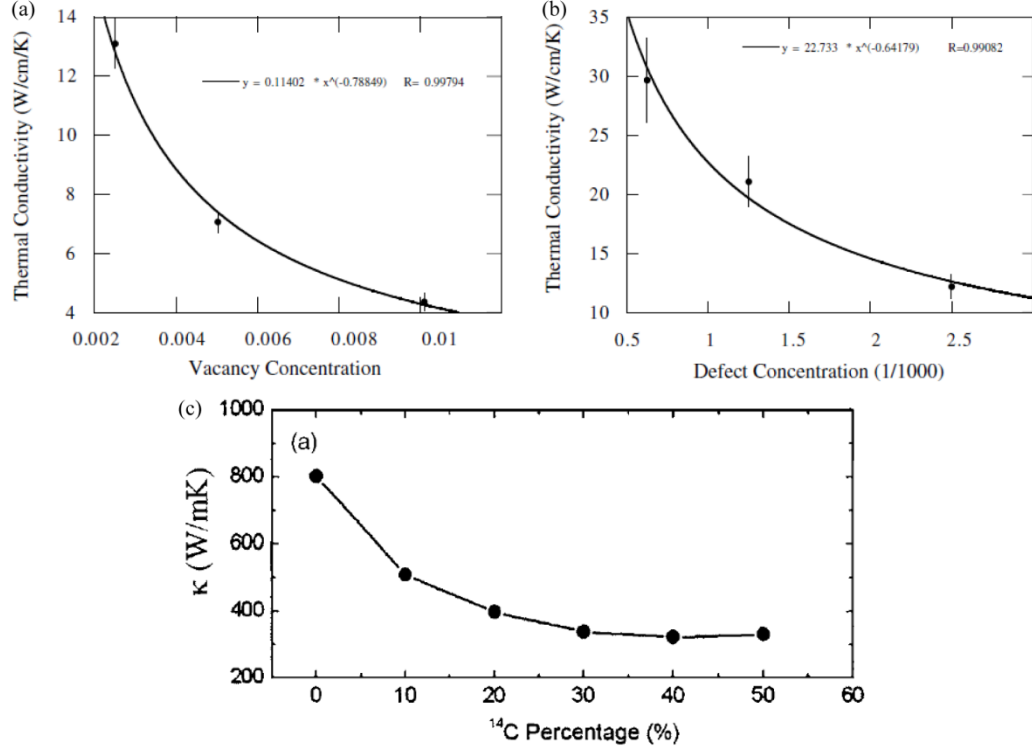


Figure 2.8: Effect of Defects on Thermal Conductivity. Effect of (a) vacancy and (b) (5,7,7,5) defect concentration from Che *et al.* [1] using MD simulations. The solid lines are the best fit to the molecular dynamics simulations. (c) Effect of ^{14}C isotope impurity as computed by Zhang and Li [11] using non-equilibrium molecular dynamics simulations.

For the (10,10) nanotube investigated, the thermal conductivity decreased by nearly a factor of 3 as defects of either kind are introduced into the system. The magnitude of the reduction is smaller for the (5,7,7,5) defect than for a vacancy because the basic bonding characteristic is not changed significantly. Zhang and Li [11] investigated the reduction in thermal conductivity due to the addition of ^{14}C and ^{13}C to a pure ^{12}C (5,5) single-wall nanotube (see Figure 2.8). The thermal conductivity drops by more than a factor of two when 50% of the ^{12}C are replaced with ^{14}C and similar results were found for the ^{13}C impurities. The impurities also changed the temperature dependence of the thermal conductivity by impacting the phonon-phonon scattering mechanisms within the nanotube. Impurities can cause localization of high-frequency phonons, which can increase the contribution of low-energy, long wavelength phonons to conduction. Yan *et al.* [99] discussed that although individual tubes in a defect-free MWCNT act

independently due to the weak interwall coupling, the presence of defects can cause scattering in all directions and link together different walls of the MWCNT. Pettes and Shi [60] observed no defects in single- and double- walled nanotubes using transmission electron microscopy, but the multiwalled tubes were found to have a high density of defects (30 to 77 dislocations per micron, increasing with the number of shells). The distance between defects (13 to 29 nm) correlated well with the estimated phonon mean free path within the MWCNTs (4 to 30 nm) [60]. Ivanov *et al.* [108] found that annealing a vertically-aligned MWCNT array in argon at 2800 °C for 2 hours significantly reduced the sidewall defects increasing the thermal conductivity by up to a factor of 5. These studies show that CNT defects can significantly impair thermal conduction, reducing it by more than half even at low defect densities.

2.3 Thermal Conduction in Carbon Nanotube Arrays and Mats

Carbon nanotubes can be configured into a variety of materials including randomly oriented mats or vertically aligned arrays of nanotubes. Randomly oriented nanotube mats do not take full advantage of the high thermal conductivity along the axis of the nanotube, preventing the mats from having high thermal conductivity. Aligned arrays of CNTs can better take advantage of the high thermal conductivities of individual nanotubes reported in the previous sections of this review. The conductivities of aligned CNT materials are governed by the packing fraction of CNTs, boundary resistances between the nanotube array and the substrate or other material, and by damage or defects that may be present in the nanotubes as a result of fabrication details including compression.

Several research groups investigated and improved the thermal properties of vertically aligned CNT (VACNT) arrays, for which the boundary resistance can dominate the total measured thermal resistance. Figure 2.9 shows a typical configuration including the substrate a second material, in this case a deposited metal on top of the CNT film. The total thermal resistance of the sample includes the thermal resistance between the CNT layer and its growth substrate, the volumetric thermal resistance of the CNT array, and the thermal resistance between the free surface of the

*REVIEW OF THERMAL CONDUCTION PHENOMENA IN CARBON NANOTUBES
AND RELATED NANOSTRUCTURED MATERIALS*

CNT array and the top contact. This manuscript has gathered thermal conductivity data from researchers whose experimental methods are designed to separate the volume and boundary resistances. This is a challenging task for data interpretation, and has been achieved mainly using fast optical techniques including thermoreflectance [e.g., 109, 110], photothermoelectric [e.g., 111], photoacoustic [e.g., 112], and laser flash [e.g., 113] methods. Effective thermal conductivities of vertically aligned CNT arrays reported in the literature span a large range from $0.145 \text{ W m}^{-1} \text{ K}^{-1}$ [114] to $267 \text{ W m}^{-1} \text{ K}^{-1}$ [115, 116]. In some experiments it was not possible to separate the intrinsic thermal conductivity of the array from the boundary resistance. In these cases, the total resistance of the CNT array between two materials is reported (including both boundary resistances). Total thermal resistances ranged from 5 to $61 \text{ mm}^2 \text{ K W}^{-1}$ [21, 44, 117].

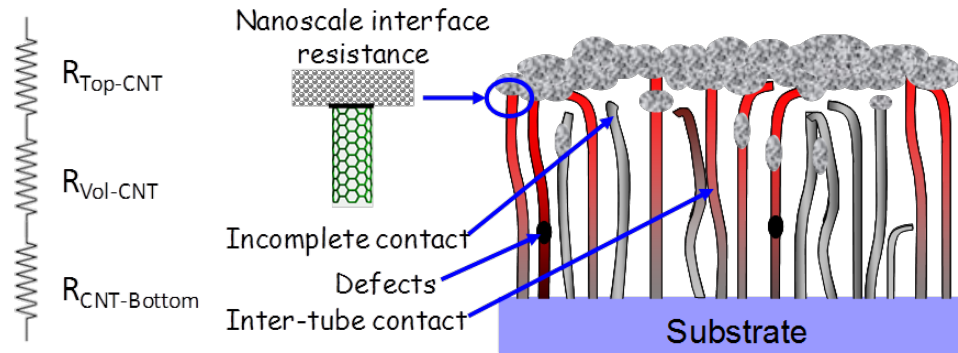


Figure 2.9: Schematic showing the sources of thermal resistance in an aligned CNT array including thermal boundary resistance between the growth substrate and the CNT film, the volumetric thermal resistance of the CNT film, and the thermal boundary resistance between the free surface of the CNT and the metals or other material deposited or placed on top of the CNT layer. The volumetric thermal resistance of the CNT has contributions due to defects, inter-tube contacts, and the intrinsic thermal resistance of the individual CNTs. The color gradients in the schematic show that for a top-heated CNT array, only nanotubes in contact with the top heat source and the bottom substrate transfer heat efficiently to the substrate.

In an ideal array of vertically aligned CNTs, each individual CNT makes complete contact with both surrounding surfaces and straight and free of defects. In this case, the total conductance of the CNT array is the sum of the conductances of the individual tubes. In realistic arrays, incomplete contact of the CNTs to the surfaces reduces the

number of CNTs contributing to heat conduction and forces heat to transfer between nanotubes. Additionally, defects and inter-tube contacts may increase the volumetric contribution to the thermal resistance. The measured or physical CNT thermal conductivity is related to the volumetric resistance by $k = L/(R_{Vol-CNT} A)$, where the volumetric resistance includes the intrinsic thermal resistance due to the nanotube as well as the resistance due to defects and inter-tube contact resistances for heat transfer pathways involving multiple nanotubes.

2.3.1 Thermal Conductivity

If the nanotubes are assumed to function independently and all provide good contact to the top and bottom contacts, then the film thermal conductivity should scale linearly with the packing fraction. While the route to higher conductivity might appear to be increasing the packing fraction, this also increases the density of inter-tube contacts and the associated reductions in CNT thermal conductivity as discussed later in this section. While for randomly oriented nanotubes, the contact points may provide a modest improvement in the conductivity by enabling additional heat flow paths, in general the contacts can be assumed to reduce the conductivity in aligned nanotubes owing to the reduced conductivity of the tubes. One exception to this argument might be the situation when a small fraction of the nanotubes is in contact with an interface, for which case the contact between nanotubes could diminish the effective thermal contact resistance.

Figure 2.10 shows the thermal conductivity of CNT samples from literature as a function of the volume fraction CNTs. Data for individual nanotubes are represented at the right side of the plot where the volume fraction is unity. A simple estimate of the thermal conductivity of aligned arrays of nanotubes, k_{array} , scales the thermal conductivity of individual nanotubes, k_{CNT} , by the volume fraction of CNTs, VF :

$$k_{array} = VF \cdot k_{CNT} = \frac{N_{CNT}}{A_{array}} A_{CNT} k_{CNT} . \quad (2.25)$$

*REVIEW OF THERMAL CONDUCTION PHENOMENA IN CARBON NANOTUBES
AND RELATED NANOSTRUCTURED MATERIALS*

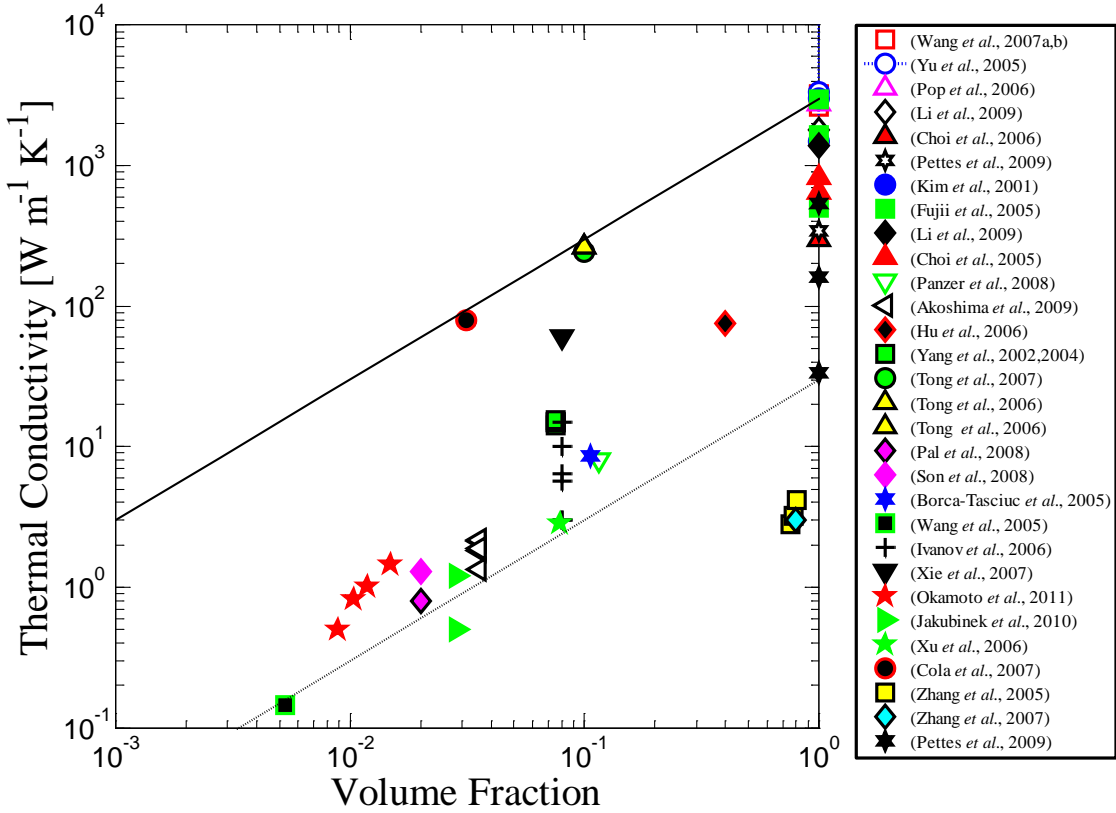


Figure 2.10: Intrinsic thermal conductivity as a function of volume fraction for aligned CNT films. These data are for the intrinsic thermal conductivity of the arrays, which have been determined separately from the interface resistances. The solid line shows the predicted film thermal conductivity for an ideal array of nanotubes each with an individual thermal conductivity of $3000 \text{ W m}^{-1} \text{ K}^{-1}$, while the dashed line shows the predicted film thermal conductivity with an individual CNT conductivity of $30 \text{ W m}^{-1} \text{ K}^{-1}$. Individual nanotubes thermal conductivities are provided on the left axis with volume fraction = 1. The volume fractions of aligned arrays range up to about 0.2, though unaligned densified arrays can achieve higher volume fractions. The densified arrays of Zhang *et al.* [118, 119] report volume fractions of $\sim 0.8-0.9$ through spark plasma sintering of unaligned CNT mats. All of the nanotube arrays perform lower than predicted by the high thermal conductivity of individual nanotubes, however, recent data is approaching that limit as nanotube array fabrication improves and the resistances at the interfaces are addressed.

For well aligned CNT arrays, the volume fraction is equivalent to the area fraction and is calculated from the number of CNTs per unit area, $\frac{N_{\text{CNT}}}{A_{\text{array}}}$. For well aligned CNT arrays, the volume fraction is equivalent to the area fraction and is calculated from the number of CNTs per unit area, $\frac{N_{\text{CNT}}}{A_{\text{array}}}$. There is some uncertainty in the reported values

for the volume fraction for CNT arrays as it is difficult to measure accurately. Some papers report the number of tubes per unit area (as counted from microscope images), while in other cases the volume fraction is estimated from comparison of the density of a CNT array to the density of graphite.

The majority of the vertically aligned CNT samples discussed in the literature have reported conductivities that fall well below predictions, indicated by the solid line in Figure 2.10, considering $3000 \text{ W m}^{-1} \text{ K}^{-1}$ for an individual tube. Some samples correspond to individual nanotube thermal conductivities lower than $20 \text{ W m}^{-1} \text{ K}^{-1}$, indicating factors beyond the CNT density degrade the thermal performance of some vertically aligned CNT arrays. For comparison, the dashed line in Figure 2.10 indicates the predicted thermal conductivity for individual nanotubes within the arrays have thermal conductivity of $30 \text{ W m}^{-1} \text{ K}^{-1}$. The high thermal conductivity (exceeding $250 \text{ W m}^{-1} \text{ K}^{-1}$ at $\sim 10\%$ volume fraction CNTs) reported by Tong *et al.* [115, 116] shows promise for fabricating vertically aligned CNT arrays which take full advantage of the high thermal conductivity reported for individual CNTs. The thermal diffusivity and thermal conductivity in aligned CNT arrays is highly anisotropic, such that the axial thermal conductivity is as much as 110 times greater than the radial conductivity [108, 111, 115, 116, 120].

Akoshima *et al.* [121] reported a technique to reduce the distance between CNTs in free- standing SWCNT arrays increasing the density by a factor of 15 and leading to a significant increase in film thermal conductivity. For aligned densified MWCNT arrays infiltrated with epoxy, Marconnet *et al.* [122] found that the thermal conductivity improved with increased CNT array density. However, the thermal conductivity did not follow the linear trend expected with volume fraction, nor did it increase as rapidly as expected if each CNT contributes with the thermal conductivity $\sim 1000 \text{ W m}^{-1} \text{ K}^{-1}$. Prasher *et al.* [123] showed through modeling efforts that random mats of nanotubes are as thermally insulating as polymers. If the inter-tube contact resistance is high, the large number of tube-tube contacts in randomly-oriented CNT films, or even poorly-oriented VACNT arrays, would make any pathway for heat conduction involving multiple CNTs highly resistive.

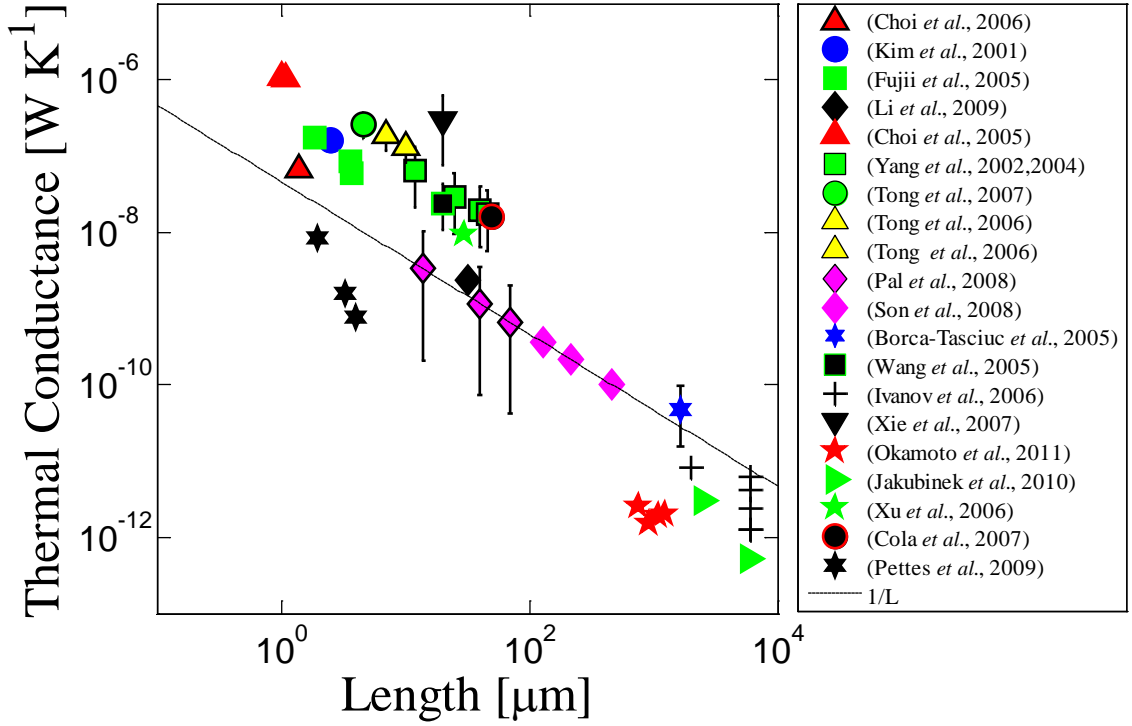


Figure 2.11: Individual nanotube thermal conductances plotted as a function of nanotube length, as extracted from reported measurements for arrays of MWCNTs and from measurements of MWCNTs. Dashed line shows L^{-1} trend of the thermal conductance which is expected if the thermal conductivity of a nanotube saturates at lengths longer than the mean free path. Error bars due to uncertainty or variation in nanotube diameters in the arrays.

Figure 2.11 shows the thermal conductance of an individual nanotube, G_{CNT} , extracted from measurements of arrays of nanotubes as a function of nanotube length:

$$G_{CNT} = \frac{k_{array}}{VF} \frac{A_{CNT}}{L}, \quad (2.26)$$

where k_{array} is the measured thermal conductivity of the entire array, A_{CNT} is the cross-sectional area of an individual nanotube in the array, L is the height of the nanotube array. The L^{-1} trend observable in Figure 2.3 for individual nanotubes is also observed in the array data in Figure 2.11 for lengths up to 1 mm, indicating that the thermal conductivity saturates with length. Above 1 mm, the introduction of defects during CNT growth may impede conduction. The differences between conductivities measured for individual nanotubes and those deduced from array data may result in part from differences in diameter or quality. For the MWCNT arrays, the diameters range from 10

to 200 nm, while in the measurements of individual of MWCNTs, the diameters varied from 8.2 to 46 nm. Within a single CNT array, there is a distribution of nanotube diameters.

Growth parameters, including the choice of substrate and adhesion layers on the substrate, deposition temperature, and catalyst material, govern the quality of the vertically aligned carbon nanotubes and therefore the thermal properties of the arrays. Typically thin films of titanium, aluminum, and nickel are deposited on silicon substrates for optimal CNT growth using chemical vapor deposition with methane as carbon source [21, 44, 117, 124]. Titanium improves adhesion to the silicon substrate, while aluminum activates the nickel catalyst layer. The quality of the CNT growth, and the total thermal resistance of the sample, can depend strongly on the thickness of the aluminum layer and on whether the substrate annealed prior to CNT growth [44]. Zhang *et al.* [44] found that annealing the substrate before depositing the nickel catalyst was necessary to achieve vertically aligned CNT growth and the VACNT growth was further improved by annealing the substrate again after the catalyst deposition. Using a nickel catalyst layer, Yang *et al.* [110, 125] obtained vertically aligned CNT arrays without the titanium adhesion or aluminum activation layers. For their high thermal conductivity CNT films, Tong *et al.* [115] used CVD with ethylene as carbon source to grow the films on silicon wafers with a 10 nm aluminum film and 10 nm iron film as a catalyst. For some samples, an additional layer of molybdenum underneath the Al film improved adhesion. Cola *et al.* [112] grew high thermal conductivity arrays on successive layers of 30 nm titanium, 10 nm aluminum, and 3 nm of iron on copper films. Gao *et al.* [126] controlled growth parameters including the number density of Fe catalyst nanoparticles, thickness of the catalyst layer, and carbon precursor flow rate to optimize the density and CNT alignment within their VACNT films and achieved low thermal resistance by optimizing optimized conditions. During microwave plasma chemical vapor deposition of MWCNT films, Cola *et al.* [127] controlled the growth surface temperature and found that higher growth temperatures resulted in increased nanotube diameters and reduced thermal resistance (from 8 nm diameter and 19 mm²K/W at 500 °C to 40 nm diameter and 7 mm²K/W at 800 °C). Many other

*REVIEW OF THERMAL CONDUCTION PHENOMENA IN CARBON NANOTUBES
AND RELATED NANOSTRUCTURED MATERIALS*

combinations of catalysts, substrates, and carbon sources are used to grow aligned carbon nanotube arrays.

The simulations and measurements of individual CNTs with defects discussed in Section 2.2.4.3 showed that the thermal conductivity decreases significantly with increasing defect concentration. Assuming a fixed defect concentration, the probability of a defect in occurring within a given CNT increases with the length, and thus arrays of longer tubes may exhibit a lower effective conductivity than shorter arrays of identical quality tubes. The study of growth kinetics of CNTs shows significant changes in CNT alignment and density with growth time within VACNT arrays [128, 129]. These effects could explain why the short nanotubes ($L < 10 \mu\text{m}$) of Tong *et al.* [115, 116] showed high film thermal conductivities, with the extracted individual nanotube thermal conductivity as high as $2650 \text{ W m}^{-1} \text{ K}^{-1}$. Figure 2.12 shows the individual CNT thermal conductivity extracted from the effective arrays thermal conductivity and volume fraction from the data in the literature.

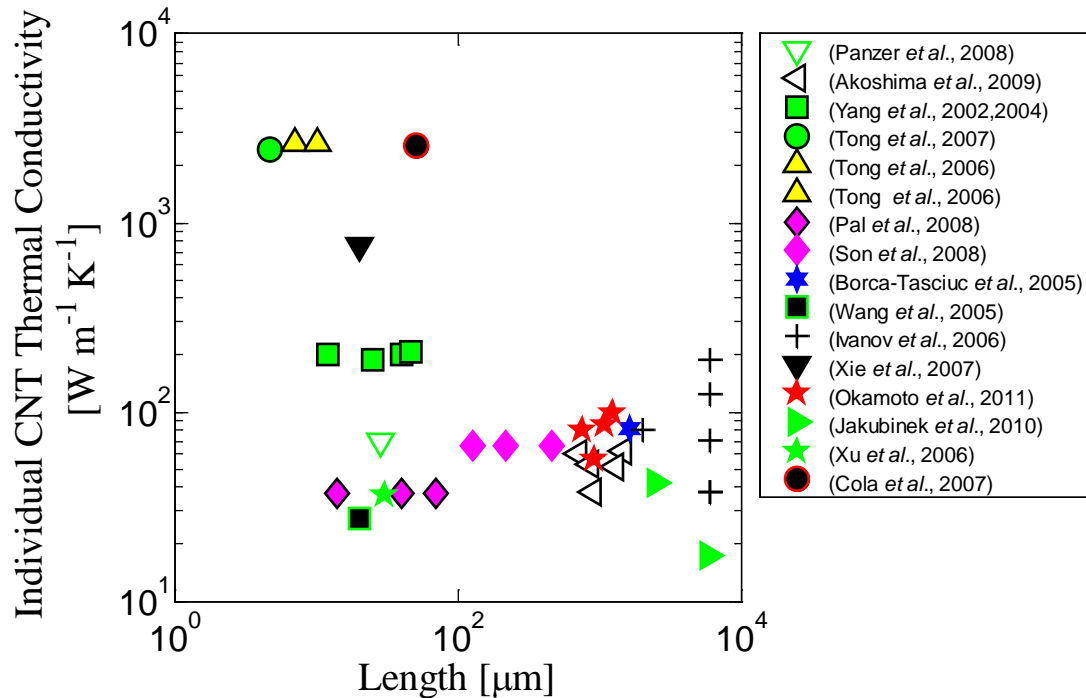


Figure 2.12: Individual CNT thermal conductivities as a function of length extracted from reported data of the thermal conductivity or thermal conductance of CNT arrays.

While experimental estimations of the mean free path of phonons in individual carbon nanotubes yielded values as high as $1.5\ \mu\text{m}$ [58, 59], the mean free path in films and bundles may be considerable shorter with corresponding lower thermal conductivity. Yang *et al.* [110] estimate a phonon mean free path of only 20 nm in their multi-wall nanotube arrays. The reduced mean free path could be a result of localized defects or tube-tube contact providing additional scattering sites for the phonon energy carriers. Chalopin *et al.* [130] modeled the effect of crossing nanotubes using molecular dynamics. The phonon transmission through a single-wall carbon nanotube was reduced very slightly when a second nanotube crosses it. Furthermore, the interface thermal conductance from one nanotube to the second nanotube was between 1 and 100 pW K^{-1} from 5 to 1000 K for all chiralities simulated [130]. By extending these simulations to a randomly arranged pellet of nanotubes, the authors found the thermal conductivity in the dense limit is approximately $5\ \text{W m}^{-1}\ \text{K}^{-1}$ [130]. This is the same order of magnitude observed by the experiments of Zhang *et al.* [118, 119] on dense unaligned carbon nanotube samples (2.8 to $4.2\ \text{W m}^{-1}\ \text{K}^{-1}$). Using both molecular dynamics and atomistic Green's function simulations, Prasher *et al.* [123] found an interface thermal conductance of $50\ \text{pW K}^{-1}$ for crossing SWCNTs. However, simulations using these models for individual tube-tube contacts overestimated the thermal conductivity of randomly-oriented beds of CNTs. Simulations of two nanotube junctions spaced more closely together than the coherence length of phonons within the CNTs yielded a contact conductance one order of magnitude smaller than that for a single junction and an overall thermal conductivity consistent with experiments [123]. Yang *et al.* [131] measured the thermal contact conductance of large crossing CNTs with diameters of 74 and 121 nm to be $100\ \text{nW K}^{-1}$. To compare with simulations of 1.4 nm diameter crossing nanotubes, a contact conductance of $21\ \text{pW K}^{-1}$ is estimated assuming the contact conductance scales with diameter. For bundles of MWCNTs, Aliev *et al.* [132] found that the thermal conductivity decreased by up to a factor of 4 relative to that of individual nanotubes. This suggested that within a single CNT certain phonon modes were suppressed as a result of contact and coupling with other nanotubes within the bundle [132]. In general, the high tube-tube contact resistance and modifications to the phonon modes limit the usefulness of randomly-oriented CNT films for thermal

*REVIEW OF THERMAL CONDUCTION PHENOMENA IN CARBON NANOTUBES
AND RELATED NANOSTRUCTURED MATERIALS*

applications and more work is needed in understanding the impact of CNT-CNT contacts in aligned CNT arrays. As sketched in Figure 2.13, inter-tube contact may increase the thermal resistance of a CNT array by providing additional sites for phonons or by damping phonon modes.

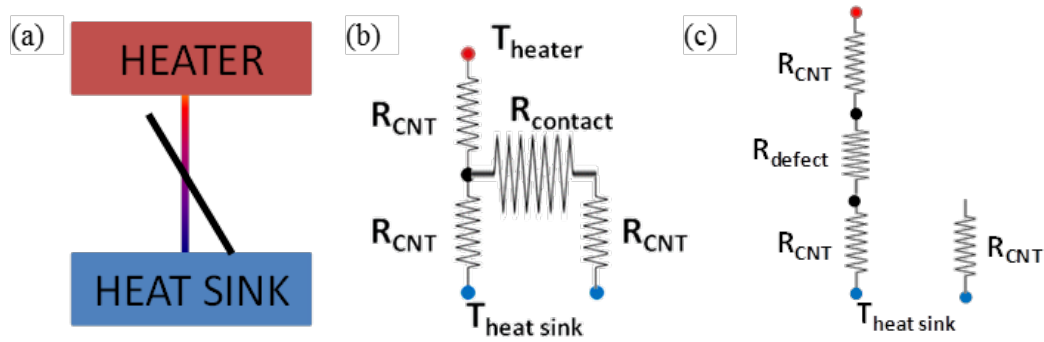


Figure 2.13: (a) Schematic and resistance models illustrating the conduction by two nanotubes in contact. In this example, one nanotube makes contact with both a heater and a heat sink. A second nanotube crosses the first but makes contact only with the heat sink. (b) Resistor network describing nanotubes in contact. While the second nanotube provides a second pathway for heat to transfer to the heat sink, the contact also provides a scattering site for the energy carriers. If the contact resistance is large, instead of aiding in the thermal conduction, the major effect of the second nanotube is to add a defect resistance to the conducting nanotube as modeled approximately by the extra resistor in the network in (c).

2.3.2 Boundary Resistance

Interface resistances play an important role in the thermal conduction through CNT arrays and can be the dominant source of resistance. For the study of as-deposited films, the resistances of the growth interface with the substrate and with any films deposited or mechanically affixed after growth. The contact resistance at the interface between the nanotube array and the growth substrate has been found to be quite low, in the range of $0.022\text{--}0.03 \text{ mm}^2 \text{ K W}^{-1}$ [110, 114] for CNTs grown on silicon. In other cases such as MWCNTs grown on SiO_2 , the interface resistance has been larger, $\sim 50 \text{ mm}^2 \text{ K W}^{-1}$ [111]. When metals are deposited on the top surface of the array, or another material is brought in contact with the top surface of the array, the interface resistance of that interface tends to be significantly larger. For example, Tong *et al.* [115] found a thermal resistance of $1.1 \text{ mm}^2 \text{ K W}^{-1}$ between the CNT array and silicon growth substrate, but

$11.1 \text{ mm}^2 \text{ K W}^{-1}$ between the CNT array and the Cr and Au coated glass piece placed on the top surface. Attaching the CNTs to the SiO_2 substrate using $1 \text{ }\mu\text{m}$ of indium significantly reduced the resistance of the CNT-glass interface to $0.29 \text{ mm}^2 \text{ K W}^{-1}$ [115], most likely due to increasing the engagement with the MWCNTs. Similarly, Cola *et al.* [133] observed a temperature-dependent hysteresis of the thermal boundary resistance of SiC-MWCNT-Ag interfaces. Specifically, the total thermal resistance decreased after the heated to $250 \text{ }^\circ\text{C}$, possibly due to improved contact to the Ag resulting from thermally-induced diffusion of Ag into the MWCNT array [133]. Several methods have been developed to bond CNT arrays to substrates other than their growth substrate. These include indium solder [115, 116], Palladium thiolate [134], electrothermal [135], and thermocompression [136-138] bonding techniques, all of which have shown significant improvements in the total thermal resistance compared to unbounded interfaces.

The roughness of the CNT array and contacting surfaces can make a difference in the fraction of CNTs which make contact with the surfaces. Incomplete contact at the interfaces of the CNT and substrate can reduce the effective volume fraction of CNT participating in heat transfer [109] and amplify the interface resistances at the nanoscale between individual CNTs and the substrates. The TEM image in Figure 2.14 of a cross-section of the metal-SWCNT interface reveals that near the interface there are an increased number of voids and lower volume fraction of CNTs compared to deeper within the array. The variations in CNT heights can lead to an increase in the apparent resistance of the array since a large fraction of tubes do not completely contact both the top metal and the substrate. Panzer *et al.* [109] used a 10 ns thermoreflectance technique to extract the effective volume fraction of SWCNTs within an array which participate in heat transfer from the effective heat capacity of the film. During transient diffusion normal to the film, only those nanotubes in thermal contact with the top metal layer absorb heat and contribute to the experimentally observed heat capacity. These authors found an order of magnitude fewer nanotubes contribute to the thermal properties of the nanotube array ($2.5 \times 10^{15} \text{ m}^{-2}$) than the expected nanotube density based on the catalyst preparation ($8.7 \times 10^{16} \text{ m}^{-2}$) [109]. Using the reduced CNT number density, the contribution to the thermal conductivity estimated for an individual nanotube in

*REVIEW OF THERMAL CONDUCTION PHENOMENA IN CARBON NANOTUBES
AND RELATED NANOSTRUCTURED MATERIALS*

excellent contact with the interface was found to be $\sim 2300 \text{ W m}^{-1} \text{ K}^{-1}$. Many nanotubes make little contribution to the heat transfer. The thermal resistance of CNT arrays has been shown to decrease with applied pressure [21, 112, 117, 139], most likely due to the effects of an increasing the fraction of CNTs within the array contributing to heat conduction and increasing the real contact area [112, 117].

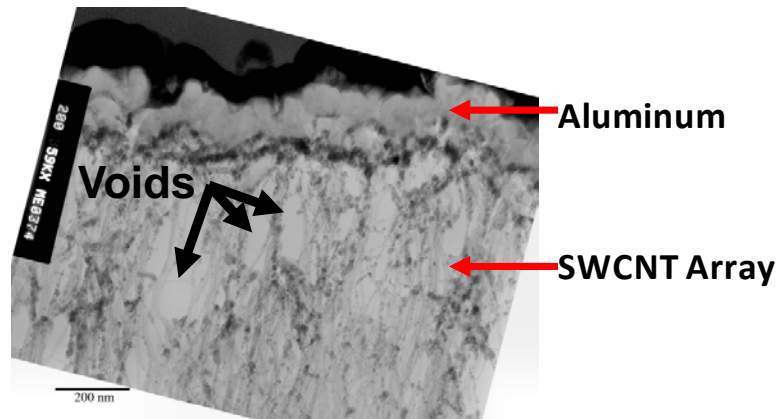


Figure 2.14: Representative TEM of Single-Wall CNT Array coated with thin film of aluminum from Panzer *et al.* [140] showing voids within the SWCNT array and, qualitatively, the regions of incomplete contact between the nanotubes with the aluminum layer.

The interface between a CNT and a bulk medium differs from the standard contact between two bulk media as the carbon nanotube confined geometry exhibits may lead to quantum effects and this contact geometry requires new models to describe the conduction physics. Using a lattice dynamics approach, Panzer and Goodson [141, 142] studied the junction between 1D lattice and 3D face centered cubic lattice, as well as the junction between 1D and 2D square lattices. Even when two lattices have the same speed of sound, atomic spacing, and atomic mass, phonon transmission is impaired by the change in dimensionality. At room temperature, a maximum thermal conductance of $\sim 100 \text{ pW K}^{-1}$ was found by investigating several mass and stiffness ratios for a 1D-3D junction. While the 1D-3D model does not reproduce a CNT-substrate interface exactly, it suggests that phonon transmission across the interface will be dominated by the longitudinal phonons, while transverse and torsional phonons will have negligible

contribution. Prasher *et al.* [61] studied the thermal boundary conductance between a vertically aligned CNT array and a bulk substrate in the mesoscopic regime, for which the dominant phonon wavelength was of the order of the nanotube diameter, but shorter than the nanotube length. The dominant phonon wavelength as quantified in Eq. (4) ranges from about 1 nm to several hundred nanometers depending on temperature for crystalline solids, while in carbon nanotubes it can be quite long even at moderately high temperatures [61]. Assuming perfect transmission at the boundaries of a (6,0) SWCNTs, at 100 K, ballistic conduction effects were predicted up to lengths of $\sim 55 \mu\text{m}$, while at room temperature ballistic conduction is predicted up to a length of $2.4 \mu\text{m}$ [88]. Thus the interface consists of a 1D ballistic conductor in contact with a 3D bulk medium. Using a 3D vector elastic wave model, Prasher *et al.* [61] studied the transmissivity and thermal conductance of (6,0) single-wall carbon nanotubes attached to a silicon substrate up to 55 K and found that the thermal conductance is several orders of magnitude less than that predicted with the assumption of perfect transmission at the boundaries.

Molecular dynamics simulations of CNT-substrate interfaces have also been developed. Diao *et al.* [143] modeled both a capped and uncapped carbon nanotube spanning two silicon surfaces as a function of temperature, pressure, nanotube length. Capped nanotubes have lower thermal conductances than uncapped nanotubes up to a pressure of $\sim 1.1 \text{ GPa}$. At a pressure of $\sim 1.1 \text{ GPa}$ and thermal conductance of $500 \text{ MW m}^{-2} \text{ K}^{-1}$, the thermal conductance of capped nanotubes begins to surpass the thermal conductance of uncapped nanotubes. The simulations found that more carbon atoms interact with the silicon substrate as the pressure is increased with the capped nanotubes increasing in contact more so than the uncapped nanotubes. At 0.2 GPa , the interface thermal conductance of an uncapped nanotube increased from $\sim 200 \text{ MW m}^{-2} \text{ K}^{-1}$ to $\sim 2000 \text{ MW m}^{-2} \text{ K}^{-1}$ as the temperature increased from 50 to 1200 K, which corresponds to thermal boundary resistances between approximately ~ 0.005 and $0.0005 \text{ mm}^2 \text{ K W}^{-1}$). Increasing the length of the nanotube was shown to increase the interface thermal conductance. Diao *et al.* [143] attributed this to the finite size effects since the length of the nanotubes simulated was much shorter than the mean free path of the phonons and suggests that improved computational capabilities are required to extend the simulations

*REVIEW OF THERMAL CONDUCTION PHENOMENA IN CARBON NANOTUBES
AND RELATED NANOSTRUCTURED MATERIALS*

to long enough nanotubes for the thermal conductance to saturate with length. Fan *et al.* [144] investigated a (10,10) CNT bridging the gap between two silicon substrates. The contact conductance increased when the CNT was functionalized with carboxylic acid groups which bonded to the hydroxyl groups on the silicon surface. The interfacial thermal conductance increased from about $400 \text{ MW m}^{-2} \text{ K}^{-1}$ with no chemical bonds to $1480 \text{ MW m}^{-2} \text{ K}^{-1}$ with 10 chemical bonds. These values were calculated using the contact area of $A = \pi d \delta$. For comparison, the per-tube thermal contact resistance can be estimated from measurements of CNT arrays using the volume fraction and ranges from about 1 to $606 \text{ MW m}^{-2} \text{ K}^{-1}$ [110, 111, 115, 116].

All the simulations previously discussed in this section describe the contact of a CNT connected perpendicular to the surface of a substrate. Ong and Pop [145] used molecular dynamics to investigate the thermal boundary conductance of a 36.9 \AA long (10,10) CNT lying flat on a SiO_2 substrate, using the Lennard-Jones potential

$$V(r) = 4\chi\epsilon \left[\left(\frac{\sigma}{r} \right)^{12} - \left(\frac{\sigma}{r} \right)^6 \right], \quad (2.27)$$

where ϵ is the energy parameter, σ is the distance parameter, r is the interatomic distance, and χ is a scaling factor. This horizontal contact geometry occurs often in the measurements of individual nanotubes. Additional, when VACNT arrays are brought into contact with another material after growth, some of the CNTs bend. This bending results in an elongated contact region as approximately represented in the sketch in Figure 2.9. The absolute magnitude of the thermal boundary conductance predicted by Ong and Pop [145] depended linearly on the scaling parameter in the Lennard-Jones potential. Assuming a scaling factor of $\chi = 1$, at room temperature, the thermal boundary conductance per unit area was estimated to be $58 \text{ MW m}^{-2} \text{ K}^{-1}$, independent of diameter when the contact area is the product of the length and the diameter. The thermal boundary conductance increased approximately as $T^{1/3}$ from 200 to 400 K and an approximation to the molecular dynamics calculations yielded

$$g \approx 0.05D\chi \left(\frac{T}{200} \right)^{1/3}, \quad (2.28)$$

where g is the thermal conductance per unit length in $\text{W m}^{-1} \text{K}^{-1}$, D is the nanotube diameter in nanometers, and T is the temperature in Kelvin. From this expression, for a 1.7 nm diameter CNT at room temperature, $g \approx 0.1 \text{ W m}^{-1} \text{K}^{-1}$, similar to the previously measured value from Pop *et al.* [75] of approximately $0.17 \text{ W m}^{-1} \text{K}^{-1}$ for a 2 to 3 nm diameter CNT on a Si substrate with a thin SiO_2 layer. Maune *et al.* [146] estimated a thermal contact conductance of $\sim 0.3 \text{ W m}^{-1} \text{K}^{-1}$ for a CNT grown on a sapphire substrate. From the measurement of an individual 14 nm diameter MWCNT lying on a metal electrode [64], the contact conductance per unit length is estimated to be $0.5 \text{ W m}^{-1} \text{K}^{-1}$ and the contact conductance per unit area is estimated to be $35 \text{ MW m}^{-2} \text{K}^{-1}$.

2.3.3 Applications

For electronics packaging applications, the CNT arrays are promising as thermal interface materials and the total thermal resistance is a critical metric. The total resistance of a thermal interface material (TIM) includes both boundary resistances and the intrinsic thermal resistance. Optimal thermal interface materials also benefit from a variety of other attributes including a low elastic modulus, E , which helps accommodate mismatch in the coefficient of thermal expansion between the hot surface and the heat sink. Conventional thermal interface materials include greases, gels, phase change materials, and metallic solders. Polymeric thermal greases have a relatively high thermal resistance, but have low elastic modulus. In contrast, metallic solders have lower thermal resistance but have much higher stiffness.

Figure 2.15 compares thermal resistance data for CNT films with conventional TIM materials, showing that the total thermal resistance of CNT arrays can be better than thermal interface greases and even approaches those of metallic solders. The solid line in the figure shows that an ideal CNT array with 3% volume fraction and negligible boundary resistance could achieve lower thermal resistance than metallic solders of the same thickness. The extremely low CNT density and large aspect ratio of individual CNTs in bulk CNT films provides the possibility that the CNT array could have lower elastic modulus than even the conventional greases, making the promising for thermal interfaces. Very recent work has used a microfabricated silicon resonator to measure the

in-plane modulus of aligned MWCNT films, yielding values between 10 and 500 MPa that are well below those of conventional interface materials [128].

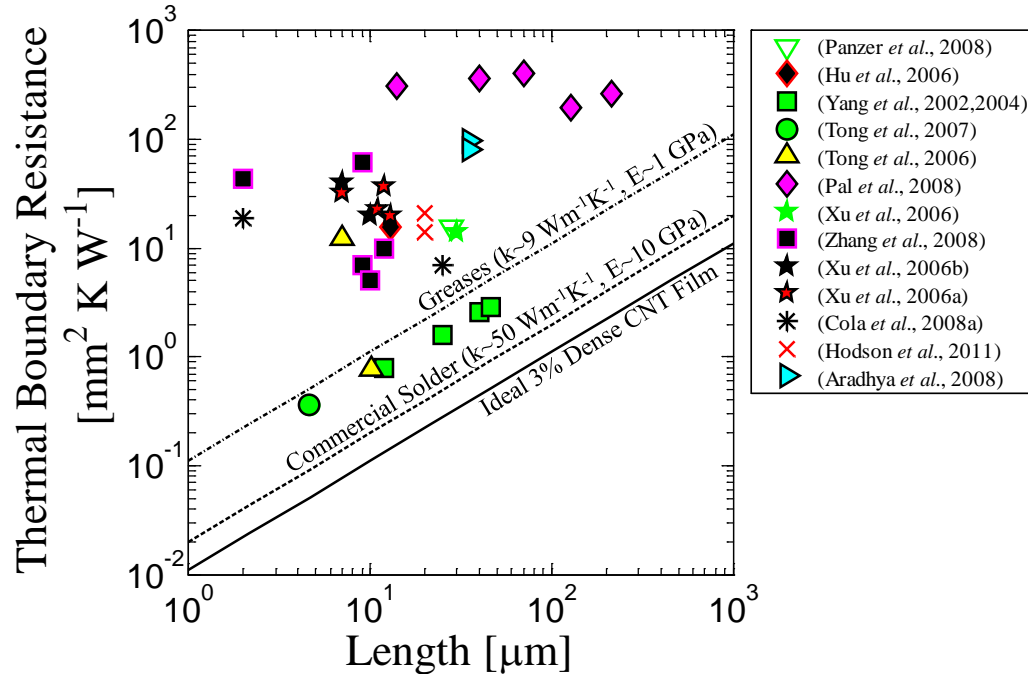


Figure 2.15: Total thermal resistance of CNT arrays plotted according to length. The total thermal resistance includes the thermal boundary resistance between growth substrate and CNT film, the intrinsic thermal resistance of the CNT film, and the thermal boundary resistance between the free surface of the CNT and the metals or other material deposited or placed on top of the CNT layer. The solid line shows the lower limit for the thermal resistance of a CNT array at a packing density of 3 percent if each individual CNT has a thermal conductivity of $3000 \text{ W m}^{-1} \text{K}^{-1}$ and the thermal boundary resistance is negligible. The dot-dashed line shows an approximate lower bound on thermal resistance of commercial thermal greases used for thermal interface materials. Thermal greases and phase change materials have low thermal conductivities (on the order of $0.1\text{-}10 \text{ W m}^{-1} \text{K}^{-1}$). The dashed line shows the approximate thermal resistance of commercial alloy solders. Metallic solders have higher thermal conductivities (on the order of $40\text{-}90 \text{ W m}^{-1} \text{K}^{-1}$). Some of the best data for CNT arrays as thermal interface materials have achieved total thermal resistances less than commercially available greases, gels, and phase change materials and approaching that of metallic solders.

2.4 Conclusions

In the last two decades, thermal conduction in CNTs has been investigated through the modeling and experimental efforts of many researchers. The high thermal conductivities of CNTs combined with their electrical and mechanical properties can

yield bulk CNT materials with interesting and unique combinations of properties. Understanding thermal conduction in individual nanotubes is necessary for understanding the thermal conduction in bulk CNT materials.

Depending on growth parameters, the diameter, chirality, length, and quality of CNTs can vary significantly impacting the thermal conduction properties. While it is possible to model the effect of chirality and diameter, it is challenging to determine the chirality of nanotubes experimentally and there is no clear trend of thermal conductivity and diameter consistent between the different models. The experiments show a reduction of thermal conductivity with increasing diameter. Nanotubes can be grown with lengths exceeding several millimeters, which is much longer than the phonon mean free path. While several models have been developed for ballistic conduction appropriate for nanotubes shorter than the mean free path, the majority of CNTs and CNT films experimentally characterized are diffusive thermal conductors at room temperature and the thermal conductivity is independent of length. Several models showed that defects including vacancies, changes to the bond structure, and impurities significantly reduce the thermal conductivity of individual nanotubes. Experimentally it is difficult to directly observe and isolate the impact of defects. Ivanov *et al.* [108] found that the thermal conductivity of bulk CNT arrays increased after annealing at high temperatures, possibly due to the reduction in the number of sidewall defects observed with high resolution TEM. Pettes and Shi [60] found that for individual nanotubes the thermal conductivity decreased with increasing defect concentrations. To ensure high thermal conductivity of bulk CNT materials, high quality CNTs are required.

The thermal resistances for both CNTs and bulk CNT materials have two components: the intrinsic thermal resistance of the nanotubes and the thermal boundary resistance between the nanotubes and surrounding materials (i.e. substrate, deposited layers, etc). For individual CNTs, the intrinsic thermal resistance must be optimized by controlling the growth quality and considering effects of geometry. In bulk CNT materials, increasing the CNT volume generally decreases the intrinsic thermal resistance of the material by increasing the number of nanotubes per unit area. As the intrinsic thermal conductivity of CNT arrays has been improved through optimization

*REVIEW OF THERMAL CONDUCTION PHENOMENA IN CARBON NANOTUBES
AND RELATED NANOSTRUCTURED MATERIALS*

of growth parameters, the limiting factor in implementing CNTs in practical applications is the high thermal boundary resistance between CNTs and surrounding materials. Reducing the thermal boundary resistance and increasing the fraction of CNTs contributing to the heat conduction is necessary for creating CNT films with desirable thermal properties.

CHAPTER 3: THERMAL CONDUCTION IN CARBON NANOTUBES FILMS AND COMPOSITES

3.1 Introduction

Efficient heat dissipation is critical for reliability and performance of integrated circuits, thermoelectric modules, and high power electronics. Thermal interface materials (TIMs) require low thermal resistance to transfer heat effectively and a low elastic modulus to accommodate the mismatch in thermal expansion at the interface. There is a trade-off between these two properties for conventional TIMs. Solders have low thermal resistivity but must be deposited in thick layers to avoid failing due to mechanical stresses. Greases and gels have higher thermal resistivity but can easily accommodate thermally induced stresses.

Vertically aligned arrays of carbon nanotubes leverage the high axial thermal conductivity of individual CNTs [68] while maintaining a low elastic modulus [128] due to the high aspect ratio and flexibility of nanotubes, making them an ideal material for TIMs. In recent years, CNT film thermal conductivity as high as solders have been reported [116]. However, the total CNT film thermal resistance, which includes both the intrinsic thermal resistivity and the thermal interface resistances between the CNT film and surrounding materials, is the key thermal metric for TIMs. The total thermal resistance can be reduced by increasing the pressure at the interface between the TIM and surrounding materials or using metal films or solders to enhance contact conductance at the interface. However, these bonding methods are challenging to adopt in a production line and do not easily accommodate variations in CNT thickness.

This chapter investigates two methods of enhancing the thermal performance of CNT-based films and composites. First, mechanical-densification of vertically aligned CNT films is used to enhance the intrinsic thermal conductivity of CNT films. Section 3.2 discusses thermal conduction measurements of mechanically-densified, vertically-aligned CNT films. This is extended to the mechanically-densified CNT-based composites in Section 3.3. A cross-sectional infrared (IR) microscopy technique is used to evaluate the thermal conductivity as a function of CNT length and film volume

fraction. The IR microscopy technique is improved through the integration of reference layers to measure the heat flux. The data is interpreted considering the impact of CNT density on thermal conduction considering boundary resistances, increased defect concentrations, and the possibility of suppressed phonon modes in the CNTs. Second, a novel bonding method is developed in Section 3.4 utilizing electrodeposited copper films to enhance the engagement of CNT film to surrounding materials. Improved engagement of the CNTs improves the CNT film thermal conductivity and is intended to reduce the CNT-copper boundary resistance.

3.2 Thermal Conduction in Mechanically-Densified, Aligned CNT Films

The thermal conductivity of vertically-aligned CNT films is measured using cross-sectional infrared microscopy. Aligned CNT films consisting of 1 *vol.%* dense, 8 nm diameter MWCNTs are grown *via* chemical vapor deposition with a controlled and aligned morphology as described in previous work [147, 148].

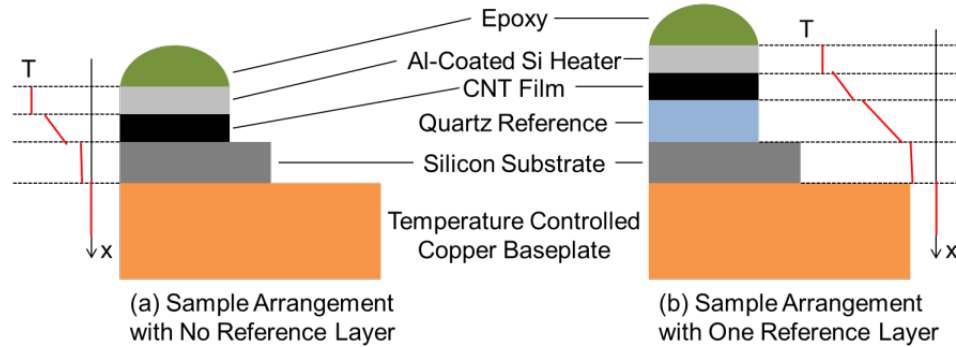


Figure 3.1: *Sample geometries for thermal characterization of CNT films.* (a) *Original sample geometry with no reference layer.* The heat flux across the sample film is calculated from the current and voltage applied to the aluminum-coated silicon heater and the cross-sectional area of the CNT film. The infrared microscope is used to generate a two-dimensional temperature map across the length of the CNT film and surrounding materials. The two-dimensional temperature map is reduced to a one-dimension temperature profile (as sketched next to the sample geometry) by averaging in the direction perpendicular to the heat flux. From the heat flux and temperature gradient in the CNT film, the thermal conductivity of the CNT film is calculated with Fourier's law. (b) *Modified sample geometry with a quartz reference layer.* The infrared microscope is used to generate a two-dimensional temperature map across the length of the CNT film, quartz reference layer, and surrounding materials. With this geometry, the heat flux is calculated from the known thermal conductivity of quartz and the measured temperature gradient in the quartz. With the heat flux calculated from the quartz region and the temperature gradient in the CNT film, the thermal conductivity of the CNT film is calculated using Fourier's law. The modified geometry improves the estimate of the heat flux through the sample as in the original geometry, some of the power dissipated in the heater is lost through convection on the epoxy-coated side of the heater.

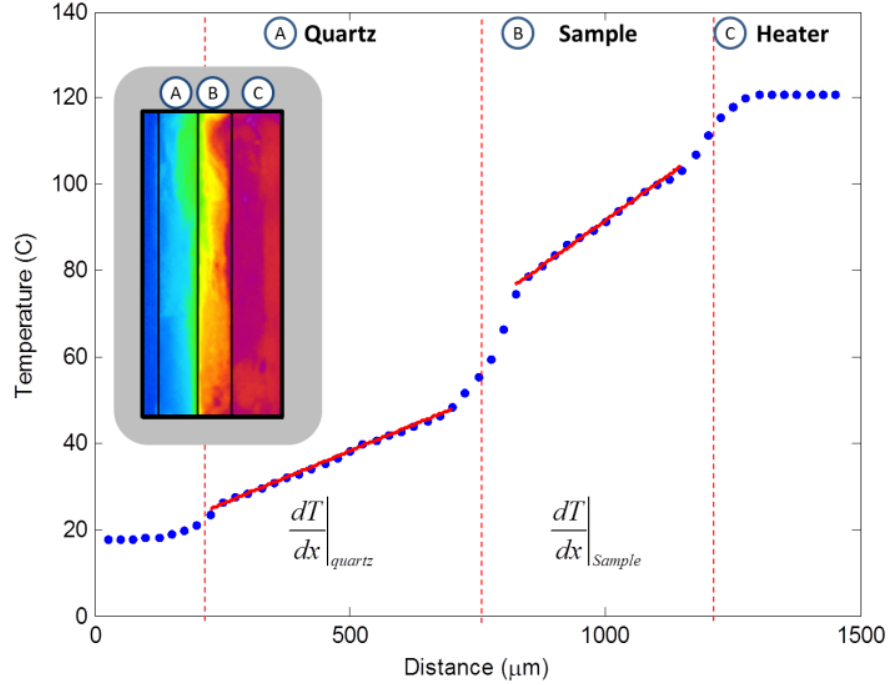


Figure 3.2: Temperature profile across the CNT film and quartz reference layer. Inset shows the two-dimensional temperature map spanning the (a) quartz reference layer, (b) CNT sample film, and (c) aluminum-coated silicon heater. The two-dimensional temperature map is averaged in the direction perpendicular to the heat flux to generate the 1-d temperature profile. The slopes in the linear portions of the curve are used for calculating the thermal conductivity, while the jump in temperature between region (a), (b), and (c) are indicative of thermal interface resistances.

For infrared thermal characterization, the CNT film is sandwiched between a heater and a cooled copper baseplate as shown in Figure 3.1(a). The heat flux through the sample is measured from the current and voltage applied to the heater and the temperature gradient across the sample is measured from the two-dimensional temperature map recorded using infrared microscopy (see Figure 3.2). A modified sample geometry including a quartz reference layer (shown in Figure 3.1(b)) is used to improve the accuracy of the heat flux measurement. From the measured heat flux and the temperature gradient in the CNT film, the thermal conductivity of the CNT film can be determined using Fourier's law:

$$q'' = -k_{CNT} \frac{dT}{dx} \Big|_{CNT} \rightarrow k_{CNT} = \frac{IV}{A_{CNT} \frac{dT}{dx} \Big|_{CNT}} = k_{quartz} \frac{\frac{dT}{dx} \Big|_{quartz}}{\frac{dT}{dx} \Big|_{CNT}}, \quad (3.1)$$

where q'' is the heat flux through the CNT film, k_{CNT} and k_{quartz} are the CNT and quartz thermal conductivities, $\left. \frac{dT}{dx} \right|_{CNT}$ and $\left. \frac{dT}{dx} \right|_{quartz}$ are the temperature gradients in the CNT and quartz, A_{CNT} is the cross-sectional area of the CNT film, and I and V are the current and voltage applied to the heater.

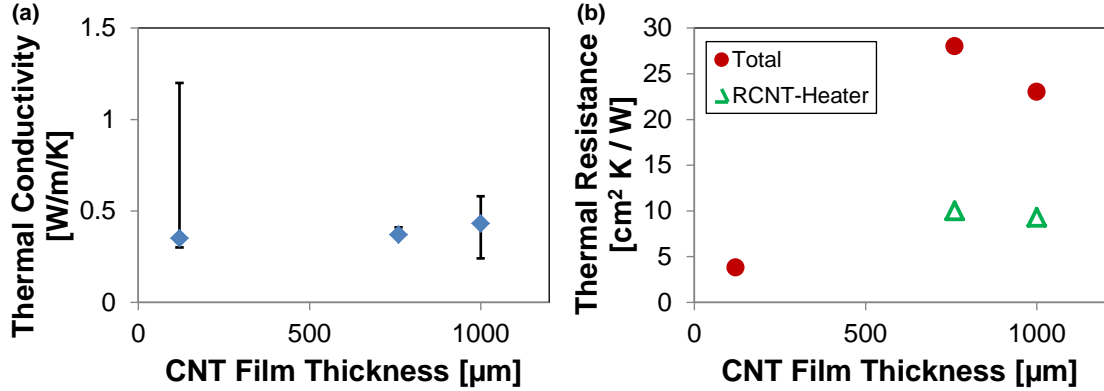


Figure 3.3: Effect of length on the (a) thermal conductivity and (b) thermal resistance of 1 *vol.%* dense, vertically-aligned MWCNT films. No length dependence of the thermal conductivity is observed. The total thermal resistance (circles) consists of the thermal resistance between the CNTs and the heater (triangles), the intrinsic resistance through the thickness of the CNT film, and the resistance between the CNT-film and the growth substrate. For the thinnest sample, the resistance between the CNT film and the heater was smaller than resolvable with this technique. Note that no reference layer is used in these measurements.

Three samples (120, 760, and 100 μm thick) of 1 *vol.%* dense, multi-walled carbon nanotube films are measured to study the impact of film thickness. No variation in the thermal conductivity with thickness is observed (as shown in Figure 3.3(a)) indicating that thermal transport is diffusive in these films. Estimates of the phonon mean free path in literature at room temperature range up to 1.5 μm [58, 59] confirming that diffusive thermal transport is expected at these length scales (for more details on phonon transport in CNTs, see Chapter 2). The total thermal resistance of the CNT films is the sum of the resistance between the CNT film and the heater, the intrinsic thermal resistance of the CNT film ($R''_{CNT} = L/k_{film}$), and the thermal resistance between the CNT film and the growth substrate. Figure 3.3(b) shows the total thermal resistance and $R''_{CNT-Heater}$ for these films. For the 120 μm thick sample, the resistance between the heart and the CNT film is smaller than could be resolved with this technique. Specifically, the temperature drop across the interface, ΔT , is smaller than could be

resolved by the microscope. For the thicker samples, this interface is comparable to the intrinsic film resistance. For all sample, the resistance between the CNT film and the growth substrate is smaller than resolved by this technique.

Generally, the total thermal resistance of these films is quite high, ranging from 4 to $28 \text{ cm}^2 \text{ K} / \text{W}$. In comparison, the thermal resistance of most conventional thermal interface materials (greases, gels, solders) is significantly less than $1 \text{ cm}^2 \text{ K} / \text{W}$. In part, this is due to the thickness of the CNT arrays. Reducing the CNT thickness from hundreds of microns to 1 micron would reduce the intrinsic thermal resistance of the film by two orders of magnitude. However, the interface resistances between the CNT film and surrounding materials would still be quite large and alternative bonding methods are required to improve those thermal resistances (for an example, see section 3.4). Assuming the CNTs act like thermal resistors in parallel, increasing the number of CNTs per unit area should also increase the thermal conductivity of the CNT film and reduce the thermal resistance of the film.

Mechanical densification through bi-axial mechanical compression is investigated as a method of increasing the film thermal conductivity. The aligned arrays are grown as described above and densified using mechanical compression. Several samples were measured using the cross-sectional infrared microscopy technique described above using quartz reference layers to measure the heat flux through the sample films. Figure 3.4 shows the thermal conductivity of the densified CNT films as a function of volume fraction. Although it was expected that the CNT thermal conductivity would increase linearly with volume fraction (*i.e.* if the CNTs are considered 1D conductors in parallel), the measured thermal conductivities are quite scattered. Furthermore, the thermal conductivities are much lower than anticipated, assuming an individual CNT thermal conductivity $\sim 3000 \text{ W/m/K}$, as had previously been reported for measurements of individual carbon nanotubes. Raman spectroscopy of MWCNT films is used to provide a very approximate indication of the impact of compression on quality. The Raman spectrum does indicate a high concentration of defects. However, the ratio of the G (graphite) band to the D (defect) band in MWCNT films shows no detrimental effect of densification on quality of the MWCNT films at the maximum compression (20 vol. % MWCNTs) [149]. Thus, it is likely that the individual nanotubes which make up the

CNT forest have thermal conductivities much lower than ideal and that improvements to the underlying CNT quality would lead to higher thermal conductivity films. The scatter in the results may also be due to rough contact surfaces combined with highly anisotropic conduction though the forest limiting the fraction of CNT contributing to heat transfer. Additionally, it is possible that the surface roughness depends on the degree of densification leading to a varied surface contact for each sample. While the infrared microscopy technique allows spatial separation of intrinsic thermal resistance from interface resistances, increased surface roughness may limit the number of CNTs in contact with the hot and cold side of the set-up and thus the measured film thermal conductivity could be less than under ideal contact conditions. Cola *et al.* [112] observed increased thermal performance of CNT films under increasing pressure, suggesting that the pressure improves the contact between the CNT and surrounding material.

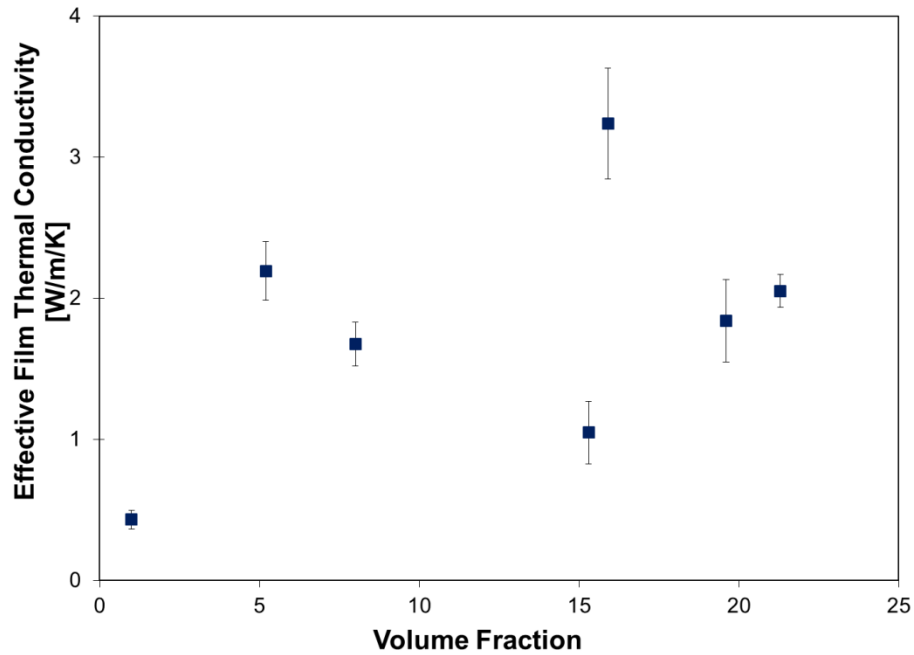


Figure 3.4: Thermal conductivity of mechanically-densified MWCNT films as a function of volume fraction. Note that a single quartz reference layer is used in these measurements to determine the heat flux through the sample film.

3.3 Thermal Conduction in Aligned Carbon Nanotube-Polymer Nanocomposites with High Packing Density[†]

3.3.1 Overview

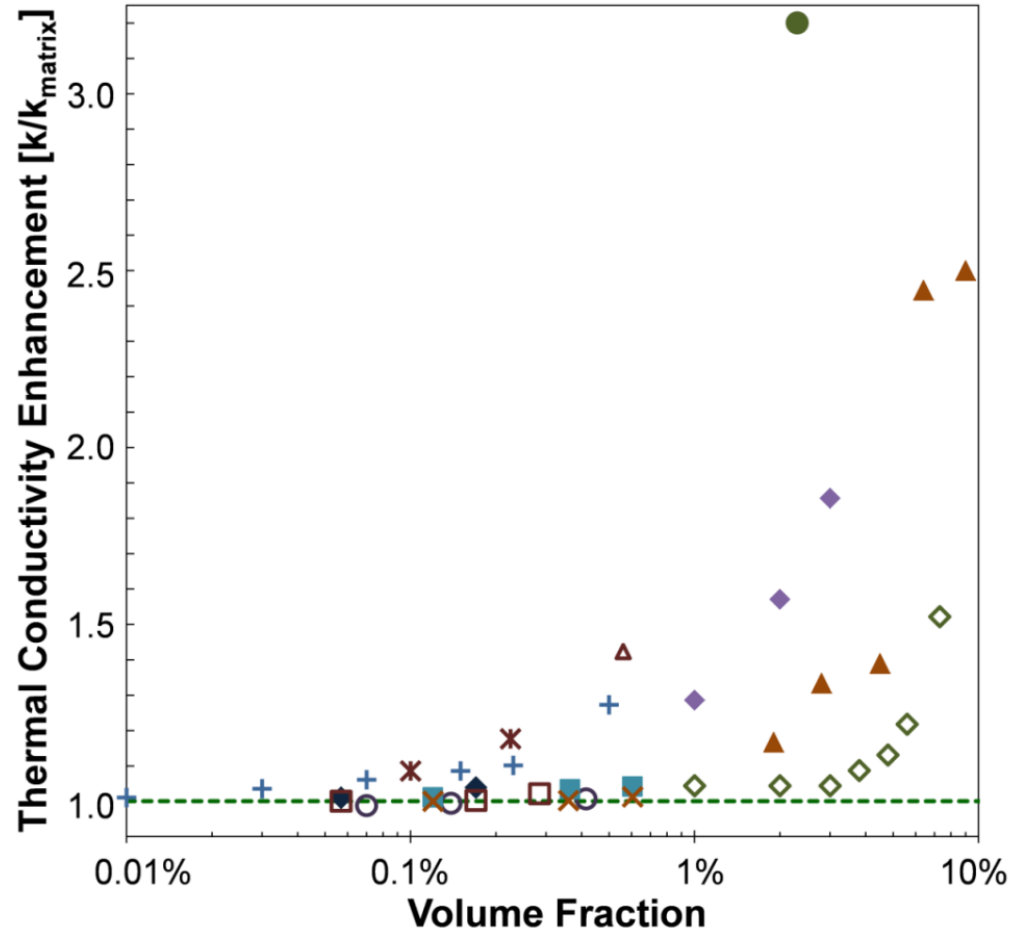
Aligned CNT polymer nanocomposites (A-CNT-PNCs) can benefit a variety of applications including electronics thermal management. Individual carbon nanotubes (CNTs) can have thermal conductivities near $3000 \text{ W m}^{-1} \text{ K}^{-1}$ and molecular dynamics simulations predict the values could be even higher [18, 64]. Vertically aligned CNT films can have volume-averaged axial thermal conductivities as high as those of metals, with reported values reaching $\sim 265 \text{ W m}^{-1} \text{ K}^{-1}$ [115, 116]. However, pure CNT forests, without binding materials, do not always offer the mechanical properties required by structural, aerospace, and other applications. Recent progress on CNT-polymer composites, in particular those featuring aligned nanotubes, promises unique combinations of thermal and mechanical properties. We report here a detailed study of conduction along aligned CNT-epoxy composites with CNT volume fractions extending an order of magnitude higher (up to 20 *vol.*%) than those of previous research. In particular, this work finds that the axial thermal conductivity is increased by a factor of 18.5 at a volume fraction of 16.7 *vol.*%, and the observed conductivity anisotropy ($k_{\text{axial}}/k_{\text{transverse}} \sim 2$ to 5) correlates well with CNT alignment. A strongly nonlinear variation of axial conductivity with volume fraction is interpreted considering CNT-epoxy boundary resistances, CNT imperfections introduced during fabrication, and modification of the phonon conduction within the nanotubes due to interactions with the matrix (*e.g.* enhanced scattering, damping of phonon modes, *etc.*).

Carbon nanotube additives have yielded only modest increases in the thermal conductivities of polymers compared to theoretical predictions, and the reasons for the relatively low conductivities are not well understood. Figure 3.5 reviews prior data for composites containing randomly-oriented carbon nanotubes and polymers (thermal conductivities near $0.2 \text{ W m}^{-1} \text{ K}^{-1}$). Low concentrations of nanotubes (<1 *vol.*%) have been shown to reduce the effective composite thermal conductivity in some cases,

[†] This section reproduced with permission from A. M. Marconnet, *et al.*, "Thermal Conduction in Aligned Carbon Nanotube–Polymer Nanocomposites with High Packing Density," *ACS Nano*, vol. 5, pp. 4818–4825, 2011. <http://pubs.acs.org/articlesonrequest/AOR-jzXZH4uAHztPHWpc5kF5>. Copyright 2011 American Chemical Society.

possibly due to void formation, and yield a modest enhancement in others [81, 150, 151]. Higher concentrations (>1 vol.%) yield larger increases in the conductivity, but generally less than twice the value of the epoxy matrix [81, 150, 152-154]. The resulting nanotube composites have a much lower thermal conductivity than predicted by effective medium theory (EMT) [155, 156], which, for example, predicts a factor of 250 enhancement in thermal conductivity when 5 vol.% randomly oriented CNTs ($k \sim 3000 \text{ W m}^{-1} \text{ K}^{-1}$) are added to an epoxy ($k_m \sim 0.2 \text{ W m}^{-1} \text{ K}^{-1}$). Possible reasons for the disparity between predictions and data include modification of the phonon conduction within the individual nanotubes by the polymer matrix [81], interfacial thermal resistances that impair thermal transport between the nanotubes and the polymer or between contacting nanotubes [123, 151, 155-159], impurities and lattice defects within individual nanotubes [108, 159-162], and the formation of voids in the CNT-polymer composite [163, 164].

This work investigates the impact of CNT density on the thermal conductivity of nanocomposites consisting of mechanically-densified, aligned multi-walled CNT (MWCNT) arrays infiltrated with an unmodified aerospace-grade thermoset epoxy. To better understand factors limiting thermal conductivity enhancement with the inclusion of nanotubes, both the axial and transverse thermal conductivities are compared with predictions from effective medium theory. The conduction mechanisms within the composites are considered to explain the observed non-linear increase in thermal conductivity with volume (packing) fraction of CNTs. Unlike unaligned, randomly-oriented nanotubes, aligned MWCNT arrays can potentially provide more direct thermal conductivity pathways across the entire composite thickness, which can yield significant thermal conductivity improvements [164-166]. The present manuscript offers the first benchmark data of CNT composites with controlled CNT density allowing correlation between CNT density and composite thermal conductivity. These data complement previous work characterizing the mechanical and electrical properties of these mechanically densified aligned CNT composites (up to 20 vol.% CNTs), which showed promise for use in multifunctional applications with a factor of 3 enhancement in elastic modulus at 17 vol.% CNTs and a significant reduction in electrical resistance with increasing CNT density [147, 167].



	Matrix	CNT Details	Reference
+	Epoxy (Epon 828)	HiPCO SWCNT	Bryning <i>et al.</i> [150]
×	Epoxy (Epon 828)	Laser Oven Grown SWCNT	Bryning <i>et al.</i> [150]
●	Epoxy (Epon 862)	HiPCO SWCNT	Du <i>et al.</i> [168]
○	Epoxy (Bakelite L13i)	SWCNT	Gojny <i>et al.</i> [81]
■	Epoxy (Bakelite L13i)	DWCNT	Gojny <i>et al.</i> [81]
×	Epoxy (Bakelite L13i)	DWCNT-NH ₂	Gojny <i>et al.</i> [81]
◆	Epoxy (Bakelite L13i)	MWCNT	Gojny <i>et al.</i> [81]
□	Epoxy (Bakelite L13i)	MWCNT-NH ₂	Gojny <i>et al.</i> [81]
◆	Silicone	MWCNT	Hu <i>et al.</i> [152]
◇	Polymethylmethacrylate	SWCNT	Bonnet <i>et al.</i> [153]
▲	Polymethylmethacrylate	SWCNT	Guthy <i>et al.</i> [154]
▲	Polyethylene	SWCNT	Haggenmueller <i>et al.</i> [169]

Figure 3.5: Previous data for the thermal conductivity enhancement as a function of volume fraction for randomly dispersed CNT composites. This chart represents a subset of the available data where the matrix material has a thermal conductivity of 0.18 to 0.26 W m⁻¹ K⁻¹.

MWCNT arrays are grown using chemical vapor deposition [170], mechanically densified to increase the volume fraction [148], and infiltrated with RTM6 epoxy. The CNT alignment within the composites is examined by measuring the azimuthal angle of CNTs using scanning electron microscopy (SEM, Philips XL30), resulting in a mean-square cosine of 0.77 from averaging over 100 CNTs. Voids in CNT composites are evaluated using optical microscopy and micro-computed tomography scans (X-Tek HMXST225), and only void-free A-CNT-PNC samples are thermally characterized. Comparative infrared (IR) microscopy characterizes the axial and transverse thermal conductivities of aligned CNT nanocomposites of varying volume fraction.

3.3.2 Methods

3.3.2.1 Fabrication

Aligned CNT composites are fabricated from continuous CNTs, implemented in a controlled and aligned morphology as described in previous work [147, 148] and illustrated in Figure 3.8. In brief, aligned arrays consisting of 1 *vol.%* dense, 8 nm diameter, several millimeter long MWCNTs are grown *via* chemical vapor deposition. The aligned arrays are densified using biaxial mechanical compression and infiltrated using capillary action with epoxy (RTM6 from Hexcel), then cured to form aligned CNT nanocomposites with CNT densities between 1 *vol.%* and 20 *vol.%*. The CNT alignment was quantified by measuring the azimuthal angle θ of CNTs using scanning electron microscopy (SEM, Philips XL30). The mean-square cosine $\langle \cos^2 \theta \rangle$, with its statistical distribution among all CNTs as the weighting factor, was estimated to be 0.77 from averaging over 100 CNTs in the SEM images. Voids in CNT composites were also evaluated using optical microscopy (2D) and micro-computed tomography scan (X-Tek HMXST225, 3D). Air bubbles and epoxy-rich regions on the order of microns were at times observed and A-CNT-PNC samples with such voids were eliminated from the sample sets [149].

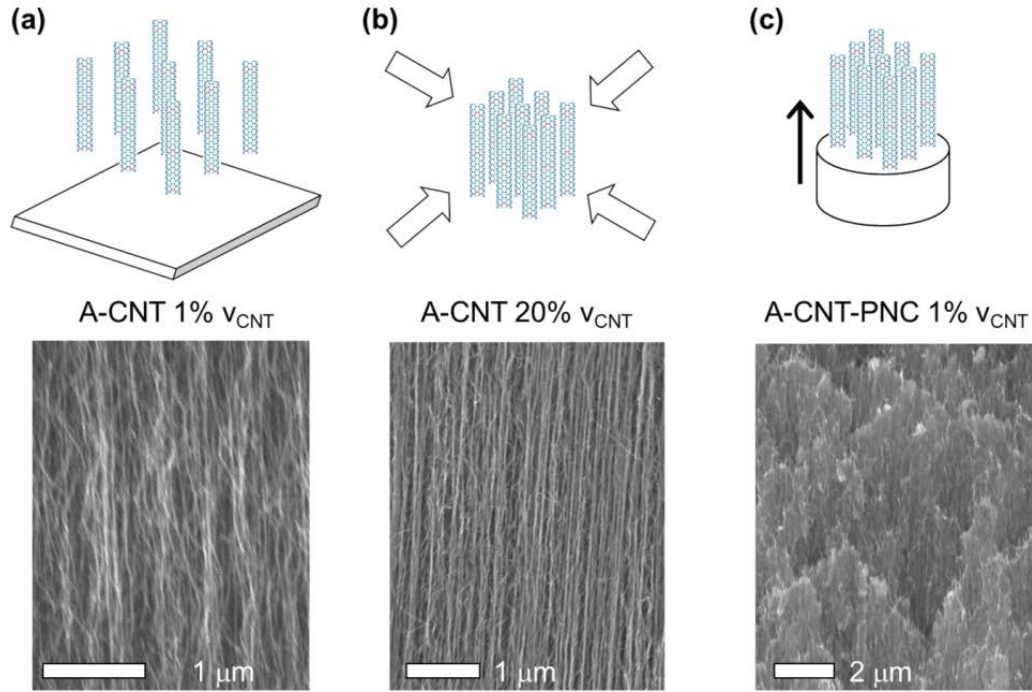


Figure 3.6: Schematic and SEMs of nanocomposite fabrication [147, 148]. (a) As grown CNT films with 1 *vol.*% CNTs. (b) Biaxial mechanical compression of CNTs up to 20 *vol.*% CNTs. (c) A-CNT-PNC fracture surface after capillary-driven epoxy infiltration of the CNT arrays.

3.3.2.2 Comparative Infrared Thermal Microscopy

The thermal conductivity is measured using a comparative method based on ASTM standard E1225, using an infrared (IR) microscope instead of thermocouples [171-173]. A one-dimensional heat flux is generated across a stack consisting of the nanocomposite sample sandwiched between two reference layers. A resistive heater (metal-coated silicon) is attached to one reference layer, and the other reference layer is affixed to a heat sink (through a silicon wafer attached to temperature-controlled copper baseplate). For the unfilled CNT arrays, the stack consists only of a heat sink (silicon wafer attached to copper baseplate), a reference layer, a sample CNT film, and a heater (metal-coated silicon). Based on preliminary work regarding the magnitude of the thermal conductivity, one of two reference materials are used for each samples in this experiment: quartz (GE Type 214) with a thermal conductivity of $1.4 \text{ W m}^{-1} \text{ K}^{-1}$ and Pyroceram 9606 (Corning Glass) with a thermal conductivity of $4 \text{ W m}^{-1} \text{ K}^{-1}$, to ensure that the temperature gradients in the sample and in the reference layers are comparable.

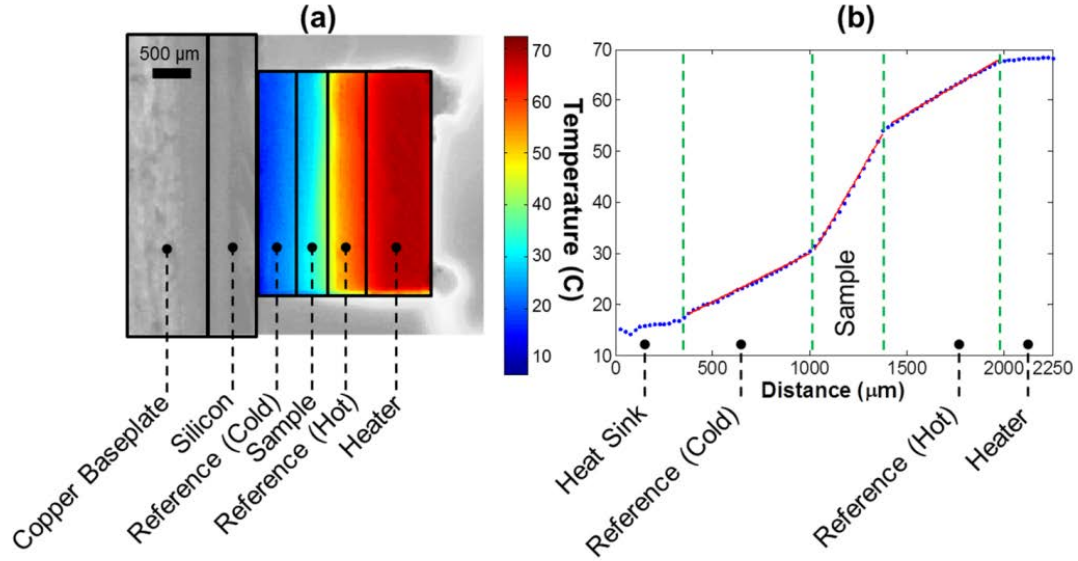


Figure 3.7: IR Microscopy technique for thermal conductivity measurements. (a) Schematic of the testing configuration with an example temperature map. The sample sandwiched between two reference layers. A metallized piece of silicon is used as a heater and the structure is affixed to a silicon substrate with silver paste. The silicon substrate is affixed to the temperature controlled copper baseplate using thermal grease. (b): Temperature distribution across sample including best fit slopes for both reference regions and the sample (temperatures averaged across the width of sample, i.e. each column in image (a)).

Fourier's law describes heat transport for each layer in the sample. The samples are prepared such that all layers in the stack have the same cross-section and the heat flux is constant across the sample and two reference layers. Thus, the ratio of the thermal conductivity of the sample and the reference material can be determined from a ratio of the temperature gradient in the sample and the reference layer. The use of two reference layers allows the relative importance of any other heat transfer mechanisms, such as convective and radiative loss, compared to the conduction through the sample stack to be determined. Also, the use of reference layers eliminates possible error due to electrical losses in the wiring and connections supplying power to the heater and due to convection to the air on the topside of the heater. The relevant surfaces of the composite which come in contact with the reference layers are polished to a roughness of less than 3 nm and coated with 200 nm of platinum to enhance contact. The sample stack is assembled using a silver epoxy (Duralco 120, Cortonics). The surfaces of the

reference-sample-reference stack facing the IR camera view are also polished, and then coated with a thin film of carbon (SPRAYON Dry Graphite Lubricant, Sherwin Williams) to enhance emissivity. For the unfilled CNT arrays, no surfaces are polished or coated with platinum and the stack is bonded together using colloidal graphite (Ted Pella, Inc.) and the surfaces of the reference layer are also coated with the colloidal graphite to enhance emissivity.

For a given heater power, a two-dimensional temperature map is recorded with the infrared microscope. The microscope uses a 256x256 InSb focal plane array for detecting wavelengths ranging from 3 to 5 μm . The IR microscope has a temperature sensitivity of 0.1 K and spatial resolution of up to 2 μm . Within each temperature map, the regions containing the reference layers and sample are identified and the temperature is averaged in the direction perpendicular to the heat transport to yield temperature versus position graphs, as shown in Figure 3.8. The temperature gradient in each region of the stack is determined using a least-squares fitting routine. For a robust measurement, thermal maps are recorded and the thermal gradients are calculated as the power is increased. Boundary resistances between the different layers in the stack can be spatially separated from the temperature gradients associated with the material's intrinsic thermal conductivity.

3.3.3 Results & Discussion

The measured thermal conductivities (Figure 3.8) are comparable with or greater than those reported previously for other aligned CNT nanocomposites [164, 165], but the data fall well below the best data for CNT films without an epoxy matrix [109, 112, 115, 116]. The axial thermal conductivity of the composites ranges from 0.46 to 4.87 $\text{W m}^{-1} \text{K}^{-1}$ as the nanotube density increases from 1 *vol.%* to 16.7 *vol.%*. The axial thermal conductivity of the composites is comparable to the thermal conductivity of unfilled, aligned, densified MWCNT films which ranges from 0.29 to 3.6 $\text{W m}^{-1} \text{K}^{-1}$ as shown in Figure 3.8. The unfilled arrays were fabricated in the same manner as the composites and measured with a similar comparative infrared microscopy technique as the composites with minor differences as noted in the *Section 3.3.2: Methods*.

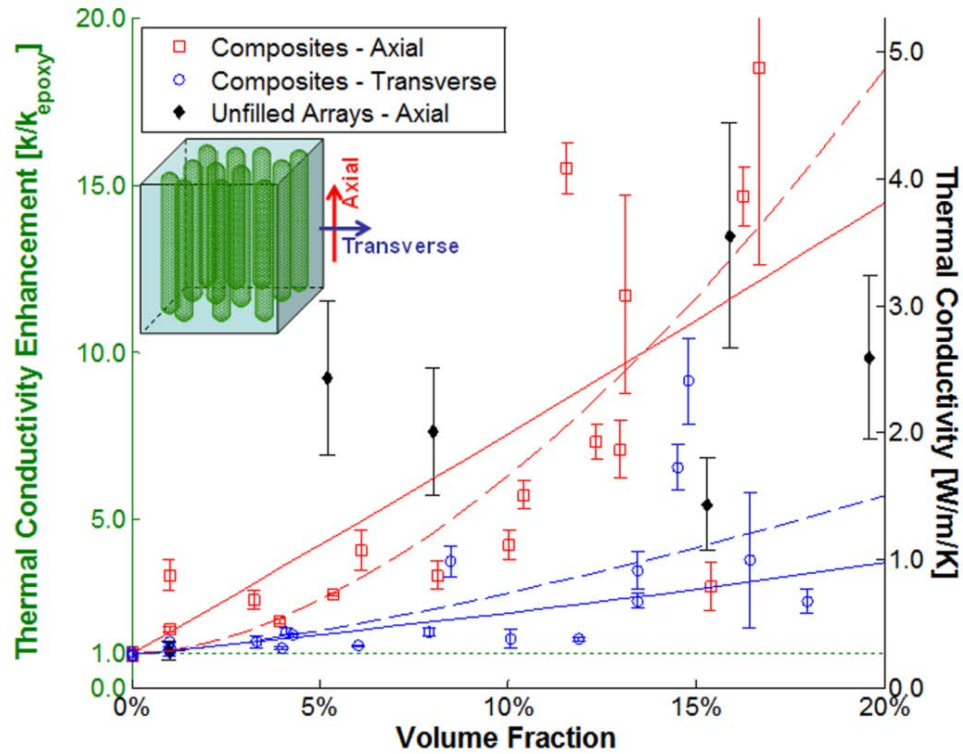


Figure 3.8: The axial (\square) and transverse (\circ) thermal conductivity of CNT nanocomposites and unfilled CNT forests (filled diamonds) as a function of volume fraction. The schematic below the legend shows the axial and transverse measurement directions for the aligned CNT composites. Best fits from the effective medium approach (solid lines) and with a power law (dashed line) are shown for the composite data. For the effective medium approach, the axial and transverse thermal conductivities are fit simultaneously with a non-linear least squares algorithm, assuming an alignment factor of 0.77 from the SEM analysis, with two free parameters: the individual CNT thermal conductivity ($22.1 \text{ W m}^{-1} \text{ K}^{-1}$) and the CNT-polymer boundary resistance ($<1 \times 10^{-9} \text{ m}^2 \text{ K W}^{-1}$). For the power law relationship $(k_e - k_m) = A \cdot f^B$, the prefactor, A , and the exponent, B , are fit with a non-linear least squares algorithm, while the measured matrix thermal conductivity, $k_m = 0.26 \text{ W m}^{-1} \text{ K}^{-1}$, is held constant. The fitted values are $A = 72.9 \text{ W m}^{-1} \text{ K}^{-1}$ and $B = 1.72$ for the axial thermal conductivity and $A = 11.3 \text{ W m}^{-1} \text{ K}^{-1}$ and $B = 1.37$ for the transverse thermal conductivity. The dashed green line indicates the thermal conductivity of the epoxy.

For the axial direction in the aligned composites, a simple model considering nanotubes conducting heat parallel with the polymer matrix predicts that the thermal conductivity increases linearly with volume fraction. A linear fit to the axial data in Figure 3.8 provides an estimate of $18.5 \text{ W m}^{-1} \text{ K}^{-1}$ for the thermal conductivity of the individual nanotubes in the matrix, much lower than the previous measurements of

individual nanotubes. However, the axial thermal conductivity for the composites does not follow a simple linear trend, instead the increase in thermal conductivity with volume fractions above 10% appears much greater than at lower volume fractions suggesting that the density of nanotubes is not the only factor influencing the thermal conductivity. The non-linearity of the data in Figure 3.8 for the aligned CNT composites is similar to the data for the randomly-oriented composites presented in Figure 3.5, although the magnitude of the thermal conductivity enhancement is much greater for these aligned composites. The thermal conductivity for the transverse direction remains near the thermal conductivity of the base epoxy increasing slightly with volume fraction below ~ 10 vol.%. The highest measured transverse thermal conductivity is $2.41 \text{ W m}^{-1} \text{ K}^{-1}$ at 14.8 vol.%. For both the axial and transverse direction, at high volume fractions (> 10 vol.%), significant differences in the thermal conductivity are observed for samples of similar CNT densities indicating that variations in sample quality may impact the thermal conductivity. While isotropic thermal conductivity is expected and observed for randomly dispersed nanotube composites, the CNT alignment in these composites results in a significantly anisotropic thermal conductivity ($k_{axial}/k_{transverse} \sim 2$ to 5). The axial thermal conductivity increases more rapidly with volume fraction than the transverse thermal conductivity, resulting in a higher degree of anisotropy at higher volume fractions.

There are several possible explanations for the thermal conductivities reported here for composites, which are lower than expected for CNT-based materials and also lower than those reported for thin, unfilled and uncompressed CNT arrays. The same conduction mechanisms that reduce the thermal conductivity also dictate the non-linear trend in thermal conductivity with volume fraction. First, the quality of the CNT film used for composites strongly impacts the composite performance. Measurements and simulations of individual nanotubes highlight the very high thermal conductivities of pristine nanotubes leading to impressive predictions of the behavior of bulk materials fabricated from CNT films. But even for unfilled CNT arrays, the reported effective thermal conductivities range from less than $1 \text{ W m}^{-1} \text{ K}^{-1}$ (e.g. [114]) to over $250 \text{ W m}^{-1} \text{ K}^{-1}$ (e.g. [115, 116]). The effective thermal conductivity of the unfilled CNT arrays in this study, which form the basis of the composites used in this work ranges from 0.29 to

3.6 W m⁻¹ K⁻¹ over the range of volume fractions investigated. The low thermal conductivity for the unfilled arrays is governed by the quality of the CVD grown nanotubes and the challenge in making good thermal contact with all the nanotubes within the film. Thus, when filled with epoxy ($k \sim 0.26$ W m⁻¹ K⁻¹ for the RTM6 used here), the composite thermal conductivity will not be as high as predicted from the measurements of individual nanotubes. The effective thermal conductivity of bulk materials containing nanotubes depends on many properties of the CNT component, including the individual CNT conductivity, CNT density, morphology, and contact resistances. In particular, defects within individual nanotubes, including lattice defects, impurities, and amorphous carbon, lead to reduced thermal conductivities of the individual nanotubes, and hence of their bulk materials. Raman spectroscopy of MWCNT films is used to provide a very approximate indication of the impact of compression on quality. The ratio of the G (graphite) band to the D (defect) band in MWCNT films shows no detrimental effect of densification on quality of the MWCNT films at the maximum compression (20 vol.% MWCNTs) [149]. Improvements in thermal conductivity for CNT films and composites have been observed after various treatments such as annealing [108, 162], nitric acid treatments [161, 162], and centrifugation (for unaligned films) [160]. In order to form high thermal conductivity composites, the thermal conductivity of the constituent CNTs must be consistently high, and this is not always achieved in the quantities needed for fabricating nanocomposites.

Second, contact regions between nanotubes, which occur even in the best aligned CNT films, impact thermal performance of any CNT composite. These contact points serve both as scattering sites for phonons propagating along contacting nanotubes, reducing the individual nanotube thermal conductivity, and as a route for heat conduction between the nanotubes with additional thermal resistance across the interface. The magnitude of the thermal boundary resistance at CNT-CNT contacts strongly influences the effective conductivity of the composite material. A higher contact resistance diminishes the thermal conductivity of the ensemble. Prasher *et al.* [123] show that the thermal conductivity of a randomly-oriented bed of MWCNTs is controlled by the CNT-CNT thermal contact resistance which is orders of magnitude larger than the intrinsic thermal resistance of a CNT. If the thermal boundary resistance

between nanotubes is small, as the volume fraction increases and more CNT-CNT contacts are formed, the composite thermal conductivity increases. Percolation theory predicts that above a threshold volume fraction, the filler particles (CNTs) form a network which bridges the entire thickness of the composite leading to more effective heat transport across a sample [152, 157]. Kumar *et al.* [157] computationally analyzed percolation in 2D networks of CNTs, finding that the CNT-CNT and CNT-substrate thermal resistances influenced the thermal conductivity, even below the threshold volume fraction required to form chains of filler CNTs bridging the entire sample thickness. In contrast, in the axial direction, the nanotubes in the composites studied in this work should bridge the entire thickness of the sample in the axial direction regardless of the volume fraction. But in the transverse direction and in the axial direction if some CNTs do not traverse the entire sample thickness, densification may lead to the formation of percolation networks which bridge the entire thickness of the sample. Meshot and Hart [174] have shown variations in CNT alignment and entanglement from the top to bottom of similar CVD grown MWCNT arrays. Panzer *et al.* [140] showed that not all nanotubes physically present in a aligned array contribute to heat transport due to a lack of engagement of all the CNTs with the heat source and sink. As the alignment and continuity of the nanotubes varies throughout the array, CNT-CNT contacts become increasingly important for effective heat transport across the composite.

Third, CNT-polymer boundary resistance impacts the effective thermal conductivity of CNT-polymer composites. In unaligned CNT composites, the individual CNTs do not bridge the entire thickness of the composite and the CNT-polymer boundary resistance is critical. One of the main advantages of the composites studied in this work is that the CNTs themselves are well-aligned and span the entire thickness of the polymer in the axial direction providing direct pathways for heat transport across the composite. In theory, for these composites, the CNT-polymer boundary resistance is only important for the conductivity transverse to the CNT axis. However, if some of the CNTs fail to extend to the surface of the polymer, the CNT-polymer thermal boundary resistance will impact the axial conduction as well.

Furthermore, phonon modes within CNTs can be damped and scattered by the polymer matrix reducing the thermal conductivity of the CNTs themselves [81, 151]. Gojny *et al.* [81] showed that the thermal conductivity enhancement for MWCNTs dispersed in epoxy was larger than that of single-walled CNTs (SWCNTs) as MWCNTs have inner shells which conduct phonons efficiently despite the outer shell interacting with the polymer matrix. This damping of phonon modes within the outer shells of nanotube may be a possible reason for the reduction of the thermal conductivity of the nanotubes, especially when high quality nanotubes form the basis of the composite.

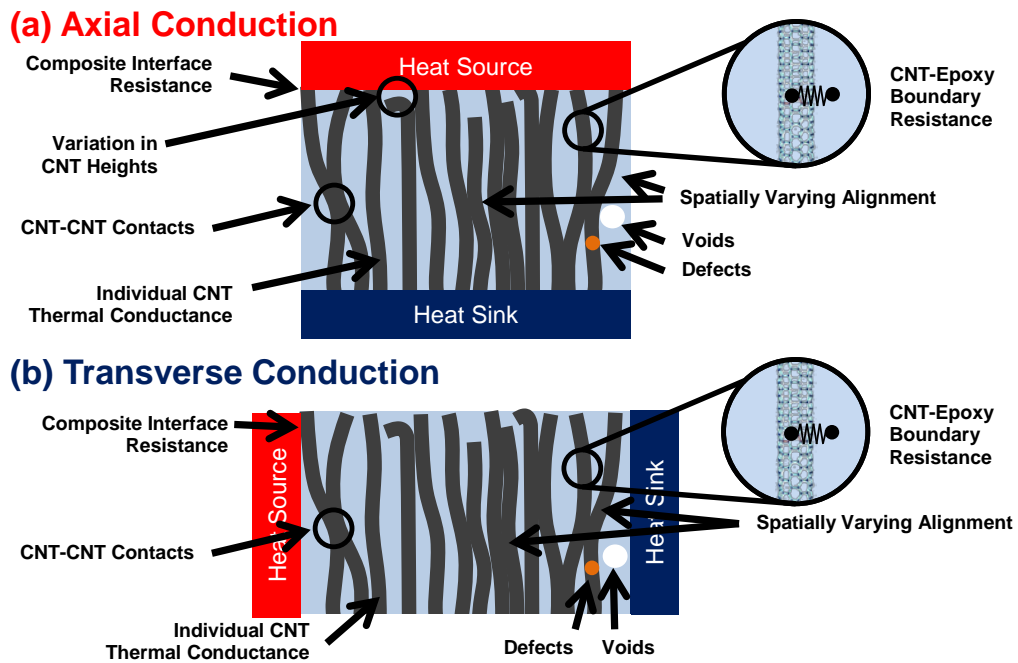


Figure 3.9: Cartoon illustrating of key mechanisms impacting thermal conduction in CNT composites including variations in the intrinsic CNT thermal conductance, interface resistances, variations in CNT lengths, spatially-varying CNT alignment and CNT-CNT contacts, as well as defects within CNTs and voids in the polymer matrix.

Figure 3.9 summarizes the key mechanisms impacting thermal conduction in vertically-aligned CNT composites. The effect of CNT-CNT contacts is the most likely cause of the non-linearity in the thermal conductivity with increased density, while the low thermal conductivity of the constituent CNT arrays dictates the low thermal conductivity compared to pristine nanotubes. The number of contact points and the area of each contact could be affected by the biaxial compression and by the addition of

epoxy to the composite. Increasing area of contact should reduce the contact resistance, while increasing contacts may lead to increased scattering but more opportunities for heat to transfer between neighboring nanotubes. The CNT-polymer boundary resistance may also contribute to the non-linearity of the thermal conductivity with increased density, particularly in the direction transverse to the CNT axis. All nanotubes in this work are grown following the same procedure, so the CNT array quality should be consistent even at high volume fractions. The scatter in the data for unfilled arrays may arise from variations in the quality of thermal contact to the substrate after densification. Poor contact between the substrate and the nanotubes, combined with minimal conduction between nanotubes, may lead to few pathways for thermal conduction across the CNT array. For PNCs, the matrix can aid in spreading the heat between nanotubes, especially at the contact surfaces.

Effective medium theory [156] has been used to model the thermal conductivity of CNT-polymer composites in the axial and transverse directions. The CNT-polymer boundary resistance dictates the curvature of the transverse thermal conductivity with increased CNT volume fractions. Relatively small values of CNT-polymer boundary resistance ($<1 \times 10^{-9} \text{ m}^2 \text{ K W}^{-1}$) are required to see the positive curvature observed with these experiments. When fitting effective medium theory to the data, little non-linearity in the EMT prediction is observed, as seen in Figure 3.8. The generally aligned, but wavy, entangled, cylindrical CNTs are modeled as unaligned ellipsoidal particles with a large aspect ratio. The alignment factor, $\langle \cos^2(\theta) \rangle$, varies from 0.33 for completely randomly oriented particles to 1 for particles whose axis aligns perfectly (i.e., collimated) with the direction of heat transport. Fitting both the axial and transverse thermal conductivity data predicts an individual CNT thermal conductivity of $22.1 \text{ W m}^{-1} \text{ K}^{-1}$ and a boundary resistance $<1 \times 10^{-9} \text{ m}^2 \text{ K W}^{-1}$, assuming an alignment factor of 0.77 from the SEM analysis. This EMT model incorporates the thermal boundary resistance between the CNT and the polymer, R_{bd} , but neglects direct CNT-CNT conduction. Considering the axial direction, the model elliptical particle may represent a heat transfer pathway consisting of more than one nanotube, in which case, the effective thermal conductivity predicted includes the intrinsic thermal conductivity and thermal

boundary resistances and requires a low value of the intrinsic CNT thermal conductivity to achieve agreement with the data. Furthermore, by neglecting the direct CNT-CNT conduction, this model may also underpredict the CNT-epoxy boundary resistances. This may account for the disparity between our estimate of CNT-epoxy boundary resistance and values on the order of 10^{-8} to 10^{-7} m² K / W reported in literature [175, 176].

Fitting a power law relationship, similar to the results of percolation theory, to the increase in the axial thermal conductivity above the polymer matrix gives a better approximation of the trend in the data leading to the relation $(k_{e,a} - k_m) = \left(72.9 \frac{W}{m \cdot K}\right) f^{1.72}$. The fit to the transverse conductivity leads to a different exponential relationship with a slightly lower exponent: $(k_{e,t} - k_m) = \left(11.3 \frac{W}{m \cdot K}\right) f^{1.37}$. The power law relation suggests that there are an increasing number of pathways for heat transport generated by increasing volume fraction.

3.3.4 Summary

In conclusion, the first benchmark study of the thermal conductivity of aligned MWCNT polymer nanocomposites as a function of varying CNT volume fraction is reported. Axial thermal conductivities up to $4.87 \text{ W m}^{-1} \text{ K}^{-1}$ with 16.7 vol.% CNTs (a factor of 18.5 enhancement in thermal conductivity) are reported for the axial direction, much greater than reported in studies of unaligned CNT composites. While the thermal conductivity enhancement is large, it is much lower than predicted if the thermal conductivity of the individual, defect-free CNTs have thermal conductivities on the order of $3000 \text{ W m}^{-1} \text{ K}^{-1}$, but it is comparable to the thermal conductivity of the unfilled CNT arrays. The non-linear behavior of thermal conductivity with CNT volume fraction is attributed to the interaction between CNTs and between the CNT and the polymer. Future measurements of the transverse conductivity of unfilled arrays will be useful in separating out the effects of the epoxy infiltration from the effects of CNT-CNT interactions. Further model development is necessary to fully understand the impact of factors including CNT waviness, boundary resistances, and parameter variation with CNT volume fraction. In order to fabricate composites that take full advantage of the

CHAPTER 3

high thermal conductivity of individual CNTs, additional studies on aligned CNT composites are necessary including improvement of the CNT quality (through post-growth annealing processes, *etc.*) and improved epoxy infiltration to minimize CNT-CNT contacts. In addition to thermal properties, the composites also need to be engineered to obtain the desired mechanical properties for thermal interface applications.

3.4 Nanoscale Conformable Coatings for Enhanced Thermal Conduction of Carbon Nanotube Films[‡]

3.4.1 Introduction

In this section, a method to coat CNT films with thick metallic layers which could later be planarized using well established chemical-mechanical planarization techniques is presented in this section. The metal layer may enhance the thermal contact conductance between the CNT film and surrounding materials by making intimate thermal contact with the CNT tips and providing a flat surface for bonding. In this work, a thin seed layer of metal (Pd and Cu) is evaporated on the top surface of the CNT film and serves as an electrode for electroplating. By varying the electroplating duration, films of copper between 1 and 20 μm are deposited uniformly on approximately 100 μm -thick CNT arrays. The thermal conductivity of metallized CNT films is measured using a steady-state cross-sectional infrared microscopy technique and the film thermal conductivity reflects the quality of the metal-CNT engagement.

3.4.2 Fabrication

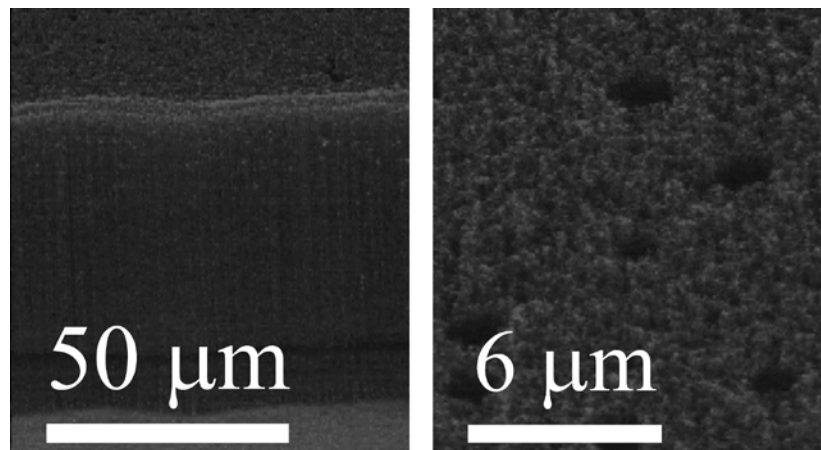


Figure 3.10: SEM images of CNT film highlighting the non-uniformity in the surface of the CNT film. SEM images courtesy of Xidex Corporation.

Five samples of $\sim 100\ \mu\text{m}$ -thick vertically aligned CNT arrays (Xidex Corp.) are electroplated with copper films. For all samples, the density of the CNT film is between 0.0105 and 0.0172 g/cm^3 , corresponding to a volume fraction of approximately 0.5 vol

[‡] This section reproduced with permission from A.M. Marconnet, *et al.* “Nanoscale Conformable Coatings for Enhanced Thermal Conduction of Carbon Nanotube Films” in *ITHERM 2012*, San Diego, CA, May 30-June 1, 2012. Copyright 2012 IEEE.

%. As shown by the scanning electronic microscope (SEM) images in Figure 3.10, the surface of the CNT array shows many defects, specifically holes in the CNT array and variations in the film thickness. Electrodeposition of a thick copper film leads to a more ideal (uniform) surface for bonding, despite the non-uniformities in the underlying CNT film.

Prior to the electroplating, a thin metal seed layer (Pd and Cu) is evaporated onto the CNT film. The Pd film enhances the adhesion of the copper to the CNTs. The copper seed layer serves as an electrode for the electrodeposition process and metal lead wires are attached to the copper seed layer using silver paste cured at 100°C for ~30 minutes.

Table 3.1: Electroplating Conditions & Film Thickness

Sample	Seed Layer	Electroplating Time (min)	Current (mA)	Film Thickness (μm)
A	5 nm Pd 200nm Cu	7	30	1 to 2
B	10 nm Pd 100nm Cu	40	15	4 to 6
C	10 nm Pd 100nm Cu	40	15	4 to 6
D	10 nm Pd 100nm Cu	80	15	8 to 10
E	10 nm Pd 100nm Cu	80	15	20

The CNT samples on their silicon growth substrate are electroplated in 2-electrode cell using a solution of $\text{CuSO}_4 \cdot 5\text{H}_2\text{O}$ and H_2SO_4 . The electroplating recipe in this work is similar to that of Yang *et al.* [177], who electroplated copper to fill the space between CNTs in the arrays to form CNT-copper nanocomposites. In our method, the metal seed layer ensures that the copper layer does not deposit between the CNTs, but rather as a continuous layer on top of the CNT film. After electroplating, the samples are immediately dipped in deionized water, then ethanol, and finally dried with dry nitrogen gas.

The electroplating parameters were chosen to generate a range of film thicknesses and Table 3.1 shows the thickness of the seed layers, the electroplating time (t_e) and

current (I_e) for each sample. Assuming the deposition is uniform across the entire area (A_e), the deposited film thickness (H_{Cu}) can be estimated by:

$$H_{Cu} = \frac{I_e t_e}{Fn_{Cu}} \frac{M_{Cu}}{A_e \rho_{Cu}}, \quad (3.2)$$

where $n_{Cu} = 2$ is the moles of electrons required for the electroplating reaction to deposit one mole of copper atoms, F is the Faraday Constant, and M_{Cu} and ρ_{Cu} are the molar mass and density of copper. The surface area for electroplating on sample A is approximately 5 cm^2 , while samples B through E are approximately 2.5 cm^2 . This total surface area includes a 2.5 mm wide region without CNTs near one edge of each sample.

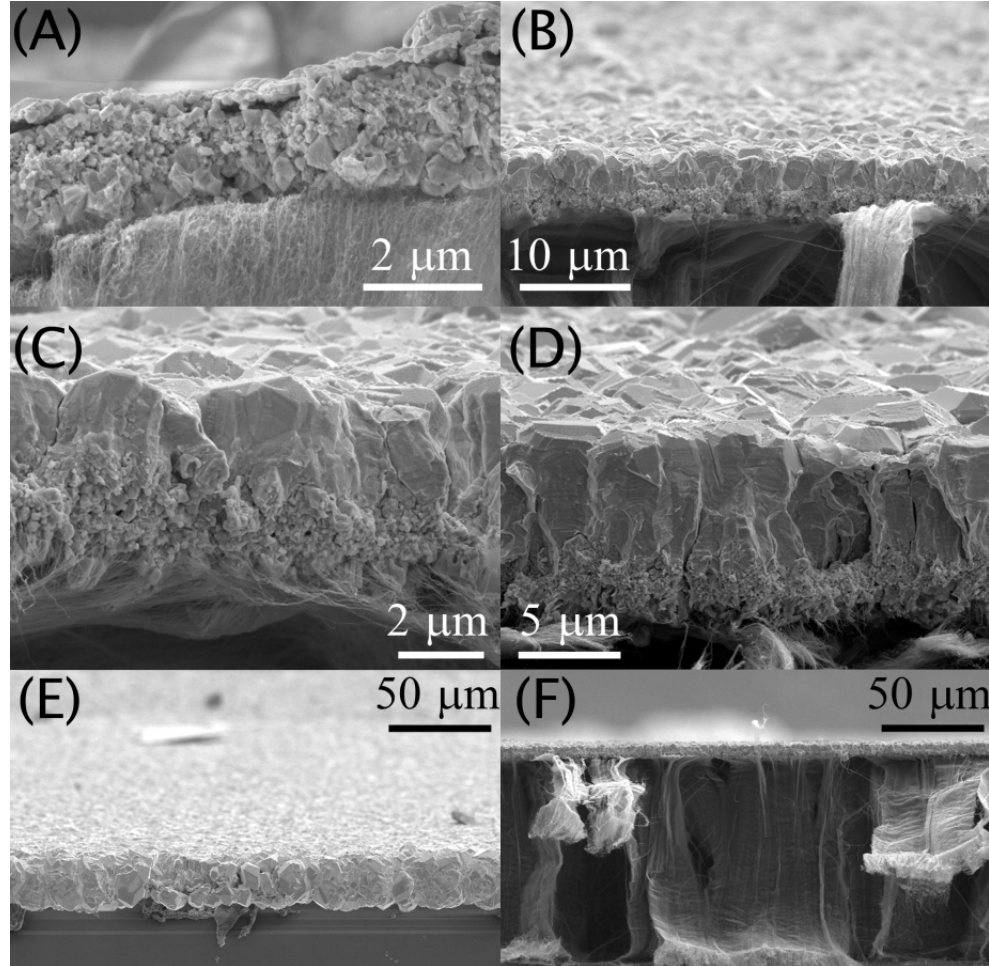


Figure 3.11: Close-up SEM images of copper films on CNT arrays. Panels (A) through (E) correspond to samples A through E. Note that the image in panel E is from a region of the sample without the CNT film. (F) Zoomed-out SEM image of electroplated copper

film on the CNT array (sample B) showing uniform coverage of the CNT film with copper.

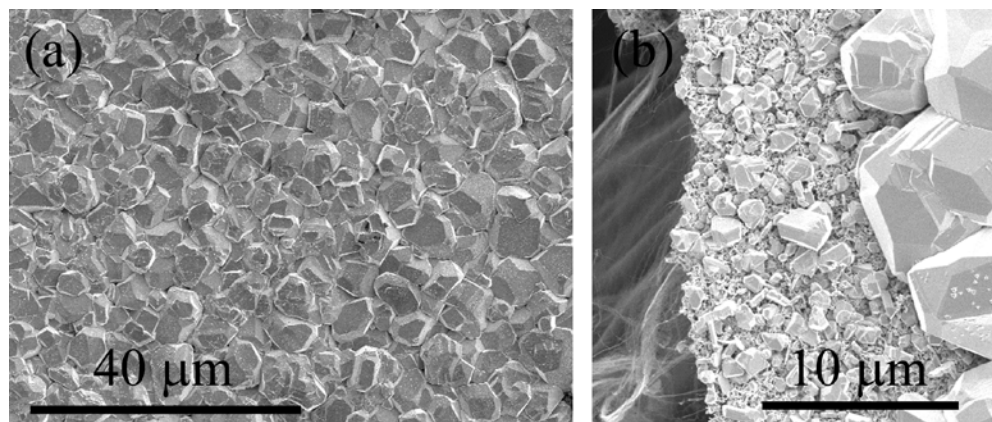


Figure 3.12: SEM images of surface of copper film (sample B) near the (a) center and (b) edge of the sample. Uniform surface roughness and grain size is observed across the top surface of the sample. In panel (b), a layer of small grains is evident below the large grains at the surface.

After electroplating samples are cleaved and imaged with a SEM. The average film thicknesses determined from SEM images (see Figure 3.11) are reported in Table 3.1. The measured thicknesses for samples A-D agree well with the expected thicknesses from Eq. (3.2). However, the film thickness for Sample E is much thicker than expected, possibly due to non-uniform electrodeposition. For samples A-D, the metal lead wire is attached directly to the copper seed layer on the surface of the CNT film. However, for sample E, the attachment of the metal lead wire delaminated a small portion of the copper seed layer from the CNT film. Thus, to permit electrodeposition on sample E, the lead wire is attached the sample edge without any CNTs. SEMs show electrodeposited copper on both the portions of the silicon substrate (*i.e.* the portions with and without CNTs). The film thickness reported in Table 3.1 for sample E is measured at a region without CNTs, near the lead attachment point and may be thicker than in other regions on the sample. The grain structure of the copper film is evident from the SEM images. Top view SEMs (see Figure 3.12) show uniform, large grains across the surface of the CNT film. Below the large grains, a layer of small grains is evident (Figure 3.12 (b)).

3.4.3 Thermal Characterization: Cross-Sectional Infrared Microscopy

Steady state cross-sectional infrared (IR) microscopy is used to measure the thermal conductivity of the metal-coated CNT film. The copper film is used as a resistive heater to heat the top side of the CNT film, while the bottom side is attached to a temperature-controlled heat sink (see Figure 3.13(a)). The square samples are cleaved into rectangles (approximately 5 mm x 15 mm) to increase the electrical resistance. Wires are attached to the edges of the copper film with silver paste. Current is passed through the copper film generating a heat flux through the CNT film and the voltage across the copper film is measured to quantify the applied heat flux:

$$q'' = \frac{IV}{A_c} \quad (3.3)$$

where I and V are the current and voltage applied to the resistive heater, A_c is the cross-sectional area of the CNT film.

Prior to measuring each sample, the IR image is calibrated by generating an emissivity map for the subsequent temperature measurements. The CNT film is brought to a uniform temperature and the calibration radiance image is recorded. From this calibration image and the sample temperature (measured with thermocouples), the emissivity at each point in the sample image is determined. When the temperature is varied across the sample, the emissivity from the calibration allows measurement of the temperature from the measured radiance.

At several applied power levels (*i.e.* different heat fluxes), an infrared microscope (Quantum Focus Instruments) measures a two-dimensional (2-d) temperature map of the cross section of the CNT film (Figure 3.13(b)). The temperature map is measured with a spatial resolution of 2 μm . The temperature gradient (dT/dx) within the CNT film is calculated from the 2-d temperature map by averaging the temperature in each row of pixels (*i.e.* in the direction perpendicular to the heat flux) to generate an average temperature profile (Figure 3.13(c)). From Fourier's law, the thermal conductivity is extracted from the linear least squares fit to the heat flux versus temperature gradient:

$$q'' = k_{film} \frac{dT}{dx}. \quad (3.4)$$

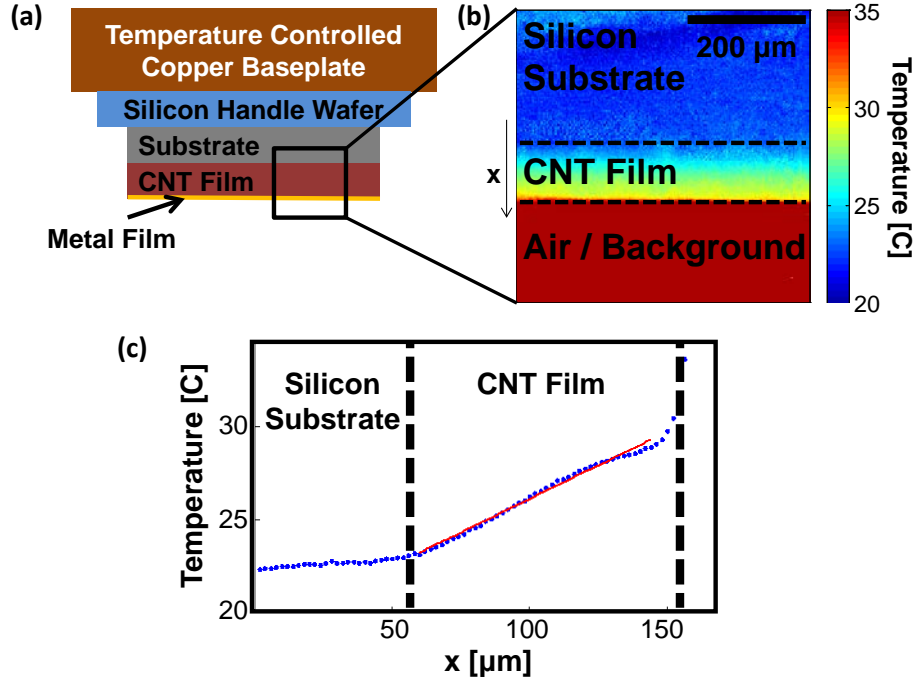


Figure 3.13: Infrared Microscopy Measurement Strategy. (a) Schematic showing metalized CNT film on the silicon growth substrate attached to a secondary silicon handle wafer mounted to a temperature controlled copper baseplate. Current passed through the metal film generates a heat flux through the CNT film. (b) Two-dimensional temperature map of the CNT film during test. The temperatures are averaged for each row of pixels in the image to yield the one-dimensional temperature profile shown in panel (c). The temperature gradient in the CNT film is calculated from a least-squares linear fit (red line) to the region of the temperature profile containing the CNT film.

The thermal conductivity of samples B and C are 2.9 ± 0.9 W/m/K and 2.7 ± 0.8 W/m/K, respectively. As shown in Figure 3.14, the thermal conductivity of the CNT films is relatively high given the low volume fraction (~ 0.5 vol. %) compared to other measured values for vertically aligned CNT arrays.

Reported values for the thermal conductivity of individual CNTs range from 300 W/m/K [57] to over 3000 W/m/K [56, 62, 64, 68-70]. Assuming the thermal conductivity of the vertically aligned CNT films scales with the volume fraction of CNTs, the solid line in Figure 3.14 shows the predicted thermal conductivity for an individual CNT thermal conductivity of $k_i = 3000$ W/m/K, while the dashed line

assumes $k_i = 30$ W/m/K. These measured thermal conductivities of samples B and C correspond to effective per nanotube thermal conductivities of at least 500 W/m/K. Defects within nanotubes, CNT-CNT contacts, and poor engagement of the CNT film by the metal film all impact the measured film thermal conductivity. Given the range of reported values for individual CNTs, the electroplating process likely did not significantly damage the nanotubes. If the individual nanotubes are ideal ($k_i = 3000$ W/m/K), the measured film conductivity indicates that roughly 10% of the nanotubes physically present in the CNT array contribute to the thermal conductivity.

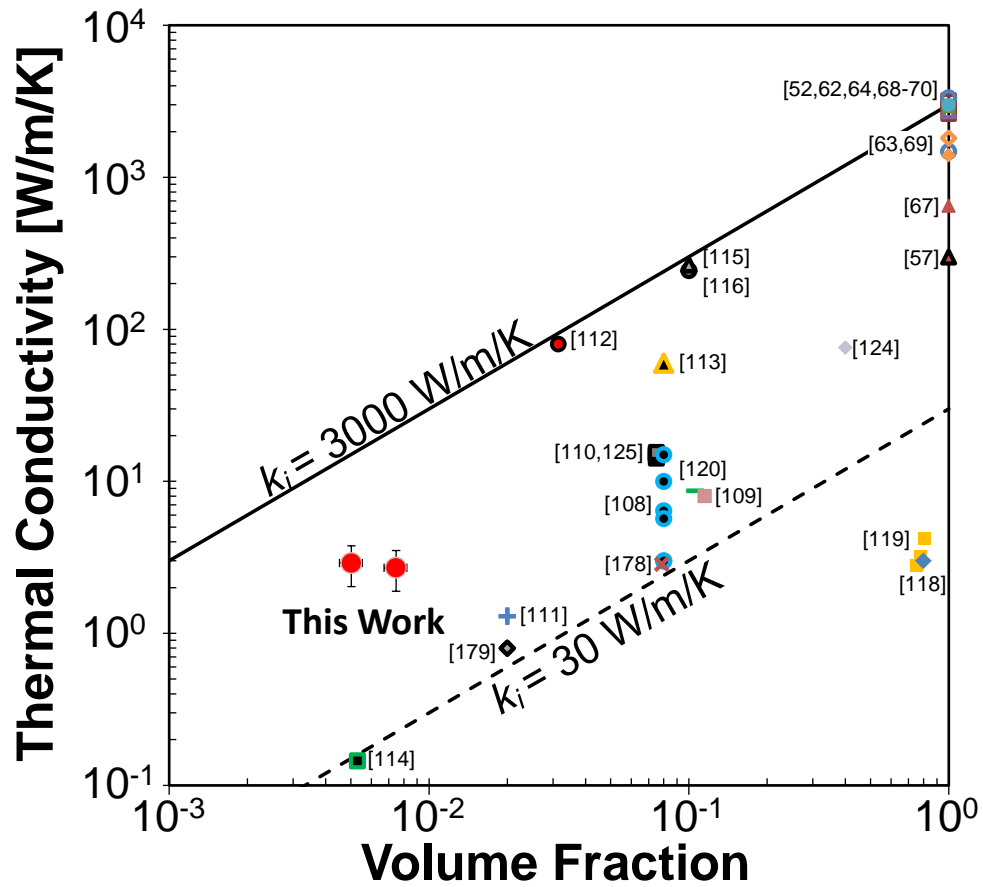


Figure 3.14: Thermal conductivity as a function of volume fraction for CNT films from this work (red circles) compared to values reported for measurements for vertically-aligned CNT arrays and individual nanotubes (volume fraction = 1). For individual nanotubes, the hollow and filled symbols indicate measurements of SWCNTs and MWCNTs, respectively. The solid line shows the ideal CNT film thermal conductivity estimated for a given volume fraction using an individual nanotube conductivity of 3,000 W/m/K, while the dashed line is the estimate using an individual nanotube conductivity of 30 W/m/K. References: [56, 57, 62-64, 67-70, 108-116, 118-120, 124, 125, 178, 179].

Since the copper film is very thin, the temperature of the metal layer cannot be resolved. Thus, the thermal boundary resistance between the metal and the CNT film cannot be determined. In future studies, the comparative cross-sectional IR method [122] will allow for more accurate determination of thermal conductivity and resolution of the boundary resistance between a reference layers and the CNT film.

3.4.4 Conclusions

A method for electrodepositing conformal thin films of copper on vertically aligned CNT arrays is demonstrated. The copper film is continuous and uniformly deposited across the thickness of the sample. The thermal conductivity of the CNT arrays after electrodeposition is measured to be nearly 3 W/m/K, which is comparatively high for such low density CNT films. If the copper film could be planarized, for instance with chemical mechanical planarization, this metallization layer could be used to provide a flat surface for bonding the CNT film to a heat sink. Future work to improve the thermal performance of these films can include metal deposition on higher density films and measurements of the thermal boundary resistance between the CNT and Cu film.

CHAPTER 4: THERMAL CONDUCTION IN NANOSTRUCTURED SILICON

4.1 Introduction

Nanostructured materials offer the possibility of thermal conductivity extremes. At one extreme, the thermal conductivities of carbon nanotubes and graphene can exceed those of metals [29]. On the other, the introduction of nanoscale boundaries such as those of nanowires [180] and grains [181] can significantly reduce the thermal conductivity. Reducing the thermal conductivity without significantly impacting the electrical conductivity and Seebeck coefficient improves the thermoelectric figure of merit. Thermal conduction in two types of nanostructured silicon is explored in this chapter. First, thermal conduction in periodically-porous silicon nanobridges is investigated through steady-state electrothermal measurements of the thermal conductivity, combined with modeling of the phonon transport including the impact of enhanced scattering and the possibility of phononic bandgaps. Second, thermal conduction in arrays of silicon nanowires with varying degrees of porosity and diameters is investigated through nanosecond transient thermoreflectance. The relative contribution to the reduction in thermal conductivity due phonons scattering external nanowire boundary scattering and phonons scattering within the porous regions of the nanowire is examined.

4.2 Phonon Conduction in Periodically Porous Silicon Nanobridges

4.2.1 Introduction

In thin silicon films, the thermal conductivity can be reduced through the introduction of nanoscale or microscale periodic pore structures sometimes referred to as “phononic crystals” [182-184]. This name makes an analogy with photonic crystal cavities, such as those in silicon [185] and other material systems [186], for which careful design of pore structures leads to a photonic bandgap associated with wavelengths comparable to the periodic length scales of the cavity. The demonstration of a phononic crystal influencing heat conduction is extremely challenging due to the

very small dominant phonon wavelengths (<5 nm at room temperature [187]), as well as the significant variation of the wavelengths of thermal phonons about the dominant value. Several groups are studying phononic crystals and are investigating modifications to the phonon dispersion relationship through the introduction of periodic pore structures [188-192]. These pores introduce a high density of interfaces that impede phonon conduction due to higher scattering rates. It is important to isolate these classical ballistic scattering effects, which are themselves challenging to precisely quantify, from any interpretation considering a modification of the phonon band structure.

While the thermal conductivity of two-dimensional periodically porous materials have been studied across a range of dimensions [26, 184], thermal transport in nanobridges with single row pores (henceforth called nanoladders), which have been used as photonic crystal cavities [23], merits more attention. These structures present an interesting opportunity to examine the impact of pore geometry and boundary scattering on thermal transport. In this manuscript, we discuss thermal transport in silicon nanoladders both from an experimental (Section 4.2.2) and analytical (Section 4.2.3) viewpoint. We use a steady-state four-probe electrothermal measurement technique to measure the thermal conductivity and a Callaway-Holland type model to further investigate effects of pore and boundary scattering.

4.2.2 Electrothermal Measurements

The thermal conductivity of the nanoladders is characterized using a four-probe, steady-state electrothermal measurement technique, similar to that of Liu and Asheghi [193, 194]. A metal film deposited on the silicon nanostructure serves as a heater and thermometer for the measurement of thermal properties. The fabrication process starts from a silicon-on-insulator wafer and requires only one lithography step to form both the nanoladder and the four electrical contact pads. The silicon device layer is thinned to ~ 200 nm using oxidation and wet etching prior to electron beam lithography. The nanoladder and probe pads are patterned using electron-beam lithography and the silicon is dry etched. Next, the SiO_2 layer beneath the silicon nanoladder device is then removed using a 6:1 solution of buffered oxide etchant for ~ 15 minutes to completely

suspend the nanoladder device. Since the oxide etchant is isotropic, in addition to the nanoladder itself, the paths to the current and voltage probe pads are also suspended. Finally, a 40 nm film of palladium is deposited on the suspended device using electron beam evaporation (Innotec ES26C). A scanning electron micrograph (SEM) of the device design is shown in Figure 4.1(a), and the suspended region is indicated by the dashed lines. A schematic of the device cross-section is shown in Figure 4.1(b). The palladium thickness H_m is calculated from the deposition rate and time. The pore diameter D , pitch S , beam width W , beam length L , and silicon thickness H are measured from SEMs.

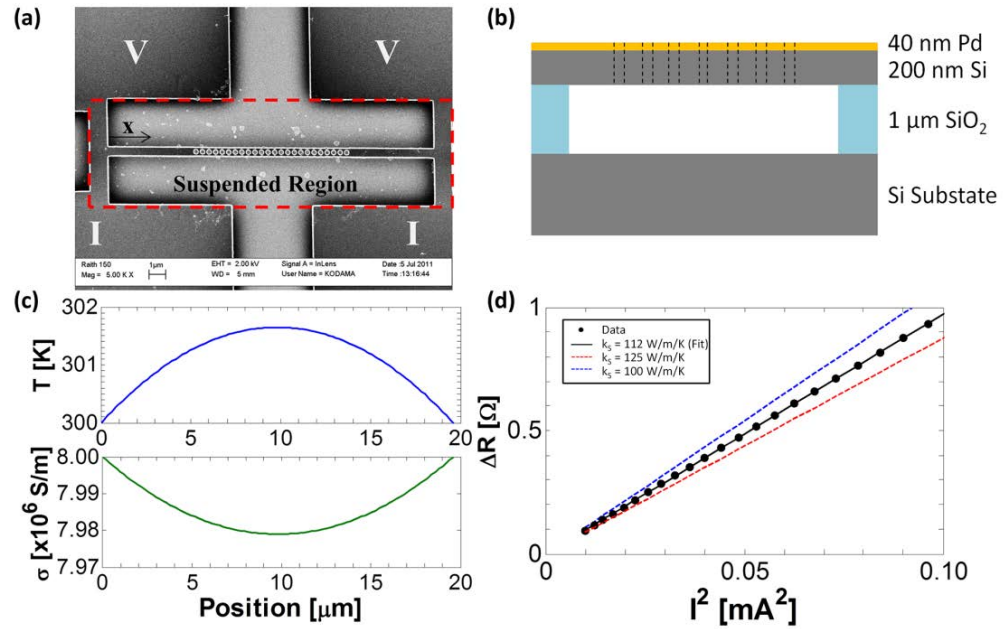


Figure 4.1: (a) SEM of a nanoladder measurement device. The nanoladder is connected to 4 electrical probe pads (two for applying current (marked I) and two for measuring voltage (marked V)). The dashed rectangle approximately marks the extent of the suspended region. (b) Cross-section of a nanoladder measurement device. The nanoladder is fabricated using electron beam lithography from a silicon-on-insulator wafer with 200 nm device layer and a 1 micron thick oxide layer. Forty nanometers of palladium is deposited on the devices and serves as both a heater and a thermometer in the system. (c) Calculated temperature profile along the nanobeam and corresponding electrical conductivity for the beam without holes at 300 mA applied current. For each current level, a numerical electrothermal model is used to calculate the temperature profile along the nanoladder and extract the increase in electrical resistance. (d) Comparison of measured and predicted increase in electrical resistance as a function of the square of the applied current for a silicon nanobeam without holes. The measured increase in resistance depends strongly on the thermal conductivity of the silicon layer as indicated by the best fit line with $k_S = 112 \text{ W m}^{-1} \text{ K}^{-1}$ (solid black line) compared to $k_S = 100 \text{ W m}^{-1} \text{ K}^{-1}$ (dashed blue line) and $k_S = 125 \text{ W m}^{-1} \text{ K}^{-1}$ (dashed red line).

Electrical current is passed through the palladium film and the temperature T increases due to Joule heating, while the electrical conductivity σ decreases proportional to the temperature. To illustrate the effect of Joule heating, Figure 4.1(c) shows the results of a numerical model of the temperature rise and associated electrical conductivity reduction for the non-porous nanobeam at the maximum applied current. In order to minimize heat loss to ambient, the experiments are carried out in vacuum (≤ 20 mTorr). COMSOL models of the nanobeam measurement structure have shown that the radiation losses are negligible for all applied current levels. The current is increased in steps and the electrical resistance R of the nanoladder is measured through the measured voltage V across the nanoladder. Figure 4.1(d) shows an example plot of the change in resistance as a function of the square of current.

The temperature coefficient of resistance α and the electrical resistivity ρ_o of the palladium film are determined for each nanoladder by measuring the resistance at low current, *i.e.* in the linear region of the I-V curves. The low current electrical resistance data at temperatures between 300 and 320 K is fit to $R(T) = R_o(1 + \alpha(T - T_o))$, where R_o is the electrical resistance at the reference temperature T_o . The temperature coefficient of resistance is $\alpha = 0.0017 \text{ K}^{-1}$. The electrical resistivity of the palladium layer on the nanoladders at 300 K is calculated from the electrical resistance and geometry. For the non-porous nanobeam and the nanoladders with 110 and 210 nm diameter pores, the electrical resistivity of the 40 nm thick palladium is $\rho_o = 28 \text{ } \mu\Omega\cdot\text{m}$ and for the nanoladder with 280 nm diameter pore, $\rho_o = 40 \text{ } \mu\Omega\cdot\text{m}$. Using Wiedemann-Franz law, the thermal conductivity of the palladium layer is estimated to be 26 and 18 $\text{W m}^{-1} \text{ K}^{-1}$ for the small and large diameter pore cases, respectively. The estimated thermal conductivity and electrical parameters are close to the value measured independently for solid palladium nanobeams of the same thickness and similar beam widths [195].

A combined electrical and thermal model is used to fit the data and extract the silicon nanoladder thermal conductivity. Heat transfer is assumed to be one-dimensional along the length of the nanoladder (x-direction), and thermal conduction in both the silicon and the palladium films are included. In the case of a uniform cross-section beam with constant thermal conductivity, the temperature profile along the beam can be computed analytically from [194]:

$$T(x) = T_o - \frac{1}{\alpha} \left(1 - \frac{\cos \gamma x}{\cos(\gamma L/2)} \right), \quad (4.1)$$

where $\gamma^2 = I^2 R_o \alpha / [WL(k_m H_m + k_s H)]$, and k_m and k_s are the thermal conductivities of the palladium and silicon layers, respectively. Using Eq. (4.1), the average electrical resistance of the beam as a function of applied current can be determined [194]:

$$R = R_o \left[\frac{2}{\gamma L} \tan \left(\frac{\gamma L}{2} \right) \right]. \quad (4.2)$$

Given the palladium thermal conductivity, the thermal conductivity of the silicon nanobeam can be extracted by fitting the data with this equation. However, this model is only valid for beams with uniform cross-sections (*i.e.* beams without holes).

For the nanoladders, we develop a numerical model to calculate the temperature profile and electrical resistance allowing for spatially varying cross-sectional area, different silicon thermal conductivities for the porous ($\sim 10 \mu\text{m}$ at center of beam) and the non-porous ($\sim 5 \mu\text{m}$ at each end of the beam) regions, and temperature-dependent palladium electrical resistivity. This model allows direct extraction of the solid silicon thermal conductivity, as opposed to an effective conductivity of the porous solid that would be obtained if the varying cross-section was neglected. Using the finite difference method, the temperature profile along the nanoladder and the increase in electrical resistance at each measured current level are calculated. The silicon nanoladder thermal conductivity is extracted by fitting the model to the resistance versus current data using a non-linear least-square fitting routine. Because the ends of the beams have no holes, the ends are assumed to have the thermal conductivity extracted for the beam without holes. Thus, only the silicon thermal conductivity in the center portion of the beam is varied in the fitting routine. Additional details of the model can be found in Section 4.2.2.1.

The thermal conductivity of one non-porous nanobeam and three nanoladders (570 nm wide, $18.8 \mu\text{m}$ long) with different pore diameters (110 nm, 210 nm, or 280 nm) are measured. Each nanoladder has 24 pores, spaced by 385 nm. The silicon nanobeam layer is 196 nm thick and the palladium film is 40 nm thick. All measured thermal conductivities are reduced from the thermal conductivity of bulk silicon. Specifically,

the extracted thermal conductivities of the nanoladders are 54, 3.7, and 3.4 $\text{W m}^{-1} \text{K}^{-1}$ for the nanoladders with 110 nm, 210 nm, and 280 nm diameter pores, respectively (see Figure 4.2). For comparison, the thermal conductivity data from Kim *et al.* [196] (in-plane) and Hopkins *et al.* [183] (out-of-plane) for two-dimensional phononic crystal films with pore spacings ranging from 500 nm to 800 nm are included in Figure 4.2.

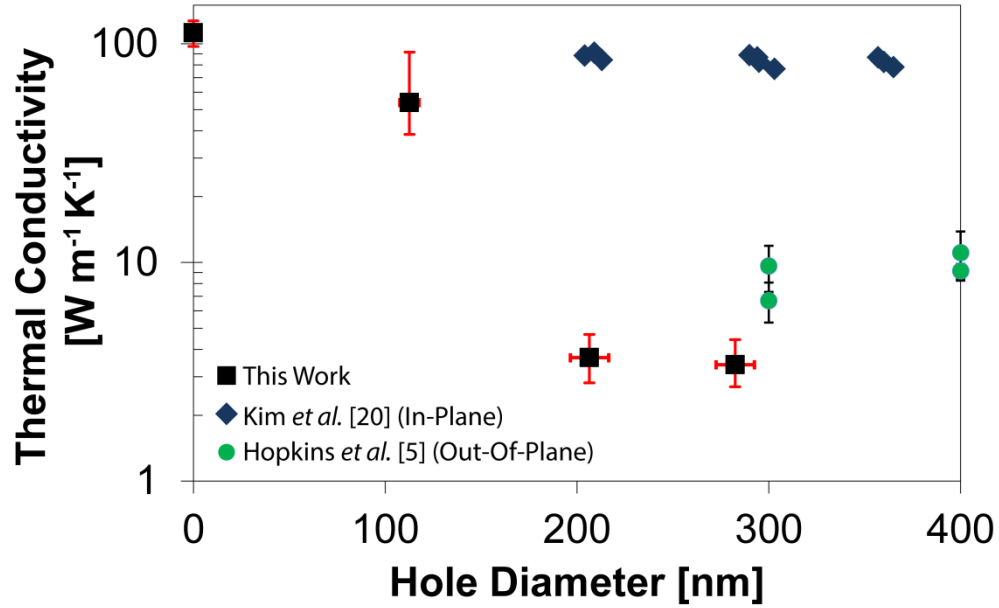


Figure 4.2: Silicon Nanoladder Thermal Conductivity. For the 200 nm thick nanoladders, the pores are spaced by 385. For the nanoladders with 110 nm diameter pores, the uncertainty in the thermal conductivity of the non-porous regions of the beam dominates the uncertainty in thermal conductivity of the porous region. For the larger diameter pore cases, the uncertainty is largely due to uncertainty in the measured value of pore diameter. For comparison, the thermal conductivity data for two-dimensional phononic crystals with pore spacings ranging from 500 nm to 800 nm fabricated from 500 nm thick Si films from Kim *et al.* [196] (diamonds, in-plane conductivity) and Hopkins *et al.* [183] (circles, out-of-plane conductivity).

Surface roughness plays an important role in the scattering of phonons in silicon nanostructures. Using molecular and lattice dynamics, He *et al.* [197] showed that the disorder at the surface of ~ 2 to 10 nm diameter pores in a periodically porous silicon film reduces the thermal conductivity compared to smooth pores. Hochbaum *et al.* [27] experimentally found that the thermal conductivity of rough silicon nanowires was significantly lower than that of smooth nanowires. As evident from SEMs (see Figure 4.1(a)), the surface roughness of these nanoladder devices is quite large and could contribute to the extremely low thermal conductivity. Additionally, past studies (*e.g.*

[198]) have shown that reactive ion etching can cause defective regions near the etched surfaces. These defective regions, in addition to the surface roughness, may contribute to the low experimentally observed thermal conductivity.

Uncertainty in the thermal conductivity of the non-porous region contributes into uncertainty in the thermal conductivity of the porous region. It has the largest effect for the smallest diameter pore case, where the thermal conductivity is closest to that of the non-porous nanobeam. If the thermal conductivity of the non-porous region is reduced by 10%, the thermal conductivity extracted for the porous region in the 100 nm diameter case increases from $54 \text{ W m}^{-1} \text{ K}^{-1}$ to $92 \text{ W m}^{-1} \text{ K}^{-1}$. In contrast, for the largest diameter holes (280 nm), a 10% reduction in the non-porous region thermal conductivity only increases the extracted thermal conductivity from $3.4 \text{ W m}^{-1} \text{ K}^{-1}$ to $3.7 \text{ W m}^{-1} \text{ K}^{-1}$. A fixed upper limit on the extracted value of the thermal conductivity of the nanoladders can be found by assuming the porous and non-porous regions have the same thermal conductivity. In this case, the extracted average nanoladder thermal conductivities are 100, 30, and $25 \text{ W m}^{-1} \text{ K}^{-1}$ for the nanoladders with 110 nm, 210 nm, and 280 nm diameter pores, respectively. In future work, the non-porous end region of the nanoladder should be eliminated for the geometry to reduce the uncertainty on the nanoladder measurements.

The geometry of the nanoladders was measured from SEMs and the surface roughness of the edges of the nanoladder and pore boundaries is evident. Edge effects in the SEM image lead to some uncertainty as to the exact location of the edge of the silicon. Additionally, some of the pores are not quite perfectly circular and there is slight variation between pore diameters within each nanoladder. The uncertainty in the pore diameter ($\pm 10 \text{ nm}$) dominates the uncertainty in thermal conductivity for the samples with 210 and 280 nm pores.

Since the extracted values of thermal conductivity for the large diameter pore nanoladder are quite low, fitting the data with a one-dimensional heat transfer model may actually underestimate the thermal conductivity. To estimate the impact of the one-dimensional heat transfer assumption, the magnitude of the extracted thermal conductivity is confirmed two additional models are considered. First, assuming that “rungs” of the nanoladder do not contribute to heat transfer, then the sides of the

nanoladder act as two parallel nanobeams of width $(W - D)/2$. In this case, the extracted thermal conductivities of the 210 nm and 280 nm pore diameter nanoladders roughly double to 6.4 and 7.3 W m⁻¹ K⁻¹, respectively. Second, a fully three-dimensional (3-D) COMSOL finite element model is used to fit the data for the 280 nm pore diameter nanoladder. Using this 3-D model, the thermal conductivity is 4.9 W m⁻¹ K⁻¹, a 45% increase of the value from the one-dimensional heat transfer assumption.

As previously mentioned, the cross-bars between the probe pads and the nanoladder are also suspended due to the isotropic etching of the SiO₂. However, they are designed with a larger cross-section than the nanobeam itself to ensure minimal thermal resistance between the end of the nanoladder and the substrate. From a simple thermal resistance point of view, the thermal resistance of the cross-bars is small in comparison to the total thermal resistance of the structure, so the temperature rise at the ends of the nanobeam is expected to be small. However, there is some heat generation in the current path portion of the cross-bar, so a COMSOL model including the cross-bars is developed to confirm the impact of this geometry. For the 280 nm pore diameter nanoladders, the extracted value of thermal conductivity does not change if the cross-beams are included in the simulation and the temperature rise at the ends of the nanobeam never exceed 1% of the maximum temperature rise in the nanoladder.

4.2.2.1 Details of the Numerical Electrothermal Model

Consider a steady-state energy balance around a differential element of the nanoladder of length Δx : $\dot{q}_{gen} + \dot{q}_{in} - \dot{q}_{out} = 0$. The rate of heat generation in the palladium film is $\dot{q}_{gen}(x, T) = \frac{I^2 \rho(T)}{A_{c,m}(x)}$, where $\rho(T) = \rho_o(1 + \alpha(T - T_o))$ and $A_{c,m}(x) = H_m W(x)$ is the cross-sectional area of the metal film. The rates of heat transfer in to (\dot{q}_{in}) and out of (\dot{q}_{out}) the differential element are due thermal conduction in both the silicon and metal layers. Assuming a spatially uniform palladium thermal conductivity, but spatially varying silicon conductivity, the energy balance becomes

$$\frac{I^2 \rho(T)}{A_{c,m}(x)} + k_m \frac{\partial}{\partial x} \left(A_{c,m}(x) \frac{dT}{dx} \right) + \frac{\partial}{\partial x} \left(A_{c,s}(x) k_s(x) \frac{dT}{dx} \right) = 0, \quad (4.3)$$

where $A_{c,s}$ is the cross-sectional area of the silicon beam. Further expansion of the differential terms, leads the differential equation:

$$\begin{aligned} & \frac{I^2 \rho_0 \alpha}{H_m W(x)} T + \left((H_m k_m + H k_s(x)) \frac{dW(x)}{dx} + HW(x) \frac{dk_s(x)}{dx} \right) \frac{dT}{dx} + (H_m k_m + H k_s(x)) W(x) \frac{d^2 T}{dx^2} \\ & = \frac{-I^2 (\rho_0 - \rho_0 \alpha T_0)}{H_m W(x)} \end{aligned} \quad (4.4)$$

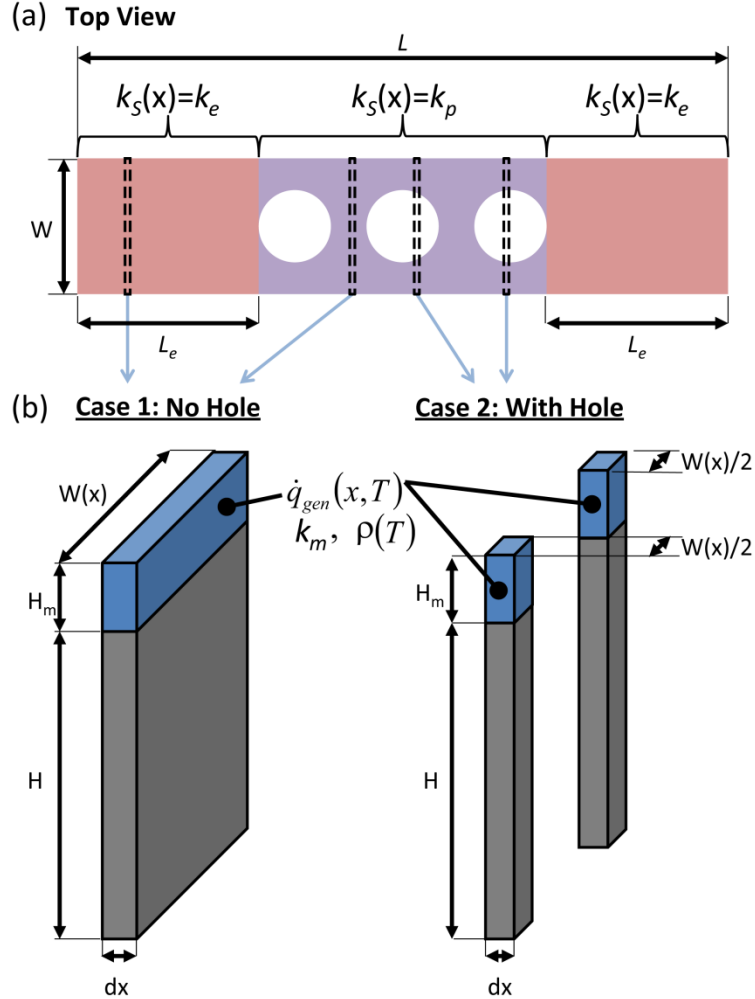


Figure 4.3: Schematic showing the geometry and key parameters for the numerical model of the temperature distribution in the nanobeams and nanoladders. (a) In the top view of the porous nanobeam, three regions of the beam are indicated including two non-porous regions at the end of the beam of length L_e where $k_s(x) = k_e$ and the porous region in the center of the beam with $k_s(x) = k_p$. Four example discretized elements are shown with dashed boxes and correspond to the discretized elements shown in panel (b). The leftmost two boxes correspond to case 1 (no hole) with the discretized element spanning the full width of the nanobeam. The rightmost two elements each contain a portion of a pore, corresponding to case 2, and consist of two sub-elements with widths less than the full beam width.

Figure 4.3 shows a schematic of the geometry considered in this model, highlighting key parameters. For the nanoladders in this work, the thermal conductivity of the silicon at the non-porous beam ends k_e is taken from the measured thermal conductivity of the non-porous nanobeam, and the thermal conductivity of the porous region k_p is assumed uniform:

$$k_s(x) = \begin{cases} k_e, & \text{where } x < L_e \\ k_p, & \text{where } L_e \leq x \leq L - L_e \\ k_e, & \text{where } x > L - L_e \end{cases} \quad (4.5)$$

where L_e is the length of the non-porous beam ends: $L_e = \frac{L - (N_h - 1)S - D}{2}$.

Using the finite difference method to expand the derivatives, we arrive at a matrix equation: $B = AT$, where the elements of B are

$$B_i = \frac{-I^2 \rho_o (1 - \alpha T_o)}{H_m W_i} \quad (4.6)$$

and the elements of A are

$$A_{i,i-1} = -\left(\frac{H_m k_m + H k_{s,i}}{4\Delta x^2} \right) (W_{i+1} - W_{i-1}) + \frac{H_m k_m + H k_{s,i}}{\Delta x^2} W_i - \frac{H W_i}{4\Delta x^2} (k_{s,i+1} - k_{s,i-1}), \quad (4.7)$$

$$A_{i,i} = \frac{I^2 \rho_o \alpha}{H_m W_i} - \frac{2(H_m k_m + H k_{s,i}) W_i}{\Delta x^2}, \text{ and} \quad (4.8)$$

$$A_{i,i+1} = \left(\frac{H_m k_m + H k_{s,i}}{4\Delta x^2} \right) (W_{i+1} - W_{i-1}) + \frac{H_m k_m + H k_{s,i}}{\Delta x^2} W_i + \frac{H W_i}{4\Delta x^2} (k_{s,i+1} - k_{s,i-1}). \quad (4.9)$$

Given the beam width and thermal conductivity as a function of position, the temperature profile along the nanoladder can be found by inverting the matrix A : $T = A^{-1}B$. The total electrical resistance of the beam is then found from summing the resistance of the differential elements of the beam $R = \sum_i \frac{\Delta x}{\rho(T_i) H_m W_i}$, accounting for the temperature dependent resistivity. Note that for regions with holes, the beam width W_i is the total width of the silicon. In other words, at positions corresponding to the center of a hole, the width of the element is $W_i = W - D$.

4.2.3 Modeling the Thermal Conductivity of Silicon Nanoladders

Thermal conductivity integral models have often been used to predict the thermal conductivity of silicon, including bulk silicon [199, 200], nanoscale thin films [193], and periodically porous silicon films [189]. These models consider the impact of the phonon dispersion relations, as well as mode- and wavevector-dependent phonon relaxation times, in order to compute the thermal conductivity. Specifically, the thermal conductivity can be computed from a Callaway-Holland type model [201]:

$$\begin{aligned}
 k &= \frac{1}{6\pi^2} \sum_j \int_q C_j(q, T) v_j(q)^2 \tau_j(q, T) \hbar^2 dq \\
 &= \frac{1}{6\pi^2} \sum_j \int_q \frac{\hbar^2 \omega_j(q)^2}{k_B T^2} \frac{\exp\left(\frac{\hbar \omega_j(q)}{k_B T}\right)}{\left(\exp\left(\frac{\hbar \omega_j(q)}{k_B T}\right) - 1\right)^2} v_j(q)^2 \tau_j(q, T) q^2 dq,
 \end{aligned} \tag{4.10}$$

where k_B is the Boltzmann constant, $\hbar = 2\pi\hbar$ is Planck's constant, and $C_j(q, T)$, $\omega_j(q)$, $v_j(q)$, and $\tau_j(q, T)$ are the specific heat, angular frequency, velocity, and relaxation time, respectively, of the phonons in branch j with wavevector q at temperature T . We first consider the dispersion relation and scattering times for bulk silicon (Section 4.2.3.1), and then include the impact of nanobeam boundary (Section 4.2.3.2) and pore boundary (Section 4.2.3.3) scattering. Finally, we estimate the impact modifying the phonon dispersion relation with a phonon bandgap (Section 4.2.3.4).

4.2.3.1 Model for Bulk Silicon

The three acoustic branches (one longitudinal and two transverse) are considered in calculating the thermal conductivity of silicon. While it is possible to generate the dispersion relations for silicon both through simulations [201, 202] and experiments [203], simplifying the dispersion relationship to an analytical form allows for rapid calculations of thermal conductivity. Debye models are often used in calculations but approximate the phonon velocity as constant [193]. Born-von Karman (sine-type) models more accurately account represent the band structure, and the required parameters from the model can be estimated from the speed of sound and atomic density of solids [204]. In this manuscript, we use a 4th order polynomial fit to the

longitudinal and transverse dispersion relationships in the $[1,0,0]$ direction calculated by Weber [202] using lattice dynamics as used previously by Hopkins *et al.* [183].

The relaxation time of phonons in bulk silicon, $\tau_{j,bulk}(q)$, is calculated with Matthiessen's Rule considering Umklapp, impurity, and boundary scattering:

$$\frac{1}{\tau_{j,bulk}(q)} = \frac{1}{\tau_{j,Umklapp}} + \frac{1}{\tau_{j,impurity}} + \frac{1}{\tau_{j,boundary}}, \quad (4.11)$$

where $\tau_{j,Umklapp}^{-1} = BT\omega_j(q)^2 \exp(-C/T)$, $\tau_{j,impurity}^{-1} = A\omega_j(q)^4$, and $\tau_{j,boundary}^{-1} = v_j(q)/E$, where A , B , C , and E are fitting parameters determined by fitting to data [183, 205]. In this manuscript, the values $A = 1.32 \times 10^{-45} \text{ s}^{-3}$, $B = 1.4 \times 10^{-19} \text{ s/K}$, $C = 152 \text{ K}$, and $E = 2.3 \times 10^{-3} \text{ m}$ are taken from Hopkins and colleagues [183, 205]. At low temperatures, if the boundary scattering term is neglected, the thermal conductivity continues to increase with decreasing temperature. Above 100 K, the predicted curves of bulk silicon conductivity are independent of the choice of the fitting parameter E . Figure 4.4 shows the thermal conductivity calculated by this model for bulk silicon.

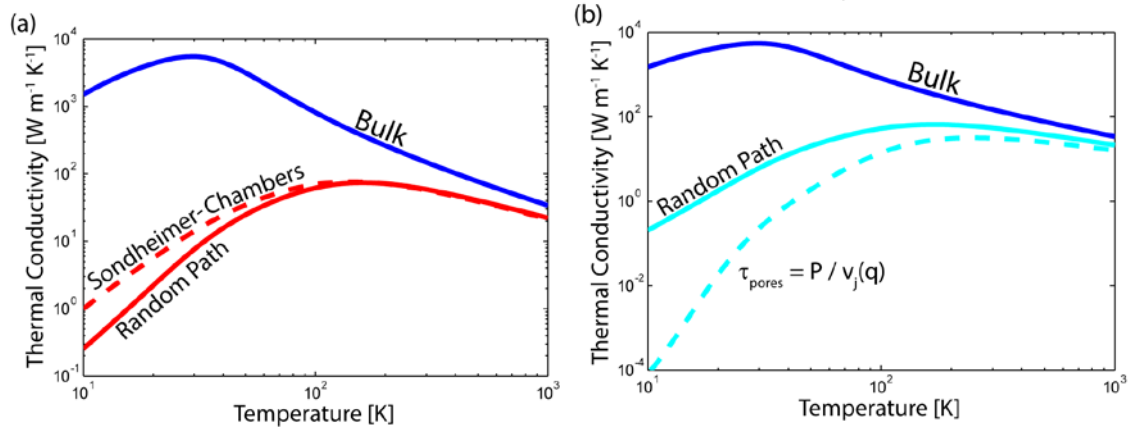


Figure 4.4: Calculated silicon thermal conductivity. (a) Comparison of bulk (blue line) and nanobeam (red lines) thermal conductivity. The estimated thermal conductivity for a rectangular nanobeam with a 550 nm x 200 nm cross-section calculated using the Sondheimer-Chambers [206, 207] approach is shown with the dashed red line and from the random phonon path calculation with the solid red line. (b) Comparison of bulk (blue line) and nanoladder (cyan lines) thermal conductivity. For 550 nm x 200 nm nanoladders with 200 nm pores spaced by 400 nm, the dashed cyan line shows the estimation from $\tau_{pores} = P/v_j(q)$, while the solid cyan line shows the estimation from the random phonon path calculation. In both cases, the reduction due to the outer nanobeam boundaries is calculated with the random phonon path calculation method.

4.2.3.2 Nanobeam Boundary Scattering

For nanostructured silicon, boundary scattering is important, even at room temperature, and modifications to the thermal conductivity integral are required. One method is to include boundary scattering in the relaxation time using Matthiessen's Rule. For cylindrical nanowires, the reduced mean free path considering the nanoscale geometry can be approximated as the nanowire diameter and the mean free path is related to the scattering rate by $\Lambda_j = v_j(q)\tau_j$. Similar geometric estimates of the reduced mean free path can be made for non-cylindrical nanobeams and thin films [102].

A second method for modeling the impact of boundary scattering takes into account the spectral dependence of boundary scattering and allows determination of the reduced relaxation time in more complex geometries. The bulk relaxation time is reduced by a conductivity reduction function F through

$$\tau_{j,r} = F\tau_{j,bulk} . \quad (4.12)$$

Expressions for the conductivity reduction function for thin wires and films have previously been derived using kinetic theory by Sondheimer [207] and Chambers [206]. Although originally derived considering electron transport, this approach is also applicable to phonon transport. Given a nanobeam with an arbitrary cross section U , a phonon originating at point O on that cross-section, traveling in the polar direction (θ, ϕ) , will scatter on the boundary at some point P after travelling a distance \overline{OP} . The conductivity reduction function for a given mean free path Λ can be calculated by integrating across the entire cross section and all polar directions [206, 207]:

$$F(U, \Lambda) = 1 - \frac{3}{4\pi U} \int_U \int_0^{2\pi} \int_0^\pi \sin \phi \cos^2 \phi \exp\left(-\overline{OP}/\Lambda\right) d\phi d\theta dU . \quad (4.13)$$

For a rectangular cross-section, a single set of reduction functions valid for a range of cross-sections can be found by non-dimensionalizing the nanobeam dimensions (the reduced thickness $\delta = H/\Lambda$ and the aspect ratio $AR = W/H$). Equation (4.13) is valid for purely diffuse scattering at the nanobeam boundary, but modifications are possible to account for specular reflections:

$$F(U, \Lambda, p) = (1-p)^2 \sum_{n=1}^{\infty} n p^{n-1} F\left(U, \Lambda/n\right), \quad (4.14)$$

where p is the fraction of phonons reflected specularly from the boundaries [206, 207]. The reduction function computed from Eqs. (4.13) and (4.14) for a rectangular nanobeam with an $AR = 2.75$ is shown in Figure 4.5(a) for purely diffuse scattering ($p=0$), as well as partially specular ($p=0.3$ and $p=0.9$). The thermal conductivity calculated with the purely diffusive reduction function for this nanobeam geometry is shown in Figure 4.4(a).

One drawback of the Sondheimer-Chambers [206, 207] method for calculating the reduction function is the time required to complete the numerical integration with sufficient accuracy, especially for non-circular nanobeams. Specifically, since many subdivisions of the cross-section and phonon propagation direction are required for accurate numerical integration, it takes several hours to generate the reduction function for a single aspect ratio. We develop a rapid method of calculating the reduction in thermal conductivity by considering the propagation of a large number of phonons starting from a random selection of points in the cross-section and with a randomized propagation direction. Similar to the boundary integral approach, we compute the distance phonons travel before scattering at a boundary. Instead of integrating across all possible start locations and propagation directions, we compute the average distance travelled by a large number of phonons with randomized start locations and propagation directions. This technique is similar to the method of McGaughey [208, 209], but fully incorporates the calculated boundary scattering reduction function with the thermal conductivity integral to estimate the reduction in thermal conductivity. More details of the method can be found in Section 4.2.3.4.

The conductivity reduction function computed for a nanobeam with aspect ratio of 2.75 is shown in Figure 4.5(a). Considering 8000 phonon paths for each step in 2500 discretization of δ , this calculation takes approximately one second to complete, significantly faster than the boundary integral method. In comparison to the Sondheimer-Chambers integral approach, the reduction function from the randomized path approach has a sharper roll-off with decreasing δ . The random path tracing method is purely geometrical with a sharp selection between the intrinsic mean free path and the boundary scattering distance for each phonon path considered. In contrast, the Sondheimer-Chambers integral includes additional terms stemming from kinetic theory.

After computing the reduction function for a range of reduced thicknesses, the thermal conductivity integral is computed and Figure 4.4(a) shows the thermal conductivity calculated using this expression.

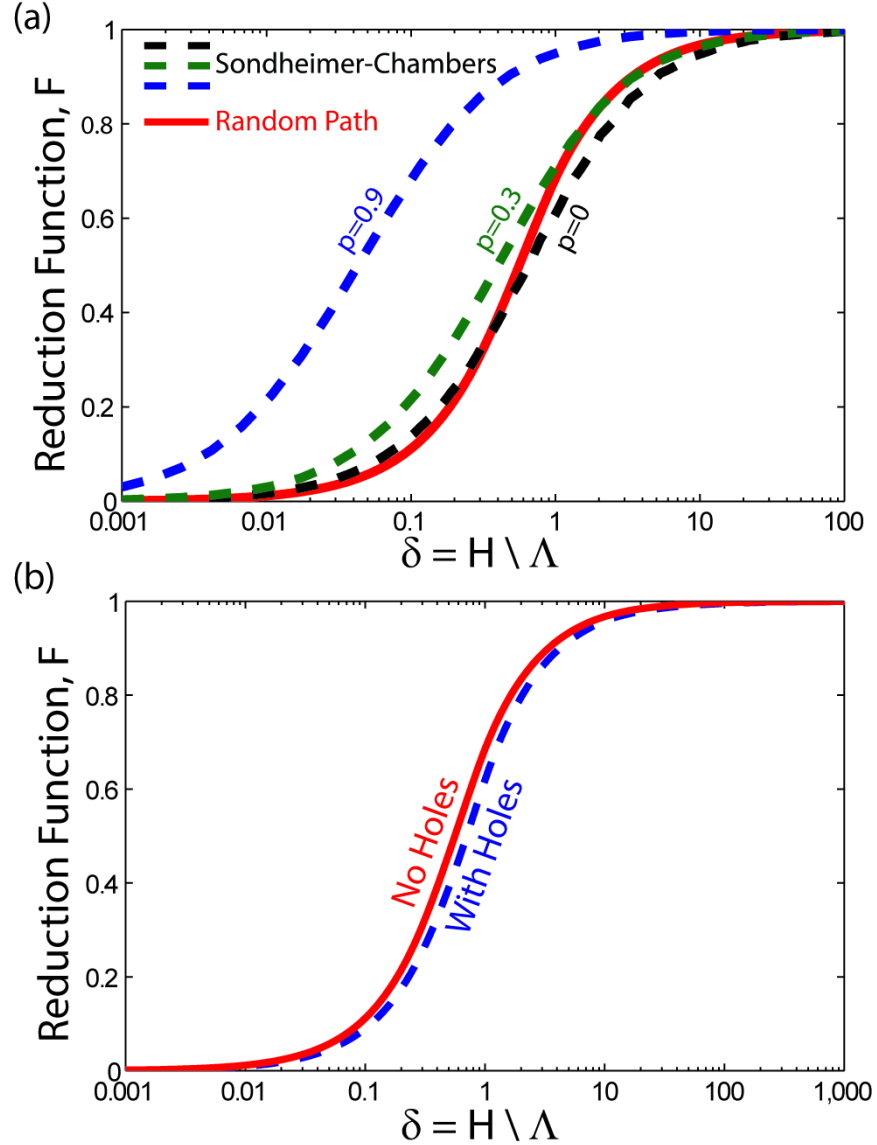


Figure 4.5: Conductivity Reduction Function. (a) Thermal conductivity reduction function for a rectangular nanobeams with $AR = W/H$ of 2.75 (no holes) following the technique of Sondheimer and Chambers [206, 207] using numerical integration (dashed lines) compared with that using the random phonon path calculation (solid line). For the Sondheimer-Chambers approach, three specularities are considered $p=0$ (fully diffuse), $p=0.3$, and $p=0.9$ (mostly specular). (b) Thermal conductivity reduction for nanoladders (blue dashed line) with $AR = 2.75$, $W/D = 2.75$, and $S/D = 2$ using the random phonon path calculation compared to that of a nanobeam without holes ($AR = 2.75$) (solid red line).

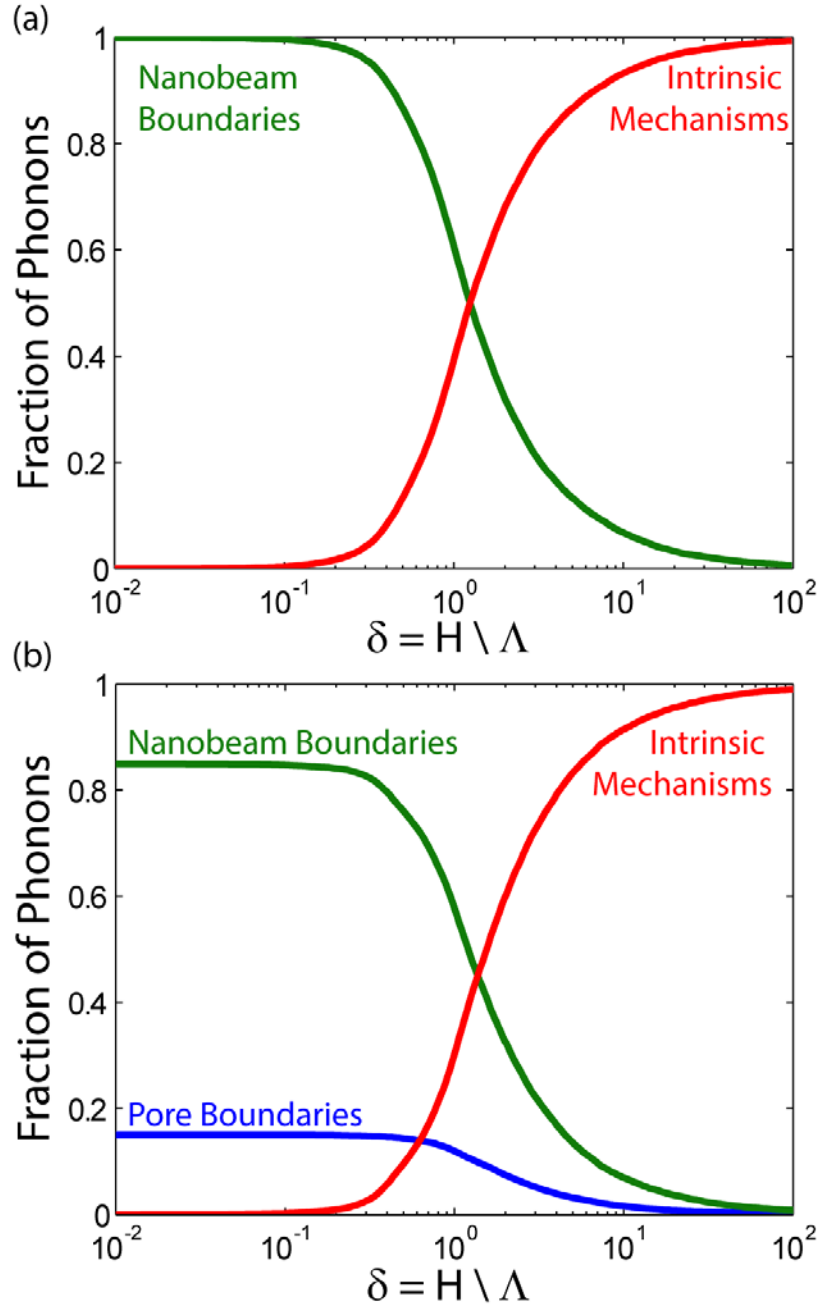


Figure 4.6: (a) Fraction of phonons scattered by boundaries (green) compared to intrinsic scattering mechanisms (red) for a nanobeam with $AR = 2.75$. (b) Fraction of phonons scattered by pores (blue) and external nanobeam boundaries (green) compared to intrinsic scattering mechanisms (red) for a nanoladder with $AR = 2.75$, $W/D = 2.75$, and $S/D = 2$.

Using the random path tracing method, the impact of boundary scattering is directly evident in the fraction of phonons scattering due to bulk processes compared to those scattering at boundaries. For a nanobeam with aspect ratio of 2.75, Figure 4.6(a) compares the effect of bulk scattering processes to boundary scattering for a range of

reduced thicknesses. As expected, when the reduced thickness is near unity, the boundary scattering and intrinsic scattering processes contribute approximately equally.

4.2.3.3 *Pore Boundary Scattering*

Beyond scattering at external nanobeam boundaries, in these nanoladder devices, the scattering at the pore boundaries play an important role in the thermal conductivity. As with the nanobeam boundaries this scattering can either be included using Matthiessen's Rule or through a conductivity reduction function. For microporous and nanoporous solids, Hopkins and colleagues [205] consider a boundary scattering term

$$\tau_{pores} = \frac{P}{v_j(q)}, \quad (4.15)$$

where P is the limiting dimension in the nanostructure, which for the two-dimensional periodically-porous structures is the distance between pore boundaries ($P=S-D$). For the case of the nanoladders, the limiting dimension is the smaller of the distance between the pores and the distance between the pore edge and the side wall of the nanobeam:

$$P = \min\left(S - D, \frac{W - D}{2}\right).$$

However, in this work, we separately account for the

nanobeam boundary scattering using the conductivity reduction function described in the previous section. Thus, to determine the impact of pore scattering alone when using Eq. (4.15), the limiting dimension considered is $P=S-D$. Figure 4.4(b) shows the reduced thermal conductivity using this approach for a nanoladder with cross-section of $550 \times 200 \text{ nm}^2$, $D = 200 \text{ nm}$, and $S = 400 \text{ nm}$.

The random mean free path approach lends itself particularly well for calculating the reduction in the mean free path due to pore scattering. A similar algorithm to that used for the nanobeam boundary scattering calculation above is used to compute the reduction function for pore scattering in the nanoladders. More details of the method can be found in Section 4.2.3.4. As illustrated by the conductivity reduction functions in Figure 4.5(b), the presence of these pores reduces the phonon scattering time only slightly more than the non-porous nanobeams of the same cross section.

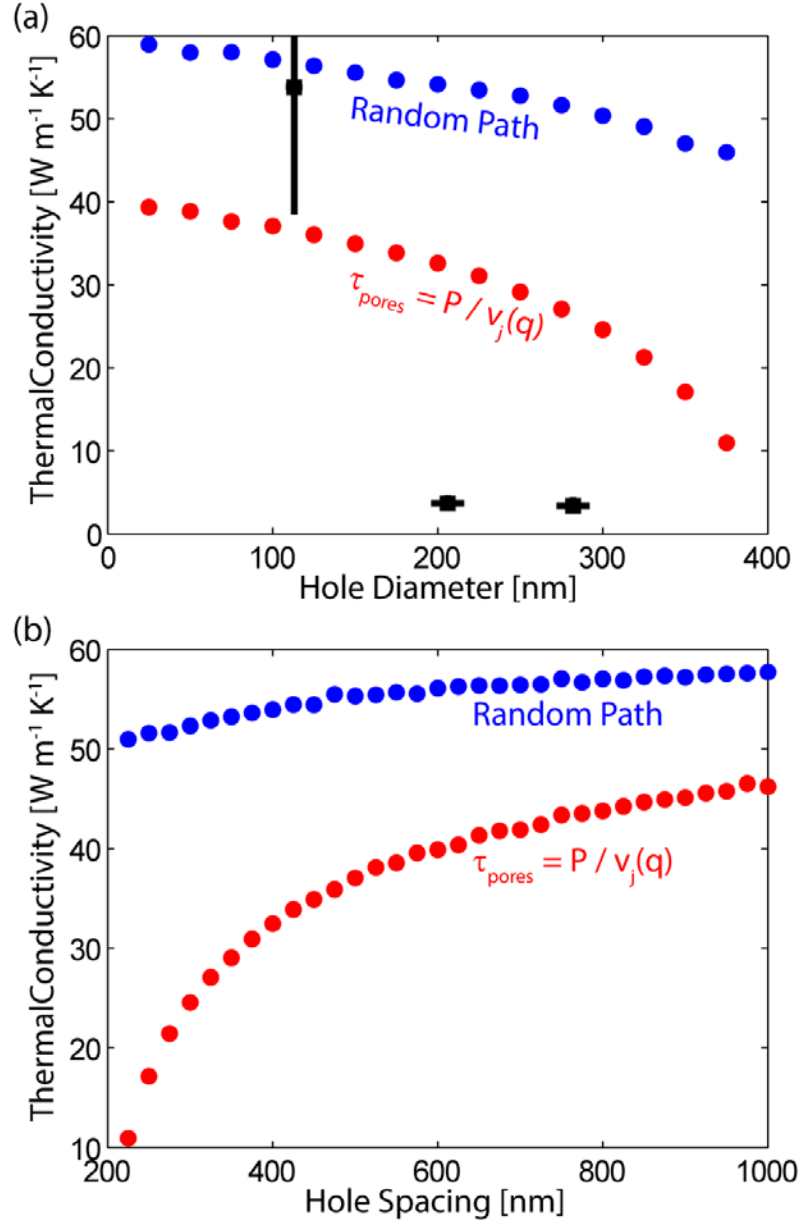


Figure 4.7: Impact of hole (a) diameter and (b) spacing on the thermal conductivity of 550 nm x 200 nm silicon nanoladders. In panel (a) the pore spacing is fixed at 400 nm and the experimental results from this work are shown with black squares. In panel (b) the pore diameter is fixed at 200 nm. Calculations using the random pore scattering model are shown in blue, while those using the model $\tau_{\text{pores}} = P / v_j(q)$ are shown in red.

Many phonons never encounter a pore, instead scattering at external nanobeam boundaries or due to bulk processes. The relative impact of scattering processes is evident in Figure 4.6(b) from fraction of phonons scattering due to bulk processes compared to those scattering at nanobeam boundaries and at hole boundaries. At most only ~15% of the phonons scatter on the pore boundaries for this geometry ($AR = 2.75$,

$W/D = 2.75$, and $S/D = 2$). Thus, the thermal conductivity predicted with this method is larger than predicted by using Eq. (4.15), as illustrated in Figure 4.4(b). The scattering term $\tau_{pores} = P/v_j(q)$ limits the mean free path of every phonon, while the random path calculation considers that some phonons do not encounter pores. However, phonon near the pores may still be impacted by the pore boundary, so the two methods could be considered bounds to the thermal conductivity reduction due to pore scattering. Figure 4.7 shows the predicted thermal conductivity using each method for a range of hole diameter and spacing for nanoladders with a cross-section of 550 nm x 200 nm.

4.2.3.4 *Details of the Random Path Tracing Phonon Scattering Model*

For a nanobeam with an arbitrary cross-section, we take the following approach to generate a reduction function analogous to that of the Sondheimer-Chambers [206, 207] approach:

- (1) Consider a single intrinsic mean free path Λ_0 (corresponding to a reduced thickness $\delta = H/\Lambda_0$).
- (2) Select a random phonon start position (x,y) and propagation direction (θ, ϕ) .
- (3) Calculate distance phonon would travel before scattering at boundary (\overline{OP}).
- (4) Calculate the mean free path of the i^{th} phonon, Λ_i , by selecting the smaller of the distance \overline{OP} and the intrinsic mean free path Λ_0 .
- (5) Repeat steps 2-4 for many start positions and propagation direction.
- (6) Compute the reduction function $F(\delta, AR) = \frac{1}{N_p \Lambda_0} \sum_{i=1}^{N_p} \Lambda_i$, where N_p is the number of paths considered in step 5.
- (7) Repeat steps 1-6 to generate the reduction function for a range of mean free paths (reduced thicknesses).

To include the effect of pore scattering, a few modifications to the algorithm for the nanobeam are required. Specifically, phonons must be allowed to start anywhere within an entire period of the pore structure and can either scatter due to bulk processes, pore boundary scattering, or scattering at the boundary of the nanobeam. Many pores must

be considered because some of the phonons may not impact the first pore but one further down the nanoladder. The new algorithm to compute the reduction function is explained below:

- (1) Consider a single intrinsic mean free path Λ_0 (corresponding to a reduced thickness $\delta = H / \Lambda_0$).
- (2) Select a random phonon start position (x,y,z) and propagation direction (θ, ϕ) .
The start position is selected so that no phonon starts in a hole. A full unit cell of the pore geometry is considered instead of a single cross section.
- (3) Calculate distance phonon would travel before scattering at an external nanobeam boundary (\overline{OP}).
- (4) Calculate distance phonon would travel before scattering at a pore boundary (\overline{OR}). The propagation path of many phonons will never intersect a pore boundary in which case $\overline{OR} = \infty$.
- (5) Calculate the mean free path of the i^{th} phonon, Λ_i , by selecting the smaller of the distances: \overline{OP} , \overline{OR} , and Λ_0 .
- (6) Repeat steps 2-5 for many start positions and propagation direction.
- (7) Compute the average of the mean free paths for this value of intrinsic mean free path, and the reduction function $F(\delta, AR, S, D) = \frac{1}{N_p \Lambda_0} \sum_{i=1}^{N_p} \Lambda_i$, where N_p is the number of paths considered in step 6.
- (8) Repeat steps 1-7 to generate the reduction function for a range of mean free paths (reduced thicknesses).

4.2.3.5 Estimate of Impact of Modified Phonon Dispersion Relationships

Several studies have shown modifications to the phonon band structure, specifically the opening of phononic bandgaps, in phononic crystals consisting of a two-dimensional array of air holes in a thin film [210, 211]. Recent experimental and theoretical work has suggested that these coherent phonon effects reduce the thermal conductivity [26, 183, 189, 201, 212]. For ~20 nm thick silicon membranes with 11 and 16 nm diameter

air holes spaced by 34 nm, Yu *et al.* [26] measured a significant reduction in the thermal conductivity, which they attributed to coherent phonon effects. For a 500 nm thick silicon membranes with periodic arrays of several hundred nanometer diameter air holes, Hopkins *et al.* [183] found that to match their model of thermal conductivity to the measured values, the phonon density of states had to be altered (in addition to including scattering effects). The nanoladder design studied in this manuscript is essentially a one-dimensional analog to the two-dimensional phononic crystal slabs.

The frequency of phonons impacted by a periodic pore structure is approximately [189]:

$$f_{ph} = \frac{\pi v_{avg}}{S}, \quad (4.16)$$

where v_{avg} is the average speed of sound in silicon. To estimate the thermal conductivity, a phonon transmission function $\Gamma(\omega(q))$ can be included in the thermal conductivity integral:

$$k = \frac{1}{6\pi^2} \sum_j \int_q \Gamma(\omega(q)) C_j(q, T) v_j(q)^2 \tau_j(q, T) q^2 dq. \quad (4.17)$$

Depending on the exact geometry and materials properties, a select band of phonon frequencies will be blocked by the structure (*e.g.* [212, 213]). However, to estimate the maximum possible impact of the porous structures, this work considers the extreme case that the phononic structure blocks all phonons up to f_{ph} such that the transmission function is

$$\Gamma(\omega(q)) = \begin{cases} 0 & \omega(q) \leq 2\pi f_{ph} \\ 1 & \omega(q) > 2\pi f_{ph} \end{cases}. \quad (4.18)$$

For 550 nm x 200 nm nanoladders with 200 nm diameter holes spaced by 400 nm, $f_{ph} = 51.4$ GHz, and the reduction in thermal conductivity due to any coherent phonon effects is small. For this geometry, including the effect of coherent phonons leads to only very small additional reduction in thermal conductivity compared to neglecting phononic effects (see Figure 4.8(a)). The impact of coherent effects is stronger at very low temperatures (below 50 K), but is still less than 0.02% of the nanoladder thermal conductivity. As shown in Figure 4.8(b), coherent phonon effects become more important if the nanoladder structure is fabricated an order of magnitude smaller in each

dimension (55 nm x 20 nm, $D = 20$ nm, $S = 40$ nm), such that the impacted frequencies shift up to 514 GHz.

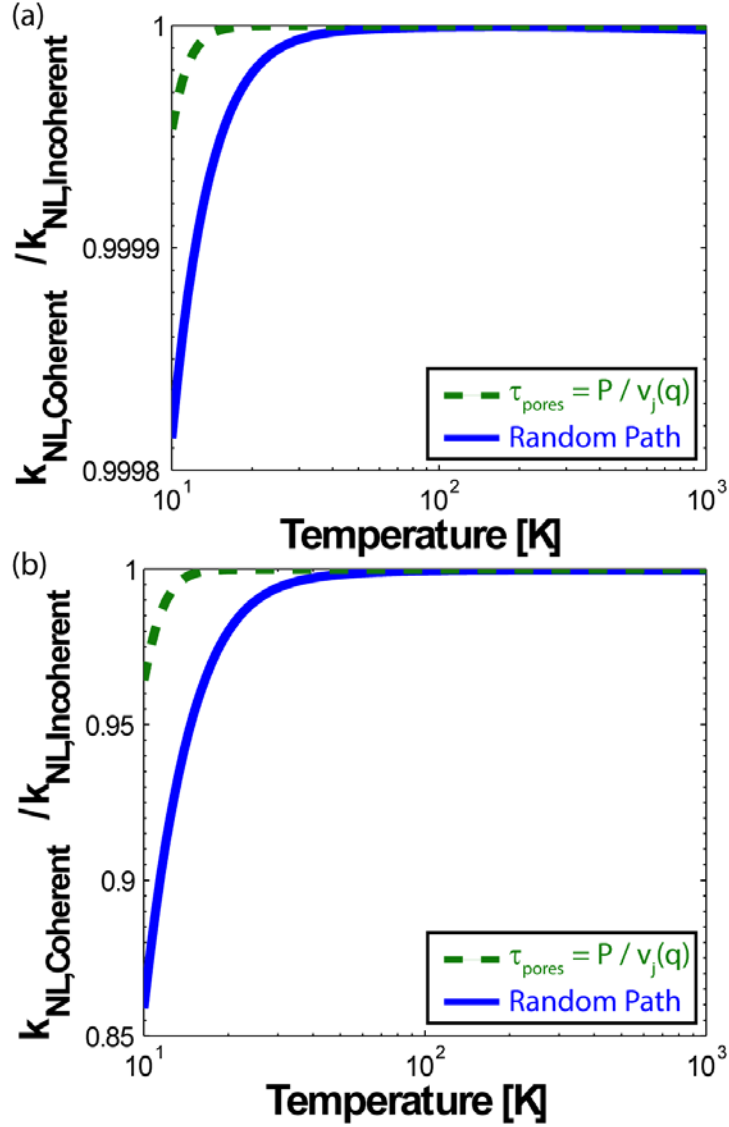


Figure 4.8: Ratio of the nanoladder [(a) 550 nm x 200 nm, $D = 200$ nm, $S = 400$ nm; (b) 55 nm x 20 nm, $D = 20$ nm, $S = 40$ nm] thermal conductivity considering coherent phonon effects to that neglecting coherent phonon effects. Calculations using the random pore scattering model are shown with solid lines, while those using the model $\tau_{pores} = P / v_j(q)$ are shown with dashed lines.

4.2.4 Concluding Remarks

The thermal conductivities of three porous nanoladders are measured using a steady-state electrothermal technique. The thermal conductivities are significantly

reduced from bulk silicon and from the nonporous nanobeam, especially for the large diameter pores. A Callaway-Holland model is used to compute reduction in thermal conductivity. The boundary scattering reduction function is computed from both a Sondheimer-Chambers approach and by tracing the paths of a large number of phonons within the nanostructure. The impact of scattering at the pore boundaries is also estimated using a random path tracing method and from the minimum pore boundary separation distance. Coherent phonon effects are considered by estimating the phonon frequencies impacted by the periodic pore structure. For these nanoladders with pores spaced by ~ 400 nm, the impact of coherent effects on the thermal conductivity is negligible ($< 0.02\%$ at $T < 50\text{K}$). However, if the dimensions are reduced even by a factor of 10, coherent phonon effects may be evident, especially at low temperatures (< 100 K). The results of the thermal conductivity model agree with the predicted thermal conductivity for the nanoladder with the smallest diameter pores, however, additional measurements and modeling work is needed to understand the reduction in thermal conductivity for the larger diameter pore structures. Surface roughness and non-uniformities in the pore geometry may contribute to the significantly reduced thermal conductivity for the nanoladders with large diameter pores.

4.3 Effects of Porosity on the Thermal Conductivity of Silicon Nanowires in Aligned Silicon Nanowire–Parylene Composites

Silicon with a high density of nanoscale features such as interfaces, porosity, and impurities can have thermal conductivities (κ) up to three orders of magnitude lower than that of the bulk Si through enhanced phonon scattering [25, 190, 197, 214-227]. For example, the thermal conductivities of nanoporous bulk Si generally decrease with increasing porosity and decreasing pore size [190, 197, 214-220] and with high porosity approach the amorphous limit (0.2-0.5 W/m/K) [214-216]. Similarly, silicon nanowires (SiNWs) with diameters significantly smaller than the bulk phonon mean free path (~ 100 to 300 nm at 300 K) were reported to have thermal conductivity values as low as 0.76 W/m/K due to strong phonon scattering at the SiNW boundary [221, 222]. Introducing surface roughness to the SiNWs leads to additional phonon scattering at length scales even smaller than the NW diameter [25, 223-226]. However, there is little investigation on the combined effects of external dimensions and internal porosity on the thermal conductivity values of SiNWs. In this work, we report the effects of internal porosity on the thermal conductivity of SiNWs of two different diameters that allow phonon propagation to span the range from ballistic to diffusive thermal transport ($d_{avg} \sim 350$ nm and 130 nm) by measuring the thermal conductivity of vertically-aligned SiNW arrays using nanosecond transient thermoreflectance (TTR). As opposed to measurements of individual SiNWs, measurements of arrays of SiNWs offer the advantage of averaging out the inherent variations that inevitably occur between individual SiNWs.

4.3.1 Fabrication

Vertically-aligned SiNW arrays are fabricated using a four-step preparation process illustrated in Figure 4.9. Two sets of vertically-aligned SiNW arrays with different diameters are fabricated (Figure 4.9 a, e) using top-down etching techniques to achieve a range of porosities (Table 4.1).

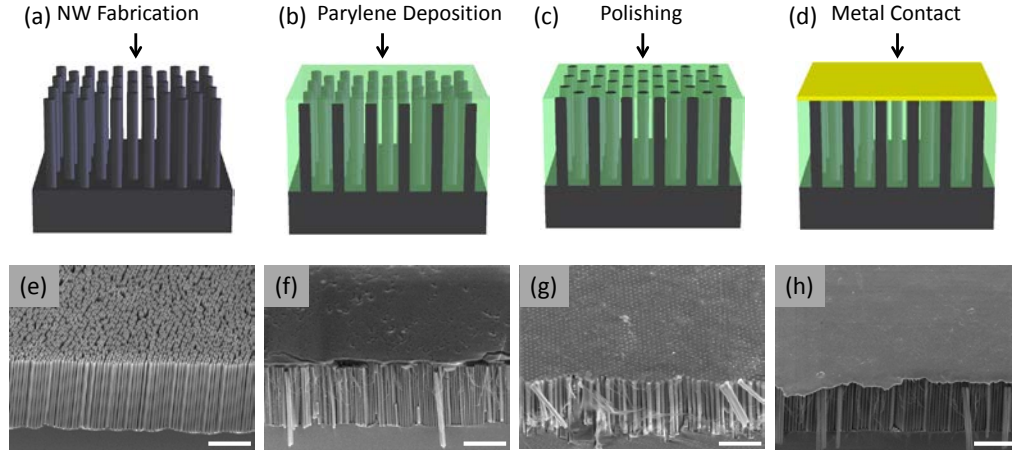


Figure 4.9: Fabrication of the vertical SiNW arrays for the nanosecond thermoreflectance measurements. (a,e) SiNW arrays are formed using the top-down etching; (b,f) Parylene is conformally deposited in between NWs and acts as a mechanical scaffold for the top metal transducer layer; (c,g) the SiNW tips are exposed by chemical mechanical polishing to ensure good thermal contact between the SiNWs and the metal film; and (d,h) a metal film is deposited over the SiNW array. The scale bars on the SEM images are 5 μm .

For the first set, the diameter ($d_{avg} \sim 300\text{-}350$ nm) and density of the SiNWs are controlled by using nanosphere lithography.[228] Specifically, a monolayer of SiO_2 spheres is deposited by the Langmuir-Blodgett method onto Si wafers (p-type, (100)) and used as a mask for the subsequent etching steps. The internal porosity of SiNWs is varied from nonporous to highly porous by changing the etching methods and conditions [229-231]. Nonporous SiNWs are formed by deep reactive ion etching (DRIE) and the resulting SiNWs have slightly smaller diameters ($d_{avg} \sim 300$ nm) than the spheres used as the etch mask [232]. Porous SiNW arrays are fabricated using metal assisted chemical etching (MACE) in a solution of 4.8 M HF and 0.3 M H_2O_2 , and the porosity is controlled by varying the metal catalyst and wafer doping concentrations [229-231, 233-235]. For low porosity nanowires, the catalyst layer consists of a 15 nm Ag film covered by 5 nm Au, while for the moderate to highly porous nanowires, a 50 nm Ag film is used as the catalyst and the initial wafer doping concentration is varied. The second set of SiNWs, with generally smaller diameters, is fabricated by using a two-step MACE process with silver salts [229, 230, 233, 236, 237]. First, the catalyst Ag film is deposited using a solution of 0.005 M AgNO_3 and 4.8 M HF for 1 minute. Then SiNWs are formed by etching in a solution with 4.8 M HF with various

concentrations of H_2O_2 (0.15 M, 0.30 M, 0.60 M and 1.20 M) to vary the SiNW porosity [229, 230, 233, 236, 237]. The resulting SiNWs have an average diameter of 130 nm, but there is significant diameter variation within the SiNW array ($d \sim 20\text{--}300$ nm). For all the samples, the SiNW length is approximately 10 μm .

Table 4.1: Summary of SiNW array diameter and porosity control.

	Diameter Control	Porosity Control
Set 1:	<i>Nanosphere Lithography</i> $d_{\text{avg}} \sim 300$ to 350 nm	<i>Etching Method and Doping Concentration</i> Non-Porous: DRIE Low Porosity: Ag/Au MACE Moderate Porosity: Ag MACE, Lightly Doped High Porosity: Ag MACE, Heavily Doped
Set 2:	<i>Silver Salts</i> $d_{\text{avg}} \sim 130$ nm	<i>MACE Etchant Solution</i> Low Porosity: 0.15 M H_2O_2 High Porosity: 1.2 M H_2O_2

Following the formation of the SiNW arrays, the gaps between SiNWs are completely filled with parylene N (poly-para-xylylene) (Figure 4.9 b, f), which has a thermal conductivity significantly lower than the SiNWs ($\kappa_{\text{parylene}} = 0.125$ W/m/K) and a high melting temperature ($T_m \sim 410$ °C). The SiNW tips are subsequently exposed via chemical mechanical polishing (CMP) to remove the parylene covering the SiNWs (Figure 4.9 c, g) allowing the SiNWs to form good thermal contact with the top metal film. Finally, a 15 nm Cr layer (for adhesion) and a 500 nm Cu layer are deposited by electron-beam evaporation on top of the SiNWs tips to form a flat, reflective transducer layer for the thermorefectance measurements (Figure 4.9 d, h).

4.3.2 Nanosecond Transient Thermorefectance (TTR)

The thermal conductivity of the vertical SiNW arrays is measured by nanosecond TTR, the details of which can be found in Panzer *et al* [238]. Briefly, the metal transducer layer that is deposited on the parylene-filled SiNW array is heated by a 3 mm diameter, 532 nm wavelength, 6 ns pulse from a Nd:YAG laser at a frequency of 10 Hz. The reflected intensity of the probe laser ($d \sim 20$ μm , 10 mW, 658 nm, continuous wave) is directly correlated to the temperature of the metal layer that is affected by the thermal conductivity of the SiNW/parylene composite. The thermal conductivity of the

SiNW/parylene composite and its interface thermal resistance at the top metal layer are extracted using a two parameter fit of the measured temperature decay trace (normalized by the maximum temperature) to the solution of a one-dimensional heat diffusion equation for a multilayer stack with surface heating. The volumetric heat capacity of the film ($C_{v,composite}$) is assumed to be the volumetric average of the heat capacity of parylene ($C_{v,parylene}$) and bulk silicon ($C_{v,Si}$): $C_{v,composite} = VF \cdot C_{v,Si} + (1 - VF) \cdot C_{v,parylene}$, where VF is the volume fraction of SiNWs within the composite (measured by SEM images). The average thermal conductivity of an individual SiNW within the array is calculated from the extracted film thermal conductivity ($\kappa_{composite}$) using the parallel resistor version of an effective medium model: $\kappa_{NW} = [\kappa_{composite} - (1 - VF)\kappa_{parylene}]/VF$, where κ_{NW} and $\kappa_{parylene}$ are the thermal conductivities of the SiNWs and parylene, respectively. These nanowire arrays are nearly ideal for the using a parallel resistor model (*e.g.* the nanotubes are straight, do not contact each other, the parylene fills the space between the nanowires without voids, and polishing ensures that nearly every nanowire is contacted by the metal transducer layer, as illustrated in the SEMs and sketches in Figure 4.9). Thus, the parallel resistor model is representative of the thermal transport pathways in this system allowing extraction of the individual nanowire thermal conductivity from the measurement of film properties. For the nanowire arrays with smaller nanowire diameters, the variation in nanowire diameter corresponds to variations in individual nanowire thermal conductivity and thus using this method to convert from film conductivity to individual nanowire thermal conductivity yields only an average value of thermal conductivity.

4.3.3 Results & Discussion

The thermal conductivity for the SiNWs with large diameters ($d_{avg} \sim 300\text{-}350$ nm) demonstrates a clear decrease with increasing porosity (Figure 4.10). The thermal conductivity of nonporous SiNWs, though with rough surfaces, is 142 ± 13 W/m/K, very close to that of bulk Si ($\kappa \sim 150$ W/m/K). Scallop, due to the DRIE etching process, leads to oscillations in the nanowire diameter from 290 to 320 nm along the length of the nanowire. Side-view SEMs show that the nanowire diameter is consistently closer to the smaller diameter top surface of the nanowire array where the SEMs used to estimate

SiNW fill fraction are taken (example top-view SEMs are included as insets in Figure 4.10). Thus, it is likely that the volume fraction is higher than estimated from the top-view SEMs, and correspondingly the thermal conductivity falls near the lower end of the uncertainty range. However, for uniformity in comparing results, the fill fraction from the top-view SEMs is reported and used in the analysis of thermal conductivity. Still, this high value of thermal conductivity suggests that for large diameter SiNWs, surface roughness at this depth and periodicity, does not cause effective phonon-external boundary scattering and therefore has little effect on the thermal conductivity. On the other hand, the internal porosity of SiNWs drastically reduces the thermal conductivity from 142 W/m/K for the nonporous SiNWs to 98 W/m/K (Au/Ag-MACE) and 51 W/m/K (Ag-MACE) for the increasingly porous SiNWs.

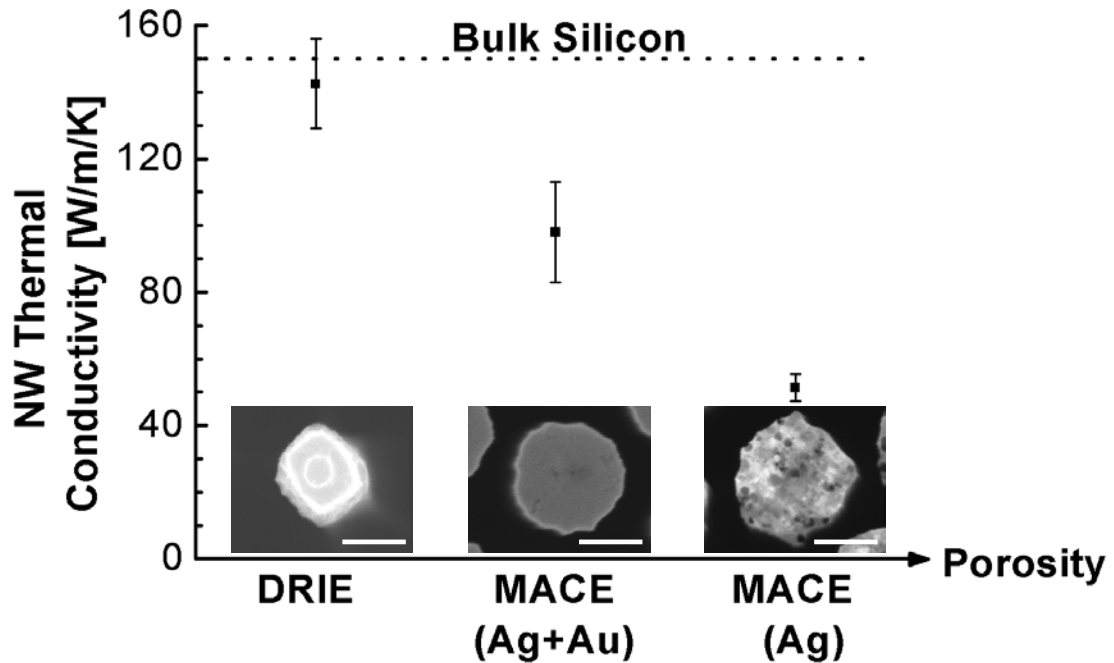


Figure 4.10: Thermal conductivity of (~ 350 nm) large diameter SiNWs (10^{14} cm $^{-3}$ p-type doping) with three levels of porosity, corresponding to different etching conditions. The thermal conductivity decreases significantly with increasing porosity. The inset images show the top view of the SiNWs and the scale bars are 200 nm.

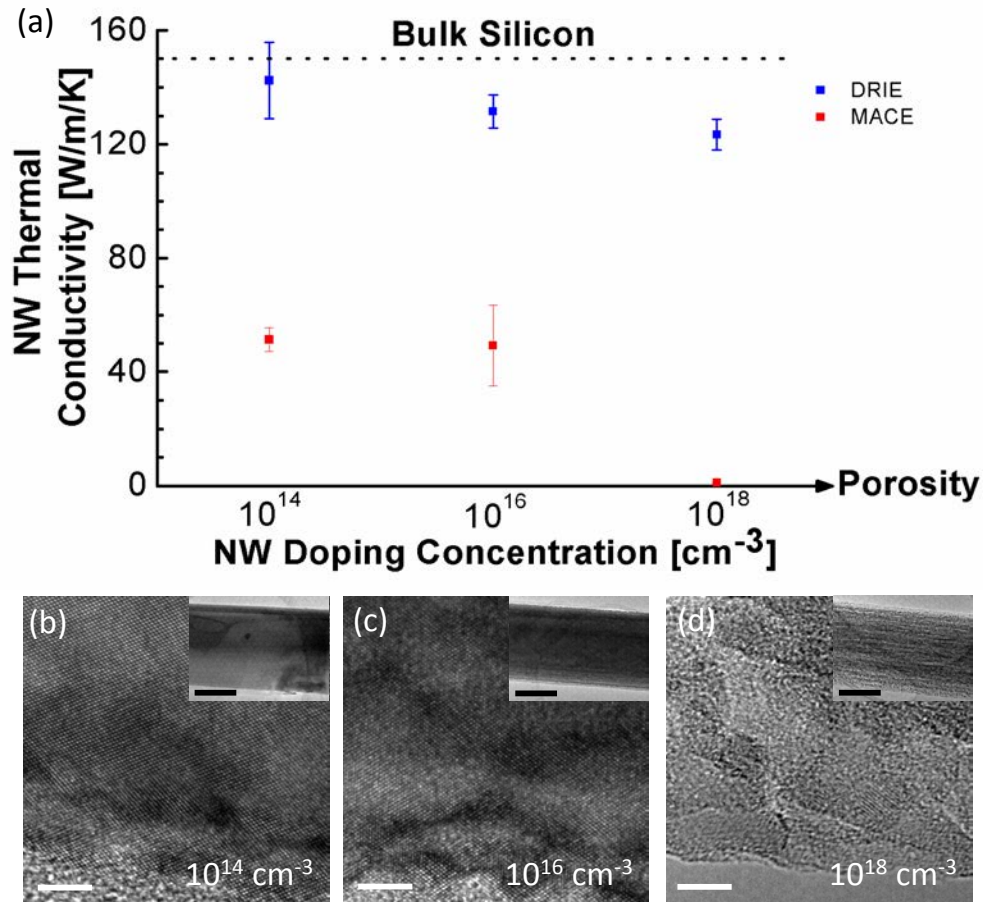


Figure 4.11: (a) Thermal conductivity of nonporous and porous SiNW arrays of large diameter as a function of doping concentrations. TEM images show the relative porosity for Ag-MACE SiNW arrays fabricated with doping concentrations of (b) 10^{14} , (c) 10^{16} , and (d) 10^{18} cm⁻³. The scale bars on the TEM and inset TEM images are 5 nm and 200 nm, respectively.

The thermal conductivities of large diameter SiNW arrays ($d_{avg} \sim 350$ nm) with three different p-type doping concentrations (10^{14} , 10^{16} , and 10^{18} cm⁻³) are further investigated for both nonporous and porous NWs (Figure 4.11). The thermal conductivity of nonporous SiNWs decreases slightly with increasing doping concentration due to the increased phonon-impurity scattering, similar to bulk Si [239, 240]. Conversely, the thermal conductivity of porous SiNWs drops to about 1 W/m/K when the doping concentration is increased from 10^{16} to 10^{18} cm⁻³. It should be noted that the main reason for the dramatic drop in conductivity with doping concentration is that higher doping concentration leads to increased porosity in SiNWs fabricated with MACE (Figure 4.11 b-d). The dopant atom sites act as preferred locations for pores

formation [229, 233, 236, 237]. In comparison to the internal NW porosity, the phonon-impurity scattering at higher doping concentration has a much smaller impact on the thermal conductivity [25, 215].

The thermal conductivities of SiNWs with small diameters ($d_{avg} \sim 130$ nm) also decrease with increasing porosity (Figure 4.12), similar to the large diameter SiNWs. However, the thermal conductivity of these SiNWs is much smaller than those of large diameter SiNWs of similar porosities (*i.e.*, the same etchant solution, 0.3 M H_2O_2). Specifically, the thermal conductivity is reduced from 51 W/m/K for the large diameter ($d_{avg} \sim 350$ nm) SiNWs to 28 W/m/K for the smaller diameter SiNWs ($d_{avg} \sim 130$ nm). This highlights the significant impact of phonon-external boundary scattering on the thermal conductivity at length scales that are smaller than the phonon mean free path. The additional reduction in thermal conductivity (to 17 W/m/K) with increasing H_2O_2 concentration for the smaller diameter SiNWs indicates that the increasing internal porosity also has a significant impact on the thermal conductivity.

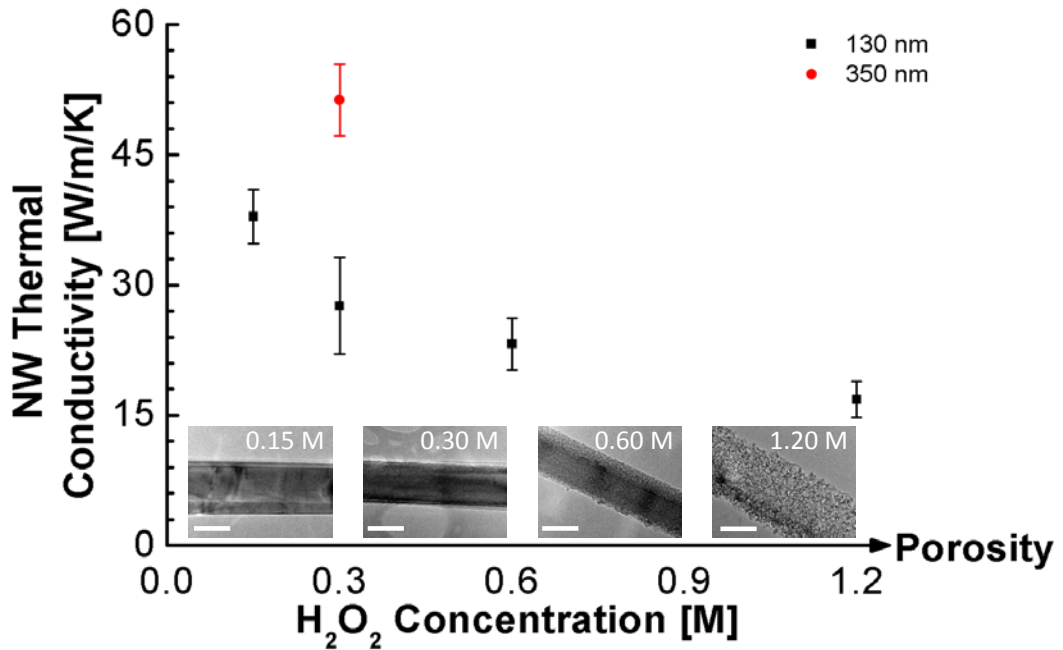


Figure 4.12: Thermal conductivity of SiNWs (10^{14} cm^{-3}) with small diameter ($d_{avg} \sim 130$ nm) as a function of porosity. For comparison, the thermal conductivity of the large diameter SiNW etched at the same condition is shown as the red circle. Increasing nanowire porosity is realized by increasing the H_2O_2 concentration during MACE, as evidenced by the inset TEM images. The scale bars on all the TEM images are 100 nm.

4.3.4 Conclusion

In summary, we measure the thermal conductivity of SiNW arrays with various nanowire diameters, doping concentrations, surface roughness and internal porosities using a nanosecond transient thermoreflectance method. When the SiNW diameter ($d_{avg} \sim 350$ nm) is larger than the phonon mean free path in the bulk silicon, the thermal conductivity shows little dependence on the doping concentration and surface roughness, but decreases significantly with increasing porosity due to phonon scattering at the pore interfaces. In contrast, when the SiNW diameter ($d_{avg} \sim 130$ nm) is smaller than the phonon mean free path, the thermal conductivity strongly depends on both the external boundary-phonon scattering and the internal pore interface-phonon scattering, leading to a significant reduction in the thermal conductivity for small diameter SiNWs.

CHAPTER 5: THERMAL CONDUCTION IN SILICON NITRIDE FILMS §

5.1 Introduction

Amorphous silicon-rich silicon nitride films with various excess silicon concentrations (SiN_x) including those with additional erbium impurities (Er:SiN_x), are promising for light sources that are compatible with silicon-based electronics.[241-245] The Er:SiN_x compound integrated with photonic crystal [241] and plasmonic structures [246] shows an enhanced photoluminescence (PL) peak at $1.54\ \mu\text{m}$ [242, 243]. Moreover, Er:SiN_x -based light emitting devices operating at $1.54\ \mu\text{m}$ have recently been demonstrated [247]. The structural, optical and electrical properties of these materials have been extensively investigated [241-243, 245]. Photonic crystal (PC) cavities fabricated from Er:SiN_x with a stoichiometric silicon nitride matrix have been pumped to transparency, which is a step towards achieving on-chip laser sources [241, 248]. However, to induce laser oscillations, it is crucial to predict and optimize the thermal behavior of the cavity as well. Device performance and stability can be improved by maximizing the thermal conductivity in order to prevent significant heating of the PC cavity. Because of the confined geometry of the proposed light sources, achieving a high thermal conductivity in the constituent materials is a dominant consideration in achieving targeted power densities. Nanostructural characteristics, such as the presence of bonding defects, are influenced by the processing conditions of the nitride films and impact the PL intensity and lifetime [243], and these same characteristics can strongly influence thermal conduction.

This work measures the effect of processing parameters, specifically Si and Er concentrations and annealing temperature, on the thermal and optical properties of silicon-rich nitride films. Optimal processing conditions considering both thermal and optical properties are explored through a systematic study of the impact of annealing temperature and silicon concentration. The thermal properties of SiN_x samples with 7

§ This section reproduced with permission from A.M. Marconnet, *et al.*, “Heat Conduction and Photoluminescence of Light-Emitting Silicon Nitride Films,” *Applied Physics Letters*, vol. 100, 2012. Copyright 2012 American Institute of Physics.

different silicon concentrations (from 44.2 to 61.8 % Si) and 6 annealing temperatures (T_{anneal} from 600 to 1100 °C), as well as those of the as-deposited films, are compared with the PL lifetime measurements of SiN_x samples. For the sample with a Si concentration of 50.0%, the impact of erbium doping on thermal conduction is investigated.

5.2 Methodology

Amorphous SiN_x samples with different excess Si concentrations are fabricated by N₂ reactive magnetron co-sputtering using Si target. Er:SiN_x films were fabricated at a constant Si concentration with varying Er concentrations. After deposition, the samples were annealed at temperatures between 600 and 1100 °C for 200 s under forming gas (5% H₂, 95% N₂) atmosphere. Details of sample preparation can be found in Ref. [242]. The SiN_x films (~400 nm thick) investigated by Time-Resolved Photoluminescence (TRPL) and Time-Domain Thermoreflectance (TDTR) measurement are fabricated in the same batch, while the Er:SiN_x films are ~1300 nm thick and SiN_x samples analyzed by nanoindentation experiments are ~1000nm-thick. A JEOL 6100 scanning electron microscope (SEM) equipped with an energy dispersive X-ray (EDX) spectrometer (Oxford Instruments) was employed to quantitatively analyze the compositional content of the SiN_x and Er:SiN_x films. Based on the result from a Monte Carlo simulation, a low electron beam voltage of 4 Kv is selected for the EDX analysis to ensure that the interaction volume of the electron beam and specimen was confined within the 400 nm top layer SiN_x films. Nanoindentation is performed at room temperature using a Triboindenter nanomechanical testing system (Hysitron Inc., MN) with a standard Berkovich tip. Both of the machine compliance and the tip area function were calibrated using a standard fused silica sample. Thermal drift is minimized by allowing thermal equilibrium to be reached inside the isothermal enclosure of the Triboindenter overnight preceding any indentation experiments. Constant loading rate control measuring scheme was chosen for Young's modulus and hardness characterization of SiN_x thin film samples. Loading and unloading rates were kept at 900 μN/s. A maximum load of 4500 μN minimizes the effects from the substrate, which restrained the displacements (penetration into the thin films) to be within 10% to 15% of the total thin film thickness.

Picosecond TDTR is a well-established pump-probe technique for measuring the thermal conductivity and interface thermal resistances of thin films [249-252]. A metal transducer layer (35 nm of aluminum, deposited on the samples for TDTR) is heated by the frequency-doubled 532 nm, 20 mW, 10 μ m diameter, 9.2 ps pump pulses from a mode-locked Nd:YVO₄ laser with a repetition rate of 82 MHz, modulated at 5 or 8 MHz for lock-in detection. The optically delayed 1064 nm, 5 mW, 5 μ m diameter probe pulses derived from the same laser reflect off the metal surface and are detected by a fast photodetector to measure the surface temperature decay. Fitting the measured thermal decay trace to the solution of the radial-symmetric three-dimensional heat diffusion equation for the multilayer stack with surface heating by a modulated periodic pulse train allows extraction of the thermal conductivity and interface resistances within the sample structure.

To resolve the effective PL lifetime, τ_{PL} , the samples are excited by the second harmonic of the Mai Tai laser at 430 nm with 100 fs pulses. The TRPL signal is dispersed through a double grating spectrometer (Acton Spectra Pro. 2300i) and detected using a single-photon counting streak camera with 10 ps time-resolution (Hamamatsu, C4770). For all the samples, the PL decay trace are fitted by a two-exponential decay model. In order to compare the lifetime data of different samples, we have defined an effective PL lifetime as $\tau_{PL} = (A_1 \times \tau_1 + A_2 \times \tau_2) / (A_1 + A_2)$. This choice is due to the strongly non-exponential nature of the time evolution of SiN_x PL.[243]

5.3 Results & Discussion

Measurements of time-dependent PL and picosecond time-domain thermorefectance of identical samples allow for direct comparison of the effect of the excess silicon in SiN_x and post-annealing temperature on both PL lifetime and thermal conductivity. The thermal conductivity of all samples ranges from 1.25 to 2.66 W m⁻¹ K⁻¹ (as shown in Figure 5.1(a)), while the thermal boundary resistance between the SiN_x layer and the metal transducer layer ranges from 3.1 to 6.5 m² K GW⁻¹ (not shown). The effective PL of SiN_x samples ranges from 0.1 ns to 1.0 ns (as shown in Figure 5.1(b)).

Samples with silicon concentration greater than 53% did not show enough PL intensity to measure the lifetime.

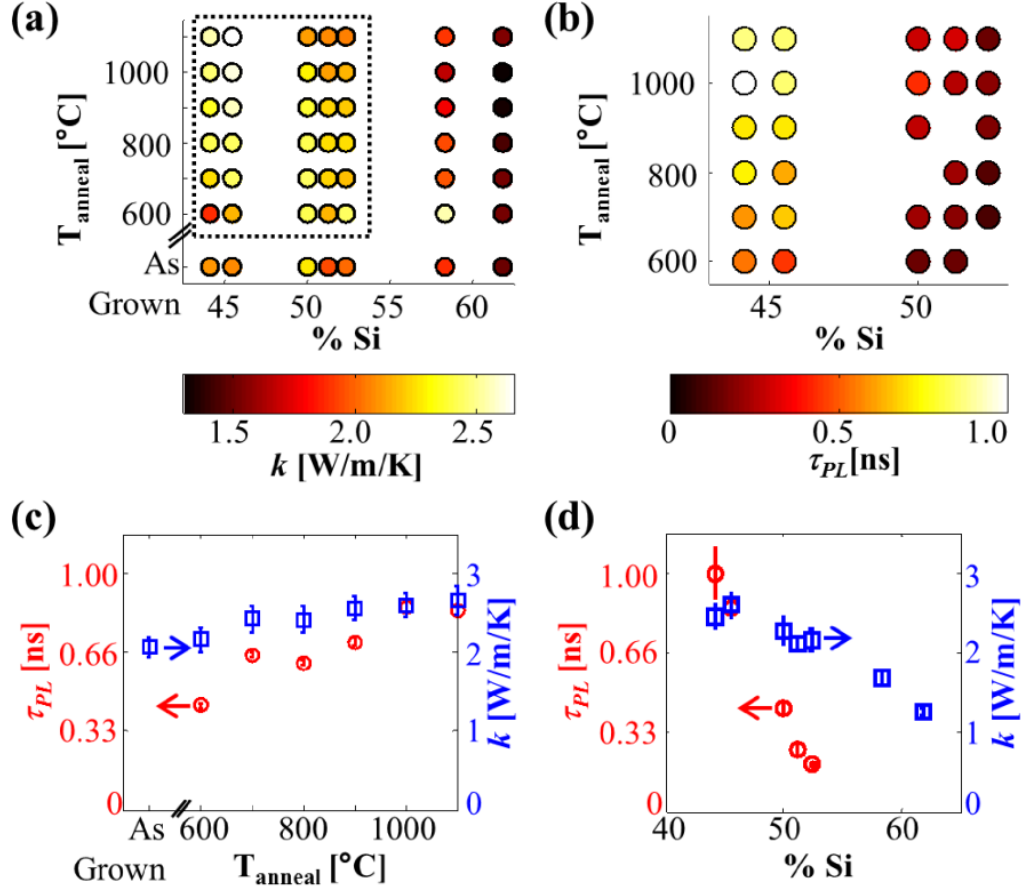


Figure 5.1: Impact of annealing temperature and silicon concentration on (a) thermal conductivity, k , and (b) effective PL lifetime, τ_{PL} . (c) Correlation of the trend of increasing thermal conductivity and PL lifetime with anneal temperature for samples with a relative Si concentration of 45.5%. (d) Correlation of the trend of decreasing thermal conductivity and PL lifetime with increasing excess silicon concentration for samples annealed at 1000 °C.

High thermal conductivity and long PL lifetime are observed at low excess silicon concentrations and high annealing temperatures. PL lifetime (τ_{PL}) depends on both radiative and non-radiative mechanisms, $\tau_{PL}^{-1} = \tau_r^{-1} + \tau_{nr}^{-1}$, where τ_r and τ_{nr} are radiative and non-radiative PL lifetimes, respectively. The PL lifetime of SiN_x is dominated by non-radiative interactions which are primarily driven by relaxations at impurity-induced and disorder-induced defect sites. To highlight the trends in thermal conductivity and

PL lifetime, Figure 5.1(c) shows the increasing thermal conductivity and PL lifetime with increasing annealing temperature for one value of excess Si concentration (45.5%), and Figure 5.1(d) shows the increasing thermal conductivity and PL lifetime with decreasing silicon concentration for one annealing temperature (1000 °C).

The thermal conductivity of the SiN_x films can be very roughly approximated as $k = \frac{1}{3}cv^2\tau_{ph}$, where c is the volumetric heat capacity, v is the acoustic velocity of the phonons, and τ_{ph} is the relaxation time of the phonons. While the use of phonon transport theory for this highly disordered material is questionable, this approach serves here to provide an approximate scaling of the trends of thermal conductivity with acoustic velocity and other properties. The heat capacity is approximately constant with stoichiometry and annealing temperature, and can be approximated as $c \sim n_a k_b$, where n_a is the atomic density and k_b is Boltzmann constant. Combined Rutherford backscattering and spectroscopic ellipsometry measurements (of Er:SiN_x samples) indicate no statistically significant change in the atomic density of the samples with increasing silicon concentration or annealing temperature, but the density, ρ , increases with the incorporation of heavier silicon atoms. Nanoindentation measurements shows that the elastic modulus, E , of the films decreases with increasing silicon concentration (as shown in Figure 5.2(a)). The acoustic velocity of phonons in the film ($v \sim \sqrt{E/\rho}$) decreases with increasing silicon concentration since the elastic modulus decreases while the density of the films increases. Figure 5.2(b) shows a comparison of the measured thermal conductivity and the predicted trends in thermal conductivity from this model assuming a constant phonon lifetime. The acoustic velocity is estimated using the best fit line to the elastic modulus data (as shown in Figure 5.2(a)) and the mass density calculated from the measured atomic density and silicon concentrations combined and the atomic masses of silicon and nitrogen. At the highest silicon concentrations, the thermal conductivity falls below the predicted value for a constant τ_{ph} indicating that in addition to reduction in acoustic velocity, the phonon lifetime also decreases with increasing silicon concentration. The phonon mean free path, $\lambda_{ph} = v\tau_{ph}$, decreases with increasing silicon concentration. The dominant sources of

phonon scattering are disorder and defects, both of which may be impacted by annealing temperature and silicon concentration. The reduced phonon mean free path with increasing silicon concentration suggests a higher concentration of defects and/or disorder in the films with high silicon concentrations. The corresponding reduction in PL lifetime (Figure 5.1(d)), also impacted by disorder and defects, agrees well with the thermal results.

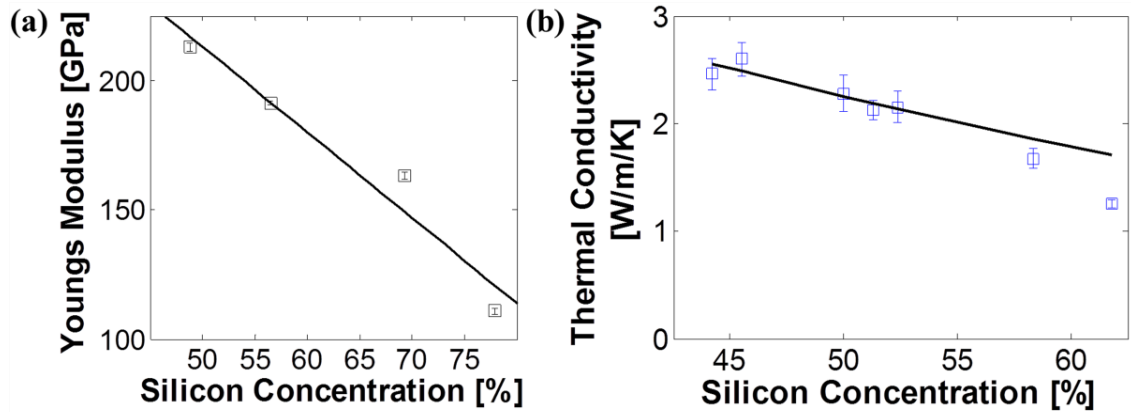


Figure 5.2: (a) Impact of silicon concentration on Young's modulus and hardness of amorphous SiN_x films. The straight line is a best fit to the data and serves mainly as a guide for the reader. (b) SiN_x thermal conductivity as a function of silicon concentration for samples annealed at 1000 °C. The solid line shows the predicted trend in thermal conductivity using the measured elastic modulus (best-fit line from (a)) in the calculation of acoustic velocity and a constant phonon lifetime estimated from a best fit to the data with relative Si concentration < 55 %.

The interplay between disorder and defect concentration could also account for the trends in thermal conductivity with annealing temperature. At low excess silicon concentrations, the thermal conductivity increases with annealing temperature. Increasing annealing temperature reduces disorder and passivates bond defects, and therefore the phonon relaxation time, thermal conductivity, and the effective PL lifetime are enhanced. At high silicon concentrations, the thermal conductivity is approximately constant with annealing temperature. The increased defect concentration related to the high excess silicon concentration may dominate over the slight reduction in disorder. At intermediate silicon concentrations (about 50% Si), a peak in the thermal conductivity is observed at annealing temperatures lower than the maximum annealing temperature,

which may be due to the interplay between intrinsic defects and thermally-induced defects such as those formed at the nanoinclusion interfaces [242].

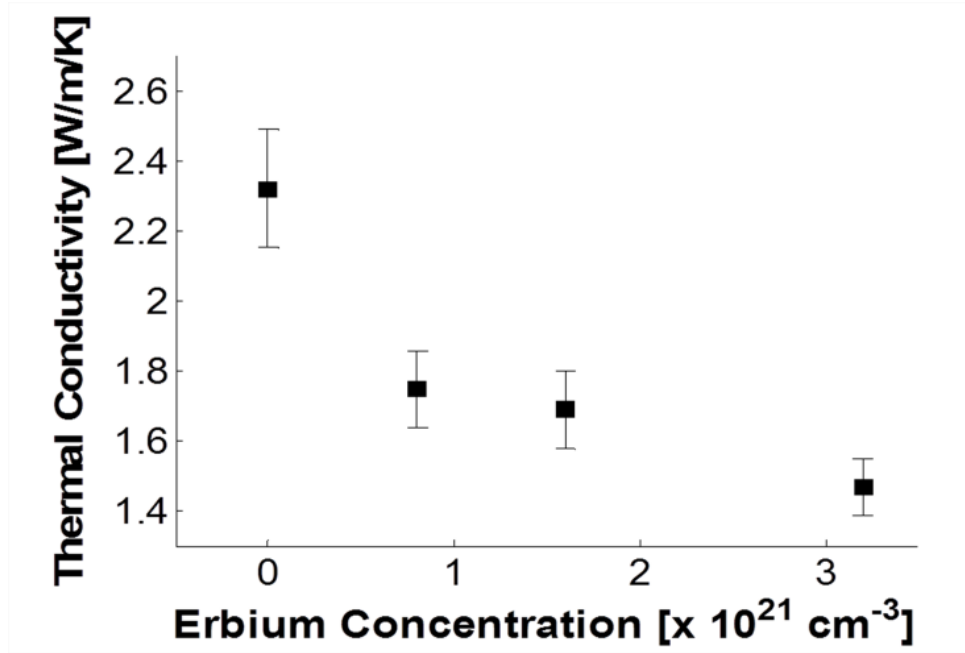


Figure 5.3: Impact of Erbium concentration on the thermal conductivity of an Er-doped silicon-rich nitride film with a relative Si concentration of 50%.

Doping SiN_x films with erbium leads to strong PL at $1.54 \mu\text{m}$ which is significant for photonic applications [242, 243]. In previous studies of similarly fabricated Erbium-doped SiN_x films, the Er PL lifetime at $1.54 \mu\text{m}$ PL efficiency, was maximized at low silicon concentrations and high anneal temperatures [243], similar to the behavior for undoped films reported here. However, doping with erbium forms another scattering mechanism impeding thermal transport and reduces the thermal conductivity. The effective PL lifetime of SiN_x also decreases due to energy transfer from SiN_x to Er ions at relatively low Er concentrations ($\sim 4 \times 10^{20} \text{ cm}^{-3}$) [242, 243]. Figure 5.3 shows the thermal conductivity of erbium doped silicon nitride films (50 % silicon) annealed at 1000°C . At an erbium concentration of $3.2 \times 10^{21} \text{ cm}^{-3}$, the thermal conductivity was reduced to 1.5 W/m/K , less than 65% of the undoped SiN_x value (2.3 W/m/K). It is well-known that large ions act as scattering centers for phonons and therefore erbium incorporation decreases the thermal conductivity. It should also be

noted that Si concentration of SiN_x decreases slightly with Er concentration which should have slightly increased the thermal conductivity.

5.4 Summary

In conclusion, both thermal and optical properties of silicon nitride films and Er-doped SiN_x depend on the post-annealing temperature, the amount of excess silicon, and erbium incorporation. The maximum thermal conductivity and longest PL lifetime were observed at low excess silicon concentrations and high annealing temperatures. We demonstrate that SiN_x thermal conductivity decreases due to reduced acoustic velocity and increased scattering of phonons, while its effective PL lifetime shortens as a result of non-radiative recombinations at defect-induced states in SiN_x . Thermal conductivity of Er: SiN_x matrix decreases with excess Er concentrations. The overlap of ideal processing conditions for both thermal and optical performance is advantageous for SiN_x and Er: SiN_x photonic crystal devices [241] and should be considered when fabricating devices to ensure the very best optical performance, while efficiently removing heat from the device regions.

CHAPTER 6: CONCLUSION

6.1 Summary

As electronic devices continue shrink and as nanostructured materials become more common, understanding their thermal properties is becoming increasingly important to device performance and reliability. Furthermore, nanostructuring leads to unique material properties and combinations of properties not naturally available in bulk materials. For example, nanostructured materials offer the possibility of thermal conductivity extremes: the thermal conductivity of carbon nanotubes and graphene can exceed that of metals, while the introduction of nanoscale boundaries (e.g. nanoscale pores [253]) yields extremely low thermal conductivity materials. Electron-crystal, phonon-glass materials are of interest for thermoelectric applications, while thermally-conductive, mechanically-compliant materials are sought for electronics packaging.

This dissertation focuses on thermal conduction in several different nanostructured materials systems from both a fundamental and an applied approach. *Carbon nanotubes films and composites* are expected to leverage the high conductivity of individual nanotubes, when the axes of the nanotubes are aligned with the direction of heat transport. Despite expectations of high thermal conductivity for the aligned CMT films and composites, defects within the nanotubes, the high density of CNT-CNT contacts, and incomplete contact between the CNTs and surrounding materials limit the thermal conductivity of the CNT-based materials (Chapter 2 and 3). Cross-sectional infrared microscopy [122] allows measurement of the intrinsic thermal conductivity, independent of the boundary resistance between the nanotube-based film and surrounding materials (Chapter 3). The first data for thermal conductivity of densified, aligned multi-wall CNT films and nanocomposites films for a range of CNT volume fractions is reported (Section 3.2 and 3.3). A 1 *vol.%* CNT composite more than doubles the thermal conductivity of the base polymer. Denser arrays (17 *vol.%* CNTs) enhance the thermal conductivity by as much as a factor of 18 and there is a non-linear trend with CNT volume fraction. A novel method for improving the thermal boundary conductance and the engagement between CNTs and heat sinks through electroplating

copper on top of vertically aligned CNT films is investigated (Section 3.4). For vertically-aligned carbon nanotubes arrays with relatively low volume fractions of CNTs (~ 0.5 vol. %), the CNT film thermal conductivity is nearly 3 W/m/K, indicating good engagement between the CNTs and the copper film.

The vast number of fabrication techniques available to create *silicon-based nanostructures* allows investigation of fundamental phonon conduction physics in nanostructures (Chapter 4). For individual nanowires, periodically porous silicon nanobridges show a significant reduction in thermal conductivities due to the pore structure [253] (Section 4.2). The thermal conductivity along the length of the silicon nanobeams is measured using a steady-state Joule heating technique (Section 4.2.2). The thermal conductivities of the porous nanobeams are reduced to as low as 3% of the value for bulk silicon. A Callaway-Holland model for the thermal conductivity is adapted to investigate the relative impact of boundary scattering, pore scattering, and phonon bandgap effects (Section 4.2.3). Measurements of the thermal conductivity of aligned arrays of silicon nanowires provide insight into the impact of nanowire geometry (diameter, surface roughness, and porosity) and doping (Section 4.3). For SiNWs with diameters larger than the phonon mean free path, porosity substantially reduces the thermal conductivity, yielding thermal conductivities as low as 1 W/m/K in highly porous SiNWs. However, when the SiNW diameter is below the phonon mean free path, both the internal porosity and the diameter significantly contribute to phonon scattering and lead to reduction in the thermal conductivity of SiNWs.

Finally, thermal conduction in *silicon-rich and erbium-doped silicon nitride thin films* depends strongly on the excess silicon concentration, annealing conditions, and erbium concentration (Chapter 5). The maximum thermal conductivity and maximum photoluminescence lifetime occur at the same processing conditions, indicating that similar mechanisms (defect concentration and disorder) impact both properties [254].

6.2 Discussion and Suggestions for Future Work

6.2.1 Individual Nanowires: Impact of Nanostructured Pores

Several open questions remain in studying the fundamentals of thermal conduction in porous nanowires and nanofilms. Silicon-based porous nanostructures are ideal for initial tests. These structures show promise for reducing thermal conductivity without significantly impacting the electrical conductivity, one method for improving thermoelectric figure of merit, ZT . Both the measurement device and nanostructure can be fabricated using electron beam lithography. Thus, many variations in pore shape, arrangement, and periodicity, can be studied (a few examples are shown in Figure 6.1). Particularly interesting is the possible impact of pore structure on the phonon dispersion relations when the pore size is comparable with the dominant phonon wavelengths. Also, the patterned silicon nanostructure can also be used as a (sacrificial) template for deposition of more exotic material. Similar patterned porous nanobeam structures are currently used as photonic crystals in a variety of material systems, and understanding the complex thermal, optical, and electrical interactions within the nanodevice may lead to improved lasers and modulators.

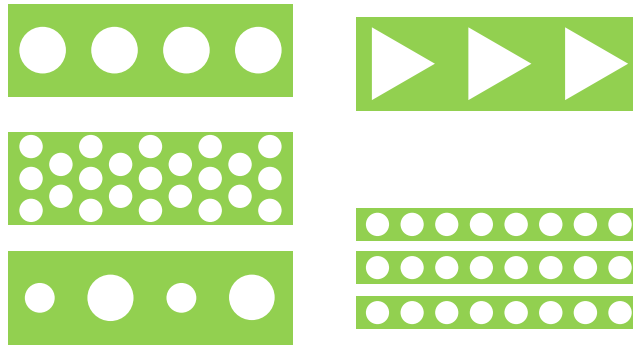


Figure 6.1: Several example geometries for electron beam lithography fabricated porous nanowire structures.

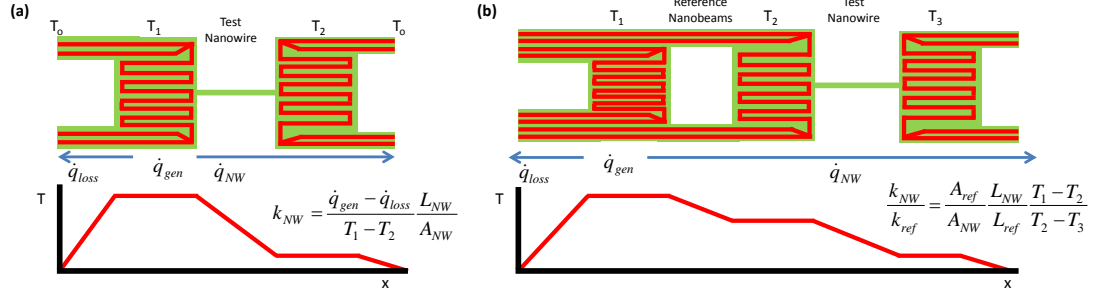


Figure 6.2: (a) Conventional nanowire measurement structure. The nanowire is suspended between two resistive heating elements. Heat generated in the left element conducts through the nanowire, but some fraction conducts through the support legs. Estimates of the conductive heat loss allow calculation of the nanowire thermal conductivity. (b) Modified nanowire measurement structure. Heat is generated in the leftmost resistive element and either conducts through the support legs or through the reference and test nanowires. The heat flux through the test nanowire is calculated from the temperature drop across the reference nanobeams (which also serve as mechanical supports).

Measurements of thermal properties of individual nanotubes or nanowires require microfabricated structures. A relatively straightforward modification to a conventional measurement structure should provide improved accuracy in the measured thermal properties. In the conventional measurement structure (Figure 6.2(a)), a nanowire is suspended between two resistive heating elements. Heat generated at one resistor flows in part through the nanowire (and also through the supports required to suspend the resistive elements) and is detected through a temperature rise at the second. Both resistors serve as temperature sensors and the nanowire thermal conductance is calculated. Losses through the support legs must be calculated to determine the actual heat flux through the nanowire. In the proposed modified design (Figure 6.2(b)), reference nanobeams and a third resistive element are added to the measurement structure. In this design, the reference nanowires are silicon beams with the metal wires connecting to the center resistive element (temperature sensor). The ratio of the test nanowire thermal conductivity to the reference beam thermal conductivity is determined from the temperature drop across each pair of resistive elements. Additional voltage probes can be added to either end of the test nanowire to measure the Seebeck coefficient.

6.2.2 Nanowire Arrays

Careful control of nanowire composition and geometry (including diameter, shape, surface roughness, etc.) will allow understanding of trends in the thermal properties, allowing optimization of the nanostructures for specific applications. As the power density of electronic systems continues to increase, removing heat efficiently from the structure become increasingly important. High conductivity metallic nanowire arrays (NWAs) appear promising as thermal interface materials, especially for high temperature applications where CNT films degrade. For thermoelectric applications, while a number of nanostructured materials can be fabricated in this manner, detailed characterization of the material properties remains challenging.

NWAs can be fabricated through electrochemical deposition of the nanowire material into nanoporous template. Both metallic and semi-conducting nanowire arrays are possible using this low-cost, scalable nanofabrication process. The pore shape, arrangement, and thickness dictate the final nanowire array geometry. While commercially-available membranes will provide a starting point for fabrication, self-assembled block co-polymer films with periodic pore structures provide more options for and control over pore shape and arrangement.

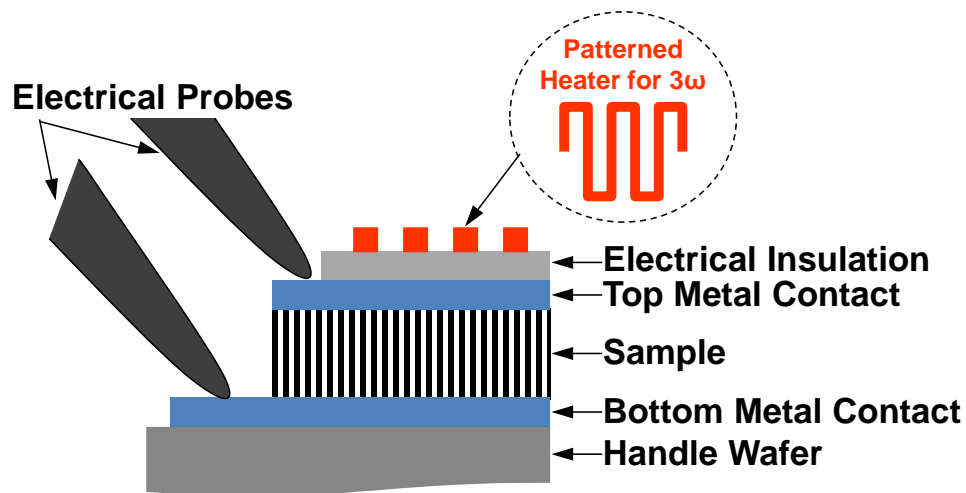


Figure 6.3: Schematic of integrated Z-meter and 3- ω characterization structure. The top patterned heater for 3- ω measurements is electrically isolated from the metal contact layer for the ZT measurement. Micromanipulator probes provide electrical connection to metalized top and bottom electrodes.

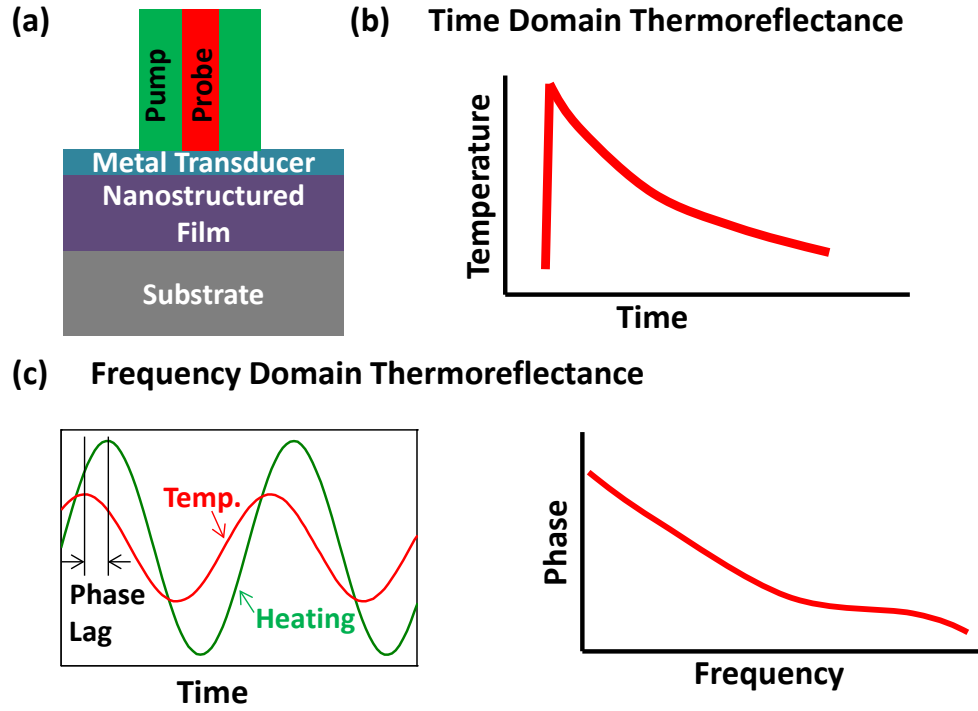


Figure 6.4: (a) Sample configuration for thermoreflectance. (b) Example probe data signal for Time Domain Thermoreflectance. The sample is heated by a pump laser pulse and the change in the reflected intensity of the probe laser corresponds to the temperature at the metal surface. The thermal properties of the sample layer govern the shape of thermal decay curve. (c) Frequency Domain Thermoreflectance. The sample is heated by a sine-wave modulated pump laser causing a periodic heat flux. The temperature rise at the metal surface lags behind the heating signal. The dependence of the amplitude and phase of the temperature signal on the frequency is governed by the thermal properties of the sample.

To characterize the thermal and thermoelectric properties of the nanostructured thermoelectric films, an integrated $3-\omega$ and Z -meter structure (Figure 6.3) and thermoreflectance methods (Figure 6.4) should provide more details about thermal and thermoelectric properties:

- The $3-\omega$ method uses electrical Joule-heating and thermometry in a metal heater line and fitting of a heat diffusion model to extract the relevant thermal properties.
- For the Z -meter technique, a sinusoidal modulated current is passed through the nanowire array, while the phase and magnitude of the voltage across the array are measured. At low frequencies, both the Seebeck effect and the

CONCLUSION

Ohmic resistance contribute to the measured voltage signal. At high frequencies, the thermal effects are reduced because the thermal diffusion length is small.

- For thermorefectance, a pump laser heats a thin metal film deposited on the nanowire array. The resulting temperature at the surface of the metal film is measured by detecting the change in reflected intensity of a low power probe laser and depends on the thermal properties.

6.2.3 Embedded Nanoparticles: Thermal Conduction & Heat Generation

Embedded nanoparticles can serve as the building blocks of materials with unique properties. An enhanced thermoelectric figure of merit has been demonstrated through embedding nanoparticles in thin films [255] and the high density of interfaces in nanoparticle-based sintered materials reduces the lattice component of thermal conductivity. The enhanced heat capacity of nanofluids containing nanoparticles consisting of a solid shell and phase-change core is advantageous for improved heat removal in fluidic cooling applications [256]. Additionally, nanofluids have been shown improve the efficiency of solar-to-thermal energy conversion, useful for power generation applications [257]. Photothermal excitation of metallic nanoparticles has been studied for materials processing applications [258] and thermal destruction of cancer tissue and drug delivery [259]. While several studies have demonstrated the viability of this photothermal nanoparticle heating, quantifying the heat absorption and temperature rise of the nanoparticles remains challenging [259].

Thermorefectance (see Figure 6.3) and the integrated $3-\omega$ and Z -meter structure (see Figure 6.4) should allow characterization of the thermal conductivity of thin nanoparticle composites and nanofluid samples. Not only will these measurements quantify the relevant composite thermal and thermoelectric properties, they indirectly give insight into the heat transfer mechanisms between the nanoparticles and the matrix. Then, to more directly study photothermal excitation of embedded nanoparticles and the heat transfer between the nanoparticle and matrix, transient absorbance measurements could be conducted. This would allow determination of the boundary resistance

CHAPTER 6

between nanoparticles and the embedding medium [260]. Initial measurements could include metallic nanoparticles in quartz, and be followed by measurements of systems more relevant for biological and energy applications.

BIBLIOGRAPHY

- [1] J. Che, *et al.*, "Thermal conductivity of carbon nanotubes," *Nanotechnology*, vol. 11, pp. 65-69, 2000.
- [2] D. W. Brenner, "Empirical potential for hydrocarbons for use in simulating the chemical vapor deposition of diamond films," *Physical Review B*, vol. 42, p. 9458, 1990.
- [3] C. W. Padgett and D. W. Brenner, "Influence of Chemisorption on the Thermal Conductivity of Single-Wall Carbon Nanotubes," *Nano Letters*, vol. 4, pp. 1051-1053, 2004.
- [4] D. W. Brenner, *et al.*, "A second-generation reactive empirical bond order (REBO) potential energy expression for hydrocarbons," *Journal of Physics: Condensed Matter*, vol. 14, pp. 783-802, 2002.
- [5] M. Grujicic, *et al.*, "Atomic-scale computations of the lattice contribution to thermal conductivity of single-walled carbon nanotubes," *Materials Science and Engineering B*, vol. 107, pp. 204-216, 2004.
- [6] M. Grujicic, *et al.*, "Computational analysis of the lattice contribution to thermal conductivity of single-walled carbon nanotubes," *Journal of Materials Science*, vol. 40, pp. 1943-1952, 2005.
- [7] S. J. Stuart, *et al.*, "A reactive potential for hydrocarbons with intermolecular interactions," *The Journal of Chemical Physics*, vol. 112, pp. 6472-6486, 2000.

BIBLIOGRAPHY

- [8] M. A. Osman and D. Srivastava, "Temperature dependence of the thermal conductivity of single-wall carbon nanotubes," *Nanotechnology*, vol. 12, pp. 21-24, 2001.
- [9] J. Tersoff, "Empirical Interatomic Potential for Carbon, with Applications to Amorphous Carbon," *Physical Review Letters*, vol. 61, p. 2879, 1988.
- [10] K. Zhang, *et al.*, "Molecular Dynamics Study on Thermal Performance of CNT-array-Thermal Interface Material," in *International Conference on Electronic Materials and Packaging*, Kowloon, Hong Kong, 2006, pp. 1-4.
- [11] G. Zhang and B. Li, "Thermal conductivity of nanotubes revisited: Effects of chirality, isotope impurity, tube length, and temperature," *The Journal of Chemical Physics*, vol. 123, pp. 114714-4, 2005.
- [12] J. Tersoff, "Modeling solid-state chemistry: Interatomic potentials for multicomponent systems," *Physical Review B*, vol. 39, p. 5566, 1989.
- [13] S. Maruyama, "A molecular dynamics simulation of heat conduction in finite length SWNTs," *Physica B: Condensed Matter*, vol. 323, pp. 193-195, 2002.
- [14] S. Maruyama, "A Molecular Dynamics Simulation of Heat Conduction of a Finite Length Single-Walled Carbon Nanotube," *Microscale Thermophysical Engineering*, vol. 7, pp. 41-50, 2003.
- [15] Y. Yamaguchi and S. Maruyama, "A molecular dynamics simulation of the fullerene formation process," *Chemical Physics Letters*, vol. 286, pp. 336-342, 1998.

BIBLIOGRAPHY

- [16] Z. Yao, *et al.*, "Thermal conduction of carbon nanotubes using molecular dynamics," *Physical Review B*, vol. 71, p. 085417, 2005.
- [17] J. R. Lukes and H. Zhong, "Thermal Conductivity of Individual Single-Wall Carbon Nanotubes," *Journal of Heat Transfer*, vol. 129, pp. 705-716, 2007.
- [18] S. Berber, *et al.*, "Unusually High Thermal Conductivity of Carbon Nanotubes," *Physical Review Letters*, vol. 84, p. 4613, 2000.
- [19] J. Tersoff, "New empirical approach for the structure and energy of covalent systems," *Physical Review B*, vol. 37, p. 6991, 1988.
- [20] W. Zhang, *et al.*, "Chirality dependence of the thermal conductivity of carbon nanotubes," *Nanotechnology*, vol. 15, pp. 936-939, 2004.
- [21] J. Xu and T. S. Fisher, "Enhancement of thermal interface materials with carbon nanotube arrays," *International Journal of Heat and Mass Transfer*, vol. 49, pp. 1658-1666, 2006.
- [22] A. S. Arico, *et al.*, "Nanostructured materials for advanced energy conversion and storage devices," *Nature Materials*, vol. 4, pp. 366-377, 2005.
- [23] Y. Gong, *et al.*, "Nanobeam photonic crystal cavity quantum dot laser," *Optics Express*, vol. 18, pp. 8781-8789, 4/12/2010 2010.
- [24] W. Liu and M. Asheghi, "Phonon--boundary scattering in ultrathin single-crystal silicon layers," *Applied Physics Letters*, vol. 84, pp. 3819-3821, 2004.

BIBLIOGRAPHY

- [25] A. I. Hochbaum, *et al.*, "Enhanced thermoelectric performance of rough silicon nanowires," *Nature*, vol. 451, pp. 163-167, 2008.
- [26] J.-K. Yu, *et al.*, "Reduction of thermal conductivity in phononic nanomesh structures," *Nature Nanotechnology*, vol. 5, pp. 718-721, 2010.
- [27] A. I. Hochbaum, *et al.*, "Enhanced thermoelectric performance of rough silicon nanowires," *Nature*, vol. 451, pp. 163-167, 2008.
- [28] J. M. Weisse, *et al.*, "Thermal Conductivity in Porous Silicon Nanowire Arrays," *Applied Physics Letters*, 2012 (Submitted).
- [29] A. Balandin, "Thermal properties of graphene and nanostructured carbon materials," *Nature Materials*, vol. 10, pp. 569-581, 2011.
- [30] A. M. Marconnet, *et al.*, "Thermal Conduction Phenomena in Carbon Nanotubes and Related Nanostructured Materials," (*under review*), 2012.
- [31] Mstroeck. *Eight Allotropes of Carbon.png*. Available:
http://en.wikipedia.org/wiki/File:Eight_Allotropes_of_Carbon.png
- [32] AlexanderAIUS. *Graphen.jpg*. Available:
<http://en.wikipedia.org/wiki/File:Graphen.jpg>
- [33] Benjah-bmm27. *Graphite-layers-side-3D-balls.png*. Available:
<http://en.wikipedia.org/wiki/File:Graphite-layers-side-3D-balls.png>
- [34] Spundun. *GraphiteUSGOV.jpg*. Available:
<http://en.wikipedia.org/wiki/File:GraphiteUSGOV.jpg>

BIBLIOGRAPHY

- [35] Stahlkocher. *Monokristalines Silizium für die Waferherstellung.jpg*. Available: [http://en.wikipedia.org/wiki/File:Monokristalines Silizium f%C3%BCr die Waferherstellung.jpg](http://en.wikipedia.org/wiki/File:Monokristalines_Silizium_f%C3%BCr_die_Waferherstellung.jpg)
- [36] NASA-GRC. (1998). *Silicon Wafer with Mirror Finish*. Available: [http://upload.wikimedia.org/wikipedia/commons/5/5d/Silicon wafer with mirror finish.jpg](http://upload.wikimedia.org/wikipedia/commons/5/5d/Silicon_wafer_with_mirror_finish.jpg)
- [37] T. Kodama, "Personal Communication," ed, 2012.
- [38] M. M. J. Treacy, *et al.*, "Exceptionally high Young's modulus observed for individual carbon nanotubes," *Nature*, vol. 381, pp. 678-680, 1996.
- [39] G. Overney, *et al.*, "Structural rigidity and low frequency vibrational modes of long carbon tubules," *Zeitschrift für Physik D Atoms, Molecules and Clusters*, vol. 27, pp. 93-96, 1993.
- [40] M. S. Dresselhaus, *et al.*, "Physics of carbon nanotubes," *Carbon*, vol. 33, pp. 883-891, 1995.
- [41] R. S. Ruoff and D. C. Lorents, "Mechanical and thermal properties of carbon nanotubes," *Carbon*, vol. 33, pp. 925-930, 1995.
- [42] E. T. Thostenson, *et al.*, "Advances in the science and technology of carbon nanotubes and their composites: a review," *Composites Science and Technology*, vol. 61, pp. 1899-1912, 2001.
- [43] R. H. Baughman, *et al.*, "Carbon Nanotubes--the Route Toward Applications," *Science*, vol. 297, pp. 787-792, August 2, 2002 2002.

BIBLIOGRAPHY

- [44] K. Zhang, *et al.*, "Study on Thermal Interface Material with Carbon Nanotubes and Carbon Black in High-Brightness LED Packaging with Flip-Chip," in *55th Electronic Components and Technology Conference*, 2005, pp. 60-65.
- [45] M. S. Dresselhaus, *et al.*, Eds., *Carbon Nanotubes: Synthesis, Structure, Properties, and Applications* (Topics in Applied Physics. New York: Springer, 2001, p.^pp. Pages.
- [46] M. S. Dresselhaus, *et al.*, "Other one-dimensional systems and thermal properties," in *Papers from the 2nd International Conference on One-Dimensional Nanostructures*, Malmo, Sweden, 2008, pp. 1613-1618.
- [47] M. S. Dresselhaus, *et al.*, "Unusual Properties and Structure of Carbon Nanotubes," *Annual Review of Materials Research*, pp. 247-278, 2004.
- [48] M. S. Dresselhaus, *et al.*, "Electronic, thermal and mechanical properties of carbon nanotubes," *Philosophical Transactions of the Royal Society of London. Series A: Mathematical, Physical and Engineering Sciences*, vol. 362, pp. 2065-2098, October 15, 2004 2004.
- [49] A. G. Mamalis, *et al.*, "Nanotechnology and nanostructured materials: trends in carbon nanotubes," *Precision Engineering*, vol. 28, pp. 16-30, 2004.
- [50] A. V. Eletskii, "Transport properties of carbon nanotubes," *Physics-Uspekhi*, vol. 52, pp. 209-224, 2009.
- [51] J. Hone, "Carbon Nanotube: Thermal Properties," in *Dekker Encyclopedia of Nanoscience and Nanotechnology*, ed New York: Marcel Dekker Inc., 2004, pp. 603-610.

BIBLIOGRAPHY

- [52] J. Hone, "Phonons and Thermal Properties of Carbon Nanotubes," in *Carbon Nanotubes*, ed, 2001, pp. 273-286.
- [53] J. W. Lee, *et al.*, "Dependencies of the thermal conductivity of individual single-walled carbon nanotubes," *Proceedings of the Institution of Mechanical Engineers, Part N: Journal of Nanoengineering and Nanosystems*, vol. 224, pp. 41-54, March/June 2010 2010.
- [54] M. S. Dresselhaus and P. C. Eklund, "Phonons in Carbon Nanotubes," *Advances in Physics*, vol. 49, pp. 705-814, 2000.
- [55] N. Mingo and D. A. Broido, "Length Dependence of Carbon Nanotube Thermal Conductivity and the "Problem of Long Waves"," *Nano Letters*, vol. 5, pp. 1221-1225, 2005.
- [56] Z. Wang, *et al.*, "Length-dependent thermal conductivity of single-wall carbon nanotubes: prediction and measurements," *Nanotechnology*, vol. 18, p. 475714, 2007.
- [57] T.-Y. Choi, *et al.*, "Measurement of the Thermal Conductivity of Individual Carbon Nanotubes by the Four-Point Three-Omega Method," *Nano Letters*, vol. 6, pp. 1589-1593, 2006.
- [58] T. Yamamoto, *et al.*, "Low-temperature thermal conductance of carbon nanotubes," *Thin Solid Films*, vol. 464-465, pp. 350-353, 2004.
- [59] J. Hone, *et al.*, "Thermal conductivity of single-walled carbon nanotubes," *Physical Review B*, vol. 59, p. R2514, 1999.

BIBLIOGRAPHY

- [60] M. T. Pettes and L. Shi, "Thermal and Structural Characterizations of Individual Single-, Double-, and Multi-Walled Carbon Nanotubes," *Advanced Functional Materials*, vol. 19, pp. 3918-3925, 2009.
- [61] R. Prasher, *et al.*, "An acoustic and dimensional mismatch model for thermal boundary conductance between a vertical mesoscopic nanowire/nanotube and a bulk substrate," *Journal of Applied Physics*, vol. 102, pp. 104312-10, 2007.
- [62] M. Fujii, *et al.*, "Measuring the Thermal Conductivity of a Single Carbon Nanotube," *Physical Review Letters*, vol. 95, p. 065502, 2005.
- [63] C. Yu, *et al.*, "Thermal Conductance and Thermopower of an Individual Single-Wall Carbon Nanotube," *Nano Letters*, vol. 5, pp. 1842-1846, 2005.
- [64] P. Kim, *et al.*, "Thermal Transport Measurements of Individual Multiwalled Nanotubes," *Physical Review Letters*, vol. 87, p. 215502, 2001.
- [65] L. Shi, *et al.*, "Measuring Thermal and Thermoelectric Properties of One-Dimensional Nanostructures Using a Microfabricated Device," *Journal of Heat Transfer*, vol. 125, pp. 881-888, 2003.
- [66] X. Zhang, *et al.*, "Short-hot-wire method for the measurement of the thermal conductivity of a fine fibre," in *15th European Conference on Thermophysical Properties*, Wurzburg, Germany, 1999, pp. 477-484.
- [67] T. Y. Choi, *et al.*, "Measurement of thermal conductivity of individual multiwalled carbon nanotubes by the 3-omega method," *Applied Physics Letters*, vol. 87, pp. 013108-3, 2005.

BIBLIOGRAPHY

- [68] E. Pop, *et al.*, "Thermal Conductance of an Individual Single-Wall Carbon Nanotube above Room Temperature," *Nano Letters*, vol. 6, pp. 96-100, 2006.
- [69] Q. Li, *et al.*, "Measuring the thermal conductivity of individual carbon nanotubes by the Raman shift method," *Nanotechnology*, vol. 20, p. 145702, 2009.
- [70] Z. L. Wang, *et al.*, "Length-dependent thermal conductivity of an individual single-wall carbon nanotube," *Applied Physics Letters*, vol. 91, pp. 123119-3, 2007.
- [71] D. Cahill, "Thermal Conductivity Measurement from 30-K to 750-K: The 3-Omega Method," *Review of Scientific Instruments*, vol. 61, pp. 802-808, 1990.
- [72] I. K. Hsu, *et al.*, "Optical measurement of thermal transport in suspended carbon nanotubes," *Applied Physics Letters*, vol. 92, pp. 063119-3, 2008.
- [73] M. Lazzeri, *et al.*, "Electron Transport and Hot Phonons in Carbon Nanotubes," *Physical Review Letters*, vol. 95, p. 236802, 2005.
- [74] E. Pop, *et al.*, "Negative Differential Conductance and Hot Phonons in Suspended Nanotube Molecular Wires," *Physical Review Letters*, vol. 95, p. 155505, 2005.
- [75] E. Pop, *et al.*, "Electrical and thermal transport in metallic single-wall carbon nanotubes on insulating substrates," *Journal of Applied Physics*, vol. 101, pp. 093710-10, 2007.

BIBLIOGRAPHY

- [76] A. W. Bushmaker, *et al.*, "Direct Observation of Mode Selective Electron-Phonon Coupling in Suspended Carbon Nanotubes," *Nano Letters*, vol. 7, pp. 3618-3622, 2007.
- [77] M. Oron-Carl and R. Krupke, "Raman Spectroscopic Evidence for Hot-Phonon Generation in Electrically Biased Carbon Nanotubes," *Physical Review Letters*, vol. 100, p. 127401, 2008.
- [78] V. V. Deshpande, *et al.*, "Spatially Resolved Temperature Measurements of Electrically Heated Carbon Nanotubes," *Physical Review Letters*, vol. 102, p. 105501, 2009.
- [79] J. H. Seol, *et al.*, "Two-Dimensional Phonon Transport in Supported Graphene," *Science*, vol. 328, pp. 213-216, April 9, 2010.
- [80] W. Cai, *et al.*, "Thermal Transport in Suspended and Supported Monolayer Graphene Grown by Chemical Vapor Deposition," *Nano Letters*, vol. 10, pp. 1645-1651, 2010/05/12 2010.
- [81] F. H. Gojny, *et al.*, "Evaluation and identification of electrical and thermal conduction mechanisms in carbon nanotube/epoxy composites," *Polymer*, vol. 47, pp. 2036-2045, 2006.
- [82] D. G. Cahill, *et al.*, "Nanoscale thermal transport," *Journal of Applied Physics*, vol. 93, pp. 793-818, 2003.
- [83] L. Shang, *et al.*, "Diameter-dependant thermal conductance models of carbon nanotubes," in *7th IEEE Conference on Nanotechnology*, 2007, pp. 206-210.

BIBLIOGRAPHY

- [84] J. Wang and J.-S. Wang, "Carbon nanotube thermal transport: Ballistic to diffusive," *Applied Physics Letters*, vol. 88, pp. 111909-3, 2006.
- [85] L. G. C. Rego and G. Kirczenow, "Quantized Thermal Conductance of Dielectric Quantum Wires," *Physical Review Letters*, vol. 81, p. 232, 1998.
- [86] T. Yamamoto, *et al.*, "Universal Features of Quantized Thermal Conductance of Carbon Nanotubes," *Physical Review Letters*, vol. 92, p. 075502, 2004.
- [87] G. D. Mahan and G. S. Jeon, "Flexure modes in carbon nanotubes," *Physical Review B*, vol. 70, p. 075405, 2004.
- [88] N. Mingo and D. A. Broido, "Carbon Nanotube Ballistic Thermal Conductance and Its Limits," *Physical Review Letters*, vol. 95, p. 096105, 2005.
- [89] R. Saito, *et al.*, *Physical Properties of Carbon Nanotubes*: Imperial College Press, 1998.
- [90] R. Saito, *et al.*, "Raman intensity of single-wall carbon nanotubes," *Physical Review B*, vol. 57, p. 4145, 1998.
- [91] R. A. Jishi, *et al.*, "Phonon modes in carbon nanotubules," *Chemical Physics Letters*, vol. 209, pp. 77-82, 1993.
- [92] V. N. Popov, "Low-temperature specific heat of nanotube systems," *Physical Review B*, vol. 66, p. 153408, 2002.
- [93] V. N. Popov, "Theoretical evidence for $T^{1/2}$ specific heat behavior in carbon nanotube systems," *Carbon*, vol. 42, pp. 991-995, 2004.

BIBLIOGRAPHY

- [94] V. N. Popov, *et al.*, "Elastic properties of single-walled carbon nanotubes," *Physical Review B*, vol. 61, p. 3078, 2000.
- [95] D. Sánchez-Portal, *et al.*, "Ab initio structural, elastic, and vibrational properties of carbon nanotubes," *Physical Review B*, vol. 59, p. 12678, 1999.
- [96] E. Brown, *et al.*, "Ballistic thermal and electrical conductance measurements on individual multiwall carbon nanotubes," *Applied Physics Letters*, vol. 87, pp. 023107-3, 2005.
- [97] P. Chantrenne and J.-L. Barrat, "Analytical model for the thermal conductivity of nanostructures," *Superlattices and Microstructures*, vol. 35, pp. 173-186, 2004.
- [98] T. Yamamoto, *et al.*, "Crossover from Ballistic to Diffusive Thermal Transport in Carbon Nanotubes," *Applied Physics Express*, vol. 2, p. 095003, 2009.
- [99] X. H. Yan, *et al.*, "Effects of intertube coupling and tube chirality on thermal transport of carbon nanotubes," *Journal of Applied Physics*, vol. 99, pp. 124305-4, 2006.
- [100] J. X. Cao, *et al.*, "Thermal conductivity of zigzag single-walled carbon nanotubes: Role of the umklapp process," *Physical Review B*, vol. 69, p. 073407, 2004.
- [101] J. Hone, *et al.*, "Quantized Phonon Spectrum of Single-Wall Carbon Nanotubes," *Science*, vol. 289, pp. 1730-1733, September 8, 2000 2000.

BIBLIOGRAPHY

- [102] H. B. G. Casimir, "Note on the conduction of heat in crystals," *Physica*, vol. 5, pp. 495-500, 1938.
- [103] S. Lepri, *et al.*, "Thermal conduction in classical low-dimensional lattices," *Physics Reports*, vol. 377, pp. 1-80, 2003.
- [104] M. A. Osman and D. Srivastava, "Molecular dynamics simulation of heat pulse propagation in single-wall carbon nanotubes," *Physical Review B*, vol. 72, p. 125413, 2005.
- [105] H. Zhong and J. R. Lukes, "Thermal Conductivity of Single-Wall Carbon Nanotubes," in *2004 ASME International Mechanical Engineering Congress and Exposition*, Anaheim, CA, 2004.
- [106] J. Yu, *et al.*, "Phonons in graphitic tubules: A tight-binding molecular dynamics study," *The Journal of Chemical Physics*, vol. 103, pp. 6697-6705, 1995.
- [107] M. U. Kahaly and U. V. Waghmare, "Size dependence of thermal properties of armchair carbon nanotubes: A first-principles study," *Applied Physics Letters*, vol. 91, pp. 023112-3, 2007.
- [108] I. Ivanov, *et al.*, "Fast and highly anisotropic thermal transport through vertically aligned carbon nanotube arrays," *Applied Physics Letters*, vol. 89, pp. 223110-3, 2006.
- [109] M. A. Panzer, *et al.*, "Thermal Properties of Metal-Coated Vertically Aligned Single-Wall Nanotube Arrays," *Journal of Heat Transfer*, vol. 130, pp. 052401-9, 2008.

BIBLIOGRAPHY

- [110] D. J. Yang, *et al.*, "Thermal conductivity of multiwalled carbon nanotubes," *Physical Review B*, vol. 66, p. 165440, 2002.
- [111] Y. Son, *et al.*, "Thermal resistance of the native interface between vertically aligned multiwalled carbon nanotube arrays and their SiO₂/Si substrate," *Journal of Applied Physics*, vol. 103, pp. 024911-7, 2008.
- [112] B. A. Cola, *et al.*, "Increased real contact in thermal interfaces: A carbon nanotube/foil material," *Applied Physics Letters*, vol. 90, pp. 093513-3, 2007.
- [113] H. Xie, *et al.*, "Thermal diffusivity and conductivity of multiwalled carbon nanotube arrays," *Physics Letters A*, vol. 369, pp. 120-123, 2007.
- [114] X. Wang, *et al.*, "Noncontact thermal characterization of multiwall carbon nanotubes," *Journal of Applied Physics*, vol. 97, pp. 064302-5, 2005.
- [115] T. Tong, *et al.*, "Indium Assisted Multiwalled Carbon Nanotube Array Thermal Interface Materials," in *The Tenth Intersociety Conference on Thermal and Thermomechanical Phenomena in Electronics Systems (ITHERM '06)*, 2006, pp. 1406-1411.
- [116] T. Tong, *et al.*, "Dense Vertically Aligned Multiwalled Carbon Nanotube Arrays as Thermal Interface Materials," *IEEE Transactions on Components and Packaging Technologies*, vol. 30, pp. 92-100, 2007.
- [117] J. Xu and T. S. Fisher, "Enhanced thermal contact conductance using carbon nanotube array interfaces," *IEEE Transactions on Components and Packaging Technologies*, vol. 29, pp. 261-267, 2006.

BIBLIOGRAPHY

- [118] H. L. Zhang, *et al.*, "Spark plasma sintering and thermal conductivity of carbon nanotube bulk materials," *Journal of Applied Physics*, vol. 97, pp. 114310-5, 2005.
- [119] H.-L. Zhang, *et al.*, "Electrical and thermal properties of carbon nanotube bulk materials: Experimental studies for the 328--958 K temperature range," *Physical Review B (Condensed Matter and Materials Physics)*, vol. 75, pp. 205407-9, 2007.
- [120] T. Borca-Tasciuc, *et al.*, "Anisotropic thermal diffusivity of aligned multiwall carbon nanotube arrays," *Journal of Applied Physics*, vol. 98, pp. 054309-6, 2005.
- [121] M. Akoshima, *et al.*, "Thermal Diffusivity of Single-Walled Carbon Nanotube Forest Measured by Laser Flash Method," *Japanese Journal of Applied Physics*, vol. 48, p. 05EC07, 2009.
- [122] A. M. Marconnet, *et al.*, "Thermal Conduction in Aligned Carbon Nanotube--Polymer Nanocomposites with High Packing Density," *ACS Nano*, vol. 5, pp. 4818-4825, 2011.
- [123] R. S. Prasher, *et al.*, "Turning Carbon Nanotubes from Exceptional Heat Conductors into Insulators," *Physical Review Letters*, vol. 102, pp. 105901-4, 2009.
- [124] X. J. Hu, *et al.*, "3-Omega Measurements of Vertically Oriented Carbon Nanotubes on Silicon," *Journal of Heat Transfer*, vol. 128, pp. 1109-1113, 2006.

BIBLIOGRAPHY

- [125] D. J. Yang, *et al.*, "Thermal and electrical transport in multi-walled carbon nanotubes," *Physics Letters A*, vol. 329, pp. 207-213, 2004.
- [126] Z. L. Gao and *et al.*, "Fabrication of carbon nanotube thermal interface material on aluminum alloy substrates with low pressure CVD," *Nanotechnology*, vol. 22, p. 265611, 2011.
- [127] B. A. Cola, *et al.*, "Effects of Growth Temperature on Carbon Nanotube Array Thermal Interfaces," *Journal of Heat Transfer*, vol. 130, pp. 114503-4, 2008.
- [128] Y. Won, *et al.*, "Mechanical characterization of aligned multi-walled carbon nanotube films using microfabricated resonators," *Carbon*, vol. 50, pp. 347-355, 2012.
- [129] M. Bedewy, *et al.*, "Collective Mechanism for the Evolution and Self-Termination of Vertically Aligned Carbon Nanotube Growth," *The Journal of Physical Chemistry C*, vol. 113, pp. 20576-20582, 2009/12/03 2009.
- [130] Y. Chalopin, *et al.*, "Interface heat transfer between crossing carbon nanotubes, and the thermal conductivity of nanotube pellets," *Arxiv preprint arXiv:0809.2660*, 2008.
- [131] J. Yang, *et al.*, "Contact thermal resistance between individual multiwall carbon nanotubes," *Applied Physics Letters*, vol. 96, pp. 023109-3, 2010.
- [132] A. E. Aliev, *et al.*, "Thermal conductivity of multi-walled carbon nanotube sheets: radiation losses and quenching of phonon modes," *Nanotechnology*, vol. 21, p. 035709, 2010.

BIBLIOGRAPHY

- [133] B. A. Cola, *et al.*, "Carbon Nanotube Array Thermal Interfaces for High-Temperature Silicon Carbide Devices," *Nanoscale and Microscale Thermophysical Engineering*, vol. 12, pp. 228-237, 2008/09/05 2008.
- [134] S. L. Hodson, *et al.*, "Palladium Thiolate Bonding of Carbon Nanotube Thermal Interfaces," *Journal of Electronic Packaging*, vol. 133, p. 020907, 2011.
- [135] S. V. Aradhya, *et al.*, "Electrothermally bonded carbon nanotube interfaces," in *11th Intersociety Conference on Thermal and Thermomechanical Phenomena in Electronic Systems (ITHERM 2008)*, 2008, pp. 1071-1077.
- [136] R. D. Johnson, *et al.*, "Thermocompression bonding of vertically aligned carbon nanotube turfs to metalized substrates," *Nanotechnology*, vol. 20, p. 065703, 2009.
- [137] A. Hamdan and *et al.*, "Evaluation of a thermal interface material fabricated using thermocompression bonding of carbon nanotube turf," *Nanotechnology*, vol. 21, p. 015702, 2010.
- [138] R. Cross, *et al.*, "A metallization and bonding approach for high performance carbon nanotube thermal interface materials," *Nanotechnology*, vol. 21, p. 445705, 2010.
- [139] B. A. Cola, *et al.*, "Photoacoustic characterization of carbon nanotube array thermal interfaces," *Journal of Applied Physics*, vol. 101, pp. 054313-9, 2007.
- [140] M. A. Panzer, *et al.*, "Temperature-Dependent Phonon Conduction and Nanotube Engagement in Metalized Single Wall Carbon Nanotube Films," *Nano Letters*, vol. 10, pp. 2395-2400, 2010.

BIBLIOGRAPHY

- [141] M. A. Panzer and K. E. Goodson, "Thermal resistance between low-dimensional nanostructures and semi-infinite media," *Journal of Applied Physics*, vol. 103, pp. 094301-10, 2008.
- [142] M. A. Panzer and K. E. Goodson, "Erratum: "Thermal resistance between low-dimensional nanostructures and semi-infinite media" [J. Appl. Phys. **094301** (2008)]," *Journal of Applied Physics*, vol. 109, pp. 059902-1, 2011.
- [143] J. Diao, *et al.*, "Molecular dynamics simulations of carbon nanotube/silicon interfacial thermal conductance," *The Journal of Chemical Physics*, vol. 128, pp. 164708-5, 2008.
- [144] H.-B. Fan, *et al.*, "The interfacial thermal conductance between a vertical single-wall carbon nanotube and a silicon substrate," *Journal of Applied Physics*, vol. 106, pp. 034307-6, 2009.
- [145] Z.-Y. Ong and E. Pop, "Molecular dynamics simulation of thermal boundary conductance between carbon nanotubes and SiO₂," *Physical Review B*, vol. 81, p. 155408, 2010.
- [146] H. Maune, *et al.*, "Thermal resistance of the nanoscale constrictions between carbon nanotubes and solid substrates," *Applied Physics Letters*, vol. 89, pp. 013109-3, 2006.
- [147] E. J. Garcia, *et al.*, "Fabrication and Multifunctional Properties of High Volume Fraction Aligned Carbon Nanotube Thermoset Composites," *Journal of Nano Systems and Technology*, vol. 1, pp. 1-11, 2009.

BIBLIOGRAPHY

- [148] B. L. Wardle, *et al.*, "Fabrication and Characterization of Ultrahigh-Volume-Fraction Aligned Carbon Nanotube–Polymer Composites," *Advanced Materials*, vol. 20, pp. 2707-2714, 2008.
- [149] N. Yamamoto, "Multi-Scale Electrical and Thermal Properties of Aligned Multi-Walled Carbon Nanotubes and Their Composites," PhD, Department of Aeronautics and Astronautics, Massachusetts Institute of technology, Cambridge, MA, 2011.
- [150] M. B. Bryning, *et al.*, "Thermal conductivity and interfacial resistance in single-wall carbon nanotube epoxy composites," *Applied Physics Letters*, vol. 87, pp. 161909-3, 2005.
- [151] Y. Mamunya, *et al.*, "Electrical and thermophysical behaviour of PVC-MWCNT nanocomposites," *Composites Science and Technology*, vol. 68, pp. 1981-1988, 2008.
- [152] X. Hu, *et al.*, "Thermal conductance enhancement of particle-filled thermal interface materials using carbon nanotube inclusions," in *The Ninth Intersociety Conference on Thermal and Thermomechanical Phenomena in Electronic Systems (ITHERM '04)*, 2004, pp. 63-69 Vol.1.
- [153] P. Bonnet, *et al.*, "Thermal properties and percolation in carbon nanotube-polymer composites," *Applied Physics Letters*, vol. 91, pp. 201910-3, 2007.
- [154] C. Guthy, *et al.*, "Thermal Conductivity of Single-Walled Carbon Nanotube/PMMA Nanocomposites," *Journal of Heat Transfer*, vol. 129, pp. 1096-1099, 2007.

BIBLIOGRAPHY

- [155] C. W. Nan, *et al.*, "A simple model for thermal conductivity of carbon nanotube-based composites," *Chemical Physics Letters*, vol. 375, pp. 666-669, 2003.
- [156] C.-W. Nan, *et al.*, "Effective thermal conductivity of particulate composites with interfacial thermal resistance," *Journal of Applied Physics*, vol. 81, pp. 6692-6699, 1997.
- [157] S. Kumar, *et al.*, "Effect of percolation on thermal transport in nanotube composites," *Applied Physics Letters*, vol. 90, pp. 104105-3, 2007.
- [158] C.-W. Nan, *et al.*, "Interface effect on thermal conductivity of carbon nanotube composites," *Applied Physics Letters*, vol. 85, pp. 3549-3551, 2004.
- [159] T. Borca-Tasciuc, *et al.*, "A photo-thermoelectric technique for anisotropic thermal diffusivity characterization of nanowire/nanotube composites," in *IEEE Twenty First Annual IEEE Semiconductor Thermal Measurement and Management Symposium*, 2005, pp. 283-291.
- [160] A. Yu, *et al.*, "Effect of single-walled carbon nanotube purity on the thermal conductivity of carbon nanotube-based composites," *Applied Physics Letters*, vol. 89, pp. 133102-3, 2006.
- [161] H. Hu, *et al.*, "Influence of the Zeta Potential on the Dispersability and Purification of Single-Walled Carbon Nanotubes," *The Journal of Physical Chemistry B*, vol. 109, pp. 11520-11524, 2005.
- [162] C. H. Liu and S. S. Fan, "Effects of chemical modifications on the thermal conductivity of carbon nanotube composites," *Applied Physics Letters*, vol. 86, pp. 123106-3, 2005.

BIBLIOGRAPHY

- [163] J. C. Grunlan, *et al.*, "Thermal and Mechanical Behavior of Carbon-Nanotube-Filled Latex," *Macromolecular Materials and Engineering*, vol. 291, pp. 1035-1043, 2006.
- [164] T. Borca-Tasciuc, *et al.*, "Anisotropic Thermal Diffusivity Characterization of Aligned Carbon Nanotube-Polymer Composites," *Journal of Nanoscience and Nanotechnology*, vol. 7, pp. 1581-1588, 2007.
- [165] H. Huang, *et al.*, "Aligned Carbon Nanotube Composite Films for Thermal Management," *Advanced Materials*, vol. 17, pp. 1652-1656, 2005.
- [166] Y. Wu, *et al.*, "Effects of surface metal layer on the thermal contact resistance of carbon nanotube arrays," *Applied Physics Letters*, vol. 87, pp. 213108-3, 2005.
- [167] H. Cebeci, *et al.*, "Multifunctional properties of high volume fraction aligned carbon nanotube polymer composites with controlled morphology," *Composites Science and Technology*, vol. 69, pp. 2649-2656, 2009.
- [168] F. Du, *et al.*, "An infiltration method for preparing single-wall nanotube/epoxy composites with improved thermal conductivity," *Journal of Polymer Science Part B: Polymer Physics*, vol. 44, pp. 1513-1519, 2006.
- [169] R. Haggenueller, *et al.*, "Single Wall Carbon Nanotube/Polyethylene Nanocomposites: Thermal and Electrical Conductivity," *Macromolecules*, vol. 40, pp. 2417-2421, 2007.
- [170] A. J. Hart and A. H. Slocum, "Rapid Growth and Flow-Mediated Nucleation of Millimeter-Scale Aligned Carbon Nanotube Structures from a Thin-Film Catalyst," *The Journal of Physical Chemistry B*, vol. 110, pp. 8250-8257, 2006.

BIBLIOGRAPHY

- [171] X. J. Hu, *et al.*, "Infrared Microscopy Thermal Characterization of Opposing Carbon Nanotube Arrays," *Journal of Heat Transfer*, vol. 129, p. 91, 2007.
- [172] H. Duong, *et al.*, "Thermal Properties of Vertically Aligned Carbon Nanotube-Nanocomposites Boundary Resistance and Inter- Carbon Nanotube Contact: Experiments and Modeling," presented at the APS March Meeting, Pittsburgh, PA, 2009.
- [173] A. Marconnet, *et al.*, "Thermal Conductivity and Boundary Resistance of Aligned Carbon Nanotube Films and their Polymeric Composites," presented at the Materials Research Society Symposium, San Francisco, CA, 2009.
- [174] E. R. Meshot and A. J. Hart, "Abrupt self-termination of vertically aligned carbon nanotube growth," *Applied Physics Letters*, vol. 92, pp. 113107-3, 2008.
- [175] S. T. Huxtable, *et al.*, "Interfacial heat flow in carbon nanotube suspensions," *Nat Mater*, vol. 2, pp. 731-734, 2003.
- [176] T. C. Clancy, *et al.*, "Multiscale modeling of thermal conductivity of polymer/carbon nanocomposites," *International Journal of Thermal Sciences*, vol. 49, pp. 1555-1560, 2010.
- [177] C. Yang, *et al.*, "Carbon Nanotube/Copper Composites for Via Filling and Thermal Management," in *Proceedings of the 57th Electronic Components and Technology Conference*, 2007, pp. 1224-1229.
- [178] Y. Xu, *et al.*, "Thermal properties of carbon nanotube array used for integrated circuit cooling," *Journal of Applied Physics*, vol. 100, pp. 074302-5, 2006.

BIBLIOGRAPHY

- [179] S. Pal, *et al.*, "Thermal and electrical transport along MWCNT arrays grown on Inconel substrates," *Journal of Materials Research*, vol. 23, p. 2099, 2008.
- [180] L. D. Hicks and M. S. Dresselhaus, "Thermoelectric figure of merit of a one-dimensional conductor," *Physical Review B*, vol. 47, pp. 16631-16634, 1993.
- [181] X. W. Wang, *et al.*, "Enhanced thermoelectric figure of merit in nanostructured n-type silicon germanium bulk alloy," *Applied Physics Letters*, vol. 93, pp. 193121-3, 2008.
- [182] J. Tang, *et al.*, "Holey Silicon as an Efficient Thermoelectric Material," *Nano Letters*, vol. 10, pp. 4279-4283, 2010.
- [183] P. E. Hopkins, *et al.*, "Reduction in the Thermal Conductivity of Single Crystalline Silicon by Phononic Crystal Patterning," *Nano Letters*, vol. 11, pp. 107-112, 2010.
- [184] D. Song and G. Chen, "Thermal conductivity of periodic microporous silicon films," *Applied Physics Letters*, vol. 84, pp. 687-689, 2004.
- [185] M. Makarova, *et al.*, "Two-dimensional porous silicon photonic crystal light emitters," in *2006 Conference on Lasers and Electro-Optics and 2006 Quantum Electronics and Laser Science Conference*, Long Beach, CA, 2006, pp. 1-2.
- [186] Y. Gong, *et al.*, "Linewidth narrowing and Purcell enhancement in photonic crystal cavities on an Er-doped silicon nitride platform," *Optics Express*, vol. 18, pp. 2601-2612, 2010.

BIBLIOGRAPHY

- [187] K. Esfarjani, *et al.*, "Heat transport in silicon from first-principles calculations," *Physical Review B*, vol. 84, p. 085204, 2011.
- [188] S. Benchabane, *et al.*, "Silicon phononic crystal for surface acoustic waves," in *2005 IEEE Ultrasonics Symposium*, 2005, pp. 922-925.
- [189] P. E. Hopkins, *et al.*, "Phonon considerations in the reduction of thermal conductivity in phononic crystals," *Applied Physics A*, 2010.
- [190] J.-H. Lee, *et al.*, "Nanoporous Si as an Efficient Thermoelectric Material," *Nano Letters*, vol. 8, pp. 3750-3754, 2008.
- [191] S. Mohammadi, *et al.*, "Demonstration of large complete phononic band gaps and waveguiding in high-frequency silicon phononic crystal slabs," in *2008 IEEE International Frequency Control Symposium*, 2008, pp. 768-772.
- [192] R. H. Olsson III and I. El-Kady, "Microfabricated phononic crystal devices and applications," *Measurement Science and Technology*, vol. 20, p. 012002, 2009.
- [193] W. Liu and M. Asheghi, "Thermal Conductivity Measurements of Ultra-Thin Single Crystal Silicon Layers," *Journal of Heat Transfer*, vol. 128, pp. 75-83, 2006.
- [194] W. Liu and M. Asheghi, "Thermal conduction in ultrathin pure and doped single-crystal silicon layers at high temperatures," *Journal of Applied Physics*, vol. 98, p. 123523, 2005.
- [195] T. Kodama, *et al.*, "In-plane thermal conductivity measurement on nanoscale conductive materials with on-substrate device configurations," presented at the

BIBLIOGRAPHY

IEEE Intersociety Conference on Thermal and Thermomechanical Phenomena in Electronic Systems (ITHERM), San Diego, CA, 2012.

- [196] B. Kim, *et al.*, "Thermal conductivity manipulation in single crystal silicon via lithographically defined phononic crystals," in *2012 IEEE 25th International Conference on Micro Electro Mechanical Systems (MEMS)*, 2012, pp. 176-179.
- [197] Y. He, *et al.*, "Thermal Transport in Nanoporous Silicon: Interplay between Disorder at Mesoscopic and Atomic Scales," *ACS Nano*, vol. 5, pp. 1839-1844, 2011.
- [198] G. S. Oehrlein, "Dry etching damage of silicon: A review," *Materials Science and Engineering: B*, vol. 4, pp. 441-450, 1989.
- [199] M. G. Holland, "Analysis of Lattice Thermal Conductivity," *Physical Review*, vol. 132, p. 2461, 1963.
- [200] J. Callaway, "Model for Lattice Thermal Conductivity at Low Temperatures," *Physical Review*, vol. 113, pp. 1046-1051, 1959.
- [201] C. M. Reinke, *et al.*, "Thermal conductivity prediction of nanoscale phononic crystal slabs using a hybrid lattice dynamics-continuum mechanics technique," *AIP Advances*, vol. 1, pp. 041403-14, 2011.
- [202] W. Weber, "Adiabatic bond charge model for the phonons in diamond, Si, Ge, and α -Sn," *Physical Review B*, vol. 15, pp. 4789-4803, 1977.
- [203] B. N. Brockhouse, "Lattice Vibrations in Silicon and Germanium," *Physical Review Letters*, vol. 2, pp. 256-258, 1959.

BIBLIOGRAPHY

- [204] C. Dames and G. Chen, "Theoretical phonon thermal conductivity of Si/Ge superlattice nanowires," *Journal of Applied Physics*, vol. 95, pp. 682-693, 2004.
- [205] P. E. Hopkins, *et al.*, "Origin of reduction in phonon thermal conductivity of microporous solids," *Applied Physics Letters*, vol. 95, pp. 161902-3, 2009.
- [206] R. G. Chambers, "The Conductivity of Thin Wires in a Magnetic Field," *Proceedings of the Royal Society of London. Series A, Mathematical and Physical Sciences*, vol. 202, pp. 378-394, 1950.
- [207] E. H. Sondheimer, "The mean free path of electrons in metals," *Advances in Physics*, vol. 1, pp. 1-42, 1952/01/01 1952.
- [208] A. McGaughey, "Phonon Transport in Thin Films," in *7th US-Japan Joint Seminar on Nanoscale Transport Phenomena - Science and Engineering*, Shima, Japan, 2011.
- [209] A. J. H. McGaughey and A. Jain, "Nanostructure thermal conductivity prediction by Monte Carlo sampling of phonon free paths," *Applied Physics Letters*, vol. 100, pp. 061911-3, 2012.
- [210] T. Gorishnyy, *et al.*, "Direct observation of a hypersonic band gap in two-dimensional single crystalline phononic structures," *Applied Physics Letters*, vol. 91, pp. 121915-3, 2007.
- [211] S. Mohammadi, *et al.*, "Evidence of large high frequency complete phononic band gaps in silicon phononic crystal plates," *Applied Physics Letters*, vol. 92, pp. 221905-3, 2008.

BIBLIOGRAPHY

- [212] I. El-Kady, *et al.*, "Manipulation of thermal phonons: a phononic crystal route to High-ZT thermoelectrics," in *Proceedings of SPIE*, San Francisco, California, USA, 2011, pp. 794615-9.
- [213] C. M. Reinke, *et al.*, "Realization of optimal bandgaps in solid-solid, solid-air, and hybrid solid-air-solid phononic crystal slabs," *Applied Physics Letters*, vol. 98, pp. 061912-3, 2011.
- [214] G. Gesele, *et al.*, "Temperature-dependent thermal conductivity of porous silicon," *Journal of Physics D-Applied Physics*, vol. 30, pp. 2911-2916, Nov 7 1997.
- [215] C. C. Yang and S. Li, "Basic Principles for Rational Design of High-Performance Nanostructured Silicon-Based Thermoelectric Materials," *ChemPhysChem*, vol. 12, pp. 3614-3618, 2011.
- [216] K. Miyazaki, *et al.*, "Heat Conduction of a Porous Material," *Journal of Heat Transfer-Transactions of the Asme*, vol. 134, May 2012.
- [217] F. X. Alvarez, *et al.*, "Pore-size dependence of the thermal conductivity of porous silicon: A phonon hydrodynamic approach," *Applied Physics Letters*, vol. 97, Jul 19 2010.
- [218] J. de Boor, *et al.*, "Temperature and structure size dependence of the thermal conductivity of porous silicon," *Epl*, vol. 96, Oct 2011.
- [219] S. Gomes, *et al.*, "Application of scanning thermal microscopy for thermal conductivity measurements on meso-porous silicon thin films," *Journal of Physics D-Applied Physics*, vol. 40, pp. 6677-6683, Nov 7 2007.

BIBLIOGRAPHY

- [220] G. Romano, *et al.*, "Mesoscale modeling of phononic thermal conductivity of porous Si: interplay between porosity, morphology and surface roughness," *Journal of Computational Electronics*, vol. 11, pp. 8-13, Mar 2012.
- [221] A. I. Boukai, *et al.*, "Silicon nanowires as efficient thermoelectric materials," *Nature*, vol. 451, pp. 168-171, 2008.
- [222] D. Y. Li, *et al.*, "Thermal conductivity of individual silicon nanowires," *Applied Physics Letters*, vol. 83, pp. 2934-2936, Oct 6 2003.
- [223] J. Lim, *et al.*, "Quantifying Surface Roughness Effects on Phonon Transport in Silicon Nanowires," *Nano Letters*, 2012.
- [224] L. Liu and X. Chen, "Effect of surface roughness on thermal conductivity of silicon nanowires," *Journal of Applied Physics*, vol. 107, Feb 2010.
- [225] M. Luisier, "Investigation of thermal transport degradation in rough Si nanowires," *Journal of Applied Physics*, vol. 110, Oct 1 2011.
- [226] P. Martin, *et al.*, "Impact of Phonon-Surface Roughness Scattering on Thermal Conductivity of Thin Si Nanowires," *Physical Review Letters*, vol. 102, Mar 27 2009.
- [227] A. R. Abramson, *et al.*, "Fabrication and characterization of a nanowire/polymer-based nanocomposite for a prototype thermoelectric device," *Journal of Microelectromechanical Systems*, vol. 13, pp. 505-513, 2004.

BIBLIOGRAPHY

- [228] C. L. Haynes and R. P. Van Duyne, "Nanosphere lithography: A versatile nanofabrication tool for studies of size-dependent nanoparticle optics," *Journal of Physical Chemistry B*, vol. 105, pp. 5599-5611, Jun 21 2001.
- [229] X. Zhong, *et al.*, "Unveiling the Formation Pathway of Single Crystalline Porous Silicon Nanowires," *Acs Applied Materials & Interfaces*, vol. 3, pp. 261-270, Feb 2011.
- [230] Y. Qu, *et al.*, "Porous silicon nanowires," *Nanoscale*, vol. 3, pp. 4060-4068, 2011 2011.
- [231] J. M. Weisse, *et al.*, "Fabrication of Flexible and Vertical Silicon Nanowire Electronics," *Nano Letters*, 2012.
- [232] E. Garnett and P. D. Yang, "Light Trapping in Silicon Nanowire Solar Cells," *Nano Letters*, vol. 10, pp. 1082-1087, Mar 2010.
- [233] Y. Q. Qu, *et al.*, "Electrically Conductive and Optically Active Porous Silicon Nanowires," *Nano Letters*, vol. 9, pp. 4539-4543, 2009.
- [234] J. M. Weisse, *et al.*, "Vertical Transfer of Uniform Silicon Nanowire Arrays via Crack Formation," *Nano Letters*, vol. 11, pp. 1300-1305, Mar 2011.
- [235] J. Kim, *et al.*, "Au/Ag Bilayered Metal Mesh as a Si Etching Catalyst for Controlled Fabrication of Si Nanowires," *Acs Nano*, vol. 5, pp. 3222-3229, Apr 2011.

BIBLIOGRAPHY

- [236] M. L. Zhang, *et al.*, "Preparation of large-area uniform silicon nanowires arrays through metal-assisted chemical etching," *Journal of Physical Chemistry C*, vol. 112, pp. 4444-4450, 2008.
- [237] C. Chiappini, *et al.*, "Biodegradable Porous Silicon Barcode Nanowires with Defined Geometry," *Advanced Functional Materials*, vol. 20, pp. 2231-2239, Jul 23 2010.
- [238] M. A. Panzer, *et al.*, "Thermal properties of metal-coated vertically aligned single-wall nanotube arrays," *Journal of Heat Transfer-Transactions of the Asme*, vol. 130, May 2008.
- [239] M. Asheghi, *et al.*, "Thermal conduction in doped single-crystal silicon films," *Journal of Applied Physics*, vol. 91, pp. 5079-5088, 2002.
- [240] G. A. Slack, "THERMAL CONDUCTIVITY OF PURE + IMPURE SILICON SILICON CARBIDE + DIAMOND," *Journal of Applied Physics*, vol. 35, pp. 3460-&, 1964.
- [241] Y. Gong, *et al.*, "Observation of Transparency of Erbium-doped Silicon nitride in photonic crystal nanobeam cavities," *Optics Express*, vol. 18, pp. 13863-13873, 2010.
- [242] S. Yerci, *et al.*, "Energy transfer and 1.54 μm emission in amorphous silicon nitride films," *Applied Physics Letters*, vol. 95, pp. 031107-3, 2009.
- [243] S. Yerci, *et al.*, "Visible and 1.54 μm Emission From Amorphous Silicon Nitride Films by Reactive Cosputtering," *IEEE Journal of Selected Topics in Quantum Electronics*, vol. 16, pp. 114-123, 2010.

BIBLIOGRAPHY

- [244] Z. H. Cen, *et al.*, "Optical Transmission and Photoluminescence of Silicon Nitride Thin Films Implanted with Si Ions," *Electrochemical and Solid-State Letters*, vol. 12, pp. H38-H40, 2009.
- [245] R. Li, *et al.*, "Carrier dynamics and erbium sensitization in silicon-rich nitride nanocrystals," *Applied Physics Letters*, vol. 93, pp. 091119-3, 2008.
- [246] A. Gopinath, *et al.*, "Enhancement of the 1.54 μm Er^{3+} emission from quasiperiodic plasmonic arrays," *Appl. Phys. Lett.*, vol. 96, p. 071113, 2010.
- [247] S. Yerci, *et al.*, "Electroluminescence from Er-doped Si-rich silicon nitride light emitting diodes," *Appl. Phys. Lett.*, vol. 97, p. 081109, 2010.
- [248] A. C. Hryciw, *et al.*, "Thermo-optic tuning of erbium-doped amorphous silicon nitride microdisk resonators," *Applied Physics Letters*, vol. 98, pp. 041102-3, 2011.
- [249] D. G. Cahill, "Analysis of heat flow in layered structures for time-domain thermoreflectance," *Review of Scientific Instruments*, vol. 75, pp. 5119-5122, 2004.
- [250] A. Schmidt, *et al.*, "An optical pump-probe technique for measuring the thermal conductivity of liquids," *Review of Scientific Instruments*, vol. 79, pp. 064902-5, 2008.
- [251] M. A. Panzer, *et al.*, "Thermal Properties of Ultrathin Hafnium Oxide Gate Dielectric Films," *IEEE Electron Device Letters*, vol. 30, pp. 1269-1271, 2009.

BIBLIOGRAPHY

- [252] J. P. Reifenberg, *et al.*, "Thermal Boundary Resistance Measurements for Phase-Change Memory Devices," *IEEE Electron Device Letters*, vol. 31, pp. 56-58, 2010.
- [253] A. M. Marconnet, *et al.*, "Phonon thermal conduction in periodically porous silicon nanobridges," (*under review*), 2012.
- [254] A. Marconnet, *et al.*, "Thermal conductivity and photoluminescence of light-emitting silicon nitride films," *Applied Physics Letters*, vol. 100, pp. 051908-4, 2012.
- [255] W. Kim, *et al.*, "Thermal Conductivity Reduction and Thermoelectric Figure of Merit Increase by Embedding Nanoparticles in Crystalline Semiconductors," *Physical Review Letters*, vol. 96, p. 045901, 2006.
- [256] Y. Hong, *et al.*, "Enhancing Heat Capacity of Colloidal Suspension Using Nanoscale Encapsulated Phase-Change Materials for Heat Transfer," *ACS Applied Materials & Interfaces*, vol. 2, pp. 1685-1691, 2010/06/23 2010.
- [257] A. Lenert and E. N. Wang, "Optimization of nanofluid volumetric receivers for solar thermal energy conversion," *Solar Energy*, vol. 86, pp. 253-265, 2012.
- [258] S. Maity, *et al.*, "Embedded metal nanoparticles as localized heat sources: An alternative processing approach for complex polymeric materials," *Polymer*, vol. 52, pp. 1674-1685, 2011.
- [259] Z. Qin and J. C. Bischof, "Thermophysical and biological responses of gold nanoparticle laser heating," *Chemical Society Reviews*, vol. 41, pp. 1191-1217, 2012.

BIBLIOGRAPHY

- [260] F. Banfi, *et al.*, "Temperature dependence of the thermal boundary resistivity of glass-embedded metal nanoparticles," *Applied Physics Letters*, vol. 100, pp. 011902-3, 2012.